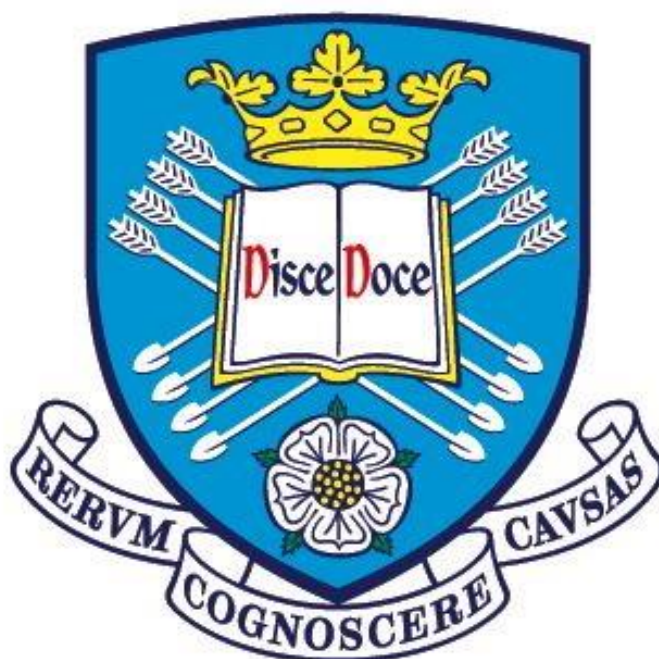


# BIOMIMETIC SYNTHESIS OF MAGNETOSOMES FOR BIOMEDICAL APPLICATION.

Thesis submitted for the degree of Doctor of Philosophy



Jennifer Bain

Supervisor: Dr S.S. Staniland

The University of Sheffield - Department of Chemistry



# ABSTRACT

Biom mineralisation is the biological control over precipitation of minerals, observed in a wide variety of organisms. In biom mineralisation processes, proteins control both the nucleation and propagation steps in the precipitation of inorganic minerals, forming complex architectures with exceptional levels of control. Magnetotactic bacteria (MTB) use biom mineralisation proteins encoded within their genome for the formation of extremely monodisperse biom mineralised magnetite nanoparticles (MNPs) within an organelle (vesicle) termed the magnetosome. Precipitation of MNPs within this internal magnetosome vesicle with the aid of biom mineralisation proteins allows such control over precipitation of high quality MNPs to be realised.

Exploitation of the magnetosome formation process *via* biomimetic precipitation within a synthetic vesicle to form an artificial magnetosome is developed throughout this thesis. This is by optimisation of a vesicle nanoreactor for incorporation of a magnetite precipitation reaction within its core. This is by encapsulation of the alkaline reagent for the ensuing magnetite co-precipitation, which was found to be the most appropriate route to intra-vesicular precipitation. Various routes to transport iron ions into the core for completion of magnetite MNP precipitation are explored. Iron transport using biokleptic, biomimetic and entirely synthetic methods of transmembrane transport all have differing precipitation outcomes. Engineering co-precipitation inside a vesicle to form a single magnetite crystal mimics the formation, and ideally the behaviour, of a magnetosome.

Mimicking MTB precipitation magnetosome formation synthetically to achieve high quality homogenous and adaptable nanoparticles (NPs), as observed with naturally biom mineralised magnetite. These particles should, have superior biomedical properties to synthetically made particles, currently used in nanomedicine, where MNPs hold potential for theranostic/drug delivery, hyperthermic and imaging applications.

# TABLE OF CONTENTS

Introduction	19	
1.1	Magnetism and Magnetite	2
1.1.1	Magnetism	2
1.1.2	Magnetite	7
1.2	Magnetite formation routes	9
1.3	Biomineralisation and Biomimetics	13
1.3.1	Biomineralisation	13
1.3.2	Magnetotactic Bacteria	15
1.4	Vesicles	19
1.4.1	Self-Assembly	20
1.4.2	Lipids	24
1.4.3	Polymers	26
1.4.4	Formation Methods	29
1.5	Biomimetics	34
1.6	Applications of Biomimetics	36
1.6.1	General Drug Delivery Applications	37
1.6.2	Applications of Magnetic Nanoparticles	38
1.6.3	MNP Properties Required for MHT	42
1.6.4	Biomedical uses of Magnetosomes	43
1.7	Artificial Magnetosomes	44
1.7.1	Biomimetic Magnetosome System	45
1.7.2	Aims and Objectives	48
2	Methods and Materials	51
2.1	Magnetite Synthesis	52
2.1.1	Room Temperature Co-Precipitation (RTCP)	52

2.1.2	Thermal Decomposition of Urea Co-precipitation	53
2.1.3	Urea and Ammonia Co-precipitation	53
2.2	Vesicle Synthesis	53
2.2.1	Liposome Formation	54
2.2.2	Polymersome Formation	54
2.2.3	Vesicle size and polydispersity control methods	55
2.2.4	Vesicle Clean up	57
<b>2.2</b>	<b>Iron transport methods</b>	<b>59</b>
2.2.5	Electrohydrodynamic Atomisation Vesicle Synthesis	59
2.3	Iron Transport	60
2.3.1	biological transporters	60
2.3.2	A23187 divalent ionophore	61
2.3.3	Electroporation	61
2.3.4	<i>In-situ</i> incorporation	62
2.4	Iron ion transports assays	62
2.4.1	Carboxyfluorescein	62
2.4.2	Ferene	63
2.4.3	Prussian Blue	63
2.4.1	Resazurin	65
2.5	Control of particle formation	65
2.6	Protein cloning and purification Methods	66
2.6.1	Gene Cloning	66
2.6.1	Protein Preparation	71
2.7	Characterisation and Instrumentation	75
2.7.1	Vesicle Characterisation	75
2.7.2	Spectrographic Techniques	80
2.7.3	Magnetic Measurements	84
2.7.4	Protein Characterisation	85
2.7.5	Magnetic Hyperthermia Measurements	88

3	Magnetite formation and quantification of iron ion transport	90
3.1	Introduction	91
3.2	Routes to magnetite Formation	92
3.2.1	Thermal decomposition of Urea	95
3.2.2	Combined Urea/Ammonia decomposition	96
3.2.3	Room Temperature Co-precipitation of Magnetite	97
3.3	Magnetite formation summary and further work	100
3.4	Membrane transport assays	103
3.4.1	Measurement of inter-vesicular redox potential	104
3.4.2	Quantification of ferric/ferrous ion transport	106
3.4.3	Vesicles Leakage assay	109
3.5	Ways Forward and Conclusions	110
4	Vesicle Formation: Optimisation of the Formation of Liposomes and Polymersomes	113
4.1	Introduction to Vesicle Formation	114
4.2	Liposomes	115
4.2.1	Phospholipid selection	115
4.2.2	liposome formation	122
4.2.3	Liposome Formation Discussion	129
4.3	Polymersomes	130
4.3.1	Polymer Properties	130
4.3.2	Polymersome formation	134
4.3.3	Polymersome Formation Discussion	145
5	Biomimetic transport systems	147
5.1	Introduction to Biomimetic Transport Systems	148
5.2	Bacterial Iron Transporters	149
5.2.1	Cloning of Iron Transporters	152
5.2.2	Expression of Iron Transporters	155
5.2.3	Transporter Purification	158

5.2.4	Incorporation into vesicles	160
5.3	Ionophore iron transport	161
5.3.1	A23187 incorporation into polymersomes	161
5.4	Biomimetic Transport Systems Discussion	164
6	Synthetic Transport Systems	167
6.1	Introduction to Synthetic Reagent Transport	168
6.2	Electroporation of Vesicle Membranes	169
6.2.1	Electroporation of Liposomes	169
6.3	Electroporation of Polymersomes	176
6.3.1	Di-block Polymersomes	176
6.3.2	Tri-block Polymersomes	186
6.3.3	Carboxylic Acid Terminated RAFT Synthesised Polymersomes	192
6.4	Optimisation of electroporation	193
6.5	Room Temperature: Incorporation of Iron into RAFT Polymersomes	198
6.6	Discussion of Synthetic Transport Systems	202
7	High-throughput Synthesis and Electroporation of Vesicles	205
7.1	Introduction to High-throughput Synthesis using Electrohydrodynamic Atomisation (EHDA)	206
7.2	High throughput Vesicle Formation using EHDA	208
7.2.1	Optimisation of EHDA	208
7.3	Synthesis of Magneto-liposome 'Artificial Magnetosomes'	213
7.4	Characterisation of Magneto-liposome 'Artificial Magnetosomes'	218
7.4.1	Electron Microscopy of Magneto-liposome 'Artificial Magnetosomes'	218
7.4.2	Raman Spectroscopy of Magneto-liposome 'Artificial Magnetosomes'	220
7.4.3	Fluorescence of Magneto-liposome 'Artificial Magnetosomes'	221

7.4.4	Bulk Magnetic Properties of Magneto-liposome ‘Artificial Magnetosomes’	222
7.5	Adaptability of EDHA for Artificial Magnetosome Synthesis	224
7.5.1	DOPC Magneto-Liposomes <i>via</i> EHDA	224
7.5.2	Microscopy of DOPC Magneto-liposomes <i>via</i> EDHA	225
7.6	Discussion of EHDA Magneto-vesicle Synthesis	226
8	Biom mineralisation of iron oxides	227
8.1	Introduction to the Biom mineralisation of Iron Oxides	228
8.2	Proteins Used in Synthetic Vesicles	229
8.3	Magnetite Biom mineralisation Protein Properties and Purification	230
8.3.1	Proteins	230
8.3.1.2	Mms	231
8.4	Protein Effects on <i>In Vitro</i> Precipitation	237
8.4.1	MmsF in Mineralisation Reactions	237
8.4.2	Mms6	238
8.4.3	Coiled-coils	239
8.5	Vesicle Incorporation of Biom mineralisation Proteins	241
8.5.1	Lipids and Proteins	241
8.5.2	Polymers and Coiled-coils	244
8.6	Biom mineralisation within Vesicles: Discussion	245
9	Biomedical Application of Magneto-vesicles	248
9.1	Introduction	249
9.2	<i>In vitro</i> Magnetic Hyperthermia Tests	250
9.2.1	Calibration of the Magnetherm	250
9.2.2	Magneto-vesicle Heating Capability	252
9.3	Magneto-vesicles as MRI Contrast Agents	259
9.3.1	Calibration of measurements	259
9.3.2	Magneto-vesicle MRI measurements	262
9.3.3	Altering the Iron Concentration: Effects in MRI	264

9.4	Discussion of Biomedical Applications of Magneto-vesicles	267
10	Future work and Conclusions	269
10.1	Conclusions	270
	10.1.1 Vesicle Optimisation for Mineralisation	270
	10.1.2 Characterisation of Magneto-vesicles for use in Biomedical Applications	274
10.2	Future Work	274
11	Bibliography	277
12	APPENDIX	292

# LIST OF TABLES

Table 1.1	Physio-chemical properties of Magnetite
Table 1.2	Chapter summary of project
Table 2.1	Components of protein cloning and expression recipes
Table 2.2	Buffers and solution in biology protocols
Table 3.1	Summary of magnetite precipitation routes
Table 4.1	Phospholipids investigated for liposome formation
Table 4.2	Outcomes of high throughput phospholipid screening
Table 4.3	Polymers investigated for polymersome formation
Table 5.1	Properties of iron transporters investigated
Table 7.1	Single axial experiments for EHDA vesicle synthesis
Table 7.2	Optimisation of EHDA parameters
Table 7.3	Optimisation of EHDA parameters for synthesis of DSPC liposomes
Table 9.1	ILP values of magneto-vesicle samples
Table 10.1	Summary of various methods used throughout the project

# LIST OF FIGURES

Figure 1.1	MH Curve schematic
Figure 1.2	Schematic of MNP magnetic moment alignment
Figure 1.3	Schematic of particle size versus coercivity
Figure 1.4	Schematic of magnetite structure
Figure 1.5	Iron oxide formation Pourbaix diagram
Figure 1.6	Natural biomineralisation within organisms
Figure 1.7	Formation of the MTB magnetosome
Figure 1.8	Schematic of critical micelle concentration as a function of monomer concentration
Figure 1.9	Schematic of forces governing self-assembly
Figure 1.10	Determination of packing factor in self-assembly
Figure 1.11	Schematic of di-block and tri-block polymer structure
Figure 1.12	Schematic of asymmetric vesicle preparation <i>via</i> inverted emulsion
Figure 1.13	Schematic of cDICE formation of asymmetric vesicles
Figure 1.14	Synthetic magnetosome formation by Mann <i>et al</i>
Figure 1.15	Hypothesis of transmembrane transport of ions
Figure 1.16	Schematic of overall objective of the thesis
Figure 2.1	Schematic of extrusion of vesicles.
Figure 2.2	Schematic of size exclusion chromatography (SEC)
Figure 2.3	Schematic of EHDA synthesis of vesicles
Figure 2.4	Schematic of Iron transport assays
Figure 2.5	Schematic of Polymerase Chain Reaction
Figure 2.6	Schematic of DNA Digestion and Ligation
Figure 2.7	Schematic of Transmission Electron Microscopy
Figure 2.8	Schematic of Gel Electrophoresis
Figure 3.1	pH profiles of magnetite formation
Figure 3.2	TEM and grainsize analysis of particles produced by thermal decomposition co-precipitation with urea
Figure 3.3	TEM and grainsize analysis of particles produced by room temperature co-precipitation with NaOH
Figure 3.4	Optimisation of hydroxide concentration
Figure 3.5	Magnetic nanoparticle x-ray diffraction patterns
Figure 3.6	Resazurin assay calibration data
Figure 3.7	Ferene assay calibration data
Figure 3.8	Prussian Blue assay calibration data
Figure 3.9	Carboxyfluorescein assay calibration data
Figure 4.1	Plot of average of vesicle size produced with each formation method
Figure 4,2	TEM and grainsizing of each liposome sample investigated

- Figure 4.3 Schematic of PEG-PHPMA/PMPC-PHPMA Mms6 mimic protein
- Figure 4.4 TEM and grainsizing of each di-block polymer investigated
- Figure 4.5 TEM micrograph of PBD-PEO polymersomes encapsulating NaOH
- Figure 4.6 TEM micrograph of PBD-PEO polymersomes encapsulating  $\text{CO}(\text{NH}_2)_2$
- Figure 4.7 TEM micrograph of PMOXA-PDMS-PMOXA polymersomes formed by alternative methods
- Figure 4.8 Synthesis route for the reversible addition fragmentation chain transfer (RAFT) polymerisation of PMPC-PHPMA
- Figure 4.9 Comparison of the effect of variation of PMPC block length in PEG<sub>113</sub>-PHPMA<sub>400</sub>/30% PMPC<sub>28</sub>-PHPMA<sub>400</sub> polymersomes
- Figure 4.10 TEM micrographs of PEG<sub>113</sub>-PHPMA<sub>400</sub>/30% PMPC<sub>28</sub>-PHPMA<sub>400</sub> produced under different conditions.
- Figure 5.1 Hydropathy plot for each iron transporter
- Figure 5.2 Gel electrophoresis of *magA* PCR product
- Figure 5.3 Gel electrophoresis of *mamMB* PCR product
- Figure 5.4 Dot blot of expression trial with each iron transporter
- Figure 5.5 Western blot of MamMB
- Figure 5.6 TEM micrograph of MamMB incorporation into DPhPC liposomes
- Figure 5.7 TEM micrographs of ionophore incorporation into polymersomes
- Figure 6.1 TEM micrographs of electroporated liposomes containing NaOH
- Figure 6.2 TEM micrographs of electroporated liposomes containing  $\text{CO}(\text{NH}_2)_2$
- Figure 6.3 TEM micrographs of electroporated polymersomes containing  $\text{CO}(\text{NH}_2)_2$
- Figure 6.4 TEM micrographs of electroporated polymersomes containing NaOH
- Figure 6.5 Schematic of hypothesised mechanism of electroporation
- Figure 6.6 EDX spectrum of PBD-PEO magnetopolymersomes
- Figure 6.7 SQUID analysis of magnetopolymersomes
- Figure 6.8 Assay of NaOH leakage during polymersome electroporation
- Figure 6.9 TEM micrograph of electroporated PMOXA-PDMS-PMOXA
- Figure 6.10 TEM micrograph and grainsizing of electroporated and control PMOXA-PDMS-PMOXA polymersomes
- Figure 6.11 Schematic of hypothesised mechanism of electroporation of tri-block polymersomes
- Figure 6.12 TEM micrographs of electroporated PEG<sub>113</sub>-PHPMA<sub>400</sub>/30% PMPC<sub>28</sub>-PHPMA<sub>400</sub>
- Figure 6.13 ICP-MS analysis of PBD-PEO magnetopolymersomes as a function of applied voltage
- Figure 6.14 Fe content in PBD-PEO magnetopolymersomes as a function of pulse number
- Figure 6.15 TEM micrographs of PBD-PEO magnetopolymersomes electroporated at different voltages/NaOH concentrations
- Figure 6.16 ICP-MS analysis of PMOXA-PDMA-PMOXA magnetopolymersomes as a function of applied voltage
- Figure 6.17 TEM micrographs of PEG<sub>113</sub>-PHPMA<sub>400</sub>/30% PMPC<sub>28</sub>-PHPMA<sub>400</sub> polymersome soaked in iron solution
- Figure 6.18 Schematic of room temperature precipitation incorporation into polymersomes

Figure 6.19	TEM micrographs of room temperature precipitation incorporation into PEG <sub>113</sub> -PHPMA <sub>400</sub> /30% PMPC <sub>28</sub> -PHPMA <sub>400</sub> polymersomes
Figure 7.1	Schematic of EHDA synthesis of vesicles
Figure 7.2	TEM micrographs of initial EHDA vesicle synthesis
Figure 7.3	TEM micrographs of control EHDA synthesised DSPC liposomes
Figure 7.4	TEM, SEM and EDX for EHDA synthesised DSPC liposomes
Figure 7.5	TEM micrographs of 750 V electroporated EHDA synthesised DSPC magneto-liposomes
Figure 7.6	Raman spectrum of EHDA synthesised DSPC magneto-liposomes
Figure 7.7	Fluorescence microscopy of Bodipy assay
Figure 7.8	300 K SQUID MH curve of EHDA synthesised DSPC magneto-liposomes
Figure 7.9	Zero field cooled SQUID MH curve of EHDA synthesised DSPC magneto-liposomes
Figure 7.10	TEM micrographs of 750 V electroporated EHDA synthesised DOPC magneto-liposomes
Figure 8.1	Sequence analysis of MmsF
Figure 8.2	Sequence analysis of Mms6
Figure 8.3	Schematic and sequence analysis coiled coil artificial scaffold
Figure 8.4	Western blot and circular dichroism of purified MmsF
Figure 8.5	TEM micrographs of MmsF proteinosome assembly
Figure 8.6	TEM micrographs of MNPs with and without MmsF protein
Figure 8.7	TEM micrographs of MNPs with and without Mms6 protein
Figure 8.8	TEM micrographs of MNPs with and without coiled coil protein
Figure 8.9	TEM micrographs of MmsF incorporated DPhPC liposomes
Figure 8.10	TEM micrographs of Mms6 incorporated DPhPC liposomes
Figure 8.11	TEM micrographs of coiled coil incorporated PBD-PEO polymersomes
Figure 9.1	Hyperthermic heating ability of various magneto-vesicles
Figure 9.2	Hyperthermic heating ability of PBD-PEO magnetopolymersomes (2500 V)
Figure 9.3	Hyperthermic heating ability of PBD-PEO magnetopolymersomes (various electroporation voltages)
Figure 9.4	Plot of relative ILP versus electroporation voltage
Figure 9.5	Control MRI images of magneto-polymersomes
Figure 9.6	R <sub>2</sub> relaxation of magneto-polymersomes
Figure 9.7	R <sub>2</sub> * relaxation of magneto-polymersomes
Figure 9.8	MRI images of magneto-polymersomes/liposomes
Figure 9.9	Optimised R <sub>2</sub> /R <sub>2</sub> * of PBD-PEO magneto-polymersomes
Figure 9.10	R <sub>2</sub> relaxation of serially diluted PBD-PEO magneto-polymersomes
Figure 9.11	[Fe] <sup>-1</sup> s <sup>-1</sup> as a function of Fe concentration and applied voltage

# ABBREVIATIONS AND DEFINITIONS

$\eta$	Viscosity	FieF	Cation diffusion facilitator protein
$\sigma$	Standard deviation	GPC	Gel permeation chromatography
$\mu\text{l}$	Microlitre	GUV	Giant unilamellar vesicle
$^{\circ}\text{C}$	Degrees Celsius	HOMO	Highest occupied molecular orbital
$\varepsilon$	Extinction coefficient	ICP-MS	Inductively coupled plasma mass spectroscopy
A	Absorbance	IGP	Ion getter pump
b	Block separation in copolymers	ILP	Intrinsic loss power
BL21	E. Coli cells for protein expression	k	Boltzmann's constant
c	concentration	K	Kelvin
CCP	Close cubic packing	kDa	Kilo Dalton
CDF	Cation diffusion facilitator	keV	Kilo electron volts
CEHDA	Co-axial electrohydrodynamic atomisation	kHz	Kilo Hertz
cDICE	Continuous droplet interface crossing encapsulation	kT	Absolute temperature
CMC	Critical micelle concentration	kV	Kilovolts
D	Diffusion coefficient	l	Incident light
DH	Hydrodynamic diameter	l0	Transmitted light
DLS	Dynamic light scattering	LB	Lysogeny Broth
DNA	Deoxyribonucleic acid	LUMO	Lowest unoccupied molecular orbital
dNTPs	Deoxynucleotides Triphosphates	LUV	Large unilamellar vesicle
DPPA	1,2-dipalmitoyl- <i>sn</i> -glycero-3-phosphate	M	Mole
E. Coli	Escherichia coli	Mam	Magnetosome associated membrane
EDX	Energy dispersive x-ray	mg	Milligram
Eh	Voltage relative to the standard hydrogen electrode	MHT	Magnetic hyperthermia treatment
EHDA	Electrohydrodynamic atomisation	ml	Millilitres

FieF	Cation diffusion facilitator protein	MLV	Multi-lameallar vesicle
MNP	Magnetic nanoparticle	SEC	Size Exclusion Chromatography
MRI	Magnetic resonance imaging	SQUID	Super quantum interference conduction device
MTB	Magnetotactic bacteria	SUV	Small unilamellar vesicle
mm	Millimetre	T <sub>abs</sub>	Absolute temperature
mM	Milli moles	TB	Terrific Broth
Mms	Magnetosome membrane specific	TEM	Transmission electron microscopy
nm	Nanometres	Tg	Glass Transition Temperature
OATZ	Oxic-anoxic transition zone	V	Volts
Oe	Oersted	x	Ratio of ferric ion to total iron
PA	Phosphatidic acid	XL10	<i>E. Coli</i> cells for gene cloning
PBD	Polybutadiene		
PBS	Phosphate buffered saline		
PC	Phosphocholine		
PCR	Polymerase chain reaction		
PdI	Polydispersity Index		
PEG	Polyethylene Glycol		
PDMS	Polydimethyl Siloxane		
pH	$-\log_{10}[\text{H}^+]$		
PMOXA	Poly (2-methyloxazoline)		
ppb	Parts per billion		
ppm	Parts per million		
R	Ratio of total iron to hydroxyl ions		
rpm	Revolution per minute		
SAR	Specific absorption rate		
SB	Super Broth		
SDS	Sodium dodecyl sulphate		

# AUTHOR DECLARATIONS AND CONTRIBUTIONS

Except where specific references have been made to other sources the work in this thesis is the original work of the author and has not been submitted wholly or in part for any other degree.

**Chapter 3:** pH traces (Figure 3.1) and XRD data (Figure 3.5) is unpublished work collected by Dr. Jonathan Bramble and Miss Lays Gierakowski respectively (previous members of the Staniland group).

**Chapter 4 and 6:** Data in these chapters were collected with the help of Enrique Muñoz Albaladejo, (BSc (Hons)) and Miguel Perez Senent (BSc (Hons)) at the University of Leeds, who assisted with collection of phospholipid data in chapters 4 and 6. Optimisation of polymersome formation was carried out with the help of Alan Lee Holmes (BSc (Hons)) (University of Leeds) in addition to Matthew E. Berry, (MChem) Catherine E Dirks (MChem) and Hugo Lynch (MSc) (University of Sheffield). All students carried out the work under my supervision and direction as part of their final year projects. Initial polymersome experiments were carried out in collaboration with the Dr. Lorena Ruiz-Perez (from the lab of Professor Giuseppe Battaglia, now at University college London). Cryogenic TEM and tomography was performed with the help of Dr Stephen Meunch and Miss Rebecca Thompson (BMS, University of Leeds)

**Chapter 5 and 8:** Protein work was carried out under the supervision of Dr. Andrea Rawlings, who designed all vectors, primers and synthetic genes, who also advised on all methods and results. All iron transporters (with the exception of MagA and MamMB), biomineralisation protein and coiled coil scaffolds have also previously been cloned expressed and purified by Dr Rawlings.

**Chapter 7:** Work in chapter 7 has been carried in close collaboration with Professor Mohan Edirisinghe, Dr. Poonam Bakshi and Mr. Meghdi Eltyab, (Department of Mechanical engineering, Univerity college London) with whom I optimised the EHDA system for artificial magnetosome synthesis with the help of their expertise.

**Chapter 9:** MRI data was collected by Dr Annuerin Kennerley (Magnetic Resonance Physicist for fMRI facility, Department of Psychology, University of Sheffield) and MHT data in figures 9.2 and 9.3 was collected by Dr Paul Southern (UCL Nanomagetics Lab). SQUID data was collected by either Dr. Paul southern or Miss Wala Dizayee ( Department of Physics, Univeristy of Sheffield).

# ACKNOWLEDGEMENTS

This project has been supported by funding from the Engineering and Physical Sciences Research Council (EPSRC). Firstly I would like to thank Sarah Staniland for not laughing me out of her office when I said I would like to take up her PhD project (following a recommendation from Professor Paul Millner). Sarah has been a great support over the last four years, keeping me busy with her off-the-wall ideas (all of which have worked!) Allowing me to cultivate my own collaborations, and visit far-flung destinations (even if I do only get three days' notice). Her drive, energy and guidance are the reason for the wide-ranging success of this project, and have spurred me on to make the most of the four years (and she let us move back to our natural environment of a Chemistry department, for which I'll be forever grateful!!). A big thank also goes to Lays Gierakowski for imparting her wealth of knowledge on me and ladened me with insider tip on vesicle making before running away to London.

Secondly thank you to the rest of the Staniland group (past and present), Andrea, Jo, (proof-reading extraordinaire) Jon, Scott, Lori, Zainab and Pawel (you make every day entertaining), and in particular the undergraduate students which have contributed to this project (Alan, Enrique, Miguel, Catherine, Matt and Hugo) thank for doing as you were told (most of the time). A special thank you to Andrea Rawlings who kept everybody in check during our epic lab move, (and still keeps us in line on a daily basis), the best thing to come out of our move is that we now work in the same department (I would other have never known the importance of tea breaks), and having the patience of a saint when it comes to my incessant molecular biology questions.

A big thank you to all of the people in the Molecular and Nanoscale Physics Group, you made the first two years of my PhD truly memorable and are still some of my close friends (particularly Jo, Meg and Spanish) which is surprising given the fact you are physicists.

To all the people who have helped me hone my expertise in such a wide and varied field particularly all those people who have spent so long showing me the ropes in the world of microscopy (In Leeds, Mike Ward, Martin Fuller, Stephen Meunch and Rebecca Thompson and in Sheffield Svet Tzokov and Chris Hill).

Thank you Beppe and Lorena for introducing me to the world of polymer chemistry and Dave Adams (University of Liverpool) and Steve Armes, Joe Lovett and Christine Fernyhough (University of Sheffield) for kindly donating batches of polymer (so that I didn't have to learn to make it!). Dr. Aneurin Kennerly has been invaluable to the biomedical success of this project and has been extremely patient in explaining MRI to a complete novice.

To all of the collaborators in Mechanical Engineering at UCL (Mohan Poonam and Meghdi), I have thoroughly enjoyed my time in your lab and getting a taste of what it is like to be engineer, huge thanks to Mohan for all of your help in trying to cement the next stage of my career and of course your highly entertaining conversations. Also at UCL thank you to Quentin Pankhurst and Paul Southern for all of your help and guidance in getting to grips with magnetic hyperthermia treatment.

Of course I should thank my mum, dad and KAB for humouring me when I said I was going back to "school" and offering nothing but encouragement and interest in my project, particular thank to my mum for her amazing dedication to proof-reading this thesis, and to KAB who has no hesitation in reminding me that no matter how much I know about vesicles I am still severely lacking in common sense. Thanks to all of "the girls" to providing a world away from Science (Particularly to Alex (Fat-arse) for her constant encouragement and volunteering to read this thing for me).

And lastly the biggest thanks to Scott (Thanks lad!) for supporting my hair-brained scheme to move to Leeds and "do" science, you packed your bags with no questions asked and we started a new life in Yorkshire, you "barely" batted an eyelid when two years later we were on the move again down to Sheffield. Not many people would have followed me round the country but I hope you've enjoyed our four year adventure as much as I have and here's to the next one wherever we may end up.

# BIBLIOGRAPHY

## **Bain and Staniland**

Bioinspired nanoreactors for the biomineralisation of metallic-based nanoparticles for nanomedicine. *Physical Chemistry Chemical Physics* (2015).

## **Bain et al.**

In situ formation of magnetopolymersomes via electroporation for MRI. *Scientific Reports* **5**, 14311, (2015).

## **Rawlings et al**

Self-assembled MmsF proteinosomes control magnetite nanoparticle formation in vitro. *Proceedings of the National Academy of Sciences* **111**, 16094-16099 (2014).

## **Bain et al**

Synthesis of ABA Tri-block co-polymer magnetopolymersomes via electroporation for potential medical application, *Polymers* (2015)

## **Bakshi/Bain et al**

Manufacturing Man-made Magnetosomes: High-Throughput in situ synthesis of biomimetic magnetite loaded nanovesicles. *Material Horizons* **Under Review**.

# CHAPTER 1:

---

## INTRODUCTION

In this introduction chapter I will discuss background relevant to the biomimetic synthesis of magnetosomes for biomedical applications. This is a multi-disciplinary study inspired by nature, spanning physics, chemistry, biology, medicine, nanotechnology and nanomaterials synthesis. Magnetism and the magnetic material magnetite are discussed in section 1.1 and biomineralisation and magnetotactic bacteria in section 1.3. Artificial vesicles are described in section 1.4, biomimetics in section 1.5 and their application in 1.6. Finally, the introduction includes a description of the aims and objectives in the context of artificial magnetosome design in section 1.7. Aspects of this chapter are based on the review Bain *et al*<sup>10</sup>

## 1.1 MAGNETISM AND MAGNETITE

The theory of magnetism as described in this section is from Blundell,<sup>11</sup> Newey and Weaver<sup>12</sup> and Pankhurst *et al*.<sup>13</sup>

### 1.1.1 MAGNETISM

The magnetic properties of a material are governed by its susceptibility to manipulation by an externally applied magnetic field. When a magnetic field is applied, electrons in an atom align with the direction of the applied field. The alignment of these electrons (parallel or antiparallel) determines whether a material is magnetic without the presence of an applied field. The measurement of a material's magnetism is represented on a MH curve, (Figure 1.1). Figure 1.1 shows the magnetisation (M) of a material, in an applied magnetic field of strength H. The susceptibility ( $\chi$ ) of a material is determined by how magnetised (M) per unit volume it becomes in the presence of a magnetic field of strength (H), this relationship is shown in equation 1.1. The MH curve is generally sigmoidal as a result of increasing magnetisation of the material, with increasing H, until a point of magnetic saturation is reached.

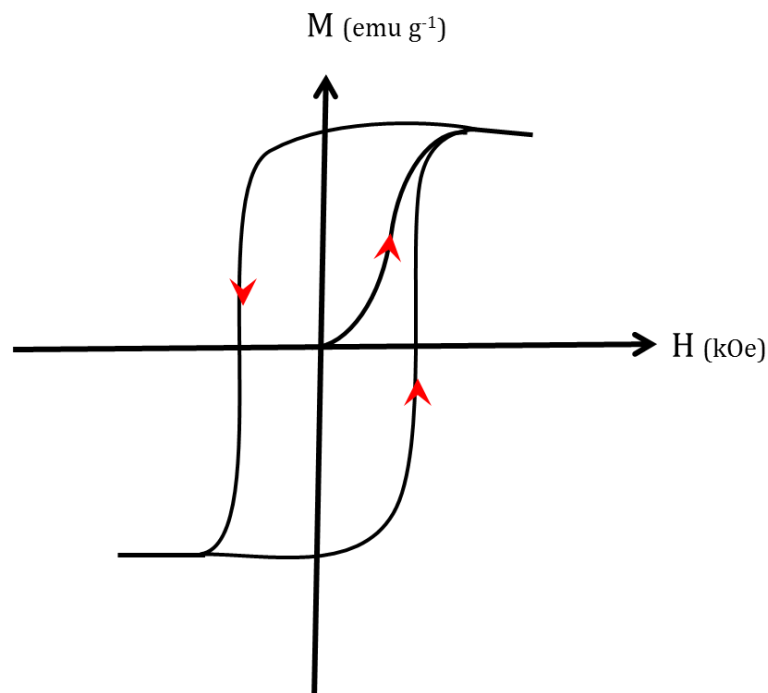


**Figure 1.1:** Schematic of a magnetic hysteresis loop (MH curve), which measures the magnetisation of a material ( $M$ ) as a function of the strength of the magnetic field ( $H$ ) as the field increases the material is magnetised in the same direction, the field is then returned back to zero and the field and the sample is magnetised in the opposite direction. This cycle is repeated with the material reaching its magnetisation saturation (a) in each direction. Arrows indicate the direction of the magnetisation. The materials coercivity is shown by (b) the strength of the externally applied field required to reorder the material back to a zero.

As the field increases the material is magnetised in the same direction, the field is then returned back to zero and the field and the sample is magnetised in the opposite direction. This cycle is repeated with the material reaching its magnetisation saturation (a) in each direction (Figure 1.1). These parameters change the hysteresis of a material, defined as the field strength required to flip the moments and realign them in the opposite field direction, once magnetisation saturation is reached. When the particle is cycled between the positive (+) and negative (-) field, it gives rise to a hysteresis loop. The width of this hysteresis is determined by the field strength needed to flip all the spins; namely its coercivity. The coercivity of the magnetic material is the point at which an externally applied field reorders the material and hence the magnetic flux of the material returns to zero.

The steepness of this curve describes how easily magnetised a material is (with more easily magnetised samples aligning at a lower  $H$ ). It is also dependent on the type of magnetism a material displays, i.e. its size/spin alignment and the material's atomic structure.

$$M = \chi H \quad (1.1)$$

All materials possess magnetic characteristics due to the atoms containing electrons. In some materials there is no remnant magnetisation of the lattice in the absence of an external magnetic field. In these materials, magnetism still exists at an atomic level in the form of diamagnetism or paramagnetism. Diamagnetism occurs when all electrons in a material are paired, in this case the material's spins align antiparallel to the field direction and therefore it is repelled in a magnetic field (Figure 1.2 b). This alignment means there is no net magnetic moment (due to no net motion of electrons, as all are paired) when a field is applied and therefore the material is weakly repelled by the field. The opposite is true in the case of paramagnetic materials, where unpaired electrons within the atomic structure show an attraction and align along the field (Figure 1.2 a). Both of these materials have a linear response in their  $MH$  curve, as the magnetism is lost when the field is removed.

More ordered atomic structures give rise to paramagnetic materials with long range ordering, which can have remnant magnetism when the external field is removed. If this ordering is antiparallel across the entire lattice, then the atomic spins cancel. This leads to zero bulk magnetic moment in these materials. Materials which have this type of bulk alignment are called antiferromagnets (AFM) (Figure 1.2 c). If the opposite is the case, and all of the atomic magnetic moments are aligned parallel to one another, then this long-range ordering causes remnant magnetism when the field is removed, the material is ferromagnetic (FOM), (Figure 1.2 d). A third situation is also possible in which the atomic magnetic moments are aligned antiparallel as in AFM materials, but, due to a difference in the size of the atomic magnetic moments, (for example, caused by difference in atomic valences) the moments do not cancel.

As a result these materials also have remnant magnetism in the absence of a field, these are known as Ferrimagnets (FIM) (Figure 1.2 e). In each case their magnetic properties are due to long range ordering of paramagnetic moments in the crystal structure, having high susceptibility ( $\chi$ ) arising from their paramagnetic coupling.

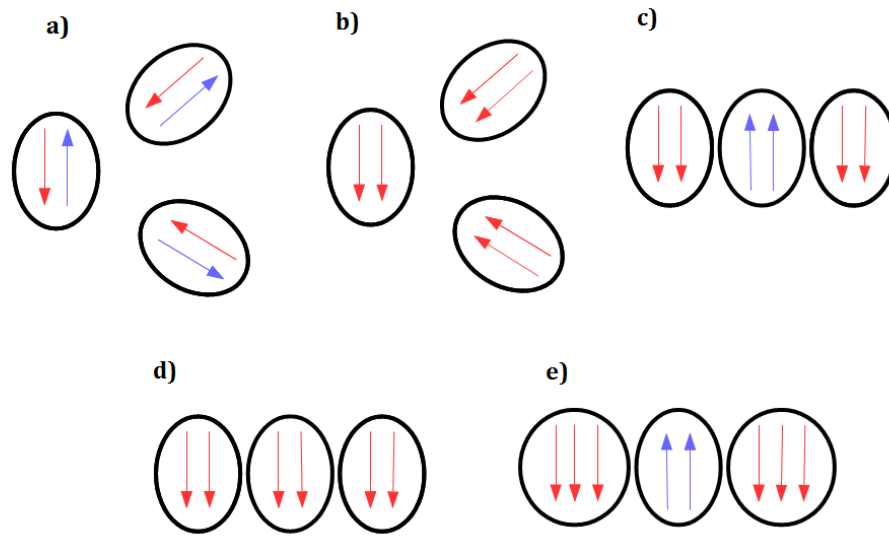


**Figure 1.2:** Atomic alignment which occurs in each type of magnetism, arrows represent the spin alignment of magnetic moments which gives rise to the magnetic properties of the material. In the case of, a) diamagnetism, which is repelled in a magnetic field b) paramagnetism, where materials are attracted in an applied field. c)-e) show the long-range ordering of moments which occur in c) antiferromagnetism (anti-parallel spins), d) ferromagnetism (parallel spins), and e) ferrimagnetism (anti-parallel different size spins) respectively.

AFM materials align in an antiparallel configuration, (Figure 1.2 c) and so the magnetic moments cancel, whereas in FOM materials electrons are aligned parallel to one another, and hence do not cancel giving an overall magnetisation (Figure 1.2 d). Similarly, moments do not cancel in the case of FIM materials, despite an antiparallel alignment of electrons. This is due to a size difference in the moments on adjacent atoms (e.g. due to a difference in valence) leading to remnant magnetism when the field is removed (Figure 1.1 e).

These effects are thermally dependent, with atomic ordering only occurring below a specific temperature, the blocking ( $T_B$ ) or Curie temperature. Above the  $T_B$ , ordering is lost and materials behave as paramagnets. In the case of FOM, AFM and FIM materials, particle size and field strength ( $H$ ) also affect the magnetic response, affecting the shape of the magnetic hysteresis loop (MH curve). This hysteresis is used to assess the magnetic hardness of a material, based on the point at which it saturates and its coercivity. These characteristics are dependent on the properties of the particle, i.e. the particles composition, size and shape (i.e. the size, orbital arrangement and electron pairing), therefore materials are classed as “soft magnets” and “hard magnets”, depending on the field strength ( $H$ ) needed for the material to be magnetised.

Nanoparticles can develop domains within their structure due to short range ordering of spins within a lattice, and the number of these domains increases as the particle size increases. These domains can build up in particles and affect their coercivity, for example a superparamagnetic nanoparticle (a single spin) will respond as a single domain (or whole particle) in a magnetic field (Figure 1.3 a). As the particle size increases and spins remain aligned in a single domain the coercivity increases (Figure 1.3 b) as a higher magnetic field strength is required to return the magnetisation back to zero (due to the additive effect of all spins in the lattice). This coercivity then begins to decrease as the particle size further increases and domain walls begin to develop. These domain walls result in an inconsistent response in a magnetic field and therefore realignment is achieved at lower field strengths (Figure 1.3 c)

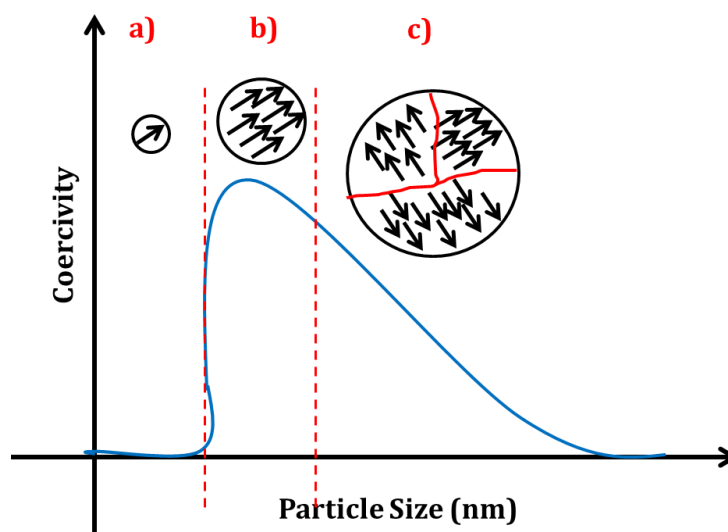


**Figure 1.3:** Schematic of domain formation in magnetic nanoparticles and its effect on coercivity as particle size is increased from a) superparamagnetic nanoparticles to b) single domain and finally c) multi-domain magnetic nanoparticles.

Therefore bigger single domain magnets (all spins in alignment) are harder to flip than smaller particles. Particles larger than single domain contain domain walls (which separate regions of aligned spins) and will flip at lower values of H. If particles fall below a certain size, superparamagnetism is observed in which the particle has a single magnetic moment, and as a magnetic field is reversed the entire particle flips to realign, in this case any hysteresis in the MH curve is lost. Other factors which have a profound effect on a particles magnetic coercivity include its shape. The shape of the particle can affect how strong a field must be for the alignment of all moments. For example, in a needle shape particle the moments can more easily align in a head to tail formation; therefore needing a lesser magnetic field strength than a spherical particle. In a spherical particle repulsive forces between adjacent moments will have to be overcome for successful alignment.

### 1.1.2 MAGNETITE

Magnetite ( $\text{Fe}_3\text{O}_4$ ) (sometimes referred to as loadstone) is the most abundant naturally occurring ferrimagnetic material. Magnetite has an inverse spinel structure comprised of  $\text{Fe}^{2+}$  and  $\text{Fe}^{3+}$  centres in a 1:2 ratio with the overall structure of  $(\text{Fe}^{2+}2\text{Fe}^{3+} \text{O}_4)$ .<sup>3,14</sup> This ferrimagnetic structure gives magnetite the highest magnetic saturation of all the iron oxides, the properties of which are outlined in table 1.1. The cubic inverse spinel lattice arises as a result of opposite spins on successive iron atoms in the magnetite crystal lattice.<sup>3</sup> The crystal structure arises from the arrangement of  $\text{O}^{2-}$  counter ions in a face centred cubic packed (FCC) lattice, in which ferric ions occupy both octahedral and tetrahedral holes, and corresponding ferrous ions are found only in octahedral sites (Figure 1.4).<sup>15</sup> Magnetite's stoichiometry  $([\text{Fe}^{3+}]_2[\text{Fe}^{2+}\text{O}_4])$  means that in isolation, the ferric ions behave as a paramagnet, being aligned in an applied magnetic field, due to their adoption of a high spin configuration.<sup>3</sup> This leads to moving charges between the mixed valences, and a net magnetic moment within the lattice, giving rise to magnetite's ferrimagnetic properties in the bulk crystal.

Property	Value
Formula	$\text{Fe}_3\text{O}_4$
Crystal lattice	Inverse spinel/Close cubic packing
Unit cell	0.839 nm
Magnetism	Ferrimagnetic
Density	$5.18 \text{ g cm}^{-3}$
Curie Temperature	850 K
Melting Temperature	$1583 \text{ }^\circ\text{C}$
$\Delta G_f$	$-1012.6 \text{ kJ mol}^{-1}$
Solubility	35.7

**Table 1.1:** Physico-chemical properties of Magnetite

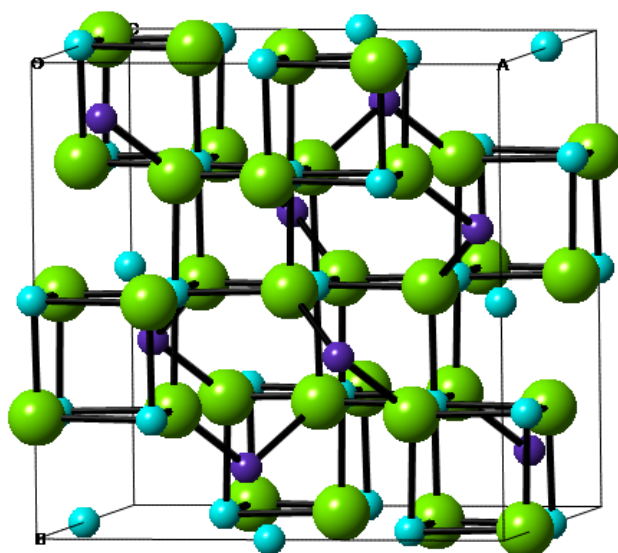


**Figure 1.4:** Inverse spinel unit cell of Magnetite showing oxygen (Green) in an FCC lattice with  $\text{Fe}^{3+}$  (Pale blue) in both the octahedral and tetrahedral holes and  $\text{Fe}^{2+}$  (Purple) in half of the octahedral holes. (Diagram made with CrystalMaker version 9.2.2)

The spin moments associated with each atom in the magnetite lattice do not cancel out as they would in the case of antiferromagnetism. This is due to a difference in the number of electrons in the ferrous and ferric iron at the octahedral sites.<sup>3</sup> The electrons associated with these ions are thermally delocalised, (which allows their movement) but when magnetite is cooled (below 118 K) these electrons become localised causing a loss of ferrimagnetism.<sup>16</sup>

Net magnetisation is also lost at temperatures above the Curie temperature of magnetite (850 K),<sup>3, 17</sup> as thermal energy causes the loss of long-range ordering and ferrimagnetism becomes paramagnetism.

Particle size is important for magnetite. MNPs generally behave superparamagnetically below  $\approx 30$  nm in size.<sup>11, 13, 18</sup> Above a certain size threshold (above  $\approx 120$  nm at ambient temperature) magnetite MNPs begin to exhibit multi-domain characteristics.<sup>11, 13, 18</sup> Domain walls (arising from multi-domain nanoparticles) in the crystal structure affect the particles magnetic response; as the spins need a higher magnetic field to overcome the energy in the domain walls and align. To achieve an efficient and consistent response in a magnetic field, single domain structure magnetite (between 30-120 nm) is required for complete homogeneity.<sup>11, 13, 18</sup>

## 1.2 MAGNETITE FORMATION ROUTES

A major consideration when studying magnetite ( $\text{Fe}_3\text{O}_4$ ) is that it is prone to oxidation. This arises from the sensitivity of the ferrous ions, which can undergo slow room temperature oxidation to form the ferric iron oxide, maghemite ( $\gamma\text{-Fe}_2\text{O}_3$ ).<sup>3, 19</sup> Distinguishing between these two iron oxides is difficult, as they share the same inverse spinel structure. When compared to magnetite (see section 1.1.2), maghemite has a ferrous ion deficiency at the tetrahedral sites. Characterisation techniques, such as XRD or Mössbauer spectroscopy, can be used to distinguish between maghemite and magnetite. However, this is non-trivial, as the differences between the two crystal structures are minor, meaning large amounts of material (in powder form) are required. Loss of absorption in the near IR-region can also indicate magnetite oxidation to maghemite, but again this is extremely difficult to pull out from the spectra.<sup>3</sup> Figure 1.5 a) shows the interchange between magnetite and the other iron oxides by processes such as dehydration, hydrolysis or oxidation, and the corresponding change in particle shape. These changes are generally related to the redox potential (Eh) and acidity (pH) of the reaction environment. Careful control of these parameters can allow for the exacting formation of a specific iron oxide, as shown in the Pourbaix diagram in figure 1.5 b).<sup>8</sup>



This means that co-precipitation of magnetite must be carried out under an atmosphere of N<sub>2</sub> or Ar. Maintaining an anoxic atmosphere makes synthesis of magnetite difficult.

The oxidation of ferrous iron to its ferric counterpart leads to the likely formation of a range of competing iron oxides. Subtle changes to the reaction conditions can induce oxidation and alter the final product including changes in: temperature, precursor oxidation state, ionic ratio, cation concentration, anion type, redox of the reaction chamber atmosphere, etc.<sup>3</sup> This delicate balance between pH and oxidation kinetics can introduce heterogeneity, causing changes in particle properties. For magnetite, this is particularly important for altering its magnetism, and also the size and shape of the resulting crystal. These properties are vital for the MNPs suitability for a particular application, where consistency and reproducibility in crystal properties is paramount. Larger, more uniform populations of pure magnetite MNPs can be produced, but generally *via* multistep processes involving increased temperature, pressure and/or toxic reagents, which more tightly control the nucleation, growth and oxidation kinetic in the reaction.<sup>20b, 20e-g</sup> There are many routes to magnetite formation such as, hydrothermal, sol-gel, flow injection and electrochemical synthesis routes.<sup>18</sup>

This section covers various routes for magnetite synthesis including; high temperature reactions and partial oxidation of iron hydroxides. Whilst all methods offer acceptable levels of purity, they vary both in technical complexity of the techniques employed, and the overall reproducibility of the synthesis route. Studies show that synthesis of magnetite without some ferrous oxidation is highly unlikely.<sup>20f</sup> Perhaps the most comprehensive assessment of magnetite formation is by Regazzoni *et al.*<sup>20f</sup> They evaluate and draw comparisons between six different methods of magnetite synthesis. The study determines that high temperature methods and/or a nucleation burst by injection of a precursor into a hot reaction solution (hot injection) yields high quality particles of defined size and shape, but involves harsh chemical and physical conditions.<sup>20e, 20f, 21</sup> The best method, in terms of particle quality, appears to be synthesis *via* hydrazine oxidation or the reduction of haematite. However, neither route is easily achievable in a standard chemistry laboratory, with both reactions requiring prolonged heating to 400 °C.<sup>20f</sup> Similarly, alkaline hydrolysis provides high quality magnetite, but again the reaction must be performed at a high temperature (500 °C).<sup>20f</sup>

Larger, more uniform octahedral particles with a relatively narrow size distribution can be achieved using oxidative routes at elevated temperatures ( $\sim 90\text{ }^\circ\text{C}$ ) by way of partial oxidation in the presence of a base (which controls the reaction pH). A ferrous iron precursor is heated to form ferrous hydroxide, which is then partially oxidised (most commonly by potassium nitrate) to form a ferrous/ferric hydroxide mixture.<sup>1a, 22</sup> Dehydration of this mixture yields magnetite, however the reaction is extremely sensitive to alterations in the reagents used (iron salt type and  $\text{OH}^-$  source), any change in the ratio of reagents, and changes in temperature.<sup>20f</sup>

Although the conversion from  $3(\text{Fe}(\text{OH})_2)$  to  $\text{Fe}_3\text{O}_4$  (the Schikorr reaction)<sup>23</sup> is possible at a lower (ambient) temperature, oxidation can mean the introduction of contaminants and by products, meaning sample purity is lost.<sup>20f</sup> Room temperature co-precipitation is achieved by raising the pH of a mixture of ferrous and ferric ions in solution, which causes precipitation of magnetite MNPs.<sup>20f</sup> Unfortunately, this route produces small, ill-defined particles, often with broad size distributions, and is liable to produce a range of iron oxides.<sup>24</sup> Particle size control can be improved by manipulating the reaction kinetics, particularly  $\text{OH}^-$  addition rates, or to use phase transformation from iron oxyhydroxides.<sup>20c</sup> Thus co-precipitation at raised temperatures can improve particle quality. Methods, such as thermal decomposition of urea to ammonia, induce magnetite precipitation by way of a temperature triggered pH rise. Here, unwanted ferrous oxidation is minimised, as the precipitation of magnetite is controlled by the rate of urea hydrolysis. Although not as environmentally friendly as at co-precipitation at room temperature, (urea hydrolysis requires heating to  $85^\circ\text{C}$ ), this heating method produces magnetite particles of a much higher standard (i.e. uniform size, shape and magnetic properties) than achieved with room temperature co-precipitation.<sup>21b, 25</sup>

Perhaps the best ambient temperature route to magnetite synthesis was developed by Lenders *et al.*<sup>20a</sup> The group successfully achieved the *in vitro* precipitation of single domain ferrimagnetic magnetite at ambient temperature using co-precipitation; a synthesis route which normally yields ill-defined nanoparticles. By controlling the reaction kinetics, they first form a ferrihydrite precursor from ferrous ions, at low pH. The pH is then slowly increased by diffusion of  $\text{NH}_3$ , which allows for a slow conversion of ferrihydrite to magnetite.<sup>20a</sup>

This achievement is mirrored by the work of Baumgartner *et al*, who also achieved co-precipitation of magnetite yielding stable single domain magnetite MNPs at pH 9 and ambient temperature, by “ultraslow” addition of reagents and constant pH adjustments, to avoid precipitation of small superparamagnetic particles.<sup>26</sup>

## **1.3 BIOMINERALISATION AND BIOMIMETICS**

### **1.3.1 BIOMINERALISATION**

Biomineralisation is the crystallisation or precipitation of an inorganic material within or around a cell or organism,<sup>27</sup> occurring in numerous organisms ranging from humans to algae.<sup>1b</sup> There are two distinct types of biomineralisation. The first is “biologically induced mineralisation” (BIM) in which the precipitation of a mineral is the by-product of a biochemical process.<sup>1b, 28</sup> In these cases, there is often little to no control over the mineral formed. The second type is “biologically controlled mineralisation” (BCM) whereby the organism deliberately forms the mineral to fulfil a function (i.e. protective (shell), structural (skeleton), attack and defence (claws and teeth)).<sup>1b</sup> In BCM, the minerals can be intricately designed to perform these functions, with the organism directing the materials to control requirements such as size, shape, toughness etc.

Transmembrane metal ion transport proteins and/or crystal morphological control proteins are commonly used by organisms to control the crystallisation of the resulting particles.<sup>1a, 29</sup> These BCM minerals generally have superior properties when compared to equivalent artificially synthesised particles. Such architectures can be seen in multiple species of bivalves, molluscs and coral, which biomineralise a hard outer shell for protection.<sup>28</sup> The coccolith is also an excellent example of this shell forming process. Coccolithophores form the coccolith plates in intracellular vesicles, and subsequently exocytose them to the exterior of the organism. The coccolith structures comprise individual biomineralised plates which then assemble into spheres to protect the organism (Figure 1.6).<sup>6, 27, 30</sup>

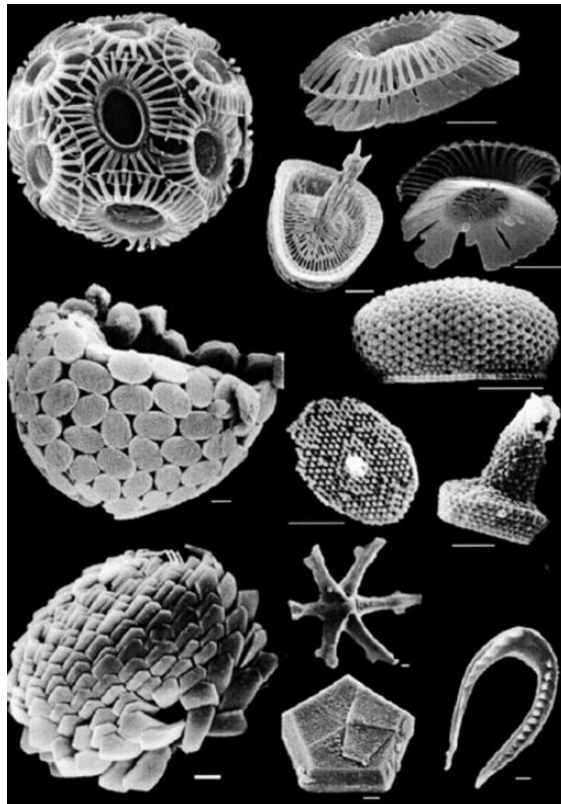


**Figure 1.6:** Natural biomineralisation within organisms. Architectures observed in nature as the result of calcium carbonate biomineralisation in coccoliths, scale bars are 1  $\mu\text{m}$  adapted from Young *et al.*<sup>6</sup>

Coccoliths have provided a model system for the study of biomineralisation mechanisms, and are indicative of the high levels of complexity that can be achieved by nature. Similarly, the diatom is a form of algae that is able to control the biomineralisation of silica using specific proteins called silaffins.<sup>28</sup> Silaffins are polycationic peptides, which are able to exert control over the precipitation of silica nanosphere networks. A lysine-lysine section within this peptide structure has proven to be responsible for the formation of the network.<sup>31</sup> When silaffins are added to an *in vitro* precipitation, there is a stark difference in the morphology of the silica formed when compared to the absence of protein.<sup>31</sup>

The *in vivo* function of these negatively charged proteins is to induce crystal phase switching from aragonite to calcite during the formation of nucleating shell tissue sheets. *In vitro* use of these proteins initiates the same crystal phase shift observed *in vivo*.<sup>32</sup>

Whilst this is by no means an exhaustive list of bioadditives, it demonstrates the versatility that can be achieved when additives are “borrowed” from nature to improve chemical reactions. Understanding the mechanism by which these organisms biomineralise can be used to inform the generation of new biomimetic and bioinspired materials.<sup>33</sup>

### 1.3.2 MAGNETOTACTIC BACTERIA

Examples of biomineralised magnetite are found everywhere, from chiton teeth to MNPs within the brains of insects, birds and humans.<sup>1b,34</sup> Arguably, the most intricate and well-studied example of magnetite biomineralisation is the formation of magnetosomes in magnetotactic bacteria (MTB).<sup>35</sup> MTB are a gram negative bacteria, of which there are evermore emerging diverse strains.<sup>36</sup> They are found in sediments and saline, brackish and fresh water all over the world.<sup>35,37</sup> Each strain has a unique genetic make-up, but common to all MTB strains is the biomineralisation of magnetic iron based minerals, typically magnetite or greigite.<sup>35,37</sup> Since their discovery by Bellini in 1963,<sup>38</sup> and rediscovery by Blakemore in 1975,<sup>35</sup> multiple research groups have emerged dedicated to understanding the mechanism of biomineralisation within these vesicles (termed magnetosomes) in magnetotactic bacteria.<sup>35,39</sup>

Magnetosomes are believed to be used as internal compasses, allowing the bacteria to passively align with a magnetic field, and navigate along the direction of the field, which is called magnetotaxis.<sup>40</sup> Magnetotaxis allows the MTB to move in response to environmental cues (such as specific levels of O<sub>2</sub> and CO<sub>2</sub>). The MTB orient themselves in their environment using the earth’s magnetic field lines, and move along them to seek out optimal redox conditions needed for their survival.<sup>40-41</sup> Magnetotaxis is believed to be used in conjunction with both aero- and chemotaxis to orientate the magnetosome in the oxic-anoxic transition zone (OATZ). The OATZ is the border between upper oxygen-rich and deeper oxygen-starved regions within water or sediment.

Magnetotaxis is the most likely reason for MTB formation, however this is heavily debated.<sup>40, 42</sup> Other alternative theories suggest that magneto-aerotaxis<sup>43</sup> is a secondary advantage of biomineralising MNPs, and the magnetosomes are a primarily a product of respiration<sup>44</sup> or detoxification.<sup>45</sup> It is known for certain that a dipole moment is produced in the MNPs, allowing the magnetosomes, and therefore the MTB, to align with geomagnetic field lines. It has also been found that some MTB in the northern hemisphere are north seeking and vice versa in the southern hemisphere.<sup>46</sup> Although these seeking species can live in the same environment,<sup>46</sup> it has been observed that north seeking bacteria are repelled by the south pole of a magnet which raises questions regarding magnetotaxis.<sup>37</sup> Whatever the reason for the formation of magnetosomes, it is clear that the MTB take advantage of the magnetic properties of the MNPs they form. They do this by exerting heavy biological control over the formation and alignment of magnetosome MNPs.

### 1.3.2.1 MAGNETOSOME FORMATION IN MTB

MTB are unique in the way in which they biomineralise exclusively magnetite or greigite nanoparticles within their magnetosomes (Figure 1.7 a).<sup>39f</sup> The mechanisms of magnetosome formation have been extensively studied, and it has been found that the proteins which control magnetosome formation are encoded by an area of the genome known as the "Magnetosome Island".<sup>39c, 47</sup> An accepted theory of MTB magnetosome formation in a well-studied species (*Magnetospirillum magneticum* AMB-1) starts with the invagination of the cytoplasmic membrane within the bacteria by the protein MamY.<sup>48</sup> This creates a budding vesicle in the membrane, which is then broken off by the protein MamU<sup>47</sup> (figure 1.7 b). These empty magnetosomes are arranged into chains by the protein MamJ anchoring them along an actin-like filament protein (MamK) inside the bacterium.<sup>49</sup> Once aligned along MamK, the empty magnetosome vesicles then recruit Mam/Mms proteins into their membrane.<sup>49</sup> This family of proteins allows for recruitment of iron to the lumen of the magnetosome through transmembrane iron-transporter proteins.<sup>39d, 50</sup>

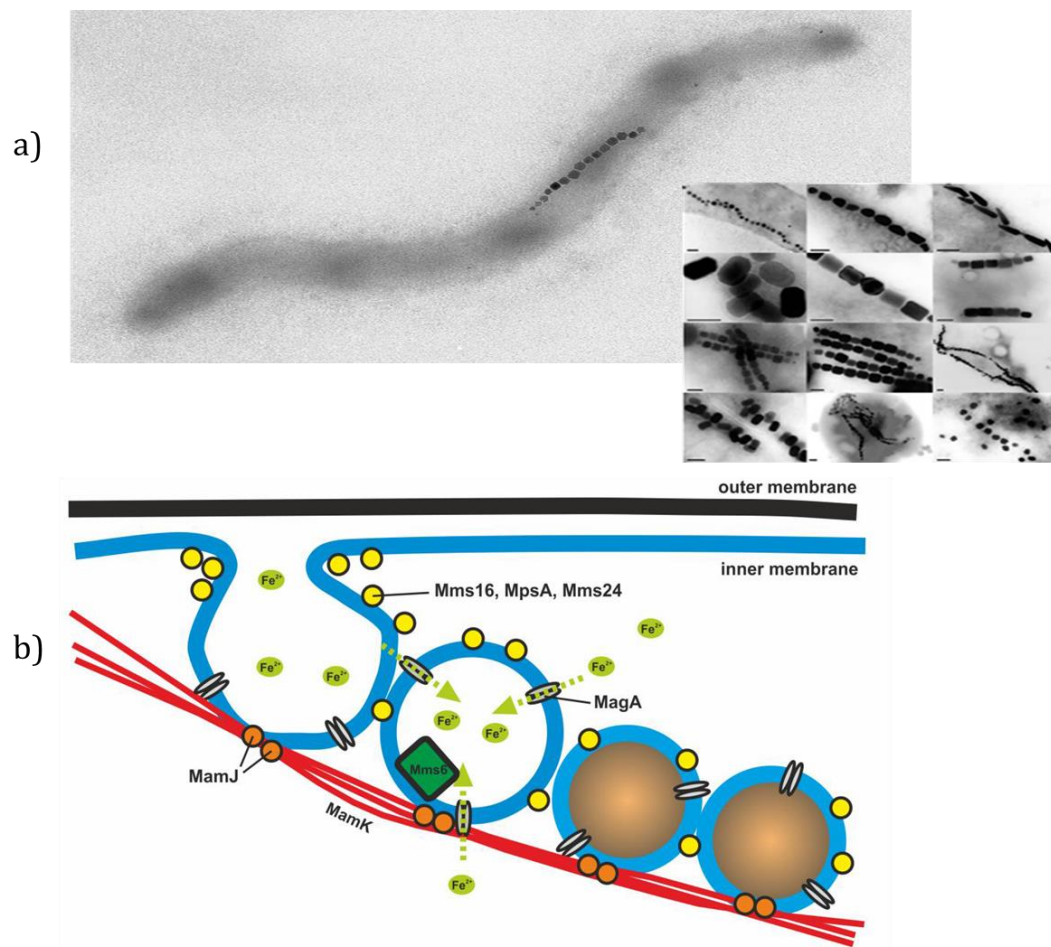


**Figure 1.7:** The formation and biomineralisation of the magnetosome in within the magnetotactic bacterium *M. magneticum* AMB-1. a) Example of *Magnetospirillum magnetotacticum* AMB-1. Adapted from Schüler *et al*<sup>51</sup> b) Schematic of formation of the magnetosome vesicle, recruitment of iron and morphological control exerted by bacterial proteins, redrawn by J. Galloway from Arakaki *et al*.<sup>39e</sup>

Current research has not managed to definitively determine which protein(s) are responsible for iron transport into the magnetosome. This is despite thorough research into many promising candidates, in particularly the proteins MamMB<sup>52</sup> and MagA.<sup>53</sup> These proteins have been assigned as antiporter systems through genomic, proteomic and re-crystallisation studies.<sup>53-54</sup> They are believed to pump protons out of the magnetosome core, increasing the internal pH, and in turn pump ferrous iron ions back in. The pH rise within the iron (II) rich magnetosome leads to the precipitation of a single magnetite nanocrystal within the magnetosome core. The size, shape and crystallinity of the magnetosome bound MNP is controlled by specific biomineralisation proteins.<sup>29b, 51</sup>

Sufficient ferrous iron concentrations are only reached in MTB due to the compartmentalisation of the reaction.<sup>39b, 49</sup> This hypothesis is supported by Stolz,<sup>55</sup> with the discovery that magnetosomes are only synthesised by MTB in cases where sufficiently high concentration of a ferrous ion source is available.<sup>39d</sup> This is supported by a study which suggests that magnetite mineralisation proceeds *via* the formation of an iron (II) precursor.<sup>56</sup> Some suggest that this iron (II) can then be oxidised to iron (III) ferrihydrite by an iron oxidase protein (MamP),<sup>56</sup> which is present in all MTB strains. This would then be followed by conversion to magnetite by continuous transport into the magnetosome of the ferrous iron.<sup>39d, 52, 53b</sup> Deletion of MamP has been shown to cause crystal defects in magnetosomes.<sup>56</sup> Genomic, proteomic, lipidomic and electron microscopy analyses have confirmed the presence of a suite of magnetosome specific proteins within the magnetosome vesicles, and has helped to assign a function to many of them.<sup>39b</sup> Studies, focussed on further gene knockout mutagenesis,<sup>52, 57</sup> genomic studies,<sup>39c</sup> and proteomic studies,<sup>54, 58</sup> are still trying to elucidate the role of these proteins. Numerous reviews<sup>24, 39c, 39e, 42, 59</sup> detail what is already known about the formation of the magnetosomes and their potential for use in a range of applications.

### 1.3.2.2 BIOMINERALISATION PROTEINS

Biomineralisation proteins are pivotal to the formation and quality of MTB produced magnetite nanoparticles. Analysis of the magnetosomal magnetite crystals has led to the hypothesis that the initial nucleation of the particle is on the [111] face specifically. This is followed by non-specific growth, and selective suppression of specific axes to yield a cubo-octahedral particle in the case of *Magnetospirillum magneticum* AMB-1.<sup>60</sup> This control is provided by the biomineralisation proteins (Mms6, Mms13, MmsF) encoded for in the magnetosome island,<sup>47</sup> which are believed to control the growth of the magnetite crystal by both promoting nucleation of Fe<sub>3</sub>O<sub>4</sub> and blocking growth of specific crystal faces, to achieve precise crystal morphology.<sup>1a</sup>

Perhaps the most well studied of these proteins is Mms6, which is a membrane protein with a single transmembrane region containing acidic iron binding sites on its C-terminus.<sup>61</sup> Mms6 is believed to play a key role as a nucleation site for iron minerals located on the magnetosome interior.<sup>1a, 61</sup> Mms6 is the first of the few studied proteins from this system to be utilised in an *in vitro* magnetite precipitation.<sup>61</sup>

When this protein is added to a room temperature co-precipitation of magnetite there is a marked improvement in the monodispersity of the particles formed.<sup>1a, 29a, 62</sup> Another MTB biomineralisation protein whose function has been investigated is MmsF. MmsF is also believed to be the biomineralisation protein responsible for the formation of magnetite.<sup>57</sup> The deletion of the MmsF gene *in vivo* leads to complete loss of magnetosome formation. Importantly, when the cluster of genes responsible for biomineralisation is deleted and only MmsF restored, the formation of the entire magnetosome is restored, indicating that MmsF is the master regulator protein within the operon.<sup>29b</sup> This, along with the other key proteins,<sup>5</sup> is believed to be responsible for control of magnetite biomineralisation and will be discussed in more detail in chapter 8.

## 1.4 VESICLES

A vesicle is a hollow spherical structure which encapsulates a body of aqueous or organic fluid, whose formation is governed by self-assembly. Vesicles are an integral part of nature, where they perform a wide variety of functions and have been widely researched since 1965.<sup>63</sup> Vesicles are vital in multiple cellular processes, including transportation and compartmentalisation in cells. MTB vesicles are composed of a lipid bilayer membrane, in which it is difficult to introduce variations and functionalisation. Adaptation of a vesicles composition can be more pronounced and better controlled in a synthetic analogue. For example, it is possible to limit vesicle formation to certain morphologies by control of the composition of the components used to assemble the vesicle.<sup>64</sup> Synthetic vesicle nanoreactors presented in the literature have facilitated the completion of numerous reactions.<sup>65</sup> One key focus of this thesis is the utilisation of vesicles formed from both naturally occurring phospholipids and from synthetic polymers, to create a nanoreactor suitable for the compartmentalisation of a magnetite precipitation reaction.

### 1.4.1 SELF-ASSEMBLY

For predictable vesicle formation, molecular level understanding of the self-assembly is key. Vesicles are generally formed from amphiphilic molecules which possess both polar and non-polar regions.<sup>66</sup> This gives rise to both hydrophilic and hydrophobic properties simultaneously, and self-assembly occurs spontaneously upon addition of an amphiphile to aqueous solution,<sup>66</sup> which arises from the hydrophobic effect.<sup>66a, 67</sup> This is because the hydrophobic portions of the molecule cannot form bonds with water either electrostatically (Van der Waals) or *via* hydrogen-bonding, due to lack of affinity between the non-polar chains and water according to Traube's rule.<sup>68</sup> This rule states that the surface tension of a system decreases threefold for each additional methylene group added to the non-polar region of an amphiphile.<sup>66a, 68</sup> When a hydrophobic molecule of a certain size is added to water, an entropic effect dominates, forcing the water to arrange itself into a cage-like structure (clathrate) around the molecule to avoid contact, resulting in an increase in the order of the system.<sup>66a, 68</sup>

Despite energy being required to promote the rearrangement, this is more energetically favourable than hydrophobic/water contact, with higher numbers of hydrophobic residues increasing assembly efficiency.<sup>69</sup> If a species is amphiphilic, each section of the amphiphile adopts the most energetically favourable conformation to satisfy their hydrophobic/hydrophilic requirements. Above a certain concentration of the amphiphile (the critical micelle concentration, or CMC), the formation of an amphiphile bilayer occurs to shield the hydrophobic portions of the molecules, and disassociation of the clathrate-like water cage.<sup>68</sup>

The lowest energy conformation is adopted by the bilayer, causing spontaneous rearrangement into a stable vesicle conformation, to ensure all hydrophobic components are shielded. The formation of the vesicles must obey the Laplace equation, (Equation 1.2) which dictates that the inner pressure ( $p_{in}$ ) must be equal to the outer pressure ( $p_{out}$ ) plus the surface tension ( $\gamma$ ) and radius ( $r$ ) of the interface.<sup>66a</sup>

$$p_{in} = p_{out} + 2\gamma r \quad (1.2)$$

The presence of hydrophobic interactions during the formation of a vesicle dictates that there must be a corresponding hydrophilic force present. This hydrophilic force adds disorder to a system, as they are able to form non-covalent bonds with water which on the macro scale forces assembly.<sup>69</sup>

$$\mu_N^0 = \mu_\infty^0 + \frac{\alpha kT}{N^{\frac{1}{3}}} \quad (1.3)$$

The assembly size is thermodynamically determined from the interaction of the free energy per molecule ( $\mu_N^0$ ), (Equation 1.3) given by the free energy per molecule ( $\mu_\infty^0$ ) and the bond energy ( $\alpha kT$ ) at a finite aggregate size ( $N$ ).  $\mu_N^0$  decreases as  $N$  increases, having a specific minimum which prevents infinite growth of an assembly. This relationship between  $\mu_N^0$  and  $N$  gives rise to the critical micelle concentration (CMC) for a vesicle (Figure 1.8).

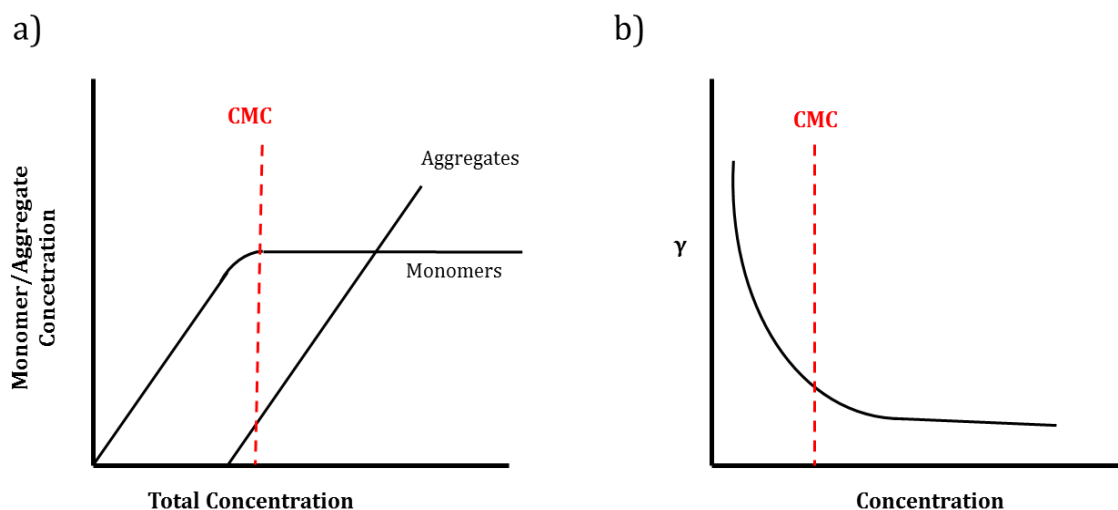


**Figure 1.8:** a) Schematic showing the effect of monomer and/or aggregate concentration on the critical micelle concentration (CMC) (dotted red line) of an amphiphile assembly. b) Schematic of how surface tension decreases as a function of increasing amphiphile concentration again yielding an amphiphile critical micelle concentration (CMC) (dotted red line).

Application of this theory to an amphiphilic molecule directs that for the polar region, it is energetically more favourable for the polar head of the amphiphile to be in contact with water than with its neighbour.<sup>70</sup>

$$N_{\text{aggregate}} = \frac{V_{\text{aggregate}}}{V} = \frac{A_{\text{aggregate}}}{a_0} \text{ therefore } \frac{V}{a_0} = \frac{V_{\text{aggregate}}}{A_{\text{aggregate}}} \quad (1.4)$$

These factors determine the aggregate geometry of an amphiphile. This is described in terms of the ratio between aggregate area ( $A_{\text{aggregate}}$ )/aggregate volume ( $V_{\text{aggregate}}$ ) and the desired polar head area ( $a_0$ )/hydrophobic tail volume ( $V$ ) (Equation 1.4).<sup>66a</sup>

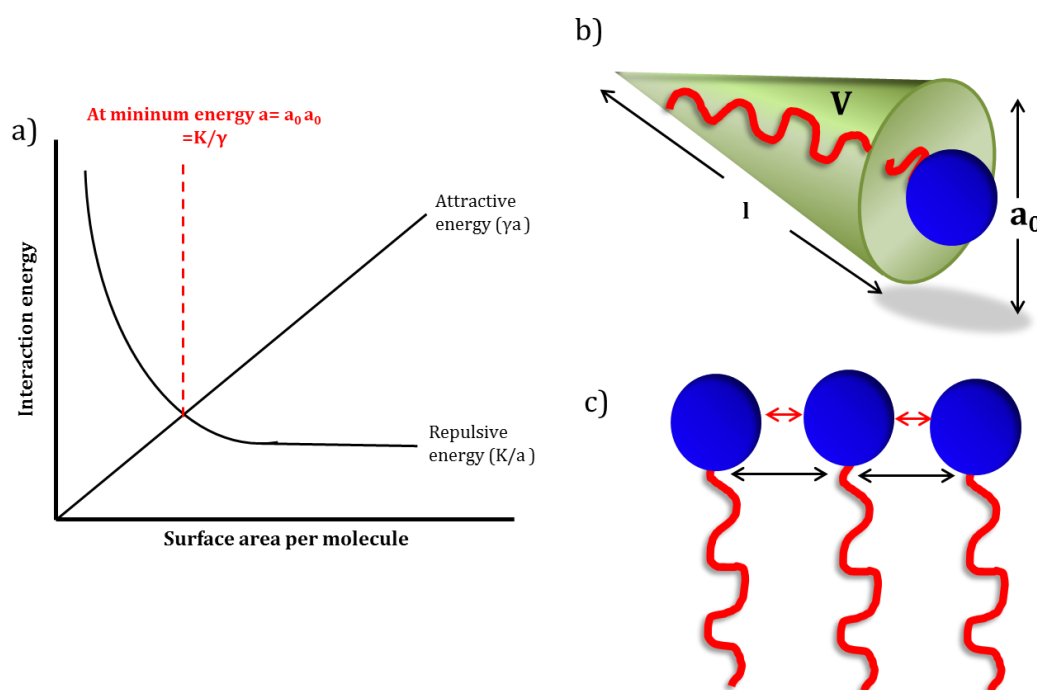


**Figure 1.9:** a) Schematic of how the attractive and repulsive forces at an amphiphiles interface as the molecules surface area increases gives rise to an optimal headgroup area ( $a_0$ ) at a minimum interaction energy, b) The parameters which define the size and packing properties of an amphiphile, these being the volume ( $V$ ) and length ( $l$ ) of the non-polar tail, and the optimal area of the polar headgroup ( $a_0$ ) and c) how the hydrophilic repulsive (red arrows) and hydrophobic attractive (black arrows) act upon an amphiphile to promote assembly.

The balance between these attractive and repulsive forces (Figure 1.5), gives rise to an optimal headgroup area ( $a_0$ ), and a corresponding packing parameter ( $\rho$ ) (Equation 1.5)<sup>66a</sup> associated with each amphiphile.

$$\rho = \frac{v}{a_0 l} \quad (1.5)$$

This ratio between the hydrophobic tail volume and optimal headgroup area; described as the packing factor ( $\rho$ ), determines the morphology adopted by the amphiphile on assembly.<sup>66a</sup> For packing factors less than 1, micelles are preferred, (Figure 1.10 a) with the length of this micelle increasing to form a cylinder (Figure 1.10 b)<sup>66a</sup> as the packing factor approaches  $\frac{1}{2}$ . Between  $\frac{1}{2}$  and 1, a bilayer is formed, the most energy favourable configuration of which is a bilayer that closes to form a vesicle (Figure 1.10 c).<sup>66a</sup> Above a packing factor of 1, the system inverts, forming first an inverted cylindrical micelle (Figure 1.10 d) and then an inverted micelle at packing factors greater than  $\frac{3}{2}$  (Figure 1.10 e).<sup>66a</sup> Knowledge of these mechanisms will allow for the exploitation of the process observed in nature and the engineering of synthetic vesicle formation in subsequent experiments.

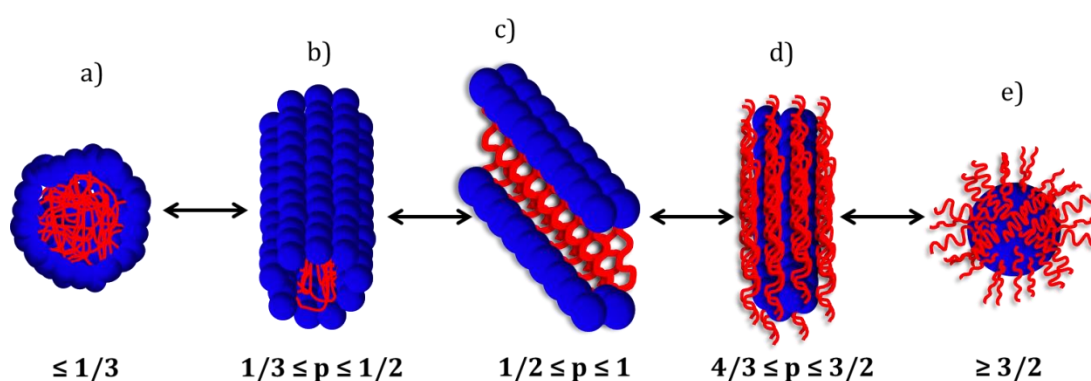


**Figure 1.10:** The packing parameters that can be achieved on assembly of an amphiphile as dictated by the ratio between tail volume and optimal headgroup surface area. Depending on this packing factor ( $\rho$ ) number, amphiphiles can form a) micelles, b) cylindrical micelles, c) bilayers (vesicles), d) inverted cylindrical micelles and e) inverted micelles. Hydrophobic tails are shown in red and hydrophilic head groups in blue.

## 1.4.2 LIPIDS

Lipids (e.g. phospholipids) self-assemble to form biological membranes and vesicles. Lipid vesicles (liposomes) have been subjected to an extensive amount of research and characterisation, as well as their applicability to a wide range of applications, including, food science, cosmetics and medicine.<sup>71</sup> Their encapsulation abilities have been widely explored, and are wide ranging, with liposomes being used to encapsulate a range of moieties, from single proteins to whole cells, *via* one preparation method.<sup>72</sup> Monnard<sup>73</sup> and Tester<sup>74</sup> previously outlined the properties of a liposome required for it to function as a nanoreactor, as requiring the reactor size to be in the nanometer range and designed to withstand changes in reaction conditions (such as temperature or pH). The composition should also allow for discriminatory diffusion as well as simultaneous and efficient encapsulation of all necessary reagents. Perhaps the most important property is inherent biocompatibility to have a chance of successful biomedical application.<sup>73</sup>

There are many classes of “lipid” including, glycerolipids, sphingolipids and sterols.<sup>75</sup> The most significant for this study is the phospholipid, which makes up between 30-80% of the molecules that self-assemble to form biological membranes.<sup>76</sup> A phospholipid is an amphiphile that has a polar head containing a phosphate group and a non-polar hydrocarbon backbone.<sup>75</sup> For liposome formation, the choice of phospholipid has a direct effect on vesicle properties. For example, a degree of fluidity must be maintained to control crucial vesicle properties including, phospholipid packing, melting temperature, and functionality, this is especially important for medical application.<sup>71a, 71b, 71d</sup> Fluidity is created by introduction of a double bond into the backbone of a phospholipid tail, which causes “kinks” in the chain; this introduces steric hindrance due to the geometry of the double bonds.<sup>69</sup> Shorter chain lengths and a higher degree of unsaturation increases bilayer fluidity and thus the ease with which proteins can be incorporated. These variations can affect the outcome of self-assembly and are easily introduced into a synthetic lipid vesicle.<sup>71a, 71d</sup>

Fluidity of a lipid bilayer can also be controlled by altering the temperature, osmotic pressure, bilayer composition, non-polar tail length and, in particular, the degree of unsaturation in the tail.<sup>77</sup>

Vesicle functionality can also be negatively affected by the presence of charge, which can create extra barriers to permeation, particularly to cations and anions.<sup>71a, 71c, 71d</sup> There are also several classifications of liposome from multivesicular and multilamellar structures to simple unilamellar vesicles, all of which can range in size from 10's of nanometres (small unilamellar vesicles) up to the micron range forming giant unilamellar vesicles (GUVs), which are incredibly unstable disassembling upon agitation.<sup>71a, 78</sup> Smaller than GUVs are multilamellar large vesicles (MLVs) and large unilamellar vesicle (LUVs), generally forming sizes around 500 nm.<sup>75</sup> Below this size range are oligolamellar vesicles (OLVs), forming between 200-1000 nm, and finally small unilamellar vesicles (SUVs), which form within the target range of the vesicles in this thesis between 20-200 nm.<sup>75</sup> These different structures and architectures arise from the preparation methods. More complex multilamellar and multivesicular structures, as well as nano-tubes, have previously been utilised in studies to mimic exocytosis.<sup>71d</sup>

The liposomes in this thesis are synthesised from phospholipids alone, and although this is not an exact mimic of the MTB bacterial membrane, or even a naturally occurring membrane, the complex composition of these naturally occurring membranes would make it almost impossible to reproduce, as an unfeasible combination of compositions would need to be explored. Phospholipids seemed the obvious choice to focus on for formation of an artificial magnetosome vesicle, as they are the most prominent class of lipid in the magnetosome membrane, making up 62 % of the bilayer composition.<sup>39b</sup>

Some manipulation of liposomes for application is possible, such as stabilisation for *in vivo* applications by the incorporation of cholesterol into the bilayer.<sup>71a, 71c, 71d, 79</sup> This increases the membrane stability, particularly in the presence of biological fluids, although this also has the disadvantage of reducing membrane permeability.<sup>80</sup> A bilayer can also be stabilised by polyethylene glycol (PEG), which causes interbilayer repulsion to overcome the Van der Waals forces present in the bilayer, thus preventing vesicle aggregation.<sup>71c</sup> The addition of PEG can also disguise the outer membrane, increasing the vesicles *in vivo* lifetime, delaying recognition by opsonins,<sup>81</sup> which allows the vesicle to release its cargo at a specific target site.<sup>71c</sup>

This lifetime can be further lengthened by control of the size, with smaller liposomes (between 50 – 200 nm) exhibiting longer circulation lifetimes.<sup>82</sup> Vesicle sizes outside of this range can have detrimental effects on the *in vivo* destination of vesicles, with smaller vesicles (<40 nm) being known to enter the liver, while those above 300 nm in diameter are more likely to accumulate in the spleen.<sup>71c</sup>

### 1.4.3 POLYMERS

Phospholipids can be restrictive and unstable with respect to functionalisation, which limits their use in nanomedicine.<sup>83</sup> In comparison, polymers can offer increased stability, low permeability and increased molecular weights, and are also highly varied and tuneable.<sup>83-84</sup> For this reason, amphiphilic copolymers have been utilised as lipid mimetics to self-assemble into polymersomes (polymer vesicles). In this case, polymer monomers with functional groups such as carboxylic acids, (to introduce polarity) mimic the phosphocholine head group of a lipid, while non-polar hydrocarbon based monomers, such poly-butadiene or poly-dimethyl siloxane, behave in the same way as a hydrophobic phospholipid tail.<sup>85</sup>

Polymer vesicles offer a flexible and often more robust material, with greater scope for modification both pre and post assembly, to accommodate a wide range of chemical conditions. This, in combination with more robust mechanical properties, makes polymersomes ideal drug delivery and diagnostic agents.<sup>84, 86</sup> One major advantage of using synthetic amphiphiles such as block copolymers is the wide range of architectures achievable by optimisation of both the polymer hydrophobicity and monomer block lengths (Figure 1.10).<sup>87</sup> The architectures achieved by block copolymers can affect both the application they are suitable for and their effectiveness in those applications.<sup>88</sup> In addition to this, it is entirely possible to engineer the monomer building blocks to closer suit the needs of the eventual application.

Polymersomes' particularly *di-block* architectures, are finding new applications across the entire field of biomedicine, offering superior properties as drug delivery vehicles when compared with lipid vesicles.<sup>83</sup>

The literature demonstrates how polymersomes can be engineered to incorporate a wide range of properties designed to meet the requirements of specific applications.<sup>83-85, 89</sup> For instance, di-block polymer drug delivery carriers have been engineered to respond to stimuli including; changes in temperature, ionic strength, pH and light.<sup>89e, 90</sup>

Numerous reviews have outlined the various properties it is possible to incorporate into a vesicle, such as photosensitivity, pH sensitivity, specific melting temperatures and chemistry which can make the resulting vesicles show stealth *in vivo*.<sup>89b, 89d, 91</sup> For example, pH can control polymer orientation during assembly, determining which of the monomer blocks make up the outer leaflet of the polymersome.<sup>89d, 92</sup> It has also been shown that specific polymersomes disassemble upon irradiation with UV light, which has huge potential for the successful release of cargo *in vivo*.<sup>89d, 92-93</sup> In terms of targeted drug delivery, the variety of moieties already functionalised on to a polymersome bilayer is outlined in the review by Pawar *et al*,<sup>89b</sup> and encompasses antibodies, peptides, carbohydrates and small organic molecules. This functionalisation can be through both covalent and non-covalent methods, depending on the polymer chemistry.<sup>89b</sup> The literature highlights the high level of adaptability offered by polymersomes, in terms of their engineered properties, functionalisation and potential for use in applications.<sup>83-85, 89</sup>

Much of this this is specific to use in biomedicine and drug delivery applications,<sup>89c, 90b, 94</sup> targeting specific biological sites, such as in the treatment of gliomas.<sup>95</sup> The creation of pH sensitive biocompatible block copolymer polymersomes allows polymersomes to form or deform in response to changes in pH. Such as self-assembly above pH 6 as a result of deprotonation of an amine in the specific polymer material studied.<sup>96</sup> The encapsulation efficiency of a polymersome can be improved by the use of microfluidics, as the laminar flow conditions within a microfluidic device result in a pH gradient at the flow interface.<sup>82, 97</sup> These properties affect the *in vivo* response, solubility, permeability, surface topology and lifetime,<sup>91, 98</sup> rendering polymersomes ideal smart nanomedical vehicles.

Most research into polymersomes has been carried out with di-block polymers.<sup>2a, 84, 86-87, 99</sup> However, ABA *tri-block* polymersomes which have a hydrophobic, hydrophilic, hydrophobic structure, thus forming a monolayer which mimic diblock polymer bilayer formation (Figure 1.11 a) and may offer alternative properties, particularly with respect to membrane transport and encapsulation.

This is due to the structure of ABA *tri-block* polymers, which consists of continuous hydrophilic, hydrophobic then hydrophilic sections, which assemble into a monolayer (Figure 1.11 b).

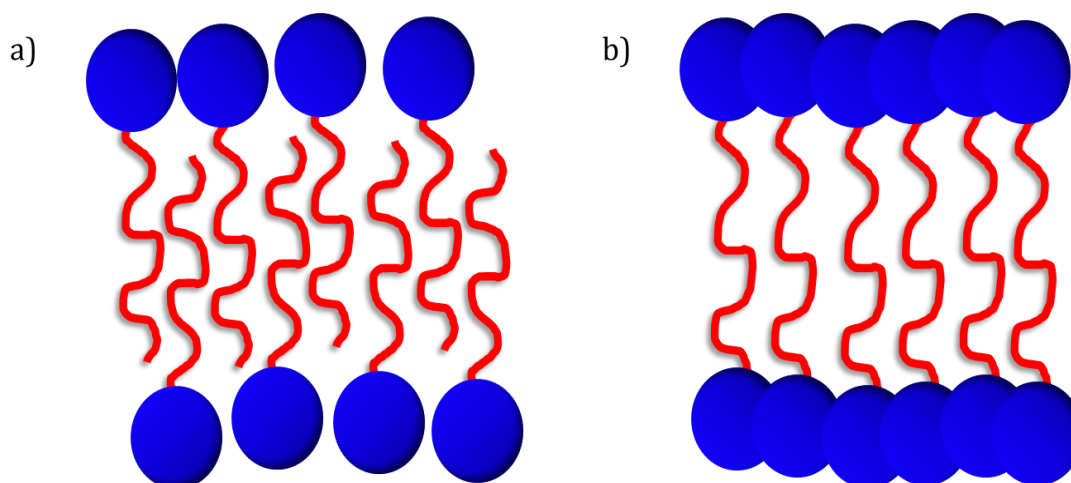


**Figure 1.11:** Schematic of vesicle bilayer formation formed using a) a diblock (AB) polymer and b) a triblock (ABA) polymer.

This monolayer has the same amphiphilic properties as a traditional polymer or lipid bilayer; therefore ABA *tri-block* polymers form the same architectures as liposomes and polymersomes in aqueous solution. The advantages of using an ABA *tri-block* for compartmentalisation of a reaction are the low permeability and end group reactivity. This could give rise to better encapsulation and maintenance of reactants, and as a consequence improve precipitation in the core. ABA polymers can be both stabilised and functionalised as with *di-block* polymers by adaptation of reactive end groups,<sup>9,100</sup> this functionality is well placed for application in biomedicine. Conversely this may raise problems with regards to trans-membrane transport of reactants.

The use of polymer medical vehicles, although a relatively new field, is having increasing success. For example Meier *et al* have successfully incorporated biological components into polymer membranes.<sup>100a</sup> This work has been further advanced by numerous other groups, by incorporation of both protein channels and enzymes.<sup>101</sup>

Much of this work is outlined in the review by Meier *et al*<sup>85</sup> which demonstrates a framework of polymersome nanoreactors for the study of ion transporters, membrane proteins and as biomineralisation scaffolds. It also suggests that block co-polymer vesicles are now competing with liposomes in their use as vehicles for both the study of biological moieties and as successful nanoreactors.

## 1.4.4 FORMATION METHODS

### 1.4.4.1 LIPOSOME FORMATION

There are a number of routes to form liposomes, including but not limited to; sonication, electroformation extrusion, coacervation (phase separation), inkjetting and microfluidics.<sup>71a, 71c, 78, 102</sup> These preparation methods allow for multiple modes of encapsulation and, in some cases, encapsulation of multiple reagents. However, some methods are not suitable for the creation of an artificial magnetosome, due to low encapsulation efficiency.<sup>72</sup> The preparation method is key to the eventual liposome size. For example, in their formation by sonication and extrusion,<sup>103</sup> the radii tends to be less than 50 nm, producing SUVs.

Whereas MLVs tend to form spontaneously, these can be converted to unilamellar vesicles by extrusion, which causes the rupture and reformation of the membrane. This technique can also be used as an effective method of encapsulation by the introduction of a new encapsulant upon reformation.<sup>103</sup>

For the preparation of GUVs, lipid film hydration or electroformation are widely used.<sup>78</sup> Biological membranes are naturally asymmetric, this asymmetry is hard to achieve synthetically.<sup>104</sup> However, more complicated preparation methods can allow for the independent design of the inner and outer leaflet of an asymmetric liposomal nanoreactor, such as the inverted emulsion method developed by Pautot *et al*.<sup>105</sup> This allows for production of a vesicle capable of withstanding two contrasting external and internal environments, thus widening the scope of the reactions liposomal nanoreactors incorporate, and is ideal for the incorporation of immiscible solutions simultaneously (Figure 1.12).<sup>105</sup>

The drawbacks of using such a complicated method include: ensuring appropriate emulsion formation as this controls the final vesicle size, and the lipid concentration in the emulsion must be kept low when compared to other preparation routes, to prevent phase separation.

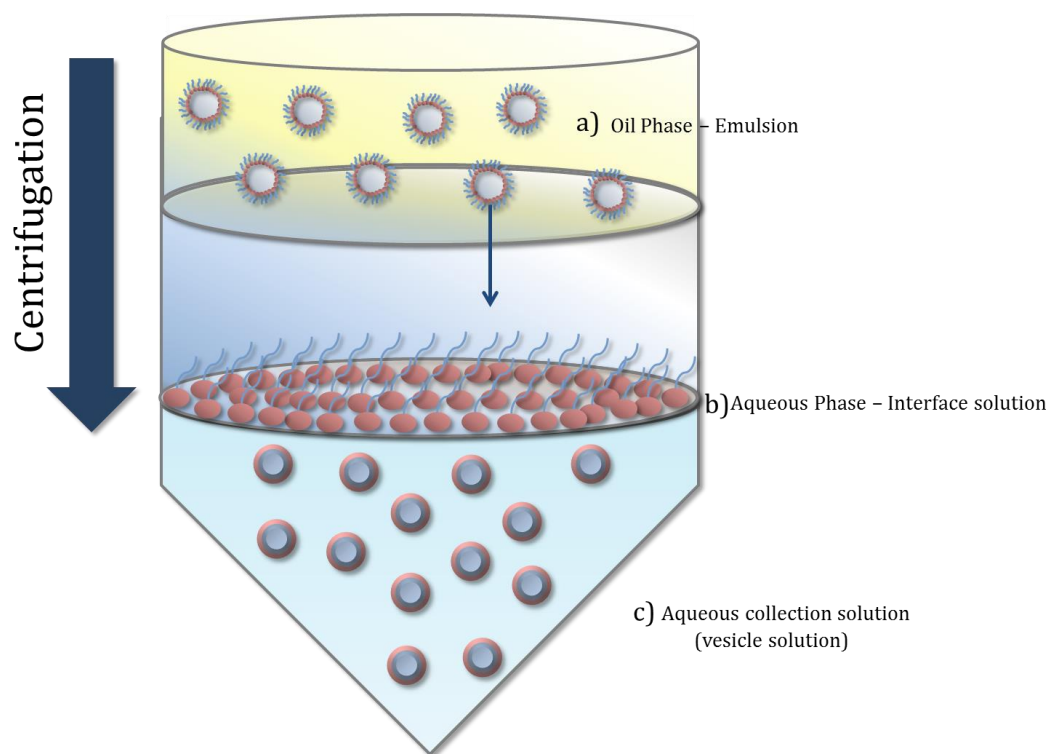


**Figure 1.12:** Schematic of Pautot's<sup>105</sup> in which a) inverted water in oil micelles are formed using the inner leaflet lipid, before being centrifuged through b) a monolayer of the outer leaflet lipid to create the bilayer of the vesicle, before c) vesicles are collected in aqueous solution.

It's also difficult to avoid oil incorporating into the bilayer.<sup>105b</sup> Vesicles can also be formed using double emulsion methods, using water/oil combinations for separation of lipid and aqueous solutions.<sup>106</sup> The vesicles can then be formed either by evaporation of a solvent layer<sup>106a</sup> or by using a droplet interface bilayer, in which two vesicles fuse at an interface bilayer, ideal for asymmetric vesicles and mixing of immiscible reagents.<sup>107</sup>

#### 1.4.4.2 POLYMERSOME FORMATION

A polymer molecular weight (of each block and also number of blocks) is fully controlled during its synthesis, and has a direct effect on the thickness of the resulting membrane, impacting polymersome stability, fluidity and diffusion properties.<sup>86, 89e, 91, 94c, 98, 108</sup> All of these properties can be tightly controlled by careful consideration of the block copolymer characteristics, paying particular attention to the molecular weight of the polymers. Polymersomes can be engineered to have superior mechanical properties when compared with liposomes. For instance, synthesis of polymersomes with increased tolerance to extreme environments, such as high pH and temperature, as a result of being a synthetic analogue.

The methodology chosen for polymer synthesis is key to the structure formed, the simplest of these routes being the addition of amphiphilic polymers to aqueous solution above the CMC (usually high concentrations) yielding micelle formation, although these easily disassemble upon dilution. Synthesis can occur *via* numerous methods such as, film rehydration, electroformation,<sup>84, 86</sup> RAFT synthesis<sup>87, 108</sup> layer by layer polyelectrolyte formation utilising charge to build up the polymer blocks in series.<sup>109</sup>

Polymersomes form most easily through film rehydration, with polybutadiene-polyethylene oxide (PBD-PEO) being one of the strongest and most commonly used polymers.<sup>110</sup> In the case of polymer formed from PBD-PEO and polybutadiene-polybutylene oxide, several structures can be achieved from the same polymer depending on the required properties. For example, simple mixing forms large, multi-lamellar polymersomes, ideal for the simultaneous encapsulation of multiple hydrophobic moieties. However the fluidity of the membrane allows for the application through various membrane pore sizes to control both the final diameter and lamellarity.<sup>99c</sup>

This can be further adapted by control of the molecular weight during polymer synthesis, which in the case of PBD-PEO can increase the bilayer from ~5 nm up to a thickness of ~20 nm with increasing molecular weight and has been shown to have a direct effect on membrane elasticity and surface tension, which leads to increased stability and fluidity simultaneously.<sup>111</sup>

Furthermore, it is possible to prevent polymersome aggregation by controlling the thickness of the outer leaflet of the polymersome as a function of PEO concentration.<sup>112</sup> The diversity observed in formation methods of polymersomes is reflected in the almost endless combination of properties that can be incorporated into a polymersome by careful selection and design of the building-block polymer materials.<sup>99a</sup>

#### 1.4.4.3 HIGH-THROUGHPUT VESICLE FORMATION

Microfluidics can offer control of vesicle formation on a large scale, by manipulation of the lipid solution flow in capillaries within the 10-100  $\mu\text{m}$  range, with complete control over solution mixing.<sup>82</sup> Microfluidic devices can be designed with multiple inlets for the introduction of solutions and mixing at specific points in the synthesis and by control of the capillary size and laminar flow rate the production of extremely monodisperse vesicle populations can be achieved.<sup>82</sup>

Similar to microfluidic devices and offering the same level of control, but with the ability to produce smaller sized vesicles, is the high-throughput production of liposomes using electrohydrodynamic atomisation (EHDA).<sup>113</sup> This is used for the synthesis of microbubbles, fibres and solid nanoparticles and for the first time in this thesis, vesicles. EHDA utilises a high electrical potential difference to induce focusing and break up of a liquid jet into small droplets<sup>113-114</sup> and is well known for generating fine droplets from micro to nano scale, by elongation of a meniscus under electrical shear.<sup>115</sup> It is a simple process involving formation, control and break up of a jet under the influence of a high electrical field. The equipment uses either a single needle or a co-axial series of needles in which, two immiscible liquids<sup>82</sup> or suspensions are pumped through concentrically aligned needles, and subjected to an applied voltage. The application of a potential on the kilovolt (kV) scale results in various modes of atomisation, and the droplet frequency (yield).<sup>116</sup> Among these, the cone jet is the most preferred jetting mode as it generates monodisperse, fine droplets of particles, in which the outer material solution encapsulates the inner. The EHDA method has many advantages over conventional methods, generating micro to nano sized monodispersed droplets. It is a flexible process which can be modified for encapsulation efficiency.

Another high throughput method, based on the previously discussed inverted emulsion method (section 1.4.4.1), is the continuous droplet interface crossing encapsulation (cDICE) (Figure 1.13).<sup>117</sup> This combines microfluidic capillary droplet with the emulsion/interface system developed by Pautot for asymmetric vesicle formation.<sup>105</sup> The cDICE method was developed by Abkarian *et al.*<sup>117-118</sup> It is a vesicle synthesis method developed using similar methodology to that described in Pautot's inverted emulsion method.<sup>105</sup>

The cDICE method (Figure 1.13) is described as being high yield and tuneable in both end vesicle size and efficiency of encapsulated content. This is as a result of careful consideration of both the lipid adsorption time; for formation of the initial inverted micelles, and subsequent recruitment of the outer lipid leaflet, by optimisation of the overall flight time ( $\tau_f$ ) of the inverted micelles through the organic oil layer.

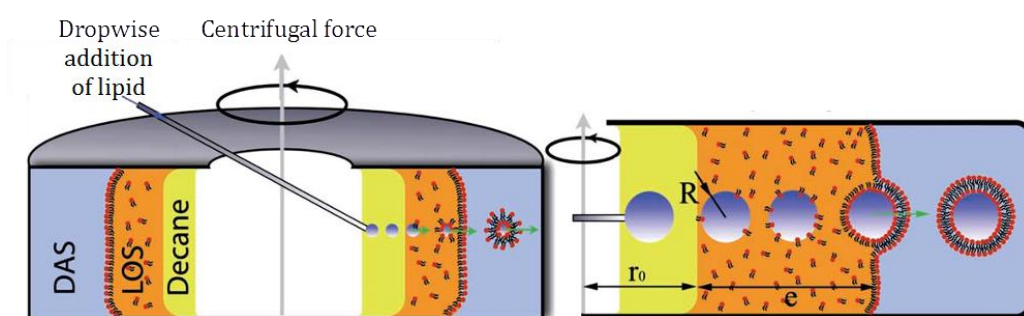


**Figure 1.13:** Schematic diagrams showing experimental set-up for the continuous droplet interface crossing encapsulation (cDICE) method. The aqueous lipid solution is added to the rotating solution into by injection directly into the organic oil layer dropwise *via* capillary. These are then centrifuged through the lipid-oil solution (LOS), at which point inverted micelles are formed, and through the 2<sup>nd</sup> lipid interface to pick up the outer lipid leaflet, into the "dispersing aqueous solution (DAS). Successful vesicle formation is achieved by careful consideration of  $R$  (the droplet radius) and the flight time ( $\tau_f$ ) through the organic layers being sufficient to ensure effective coating of the aqueous droplets. Schematic adapted from Abkarian *et al.*<sup>117</sup>.

This has advantages over the Pautot method, in that it ensures clearance of the interface solution by the inverted micelles and successful coating of the outer layer lipid; as confirmed in the paper by real time fluorescence microscopy.<sup>117</sup> The same method was used to test the Pautot method, and it was discovered that, in most cases, the centrifugation step did not give ample time for inverted micelle formation. Furthermore, in cases where the micelle was assembled, rather than pick up the outer lipid leaflet the micelles burst upon hitting the interface solution.

The improved synthesis route is achieved by incorporation of a microfluidic-like droplet addition to form the emulsion, and by use of a continually rotating system, to obtain an optimised centrifugal force; dependent on the phospholipid molecular weight, to ensure the methods success (Figure 1.13).

## 1.5 BIOMIMETICS

Nature has developed some of the most complex but effective processes observed throughout science, so is an ideal place to seek inspiration for the design of new materials. Many of the complex mineral structures seen in nature, including naturally occurring magnetosomes, are biomineralised. Whilst being known for their superior magnetic and materials properties, the magnetosomes from MTB are difficult to produce due to the bacteria's slow growth under fastidious conditions, which results in low magnetosome yields.<sup>119</sup> For instance, certain species of MTB must be grown under 1% oxygen conditions in order to produce magnetite nanoparticles. The magnetosomes harvested from MTB are also restricted to certain MNP sizes and shapes. Adapting and functionalising these particles for specific applications is therefore both limited and challenging. In addition, due to their bacterial origin, MTB derived magnetosomes have a high likelihood of generating an immune response if used for biomedical purposes *in vivo*.

It is in situations such as these that research can turn to bioinspired synthetic alternatives for compartmentalisation to create nanoreactors. Synthetic analogues can be engineered to withstand the subsequent mineralisation conditions required to make artificial magnetosomes.<sup>89c, 90b</sup> Therefore a bottom-up approach, i.e. use of a synthetic vesicle, will allow the adaptation of this nanoreactor to form a MNP containing vesicle. For example the size and composition of a synthetic nanoreactor can easily be optimised with techniques such as extrusion.<sup>120</sup> Furthermore, this means that reactions outside biological restrictions of temperature or toxicity can be accommodated by the synthetic host, in which significantly more chemical and physical adaptations are possible. This approach can be taken to creation of a synthetic magnetosome, using synthetic lipid/polymer vesicles to compartmentalise magnetite precipitation.

The incorporation of MTB biomineralisation proteins can be used to control the particle formation (if required), and to mimic the processes observed in MTB magnetosome formation.

Vesicles offer the perfect vehicle for a biomimetic approach to synthetic biomineralisation. This is evident in the work of Mann and Hannington,<sup>121</sup> and their work toward the creation of a biomimetic artificial magnetosome (Figure 1.14).

In this work vesicles were formed encapsulating ferrous iron ions, before raising the internal pH of the vesicle; *via* transmembrane diffusion of  $\text{OH}^-$  resulting in iron oxide precipitation. However due to encapsulation of a finite concentration of iron during vesicle formation, a fully mineralised vesicle core was not achieved, as evidenced by TEM (Figure 1.12).

Ongoing research has expanded this field further such as, the design of the “magnetonion,” a multilamellar vesicle, resembling an onion-like structure, in which MNPs sit within the layers of the “onion” by Faure *et al*<sup>122</sup> and Sangregorio *et al*.<sup>123</sup> Both of these systems build on Mann and Hannington’s biomimetic magnetosome system. Studies such as this and others<sup>124</sup> are critical to the development of novel biomimetic biomineralisation nanoreactors.

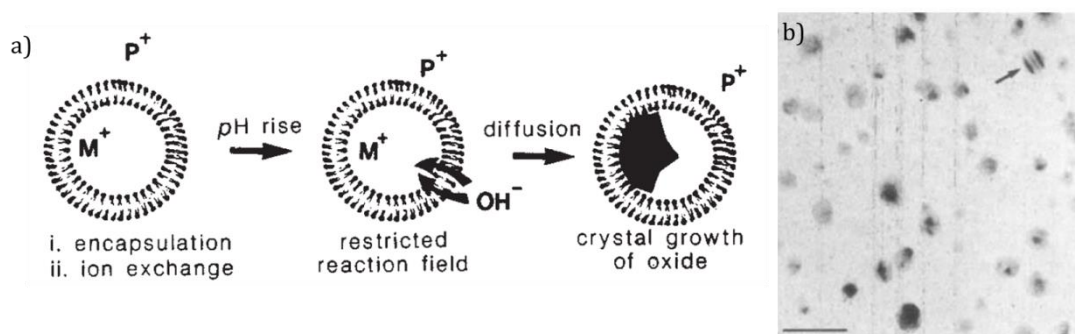


**Figure 1.14:** Taken from Mann *et al*<sup>4</sup> a) in which vesicles were used to encapsulate iron ions, the internal pH of which was increased by influx of hydroxyl ions. This diffusion leads to iron oxide formation in the core of the vesicle. b) Shows TEM of the resulting biomimetalised vesicles, which are only inconsistently filled with iron oxide.

Compartmentalisation of a reaction constrains the environment to promote nucleation processes involved in crystallisation of magnetite MNPs. This approach has also been applied to the biomimetic biomineralisation of calcite, aragonite, hydroxyapatite and silica,<sup>1c, 125</sup> demonstrating flexibility and diversity with regards to the reactions which can be incorporated into a biomimetic nanoreactor system. For biomedical application to be a reality it is necessary to obtain consistent and monodisperse mineralisation within a nanoreactor, to ensure a consistent response in a magnetic field, which remains a significant challenge.

## 1.6 APPLICATIONS OF BIOMIMETICS

Biomimetic studies have wide-ranging applications. Perhaps the most obvious application of a biomimetic system is its introduction back into a biological system to advance biomedicine. As a result of evolution, biological structures often offer superior properties for *in vivo* applications, achieving levels of control impossible to match with a purely synthetic system. Although impossible to match, we can get close to these levels of control using a biomimetic systems which have potential use for application in biomedicine. This section focusses on the biomedical applications that biomimetic systems are currently being used for and looks to potential uses in the future. Using a vesicle as the basis for a biomimetic system has the advantage of inherent multifunctionality. This arises from its structure in which numerous reactions have been successfully compartmentalised.<sup>1c, 65, 126</sup> Depending on the polarity of the molecule to be incorporated this could be on its outer leaflet, or within its hydrophobic membrane. Vesicles incorporating multiple elements with therapeutic and diagnostic potential are termed theranostics. For example, attachment or encapsulation of a drug combined with incorporation of diagnostic tools such as fluorophores or magnetic nanoparticles (MNPs) can allow for simultaneous drug delivery and optical or magnetic resonance imaging (MRI).<sup>98, 127</sup>

### 1.6.1 GENERAL DRUG DELIVERY APPLICATIONS

Many studies in the field of nanocarriers for biomedicine are now focused on development of theranostics.<sup>94b, 128</sup> Theranostics are constructed from both therapeutic and diagnostic moieties.<sup>71b, 94b, 128-129</sup> These multifunctional nanocarriers are designed to be effective, targeted vehicles that carry insoluble therapeutics, with longer lifetimes and narrower bio-distributions compared to delivery of the free drug.<sup>129</sup> Theranostics aim to allow visualisation of a treatment site (diagnostic) whilst simultaneously targeting the area therapeutically and non-invasively. Theranostic nanocarriers are based on a wide variety of architectures including vesicles, dendrimers and carbon nanotubes. These nanocarriers contain functionalities such as; MNPs, quantum dots, fluorophores and/or antibodies. These nanocarriers take advantage of the leaky uptake and reduced drainage of tumour tissue (in the case of cancer treatment).<sup>128b</sup>

A successful theranostic is defined as having four elements: 1) the carrier itself (the size of which is important for uptake), 2) a signal emitter, 3) payload (neither of which should affect the size, shape or surface chemistry of the carrier), and finally 4) a targeting ligand (for effective delivery).<sup>128b</sup> Theranostics can be engineered to release their cargo at a specific treatment site. This means that lower therapeutic doses are required than in non-targeted treatments, which significantly improves treatment efficiency and reduces side effects.<sup>71c</sup>

Targeted delivery arises from either covalent binding or hydrophobic inclusion of a targeting moiety (such as antibodies) into the membrane of the nanocontainer. Most commonly this targeting molecule will consist of immunoglobulins, which are plasma proteins used to generate an immune response.<sup>81</sup> Once at the target site, the vesicle can be engineered to become destabilised, which can cause them to fuse to cells and release their load at the target site.<sup>81</sup>

As the pH of cancerous tissues is usually acidic, this can cause a destabilisation induced when the nanocarrier (which is designed to be stable at neutral physiological pH) enter the acidic environment. Small scale pH switches can also trigger the release of the cargo<sup>75</sup> in the acidic tumour tissue. Other triggers can include fusion to cells, and targeted sequence recognition by attachment of specific antibodies on the nanocarriers to their corresponding antigens on the cancerous cells.<sup>129</sup>

The release of a drug can be engineered into the carrier. For example, Jia *et al*<sup>130</sup> use an amphiphilic polymer with a disulphide bridge connecting the polymer blocks to build their vesicles. When this disulphide is reduced by intracellular concentrations of cysteine (at higher concentrations in the cancer tissue), the drug calcein is released.<sup>130</sup> Similarly, systems which are stable at physiological temperatures (<39 °C), can be designed to release liposome attached drugs on warming (for example by application of a magnetic field). Careful selection of lipids can introduce a vesicle melting temperature of, e.g. 42°C, by either engineering the thermal decomposition of the bonding chemistry within lipids, or thermal degradation of the whole liposome to provide a temperature switch.

### 1.6.2 APPLICATIONS OF MAGNETIC NANOPARTICLES

For use in biomedical applications MNPs need to be distinctly superparamagnetic iron oxide nanoparticles of uniformly sized single domain magnetite (between 30-120 nm) so that they have a consistent and predictable response in the application.<sup>13, 18, 131</sup> This is because they are able to maintain their magnetic orientation in the absence of an applied field. If of a uniform size, the single domain MNPs are also able to produce an efficient and consistent response to an externally applied magnetic field.

Magnetic nanoparticles are already used in biosensing, cell separation and immunoassay applications.<sup>13, 18, 131</sup> MNP incorporation into a biomedical nanoreactor could introduce magnetic diagnostic and targeting functionalities, making these magnetic therapeutic moieties also a theranostic agent. Post formation loading of MNPs into a range of vesicles and nanoparticles (NPs) is of growing interest for use in targeted medical treatments.<sup>71b, 132</sup> Following magnetic separation such as from patient blood for diagnostic assays by incorporation of MNPs.<sup>133</sup> Targeted release of a drug (doxorubicin) from a magnetic nanocarrier has also been realised.<sup>134</sup> Doxorubicin release is triggered by an externally applied alternating magnetic field, which heats the iron oxide nanoparticles within the bilayer, triggering drug release.<sup>134</sup> Theranostics have huge potential in personalised medicine, as the therapeutic agent is ready to be administered at the potential treatment site, depending on a positive outcome from the diagnostic functionality of the nanocarriers.<sup>129</sup> These applications will be discussed in more detail throughout this section.

### 1.6.2.1 MAGNETIC RESONANCE IMAGING (MRI)

Magnetic resonance imaging (MRI) is a non-invasive technique which has been used internationally since the 1970's.<sup>135</sup> The technique makes use of hydrogen nuclei (supplied by protons from water) in the body. A magnetic field is used to align the protons (which are paramagnetic). When a magnetic field is applied to the body in an MRI scanner, the net magnetisation ( $M_0$ ) of protons from water in the body aligning with the direction of the field ( $B_0$ ) can be measured along the z axis ( $M_z$ ).<sup>13, 136</sup>

The magnetic moment of a proton is 3-dimensional, with a corresponding x and y moment, which precesses around  $B_0$  (z-axis) at a random orientation, known as the Larmor frequency.<sup>13, 136</sup> When a radio frequency is applied, the protons absorb energy and move away from  $B_0$ , creating  $M_{xy}$ . When this radio frequency is removed, the protons then relax back to their original alignment with the external magnetic field.<sup>13, 136</sup> This relaxation can be measured.  $T_1$  relaxation, the longitudinal or spin-lattice relaxation is due to the loss of heat to the surroundings, caused by the relaxation of  $M_z$  on the protons.

$T_2$  relaxation, the transverse or spin-spin relaxation, is the rephasing of the spins to align back with  $M_{xy}$ .<sup>13, 136</sup> A third relaxation rate can be measured, and arises from the introduction of heterogeneity in the magnetic field; such as the presence of MNPs in the locality being imaged.<sup>13, 136</sup> This is the  $T_2^*$  relaxation, and it is a combination of the transverse effects and dephasing caused by the presence of magnetic inhomogeneity.  $T_2^*$  is generally faster than  $T_1$  or  $T_2$ . When scanning, the applied radio frequencies (~60 mHz) flip protons by approximately 90°. The relaxation back to  $M_z$  is then measured.<sup>136</sup> Using electromagnetic fields applied at varying current which subsequently changes the field strength and allows the targeting of specific areas allowing imaging in all 3-dimensions.<sup>136</sup>

The MRI image is compiled using a combination of the resonance signals (the frequency and the phase) this outputs spatial information (known as K-space).<sup>137</sup> The information is subsequently converted to image slices using Fourier transform techniques, with the difference in relaxation times creating contrast in the image.<sup>127d, 136</sup> Introduction of MNPs to a target site increases the  $T_1$  and  $T_2^*$  relaxation times of the surrounding protons, providing contrast to highlight specific areas in the body.<sup>137</sup>

Therefore, directing MNPs to tumour tissue using the attachment of targeting antibodies to the magnetic nanoparticles can “light up” the affected sites during scanning.<sup>13, 138</sup> The effect on relaxation time can be controlled by altering the size of the contrast agent or composition of the material, which in turn also controls magnetic properties, as more magnetic material has increased relaxation rates providing greater contrast.<sup>139</sup>

Iron oxide MNPs have great potential as replacements for the gadolinium contrast agents that are currently used. The interaction of protons with the local magnetic field of the iron oxide MNP can significantly enhance contrast in MRI scans *in vivo*, without the toxicity of the current gadolinium based agents. The presence of an MNP provides a local magnetic field, which dramatically increases the local atomic relaxation time, resulting in darkening of this area of the image. This is achieved by ensuring that the MNP has a shorter  $T_2$  (spin-spin) relaxation time than the surrounding tissue, improving contrast between cells containing MNPs and empty cells.<sup>127d, 139</sup> MNP incorporation into drug loaded vesicles could also provide peripheral targeting of said drugs to a treatment site by localisation by applying large external magnetic field to direct the MNPs to the site of interest.<sup>127d, 89c, 90a, 140</sup>

### 1.6.2.2 MAGNETIC HYPERTHERMIA TREATMENT (MHT)

MNP magnetism can also be exploited in magnetic hyperthermia therapies. Hyperthermic therapies are based on magnetically induced heating by oscillation of an externally applied alternating magnetic field.<sup>13, 141</sup> This locally heats the area around the MNPs, and is used in the ablation of diseased tissue and/or release of heat activated drugs.<sup>127d, 142</sup> Magnetic hyperthermia treatment (MHT) is an emerging non-invasive therapy, currently in clinical trials for remote tumour ablation. This is achieved by the targeting (either using antibodies *via* manipulation with a magnetic field depending on the tumour location) of MNPs to the affected site followed by the application of an alternating magnetic field at frequencies in the range of 100-150 kHz.<sup>143</sup> The oscillating field switches the individual spins (for larger single-domain MNPs) or physically flips the whole particle (for smaller superparamagnetic MNPs). This switching or flipping can induce heating, as thermal energy is released as the spins and/or particles attempt to resist realignment with the alternating field.

This heat dissipates into the surrounding tissue, damaging or killing the diseased tissue if the temperature increase is high enough.<sup>13, 141a, 144</sup>

Heating occurs *via* two different mechanisms, dependent on the particle size. The first is by Néel rotations, in which only the magnetic moment in the particle rotates. This mechanism occurs in larger ferri- and ferromagnetic nanoparticles, and thermal energy is generated by the switching dipole moments in the crystal lattice of the MNPs. This is shown in equation 1.6, where the amount of heat generated ( $P_{FM}$ ) is found from the field frequency ( $\mu_0 f$ ) multiplied by the area of the particles hysteresis loop ( $\oint H dM$ ).<sup>13</sup>

$$P_{FM} = \mu_0 f \oint H dM \quad (1.6)$$

The second mechanism involves Brownian rotation. Here, aligning of the magnetic moment causes the whole particle to rotate, and is the case for small superparamagnetic nanoparticles.<sup>13</sup> The rotation causes shear stress as the particle flips, resulting in delivery of thermal energy to the surrounding medium.<sup>127d, 143</sup> The heating power of a particle which undergoes these rotations ( $P_{SPM}$ ) is determined from equation 1.7, where heating power of the square of the field strength ( $H^2$ ), and the particles magnetic susceptibility ( $\chi''$ ) which is frequency dependent ( $\mu_0 \pi f$ ).<sup>13</sup>

$$P_{SPM} = \mu_0 \pi f \chi'' H^2 \quad (1.7)$$

Within each regime, the heating is largely dependent on the magnetic saturation and coercivity of the MNPs, as well as the frequency of the alternating field. In the case of smaller MNPs, which physically rotate, the interaction with the MNP's surroundings is also important. The heating power of a particle is determined by calculation of its specific absorption rate (SAR) (equation 1.8), which calculates the heating power ( $P$ ) of the particles based on the mass of the MNPs in the sample ( $m_{mnp}$ ). A different method involves the calculation of the intrinsic loss parameter (ILP). The ILP uses the SAR value, but also takes account of the alternating magnetic field parameters, namely the frequency ( $f$ ) which scales linearly with  $P$ , and the field strength ( $H$ ), which scales the heating power quadratically (Equation 1.9).

$$SAR = \frac{P}{m_{mnp}} \quad (1.8)$$

$$ILP = \frac{SAR}{fH^2} \quad (1.9)$$

### 1.6.3 MNP PROPERTIES REQUIRED FOR MHT

Accurate measurements of these parameters discussed above can be made difficult by contributions from loss of thermal energy into the system. Convection currents can develop in the heating solutions which are caused by the alternating field, which can be affected by the shape of the sample vessel and position of the temperature probe. It is also possible that the applied field is inhomogeneous, which also generates undesirable heterogeneity.<sup>145</sup> These effects become more pronounced as research moves towards *in vivo* studies, as physiological fluids are also heterogeneous.<sup>145</sup> Therefore, work is ongoing to obtain a standardised approach to accurate MHT measurements.<sup>145</sup> The potential for MNPs to contribute to the efficacy of MHT is far reaching. Again, particle size and morphology are of great importance with regards to the outcomes of *in vivo* MHT. This can be seen in the study by Li *et al*<sup>146</sup>, where heating efficiencies at high and low fields with different size nanoparticles are presented. Li noted that, at a low applied field (9.6 kA m<sup>-1</sup>, 100 kHz), 8 nm particles (suspended in agar) gave the best heating (an increase of 9.3 °C), whereas at higher fields (23.9 kA m<sup>-1</sup>, 100 kHz) particles of 24 nm in diameter proved more efficient (giving an increase of 55 °C).<sup>146</sup> This demonstrates the sensitivity of MHT to subtle changes in the magnetic properties of the MNPs used, and the need for extensive optimisation and standardisation with regards to all parameters. This drive for the use of MNPs in biomedical applications requires an extremely high degree of homogeneity in both particle size and shape. Compartmentalisation of the MNP formation reaction, as is the case with formation of many biominerals, offers the levels of control and reproducibility required. Effective use of MNP is heavily dependent on the particle characteristics, size and concentration.<sup>18, 127d</sup>

#### 1.6.4 BIOMEDICAL USES OF MAGNETOSOMES

Work is ongoing to understand the extent to which bacterial magnetosomes can be modified and functionalised for biomedical application.<sup>24</sup> Their biomedical potential arises from stabilisation of the crystal within the bacterial magnetosome, which both prevents oxidation, and renders the MNP inherently biocompatible. Magnetosomes magnetic properties have proven to be superior in several applications (MRI and MHT) when compared with synthetic analogues<sup>24</sup> due to the high level of homogeneity with respect to size, shape and magnetic response. There is a concerted effort to functionalise magnetosomes for a range of extensive applications,<sup>147</sup> such as targeted therapeutics, DNA extraction, immunoassays and bio-sensing of toxic substances, as outlined by Lang *et al*<sup>24</sup> and Matsunaga *et al*,<sup>147</sup> demonstrates the potential of using magnetosomes *ex vivo* in nanomedicine.

Magnetosomes have great potential as imaging contrast agents in MRI, having an increased  $T_2$  relaxivity rate of  $146 \text{ mmol}^{-1}\text{s}^{-1}$  compared to  $62 \text{ mmol}^{-1}\text{s}^{-1}$ , for comparable dextran coated synthetic iron oxide nanoparticles.<sup>148</sup> *In vitro* work performed by Hergt *et al*<sup>141b, 149</sup> was the first to discover the magnetosomes hyperthermic potential. By immobilisation of magnetosomes in gel to test their heating capability, they found that magnetosome heating gave a SAR of 140 with a heating power of  $960 \text{ W g}^{-1}$  compared to values recorded between  $10\text{-}100 \text{ W g}^{-1}$  for synthetic MNPs.<sup>141b</sup>

*In vivo* hyperthermic heating efficiency assays of magnetosomes have also been tested by Alphandery *et al*, for the destruction of breast cancer tumour cells in a mouse model.<sup>150</sup> In this study, complete destruction of a tumour was observed following three 20 minute rounds of hyperthermia at 183 kHz and 40 mT, in the presence of 1 mg of magnetosome chains. A control sample of PEG/citrate coated iron oxide nanoparticles had no effect under the same conditions.<sup>150</sup> Furthermore, very little difference is observed in the heating efficiency between magnetosomes when in their intact chains and when disrupted from the chains. It was found that chains of bacterial magnetosomes display increased uptake into cancer cells, when compared to those disrupted from their chain assembly. This is most likely to be due to aggregation of the disrupted magnetosomes, which TEM confirms was occurring in solutions of un-linked magnetosomes.<sup>144</sup>

## 1.7 ARTIFICIAL MAGNETOSOMES

Despite their potential, MTB magnetosomes are low yield and inflexible with regards to engineering. This means that extraction from bacteria is not a feasible option for industrial scale-up. If magnetosome formation can be fully understood from first principles; particularly the role of each protein involved and how they work in concert to form the resulting MNPs, this knowledge can be used to attempt the bottom-up creation of an artificial magnetosome and thus enable superior biomimetic biomineralisation within nanoreactors. Mann *et al*<sup>4, 121a</sup> have previously achieved partial precipitation of inorganic minerals inside a vesicle by encapsulation of metal ion solutions in vesicle followed by influx of reagents to yield the precipitation.<sup>4, 121</sup> Unfortunately, it was found that encapsulation of a finite volume of iron ions limited the amount of material that could be precipitated inside the vesicle.

Similarly, high quality particles from low temperature syntheses can be vastly improved by performing precipitation within a reversed micelle (phospholipid encapsulated aqueous solution).<sup>151</sup> The Reverse micelle precipitation routes at room temperature typically tend to cause agglomeration, poor crystallinity and poor yields, and also require vast amounts of solvent (to maintain the micelle structure).

However, Lee *et al* have found that by performing reverse micelle synthesis at slightly elevated temperatures (90°C), grams of monodisperse MNPs can be obtained (without the addition of more solvent). The size of these MNPs can be adjusted by altering the iron salt concentrations.<sup>151</sup> This is a good indication of how precipitation within a vesicle could make low temperature co-precipitation routes viable for the synthesis of high quality MNPs. It is unlikely that in an artificial magnetosome system the organic components and natural materials will withstand high temperature methods. Such mineralisation conditions are most likely lead to destabilisation of the vesicle membrane. Therefore, a compromise between reaction temperature and particle quality is required. A reaction route such as the urea method,<sup>20b, 20e</sup> may be appropriate, as high temperature is required but the reduction in reaction time makes the method applicable to a wider variety of vesicle materials. However, it remains to be seen whether compartmentalisation of these precipitation routes within a vesicle affects the end product, meaning that lower temperature routes could yield more homogenous particles.

### 1.7.1 BIOMIMETIC MAGNETOSOME SYSTEM

Creation of a biomimetic magnetosome system will allow the simultaneous high-throughput creation of an adaptable, magnetised nanocarrier, whilst also serving to better understand the formation of the MTB magnetosome and function of its associated proteins. For this process to be a success, an appropriate vesicle system must be developed. This will require an optimised composition, to allow effective permeation of the membrane,<sup>152</sup> therefore consideration will need to be given to both the bilayer thickness and its fluidity.<sup>153</sup>

For the synthetic magnetosome to be successful in compartmentalisation of magnetite precipitation; a balance is required between integration of an iron transport system, while simultaneously avoiding OH<sup>-</sup> leakage. Membrane permeability is determined by a permeability coefficient (Equation 1.10)<sup>76</sup> as given by a diffusion constant (D), derived from the Nernst equation. Here the gas constant (R) and Temperature (T) is divided by Avogadro's number (N) and f which is the frictional coefficient which accounts for the viscosity ( $\eta$ ) and radius of the molecule (r) (Equation 1.11).<sup>76</sup> This diffusion constant, as well as the concentration gradient dictates the rate of transport across a membrane as a function of the membrane surface area.<sup>76</sup>

$$P = \frac{D}{x} \quad (1.10)$$

$$D = \frac{RT}{Nf} \quad \text{where } f = 6\pi\eta r \quad (1.11)$$

Transport across a membrane can be initiated by careful control of both the inner and outer pHs. Osmotic effects can be used to aid transmembrane diffusion. Increase or decrease of the outer vesicular pH can force iron ions to move across the membrane to re-establish an equilibrium by promoting diffusion across the membrane.<sup>154</sup> Ongoing studies are working towards better quantifying the effect of pH on membrane transport.<sup>124, 155</sup>

There are two general hypotheses for the mechanisms of ion transport through a vesicle bilayer membrane, as determined by molecular dynamics (Figure 1.1),<sup>156</sup> the first being the presence of a water defect in the hydrophobic region of the membrane, causing the rearrangement of the polar headgroups of the amphiphile, (Figure 1.15 a) this allows the leakage of ions through the pore. A second hypothesis, (Figure 1.15 b) is caused by the permeation of ions to the interfacial region of the membrane, which is then carried across the hydrophobic region by a “water finger”.<sup>156</sup> Which of these mechanisms facilitates this ion transport is determined by the length of the hydrocarbon chain and the ionic strength of the solute.<sup>157</sup> As well as natural diffusion, most biological transport is driven by proteins, ion channels and ionophores. Weak acids can be incorporated into a basic interior vesicle by making use of pH gradients.<sup>63</sup> Ion channels are generally driven by catalysed reactions, i.e. energy supplied by transforming ATP to ADP or by proton gradients.<sup>76</sup>

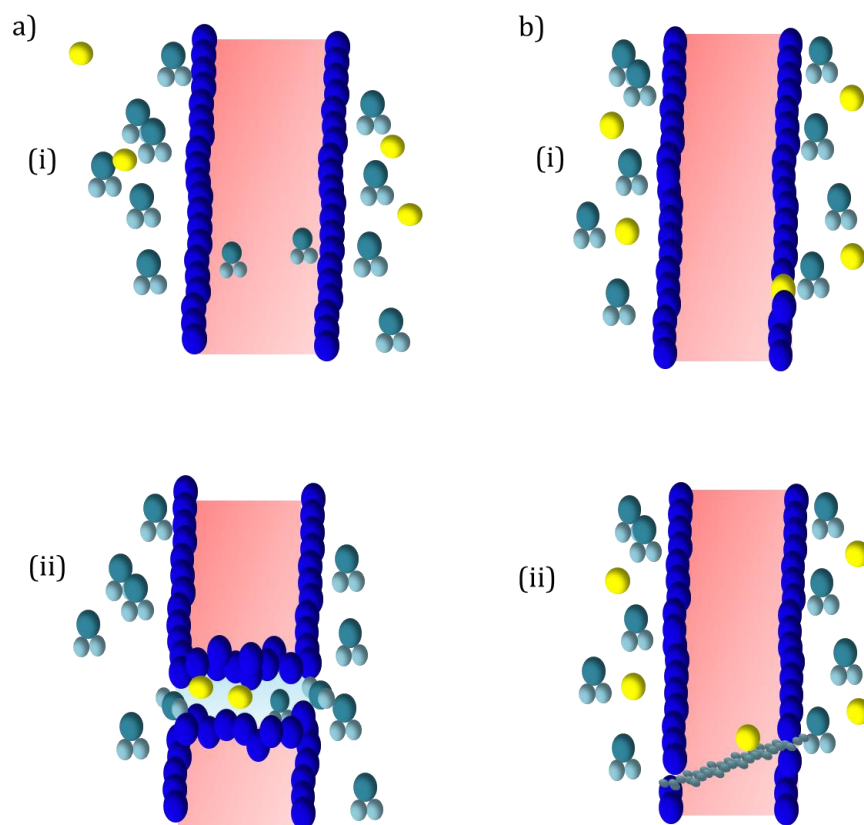


**Figure 1.15:** Transmembrane transport of ions is believed to be *via* one of two routes the first a) being penetration of water discrete water molecules into the hydrophobic region of the bilayer (i), this forces the rearrangement of the polar headgroups rearrange to shield the hydrophobic tails from water causing the formation of a pore (ii) when ions (yellow) can travel through. Alternative hypothesis b) (i) is that ions (yellow) accumulate at the interfacial region of the bilayer (ii) water then penetrates the membrane creating a “water finger” to carry the ions across the hydrophobic region of the membrane.

It is believed that ion channels in MTB are driven by the latter.<sup>52, 53b</sup> The use of membrane permeable ionophores, is one biomimetic approach to the creation of a nanoreactor. These molecules work by chelation of the ion to be transported to the ionophore, which then can move through a membrane to deliver the ion into a vesicle.

This has been explored by Chakrabati *et al*<sup>158</sup>, by the addition of a divalent specific ion channel to a vesicle system. Their study has shown how biological components can be incorporated into synthetic vesicles to mimic the ion transport processes observed in nature. This was proven by the loading both Fe<sup>2+</sup> and Ba<sup>2+</sup> into preformed liposomes *via* liposomal incorporation of Ca<sup>2+</sup> ionophore A23187.<sup>158</sup>

This ionophore has been further explored for Fe<sup>2+</sup> transport in chapter 5. Incorporation of these membrane proteins into a membrane depends on the headgroup chemistry, bilayer thickness, surface tension, curvature and stabilisation by the surrounding lipids.<sup>153</sup> The activity of ion channels, such as those used in magnetotactic bacteria, can be monitored using a tethered bilayer,<sup>64</sup> by measurement of changes in concentration, pH or ion conductance,<sup>153</sup> on either side of the membrane. However, this is not as trivial in the case of vesicles, where the core solution is extremely difficult to measure. Vesicle membrane transport can be monitored by electric potential and pH gradients as measured by lipophilic fluorescent ion probes.<sup>63, 124</sup>

Entirely synthetic membrane transport can be achieved by electroporation. This is a widely used technique in molecular biology for the introduction of DNA into a host cell.<sup>159</sup> The application of an electric potential across a cell membrane can lead to its temporary poration by the increasing electric field inducing a transmembrane potential difference, which eventually causes local defects that form pores.<sup>160</sup>

Electroporation has been previously applied to synthetic di-block polymer vesicles for the introduction of biological moieties, and is believed to undergo similar poration to that observed in natural lipid cell membranes.<sup>161</sup> The mechanism of electroporation is largely unknown; mainly due to the short time scale of pore formation, the complexity in probing the membrane, and the numbers of parameters involved. Studies of changes in phospholipid head group configuration using phosphate-nuclear magnetic resonance spectroscopy (P-NMR) and observed changes in the vesicles structure following electroporation has suggested possible mechanisms include headgroup rearrangement.<sup>162</sup>

Molecular dynamics has offered multiple hypotheses, similar to those discussed above, regarding electroporation mechanisms,<sup>160a, 163</sup> however to date it has not been possible to prove which hypothesis applies experimentally.

These studies have led to two distinct theories on what is believed to happen when an electric potential is applied to a membrane. As with natural ion leakage across a membrane, both mechanisms propose that, as a result of the generated pores, distortions in the membrane result in water penetration through a spontaneously formed hydrophobic pore.<sup>160b</sup> The lipids then rearrange to form a stable more long-lived hydrophilic pore, which grows in size and is stabilised by a drop in potential.<sup>160b</sup> This causes a decrease in the conductance. The pore formation is reversible and pores reseal over time, with the pore size, stability/lifetime depending on the surrounding pressure, the field strength and pulse time, as well as the membrane material.<sup>160b</sup>

The difference between the two mechanisms is how the distortions occur in the membrane. The most widely accepted hypothesis is the transient aqueous pore formation mechanism, where by the electric field causes local distortion and the rearrangement of the lipids due to conduction by the polar head groups.<sup>160</sup> However, this has been questioned, as the same effect is observed in the absence of polar head groups. Thus an alternative hypothesis; the water wire mechanism, has been suggested, in which the water/membrane interface aligns and undulates with the current resulting in distortion, allowing water to penetrate.<sup>160</sup> There are multiple parameters which can affect the outcome of electroporation most notably the voltage applied across the membrane, but the outcome can also be affected by factors including path length of the cuvette, sample volume, temperature, pulse length and number of pulses.<sup>164</sup>

### **1.7.2 AIMS AND OBJECTIVES**

Magnetotactic bacteria (MTB) produce single domain magnetic nanoparticles (MNPs) of a monodisperse size and shape within lipid vesicle structures termed magnetosomes.

The creation of a synthetic magnetosome inspired by the mechanisms observed within MTB can address the problems involved in producing bacterial magnetosomes in sufficient quantity and adapting them for use in *in vivo* biomedical applications. The idea of a synthetic magnetosome has been previously suggested by Mann *et al.*<sup>4, 121a, 125</sup> This thesis builds on their work<sup>4, 121a</sup> in order to mimic a filled magnetosome at the nanoscale.

Reversing Mann's system, by encapsulating base in the core of nanoscale vesicles, followed by transport of iron ions, is unique to this project. Furthermore, purification and incorporation of magnetosome specific proteins believed to be responsible for the controlled formation of both the internal vesicle and subsequent precipitation of the particle in MTB is also unique. This creates a synthetic model of a magnetosome which can then be altered and functionalised depending on application.

Synthetic magnetosomes produced as part of this project have been trialled *in vitro* for their potential as both contrast agents for magnetic resonance imaging (MRI) and therapeutics in magnetic hyperthermia treatment (MHT) of tumours (Figure 1.16). Each aspect of the synthetic magnetosome will require exploration an optimisation of the materials and synthesis routes before it can be brought together to create the final magnetosome. Table 1.2 outlines the plans for creating the synthetic magnetosome nanoreactor, and the chapter in which this is undertaken.

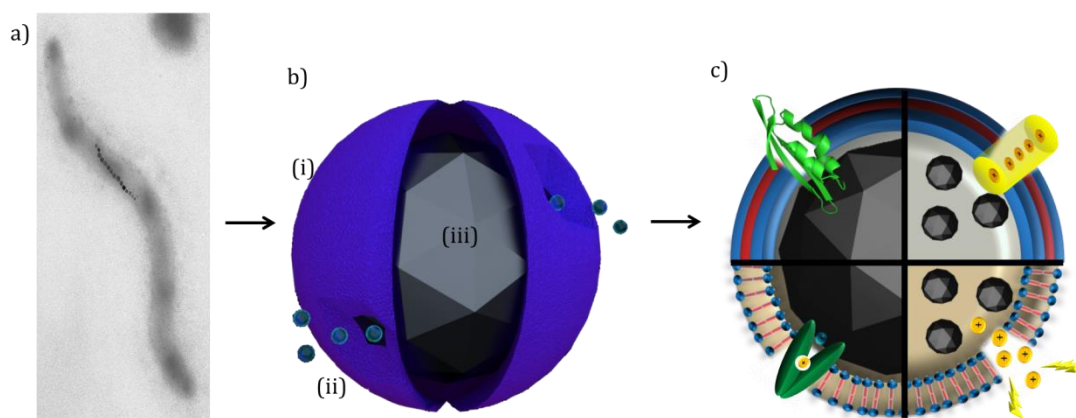


**Figure 1.16:** a) Inspiration is taken from Magnetotactic bacteria (species shown is *M. magneticum* AMB-1), which biomineralises chains of magnetite within magnetosome vesicles. b) The aim of this thesis is to copy this process synthetically by (i) creating a synthetic vesicle with a basic core (ii) followed by transport of iron ions to yield (iii) the precipitation of a single magnetite nanoparticle. c) This synthetic magnetosome can then be used for the study of MTB biomineralisation proteins and incorporation of biomedical moieties for nanomedical application.

<b>Aspect of synthetic magnetosome creation to be optimised</b>	<b>Chapter in which optimised</b>
<b>Magnetite synthesis route</b>	Chapter 3
<b>Vesicle composition</b>	Chapter 4
<b>Biological transporters</b>	Chapter 5
<b>Synthetic iron transport</b>	Chapter 6
<b>Scale up of synthetic magnetosome production</b>	Chapter 7
<b>Control of particle formation</b>	Chapter 8
<b>Biomedical potential of artificial magnetosomes</b>	Chapter 9

**Table 1.2** Plan for artificial magnetosome production.

# CHAPTER 2:

---

## METHODS AND MATERIALS

All solutions used in all methods were degassed and sparged with N<sub>2</sub> prior to use and all experiments were carried out under an inert atmosphere where possible. This was to prevent oxidation of the iron species used to ensure the precipitation of magnetite as opposed to other iron oxides. Lipids used were purchased from Avanti Polar Lipids Inc., and polymers used were purchased from Polymer Source. Other chemicals were purchased from Sigma Aldrich, unless otherwise stated.

## 2.1 MAGNETITE SYNTHESIS

There are many synthetic routes for the precipitation of magnetite, (as discussed in section 1.3.3) with each method resulting in different nanoparticle sizes and morphologies. Altering any one of a number of parameters within a specific synthesis route can result in unwanted contaminants, such as precipitation of undesirable iron oxide mineral phases, i.e. those other than magnetite (Section 1.3.2, Figure 1.3).

### 2.1.1 ROOM TEMPERATURE CO-PRECIPIATION (RTCP)

Room temperature co-precipitation<sup>20f</sup> is the precipitation of magnetite, in this instance from iron chloride salt sources. FeCl<sub>2</sub>·4H<sub>2</sub>O (10 or 100 mM, 10 ml) and FeCl<sub>3</sub>·6H<sub>2</sub>O (10 or 100 mM, 10 ml) are combined respectively in a 1:2 ratio. This reflects the stoichiometry of the final magnetite crystal structure. The reaction uses NaOH (10/100 mM, 10ml) to slowly increase the pH of the overall solution and initiate precipitation. The alkali is added drop-wise *via* a syringe driver (Harvard Instruments) at a rate of 20 μl min<sup>-1</sup> under N<sub>2</sub> bubbling to ensure homogenous mixing of reagents. This rate of addition ensures slow formation of the correct intermediates, facilitating the desired stoichiometry for the precipitation of magnetite. The resulting black precipitate tends to contain relatively small magnetic nanoparticles (after ageing) which are subsequently washed by separation with a magnet and re-suspension in water, five times to remove any non-magnetic oxides from the final product.

### 2.1.2 THERMAL DECOMPOSITION OF UREA CO-PRECIPIATION

$\text{FeCl}_2 \cdot 4\text{H}_2\text{O}$  (10 mM, 10 ml) and  $\text{FeCl}_3 \cdot 6\text{H}_2\text{O}$  (10 mM, 10 ml) are combined in a 1:2 ratio.  $\text{CO}(\text{NH}_2)_2$  (10 mM, 10 ml) is added to the mixed valence Fe solution, before being heated to 85°C and held at this temperature for four hours under  $\text{N}_2$ . This allows for decomposition of  $\text{CO}(\text{NH}_2)_2$  into  $\text{NH}_3$ . The  $\text{NH}_3$  acts as the base to drive the co-precipitation of the iron salts, resulting in the formation of a black magnetic solid. The resulting solid was washed using separation with a magnet and re-suspension in water five times.<sup>20b</sup>

### 2.1.3 UREA AND AMMONIA CO-PRECIPIATION

The method of combined urea/ammonia co-precipitation was adapted from the previously published method by Mürbe *et al.*<sup>165</sup> 10 mM iron stock solutions of  $\text{FeCl}_2$  and  $\text{FeCl}_3$  are combined at a ratio 1:2 ferrous to ferric iron salt respectively (10 mM  $\text{FeSO}_4$  can also be used as a ferrous iron source). A combination of chloride and sulphate iron salt were also used ( $2(\text{FeCl}_3):1(\text{FeSO}_4)$  10 mM). The iron salt at a volume of 8 ml is added to a urea/ammonia mix solution with urea: ammonia ratio varying from 0-100 % urea. The solution was then heated on a hotplate to 80°C and held at this temperature for four hours, under  $\text{N}_2$ . The precipitated solid was washed as described above, using magnetic separation and re-suspension in water five times.

## 2.2 VESICLE SYNTHESIS

Various methods used to synthesise vesicles using both phospholipids and block copolymers are detailed below. The methods for magnetite precipitation outlined in section 2.1 were incorporated as closely as possible into each vesicle synthesis route. Once vesicles were formed using the methods outlined below, size exclusion chromatography was used to remove the supernatant to prevent magnetite precipitation external to the vesicles (Section 2.2.4).

$\text{FeCl}_2 \cdot 4\text{H}_2\text{O}$  (10 mM, 10 ml) and  $\text{FeCl}_3 \cdot 6\text{H}_2\text{O}$  (10 mM, 10 ml) were combined in a 1:2 ratio and added to the vesicle solution before being electroporated ( $5 \times 2500$  V). Centrifugation removed excess precipitate, and tip sonication, water bath sonication and extrusion (Section 2.2.3.3) were employed to control vesicle size.

## **2.2.1 LIPOSOME FORMATION**

### **2.2.1.1 BASIC FORMATION**

Phospholipids (0.5 – 1 mg) are dissolved in 1 ml of chloroform and methanol (in a 1:1 ratio). The solvent is then removed under vacuum to form a thin lipid film. The resulting film is rehydrated with the basic solution to be encapsulated, corresponding to the desired magnetite synthesis route e.g. NaOH,  $\text{CO}(\text{NH}_2)_2$  or  $\text{NH}_3$  (Section 2.1).<sup>75</sup> The size distribution of the resulting liposomes is controlled by either bath sonication (Ultrasonic cleaner, VWR) for 30 minutes following film rehydration, tip sonication (Vibracell, Sonics) at 70 % amplitude for 15 minutes or, for a narrower size distribution, extrusion by 15 passes through a 100 nm membrane (Section 2.2.3.3).

## **2.2.2 POLYMERSOME FORMATION**

### **2.2.2.1 DI-BLOCK POLYMERSOMES**

Encapsulation within polymersomes is essentially an extension of the film hydration method used in liposome synthesis (Section 2.2.1). An A-*b*-B amphiphilic block-copolymer film ( $1\text{-}10 \text{ mg ml}^{-1}$ ) is swelled overnight in a vacuum desiccator/oven ( $40^\circ\text{C}$ ). This is then rehydrated with 1 ml base whilst stirring for 12-16 hours, before being sonicated at ambient temperature (30 minutes).

### 2.2.2.2 TRI-BLOCK POLYMERSOMES

Poly (2-methyloxzoline)-b-poly(dimethylsiloxane)-b- poly(2-methyloxzoline) (PMOXA-PDMS-PMOXA) was dissolved in 1 ml of  $\text{CHCl}_3$  in a round bottom flask. NaOH (10 mM) was added to the polymer/solvent at a rate of  $50 \mu\text{l min}^{-1}$  to give a final concentration of  $1 \text{ mg ml}^{-1}$ . The resulting mixture was then centrifuged (10 minutes at 9,800 g, Progen Genfuge, 24D microcentrifuge ) to remove any residual solvent (bottom layer) from the polymersome solution (top layer). This method was adapted by myself and Matthew Berry (MChem student) from the published method by Nardin *et al.*<sup>9b</sup>

### 2.2.3 VESICLE SIZE AND POLYDISPERSITY CONTROL METHODS

Vesicle size dispersity was controlled using a number of techniques. Each method, applied to the formation of both liposomes and polymersomes, narrowed the polydispersity of the overall vesicle population.

#### 2.2.3.1 BATH SONICATION

The application of sonic energy to a lipid or polymer solution agitates the solution, causing any vesicles formed to collapse and re-assemble. This also encourages the self-assembly of free lipids and instigates the simultaneous formation of small vesicle sizes with a narrower size distribution. Vesicle samples are subjected to bath sonication for 30 minutes at the standard frequency of the bath (Ultrasonic cleaner, VWR (45 kHz). The vial was fully submerged to ensure maximum transfer on the sonic energy into the sample.<sup>71a</sup>

### 2.2.3.2 TIP SONICATION

Tip sonication is expected to exert greater control over the size distribution of the vesicles than bath sonication. This is due to the higher frequencies and more localised sonication that can be applied to the sample. Thus the effects of tip sonication on a vesicle sample have also been investigated. Samples are heated to above their phase transition temperature if necessary (Table 4.1). Sonication (Vibracell, Sonics) is applied to the sample in a glass vial for between 15-30 minutes at amplitude of 75 % using a narrow sonication tip (3 mm). Tip sonication applies sonic energy to a sample. This in turn breaks down vesicles in the solution, but with more precision than with bath sonication. This is due to greater control of the energy supplied to the sample by optimisation of both the amplitude and tip width.

### 2.2.3.3 EXTRUSION

Perhaps exerting the tightest control over vesicle polydispersity, extrusion is the process of forcing vesicles through a membrane of a known pore size. This causes larger vesicles to break up and re-assemble into smaller ones. The size at which they reassemble is dictated by the pore size of the membrane used. The extrusion kit is assembled according to Figure 2.1 a). All filters and the membrane are soaked in the same buffer as the vesicle solution and placed in the centre of the extruder. Using gas tight syringes, the vesicle solution is passed from one syringe to the other through a 100 nm pore membrane 15 times, as shown in Figure 2.1 b). These conditions have previously been optimised by the Battaglia group (Unpublished method) to obtain monodisperse vesicles of < 100 nm. In some cases samples were first passed through a 400 nm membrane to initially decrease their size to avoid rupturing or obstructing the membrane. This extrusion method was applied to both lipid and polymer vesicle samples.

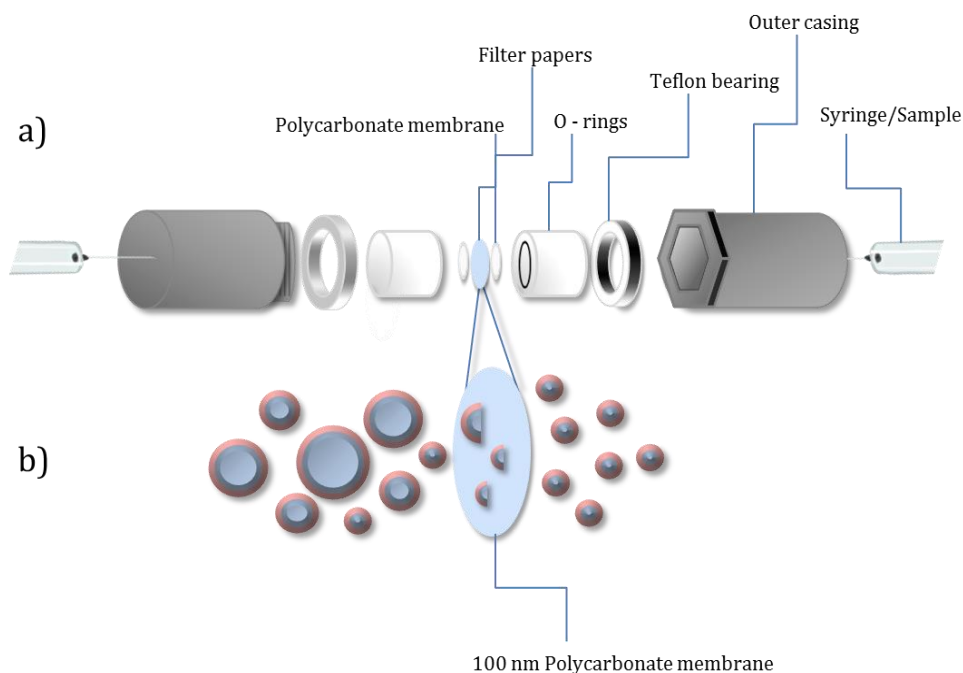


**Figure 2.1:** Extrusion is the process of passing vesicle solution through a membrane containing pores of a known size to achieve a narrow size distribution. a) Shows the assembly of the extrusion kit, in which the extrusion membrane is placed between two filter papers held in place by two O-rings to prevent solution leakage. These are screwed into place by an outer metal casing. Syringes are inserted into each end of the extruder and the solution is passed from one to the other through the membrane. b) On passing through the membrane the lipid or polymer polydisperse vesicles are forced to reassemble into a monodisperse population of a size determined by the membrane pore sizes.

#### 2.2.4 VESICLE CLEAN UP

To remove excess base following vesicle formation, vesicles are passed through a size exclusion chromatography (SEC) column.<sup>166</sup> The presence of external base solution can cause precipitation of mixed oxides on addition of the ferrous/ferric ion solution. With some of the base solutions (NaOH) this precipitation is instantaneous; inhibiting iron transport and creating undesired complex mixtures of MNP both inside and outside of vesicles. To prevent this, all vesicle solutions were separated on an SEC column to isolate vesicles and exchange the outer solution for buffer or water. SEC columns are filled with sepharose beads of a designated size and porosity.

SEC is based on size separation (Figure 2.3). As NaOH in solution is much smaller than the vesicles, the base molecules take a longer path through the column. This is because  $\text{Na}^+$  and  $\text{OH}^-$  can enter more spaces between the sepharose beads, and even the pores within the beads. This means that bigger assemblies (i.e. the vesicles) move through the column much faster. This separates them from the NaOH solution outside the vesicles, and exchanges the vesicles into the column equilibration buffer. Vesicle solutions are cleaned using GE Healthcare PD10 columns, or self-packed sepharose 4B in a 20 cm<sup>3</sup> column. In each case, the column is filled with PBS buffer; the polymer solution is then added to the column and allowed to enter the sepharose. This is then topped up with PBS buffer to push the sample through the column. The eluent from the column is collected once the solution becomes cloudy; indicating the presence of vesicles. The pH of the collection solution confirms that vesicles are exchanged into neutral pH buffer. Smaller samples of vesicles (approximately 1 ml) were cleaned up using dialysis. For dialysis, the sample is encased in snakeskin dialysis tubing (molecular weight cut off 3,500 Dalton) and placed into 2 L of PBS for 12-16 hours to allow equilibration between the inner and outer solutions.

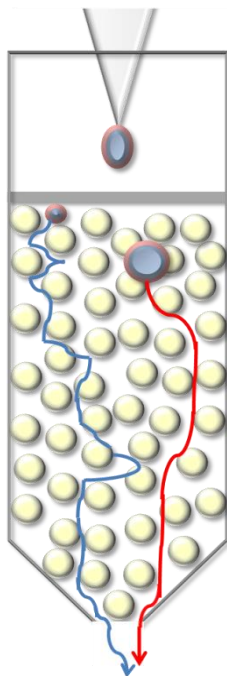


**Figure 2.2:** Size exclusion chromatography (SEC): SEC is used to clean up vesicles by addition of the vesicle solution to a sepharose column, which then moves down the column by way of gravity. The column separates suspensions by size, as bigger molecules/assemblies take a shorter path, limited by the ability to fit into the gaps between the sepharose beads (Red path). Smaller molecules, i.e. the eluent, can diffusively enter more of the spaces between beads, and so takes longer to leave the column (Blue path).

## 2.2 IRON TRANSPORT METHODS

### 2.2.5 ELECTROHYDRODYNAMIC ATOMISATION VESICLE SYNTHESIS

Technology used by the Edirisinghe group based at UCL<sup>113b, 114</sup> has been utilised as part of this project. This has been used to both automate and optimise the synthesis of both liposome and polymersomes for the production of monodisperse vesicles as vessels for the production of a synthetic magnetosome. The equipment uses a capillary tube of specific size determined by the required size of the droplets produced. A potential difference (of the order kV) is applied between the capillary and ground electrode (Figure 2.3). The applied voltage is used to control the meniscus shape on exit from the capillary, (Table 7.1) for the formation of what is known as a “Taylor cone”.<sup>115</sup> This creates a high charge density giving rise to the formation of nano-sized droplets as small as 30 nm in diameter. For the formation of base encapsulated vesicles, lipid solution and base are loaded into separate syringes that are fed into separate ports of a single capillary *via* syringe drivers at a rates varying between 5-50  $\mu\text{l min}^{-1}$ .

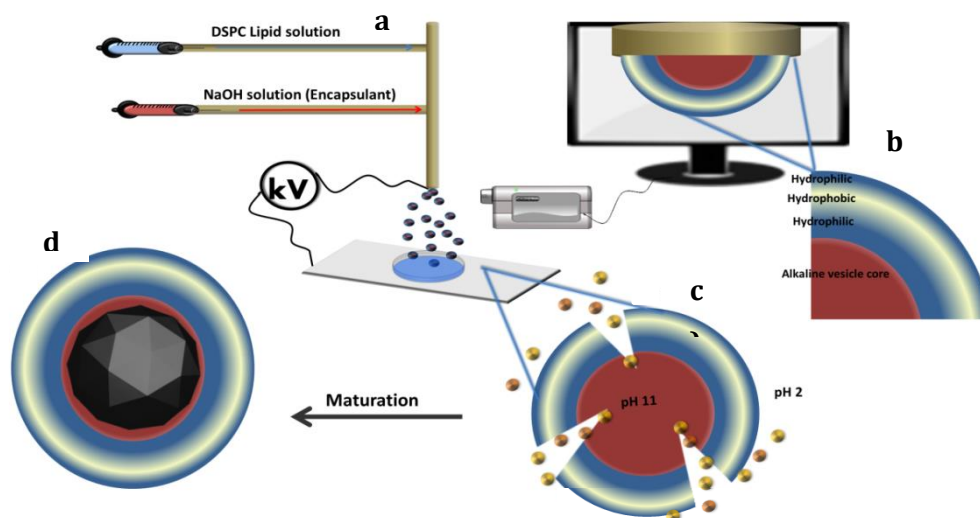


**Figure 2.3:** Electrohydrodynamic atomisation (EHDA) synthesis of vesicles: Shows a schematic of the single axial EHDA a) encapsulation of NaOH within lipid *via* EHDA jetting b) shows the composition of the resulting vesicles, c) vesicles are introduced to mixed valence iron solution and electroporated at 750 V, to yield d) a magnetic nanoparticle within the vesicle core.

The solutions then combine in the capillary, at which point self-assembly into vesicles should begin. As the solutions leave the capillary, a voltage is applied (15-20 kV) and the solution is broken down into monodisperse droplets which assemble into vesicles. The vesicles are collected in water and mixed valence iron solution ( $\text{Fe}^{2+}$  1:2  $\text{Fe}^{3+}$ , 10 mM, 1 ml) is introduced to the vesicle solution and electroporated (Section 2.3.2.1) at 750 V to aid iron transport into the core of the vesicle.

## 2.3 IRON TRANSPORT

Magnetite precipitation in the core of the vesicle is only possible if there is iron transport through the vesicle membrane. Four routes of iron transport have been explored to obtain an artificial magnetosome, starting with biological based transporters then moving to completely synthetic methods of cross-membrane transport.

### 2.3.1 BIOLOGICAL TRANSPORTERS

Biological transporters are incorporated into vesicles during vesicle formation (Section 2.2). During polymer/lipid film rehydration, the biological transporter protein is added to the stirring solution at a concentration of  $0.1 \mu\text{g ml}^{-1}$ . The vesicles are then cleaned up using SEC (Section 2.4.2). After clean up, mixed valence iron salt (1  $\text{FeCl}_2$ :2  $\text{FeCl}_3$ ) solution is added to the vesicles. The protein transporters should allow iron transport through the vesicle membrane. After incubation for 12-16 hours vesicles are again cleaned up *via* SEC (Section 2.4.2) to remove excess iron, before analysis. The success of the transporter was assessed using TEM (Section 2.6.1.1) and elemental analysis (2.6.2.4) to see if a solid, electron dense iron oxide particle was able to form within the vesicle.

### 2.3.2 A23187 DIVALENT IONOPHORE

A23187,<sup>167</sup> an ionophore, chelates divalent iron and transports this by subsequently passing across a membrane. Polymersomes (1 ml, 10 mg ml<sup>-1</sup>) with NaOH (10 mM) encapsulated and previously cleaned up *via* SEC (Section 2.4.2) were added to FeCl<sub>2</sub> (5 ml, 10 mM) which contained the A23187 ionophore, (1 μl, 1.90×10<sup>-6</sup> M). The alkali containing polymersomes are incubated in the iron/ionophore for five days to facilitate cross-membrane transport of iron. The success of the transporter was assessed using TEM (section 2.6.1.1) and elemental analysis (2.6.2.4) to see if iron oxide was able to form within the vesicle.

### 2.3.3 ELECTROPORATION

Electroporation is a technique widely used in biology for the transformation of DNA into cells. Electroporation electrically permeabilises a cell membrane by application of a pre-determined voltage.<sup>159-160, 161</sup> The mechanism by which the membrane is permeated has been widely explored, but as yet has not been confirmed (Section 1.6.3). Electroporation is used as a method of synthetic iron transport across the vesicle membrane by increasing membrane permeability. Vesicles absent of both protein transporters and/or ionophore were subjected to electroporation. Following clean up as above in section 2.2.3, iron solution (Fe<sup>2+</sup> 1:2 Fe<sup>3+</sup>, 10 or 100 mM) is added to the vesicle solution in a ratio of 1:1 vesicle:iron solution. The combined solutions are then transferred to an electroporation cuvette, which has electrode plates on either side, and chilled for approximately five minutes on ice. The solution filled cuvette is then placed into the electroporator, ensuring that the cuvette plates make contact with the electrodes. A voltage is then applied to the sample (200 – 2500 V, manually varied to optimise iron influx) with a pulse rate of 0.7 – 2 ms (automatically determined by the electroporator).

### 2.3.4 *IN-SITU* INCORPORATION

$\text{Fe}_2\text{SO}_4\cdot\text{H}_2\text{O}$  (16.6 mM) and  $\text{Fe}_2(\text{SO}_4)_3\cdot\text{H}_2\text{O}$  (15.6 mM) are combined in a volume of 10 ml of degassed water in a round bottomed flask. 1 ml of purified PEG<sub>113</sub>-PHPMA<sub>400</sub>/PMPC<sub>28</sub>-PHPMA<sub>400</sub> polymersomes (approximately 10 mg/ml) is added to the iron solution. This solution is then sealed and sparged with  $\text{N}_2$ . A total volume of 4 ml of NaOH (10 mM) is added dropwise, at a rate of 20  $\mu\text{l min}^{-1}$  by syringe driver (Harvard Instruments). On addition of NaOH, a room temperature precipitation of magnetite occurs in the presence of the polymersomes. Once complete, the particles are removed from the solution by magnetic separation. The magneto-polymersome solution was heated to 80 °C for 0.5-1 hour, at which point it flocculated and the white opaque top layer of the solution was removed by pipette.

## 2.4 IRON ION TRANSPORTS ASSAYS

To quantify iron transport, membrane permeability, and therefore the success of the various methods reported (Section 2.3); several indicators of pH, redox potential, as well as fluorescence and iron chelators have been encapsulated in vesicles. All solutions are cleaned up using SEC (Section 2.4.2) following encapsulation of the relevant indicator. UV-vis (Section 2.6.2.1) or fluorescence (Section 2.6.2.2) spectra are recorded before membrane disruption or iron transport to generate a background spectrum. Vesicles are electroporated (Section 2.3.2.1) to permeate the membrane, and spectra are re-recorded. The specific method used with each indicator explored is outlined below (Figure 2.4).

### 2.4.1 CARBOXYFLUORESCHEIN

Carboxyfluorescein<sup>168</sup> is a fluorescent dye which self-quenches at high concentration, ( $\geq 100$  mM). Upon leakage (*via* permeation or electroporation) the dye is diluted and the fluorescence signal should increase. Vesicles are rehydrated with carboxyfluorescein (100 mM) at a 10 % v/v carboxyfluorescein:lipid/polymer ratio and stirred for 12-16 hours.

Vesicles are then cleaned up by SEC (Section 2.4.2) and fluorescence measurements are taken using both a fluorimeter (Section 2.6.2.2) and using fluorescence microscopy (Section 2.6.1.5). Leakage from the vesicles is monitored using fluorimetry. Electroporation is used to facilitate leakage, and change in fluorescence signal measured.

### 2.4.2 FERENE

Ferene is an iron chelator which undergoes a colour change from yellow to blue on chelation of  $\text{Fe}^{2+}$ .<sup>169</sup>  $\text{FeCl}_2 \cdot 4\text{H}_2\text{O}$  solution is prepared at various concentrations (100 mM, 50 mM, 25 mM and 10 mM). 5 ml aliquots were combined with Ferene (10  $\mu\text{l}$  at 15  $\mu\text{M}$ ) and UV-vis spectra are recorded. 1 ml of the ferrous chelated Ferene (10 mM) is added to 3ml of NaOH (10 mM) and  $\text{H}_2\text{O}$  separately, and incorporated into polymersomes. This is used to test compatibility with NaOH, chelation affinity and detection of the solution in the vesicle core.

### 2.4.3 PRUSSIAN BLUE

A 0.1 mM solution (prepared by serial dilution) of Prussian Blue (potassium ferrocyanide ( $\text{K}_4[\text{Fe}(\text{CN})_6] \cdot 3\text{H}_2\text{O}$ ) is prepared. 10  $\mu\text{l}$  of the 0.1 mM  $\text{K}_4[\text{Fe}(\text{CN})_6] \cdot 3\text{H}_2\text{O}$  is then added to  $\text{FeCl}_2 \cdot 4\text{H}_2\text{O}$  solution prepared at a range of concentrations appropriate to prepare a standard curve from the UV-vis spectrum, the UV-vis spectrum at each concentration is then recorded to obtain a standard curve. 1 ml of  $\text{K}_4[\text{Fe}(\text{CN})_6] \cdot 3\text{H}_2\text{O}$  (10 mM) is added to NaOH (10 mM) during polymersome formation. This is again to detect compatibility with NaOH, chelation affinity and visibility of the solution in the vesicle core Vesicles are then cleaned up *via* SEC (Section 2.4.2) and recording of the UV-vis spectrum is repeated.<sup>170</sup>

## 1. Encapsulation of the detection reagent



## 2. Poration of the vesicle membrane



## 3. Quantification of membrane transport

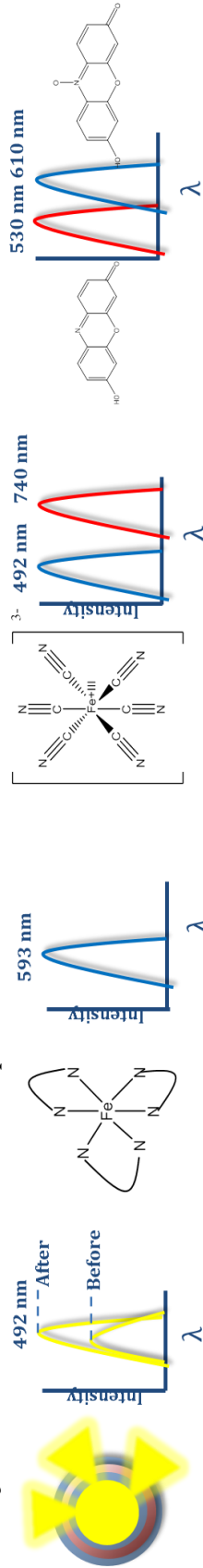


**Figure 2.4:** Iron transport assays: a) (1) Vesicular encapsulation of carboxyfluorescein at pH above self-quenching concentration (100 mM), (2) poration of the vesicle membrane causes leakage and dilution of the carboxyfluorescein, which initiates fluorescence "switch on". (3) This can then be detected using fluorimetry. b) (1) Encapsulation of Fe<sup>2+</sup> chelator ferene causes a colour change from yellow to blue (2) poration of the membrane with ferrous iron ions. (3) This colour change is measured with UV-vis spectroscopy. c) (1) Prussian blue dye reacts in a similar way following encapsulation within a vesicle and (2) poration of the membrane with either ferric or ferrous iron ion solution. (3) The colour change to either red or blue is dependent on the iron ion valency, and can be detected by using UV-vis spectroscopy. d) (1) Resazurin is again encapsulated within a vesicle. (2) poration of the membrane which causes a change in pH can be monitored by a colour change of the resazurin solution, which responds to changes in redox potential. (3) Again this colour change can be monitored using UV-vis spectroscopy.

### 2.4.1 RESAZURIN

Resazurin is a redox sensing dye which changes colour from pink to clear upon oxidation.<sup>171</sup> Solutions of  $\text{H}_3\text{COONa}$  (0.2 M) and  $\text{CH}_3\text{COOH}$  (0.2 M) are used to obtain pHs between 3.8 and 6.8, the solutions were prepared at pH intervals of 0.2. The pH was then measured using a Mettler Toledo PHE1204 pH meter. Resazurin solution (10 mM) is prepared. 10  $\mu\text{L}$  of Resazurin is added to 10 ml of each pH solution, and the UV-vis spectra are recorded. For incorporation into vesicles, 1 ml of Resazurin solution (10 mM) is also added to  $\text{FeCl}_2 \cdot 4\text{H}_2\text{O}$  (10 mM), which is then used to rehydrate a polymer film. The resulting polymersomes were cleaned up using SEC (Section 2.4.2) and UV-vis spectra are recorded.

## 2.5 CONTROL OF PARTICLE FORMATION

Polymer films are rehydrated according to the method described in Section 2.2.2.1, with 10 mM NaOH to a concentration of 10 mg  $\text{ml}^{-1}$ . During rehydration, the relevant biological transporter (protein or scaffold) is added to the rehydration solution at a concentration of 10  $\mu\text{g ml}^{-1}$ . This is then left to stir for 12-16 hours. The vesicles are then exchanged into PBS buffer using SEC (Section 2.2.4), and electroporated according to the method described in section 2.3.2.1 to facilitate iron transport. The resulting biomineralisation reaction is analysed using TEM (Section 2.6.1.1) and elemental analysis (Section 2.6.2.4) to see if iron oxide solids form within the polymersome structures.

## 2.6 PROTEIN CLONING AND PURIFICATION METHODS

### 2.6.1 GENE CLONING

#### 2.6.1.1 POLYMERASE CHAIN REACTION (PCR)

A Polymerase chain reaction (PCR) is used to efficiently select and exponentially replicate a chosen nucleotide sequence from template DNA (Figure 2.5).<sup>172</sup> During this process DNA is heated, which causes its denaturation and the formation of 2 single strands of DNA. To carry out the replication, the DNA template (0.5  $\mu\text{l}$ , 50  $\text{ng } \mu\text{l}^{-1}$ ) is combined with DNA polymerase (1  $\mu\text{g } \mu\text{l}^{-1}$ , 1  $\mu\text{l}$ ) and a supply of deoxynucleotide triphosphates (dNTP's) along with pre-designed forwards and reverse primers (1  $\mu\text{l}$ , 10  $\mu\text{M}$ ). These primers attach to the DNA template on different strands at the beginning and end of the sequence to be amplified, and importantly at a temperature below the melting temperature of the primer sequences. The temperature of the reaction is increased to the optimum for the activity of the polymerase (70-72°C). The polymerase then extends the primers for a specific amount of time determined by the number of base pairs to be replicated (Table 5.1).

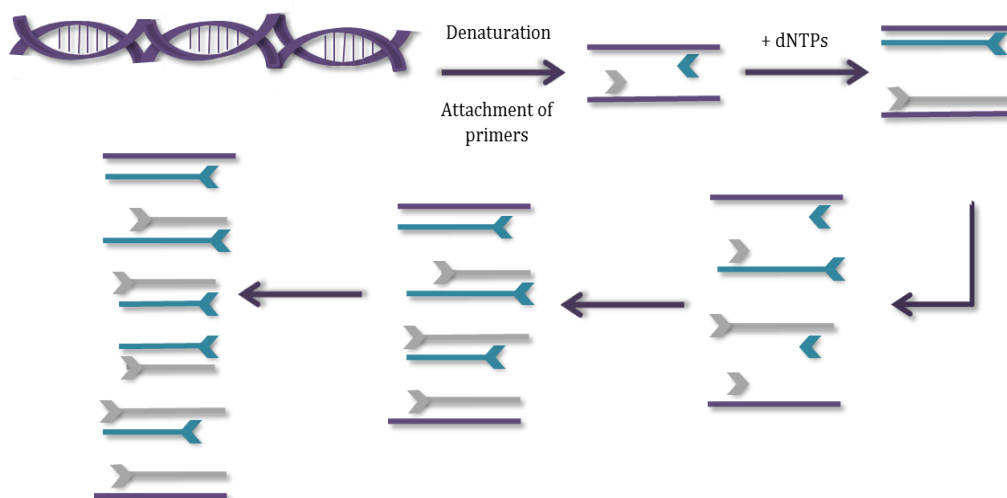


**Figure 2.5:** Polymerase Chain Reaction: To amplify a specific sequence of DNA, the DNA product is first denatured by heating. Pre-designed primers then attach to the DNA strands and read along the strand, replicating the sequence by sequential addition of dNTPs. This process is repeated multiple times with the accuracy of the replicate strand increasing with each round.

During this time the polymerase (1  $\mu$ l) attaches to the template DNA and reads along the sequence. The polymerase constructs a complimentary copy from dNTP building blocks during a second heating step to duplicate the template DNA. These steps are repeated during the extension period to exponentially amplify the required gene, with the precision of the replication improving in each round due to the position at which the primers reattach (Figure 2.5). Accuracy can then be further increased by running the final product through a PCR clean-up kit.

### 2.6.1.2 RESTRICTION DIGEST

The gene required for cloning is “cut out” of the PCR DNA product (Section 2.6.1.1) using restriction enzymes to isolate the specific sequence which codes for the eventual protein target (Figure 2.6).<sup>173</sup> The PCR product (approx. 10  $\mu$ l) is added to an enzyme compatible buffer (Table 2.1) and adjusted to the correct concentration by dilution with sterile water. The appropriate restriction enzyme (1  $\mu$ l), dependent on the restriction sites designed into the gene sequence, is added to the reaction mixture and incubated at the corresponding active temperature for approximately one hour.

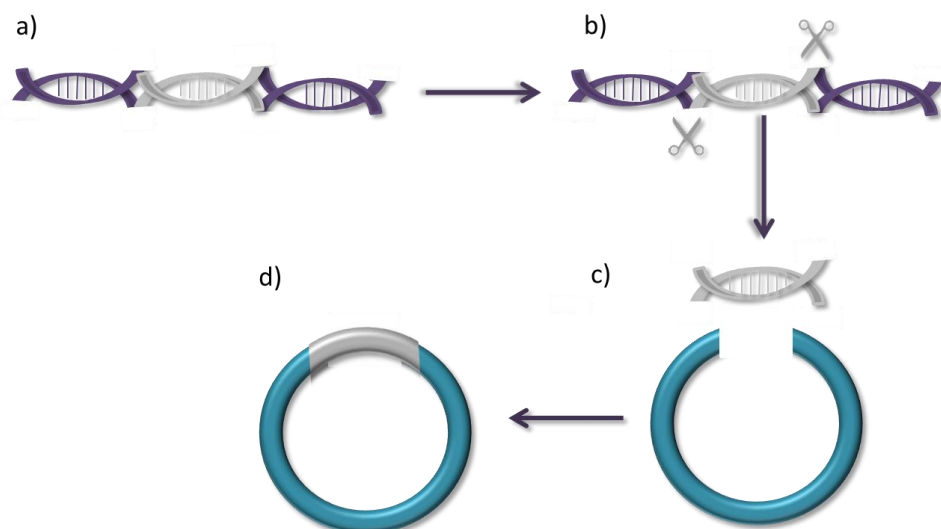


**Figure 2.6:** DNA Digestion a) The required DNA sequence is isolated using digestion enzymes which recognise the beginning and end codon in the required gene b) During incubation with the enzymes, the desired sequence is cut out of the DNA product. Ligation: c) This section of DNA is then ligated into a circular DNA vector by covalently “zipping up” the ends of the DNA fragment with the vector. d) This forms a circular piece of DNA which is now suitable for cloning.

During this incubation period, the enzymes digest; or cut the PCR DNA at specific recognition sites. These sites are generally at the beginning and end of the DNA sequence required for cloning, and are incorporated in the primer sequences used in the PCR. During this time the polymerase (1  $\mu$ l) attaches to the template DNA and reads along the sequence. The polymerase constructs a complimentary copy from dNTP building blocks during a second heating step to duplicate the template DNA. The reaction is then cleaned up *via* a PCR clean up kit or gel extraction (Section 2.5.1.6) to improve the purity of the digested sequence for ligation.

### 2.6.1.3 DNA LIGATION

The insert; or gene sequence required for cloning,<sup>173</sup> isolated during the restriction digest process, (Section 2.6.1.2) is now ligated; or covalently linked into linearised plasmid DNA (pPR-IBA1). The insert (approximately 10 ng) and the corresponding vector (pPR-IBA1, 50 ng) are combined along with “instant sticky end ligase” (New England Biolabs) (5  $\mu$ l 400 units per  $\mu$ l). The mixture is subsequently incubated at ambient temperature for 5-10 minutes. During this time the overhang sequences on the vector are “zipped up” *via* covalent linkage to the complimentary overhang sequence designed into the insert DNA (Figure 2.6). This creates a complete circular DNA plasmid suitable for cloning.

### 2.6.1.4 VECTOR TRANSFORMATION (XL10 GOLD)

DNA ligated into the appropriate vector to form circular DNA is subsequently introduced into XL10 Gold *E. Coli* cells (Agilent).<sup>173</sup> Ligated plasmid DNA (5  $\mu$ l) is added to 100  $\mu$ l of cells on ice. These are then heat shocked at 42°C for 30 seconds, which causes the formation of pores in the cell membrane allowing for uptake of the DNA vector by the cells for amplification.

After further chilling on ice for 5 minutes, the cells are combined with 300  $\mu\text{l}$  of LB growth media and agitated at 37°C for approximately 1 hour to allow the cells to recover from the heat-shock. After this time, the cells are deposited on to an LB Agar plate containing the antibiotic carbenicillin (100  $\mu\text{g ml}^{-1}$ ). The addition of the antibiotic ensures that only cells containing the pPR-IBA1 DNA are able to grow on the plates due to the presence of an ampicillin resistance gene. Plates are incubated at 37°C for up to 16 hours to allow colonies of cells to form.

### 2.6.1.5 COLONY PCR

Individual cell colonies can be picked and amplified *via* a PCR reaction to confirm the presence of the inserted vector, and more importantly the gene of interest. In this case, specific individual colonies are picked and re-suspended in 100  $\mu\text{l}$  of water. PCR reactions are prepared according to the method outlined in section 2.4.1.1, but with the addition of 1  $\mu\text{l}$  of the colony solution in place of the genomic DNA. The resulting PCR products are analysed using gel electrophoresis (see section 2.6.4.1) to determine if the target gene has been successfully incorporated into the plasmid. The remaining colony suspension is added to LB and carbenicillin for culturing at 37°C with shaking before extraction of the plasmid *via* mini prep kit (Qiagen).

### 2.6.1.6 DNA SEQUENCING

In DNA products which appear to be of the expected size (kDa) in gel electrophoresis analysis (Section 2.6.4.1) the plasmid is extracted from *E. Coli* by with a mini prep kit (Qiagen). The extract is sequenced by Beckman Genomics. A 15  $\mu\text{l}$  sample of the plasmid solution at 100  $\text{ng } \mu\text{l}^{-1}$  is sent for sequencing by PCR analysis.<sup>174</sup>

Method	Buffer/Solution	Component	Volume
<b>General Use</b>	Phosphate buffered Saline (1L) (PBS)	Sodium Chloride	80g
		Potassium Chloride	2g
		Sodium Phosphate dibasic	14.4g
		Potassium Phosphate dibasic	2.4g
		Distilled water	Make up to 1L
<b>Cell grow up</b>	LB Media	Yeast extract	5 g
		Sodium Chloride	10 g
<b>Plate grow up</b>	LB Agar	Yeast extract	5 g
		Sodium Chloride	10 g
		Agar	15 g
		Deionised water	Made up to 1 litre
<b>Dot and Western blots</b>	Blocking buffer	10 x blocking buffer (Sigma)	4 ml
		PBS Tween	16 ml
		Total Volume	20 ml
<b>Dot and Western blots</b>	Towbin transfer buffer	Tris buffer	1.5g
		Glycine	7.2g
		Methanol	100 ml
		MilliQ Water	500 ml

**Table 2.1:** Components of protein cloning and expression recipes, buffers were made to pH 7.4, and autoclaved before use.

## 2.6.1 PROTEIN PREPARATION

### 2.6.1.1 VECTOR TRANSFORMATION (BL21)

As outlined in section 2.4.1.4, a DNA vector (1  $\mu$ l) is transformed into *E. Coli* BL21 (DE3) RP (Stratagene) cells (100  $\mu$ l) using heat-shock (42 °C for 30 seconds).<sup>173</sup> LB growth media (300  $\mu$ l) is added to the transformed cells and incubated at 37°C for one hour to allow the cells to recover. Recovered cells are spread on to an LB agar plate containing the antibiotics, carbenicillin (100  $\mu$ g ml<sup>-1</sup>) and chloramphenicol (35  $\mu$ g ml<sup>-1</sup>), and incubated at 37°C for about 16 hours to allow colonies of cells to form.

### 2.6.1.2 EXPRESSIONS TRIALS

To ensure maximum efficiency in protein production, a number of auto-induction growth media were trialled to determine the optimum expression conditions for a maximum yield for each protein under analysis. For the expression trial, four media of increasing nutrient content (LB, 2YT (2 x), TB (4 x), and SB (8 x) in 400 ml volumes are inoculated with a starter culture (containing the appropriate antibiotics) of the colony of interest and incubated at 37 °C. Expression occurs spontaneously at a specific cell density. Protein expression levels are checked at three time points (24, 40 and 48 hours). At harvested time points, the protein cell pellets are re-suspended in lysis buffer (Table 2.2, 500  $\mu$ l of culture is lysed in 125  $\mu$ l lysis buffer). The lysate is then analysed using a dot blot to assess protein expression levels (Section 2.6.4.3).

### 2.6.1.3 CELL CULTURING

Transformed BL21 (DE3) RP cells are grown up over a period of 4-6 hours in 5 ml of LB supplemented with carbenicillin and chloramphenicol as before. After this time, an aliquot is taken (1 ml) and added to 400 ml of the appropriate media containing both Carbenicillin (100  $\mu$ g ml<sup>-1</sup>) and Chloronphenecol (35  $\mu$ g ml<sup>-1</sup>); (Section 2.2.5.2).

Cultures are grown under the optimised conditions (time and temperature) using auto-induction media for maximum protein production as determined by expression trial (Section 2.6.1.2).<sup>175</sup>

#### **2.6.1.4 PURIFICATION**

The 400 ml cultures are harvested by centrifugation (3000 rpm for 20 minutes in a Megafuge 40R (Thermo Scientific) using a swinging bucket rotor (75003607) to pellet cells. The pellet is re-suspended in 3 ml of PBS (0.1 M phosphate) and tip sonicated (70 % amplitude, 6 x 20 second sonication (Vibracell Sonicator, Sonics) to lyse cells; and the solution is centrifuged again (12,000 rpm for 45 minutes) to pellet cell debris. The soluble protein in the supernatant can then be isolated by affinity chromatography. This works by passing the solution through a column containing a resin which will bind protein depending on its fusion tag; Streptactin resin (IBA) for a strep tag and Nickel resin (Expedeon) for a His tag. The bound protein is then eluted using the appropriate buffer; 300 mM imidazole in PBS for a His tag and 5 mM D-desthiobiotin in PBS for a strep tag.<sup>176</sup>

Method	Component	Volume
	Sterile water	3 ml
	4 x stacking buffer <sup>^</sup>	1.25 ml
<b>SDS-Page Stacking Gel</b>	Acrylamide (30 % w/v)*	0.7 ml
	10 % Ammonium Persulphate (APS)	25 µl
	Tetramethylethylenediamine(TEMED)	20 µl
	<i>Deionised water</i>	3.4 ml
	Acrylamide (30 % w/v)*	4 ml
	4 x Conc Resolving Gel Buffer <sup>^</sup>	2.5 ml
<b>SDS-Page Resolving Gel</b>	10 % APS	60 µl
	TEMED	12 µl
	Milli Q (autoclaved)	33.5 µl
	10 x KOD Buffer (Merck)	5 µl
	MgSO <sub>4</sub> (25 mM)	3 µl
<b>PCR reaction</b>	Template DNA (50 ng µl <sup>-1</sup> )**	0.5 µl
	Forward Primer (10 µm µl <sup>-1</sup> )	1 µl
	Reverse Primer (10 µm µl <sup>-1</sup> )	1 µl

	KOD Hot Start Polymerase (1 $\mu\text{g } \mu\text{l}^{-1}$ )	1 $\mu\text{l}$
	10 x Enzyme Reaction Buffer (NEB)	5 $\mu\text{l}$
<b>Restriction digest</b>	Restriction Enzyme (NEB)	1 $\mu\text{l}$
	Sterile Water	Make up to 20 $\mu\text{l}$
	Vector (50 ng $\mu\text{l}^{-1}$ )**	2.5 $\mu\text{l}$
<b>Vector Ligation</b>	DNA Insert (50 ng $\mu\text{l}^{-1}$ )**	2.5 $\mu\text{l}$
	Instant Ligase# (NEB)	5 $\mu\text{l}$
	GoTaq green DNA polymerase# (Promega)	10 $\mu\text{l}$
<b>Colony PCR</b>	Cell suspension	1 $\mu\text{l}$
	Forwards primer (10 $\mu\text{M } \mu\text{l}^{-1}$ )	1 $\mu\text{l}$
	Reverse primer (10 $\mu\text{M } \mu\text{l}^{-1}$ )	1 $\mu\text{l}$
	MillQ water	7 $\mu\text{l}$

**Table 2.2:** Buffers and solution in biology protocols \*Acrylamide composition is equal to 37.5:1Acrylamide to *bis*-acrylamide\*\* Typical concentration #Used as per manufacturer's instructions ^See appendix for recipe

## 2.7 CHARACTERISATION AND INSTRUMENTATION

### 2.7.1 VESICLE CHARACTERISATION

#### 2.7.1.1 TRANSMISSION ELECTRON MICROSCOPY (ROOM TEMPERATURE)

This section is based on the textbook Transmission electron microscopy: a textbook for materials science. Williams, (1996)<sup>177</sup>

Transmission electron microscopy (TEM) was used to visually assess iron oxide, protein and vesicle samples; high resolution (as low as 0.2 nm) state allows for visualisation of objects in the nanoscale size range (Figure 2.7). The higher resolution achieved by using electron microscopy is the result of using an electron beam at 100-200 keV. This provides wavelengths able to observe and image samples that are smaller than the diffraction limit of light. This beam is generated from an electron gun at the top of the microscope column, with the electron source usually being in the form of either a tungsten filament or a lanthanum hexaboride (LaB<sub>6</sub>) crystal. Condenser lenses, which consist of magnetic coils, are used to concentrate and focus the beam onto the sample. A high level of detail is resolved by the interactions of the electrons as they are transmitted through the specimen, interacting with electrons in the sample, hence offering information about the internal structure. Imaging is carried out under very high vacuum. This removes the propensity for the beam to interact with anything other than the sample. The ion getter pump (IGP) further improves the vacuum by ionisation of the gas in the vessel and application of an electric potential. This causes acceleration of ions into an electrode which are then consequently immobilised, thereby creating a very high vacuum.<sup>177</sup> Both continuous film and holey carbon coated TEM grids (Agar Scientific) were used to visualise samples. The sample (5 µl) is applied to a grid and left to stand for approximately 1 minute, after which time the excess liquid is blotted off. Grids are then dried, either slowly at ambient temperature or by vacuum. Samples assumed not to contain dense iron minerals are also stained prior to TEM imaging. This is a common procedure in electron microscopy for many samples; particularly biological specimens.

This is because low electron density elements (e.g. hydrogen, carbon, and oxygen) have poor contrast in the electron beam as they are less able to interact with the transmitted electron beam. The stain is made up of a heavy metal salt. The electrons in the heavy metal interact and deflect the beam to a much greater extent than the sample. Hence the stain provides a better contrast between the stained sample and the background. The sample is added to a grid as described above. This is then followed by the heavy metal stain (2 % uranyl acetate or 0.75 % uranyl formate), which is blotted off after a 12 second staining period. The instruments used included a Phillips CM200 and CM100 and a TecnaiF20 and FEI G2 Spirit.

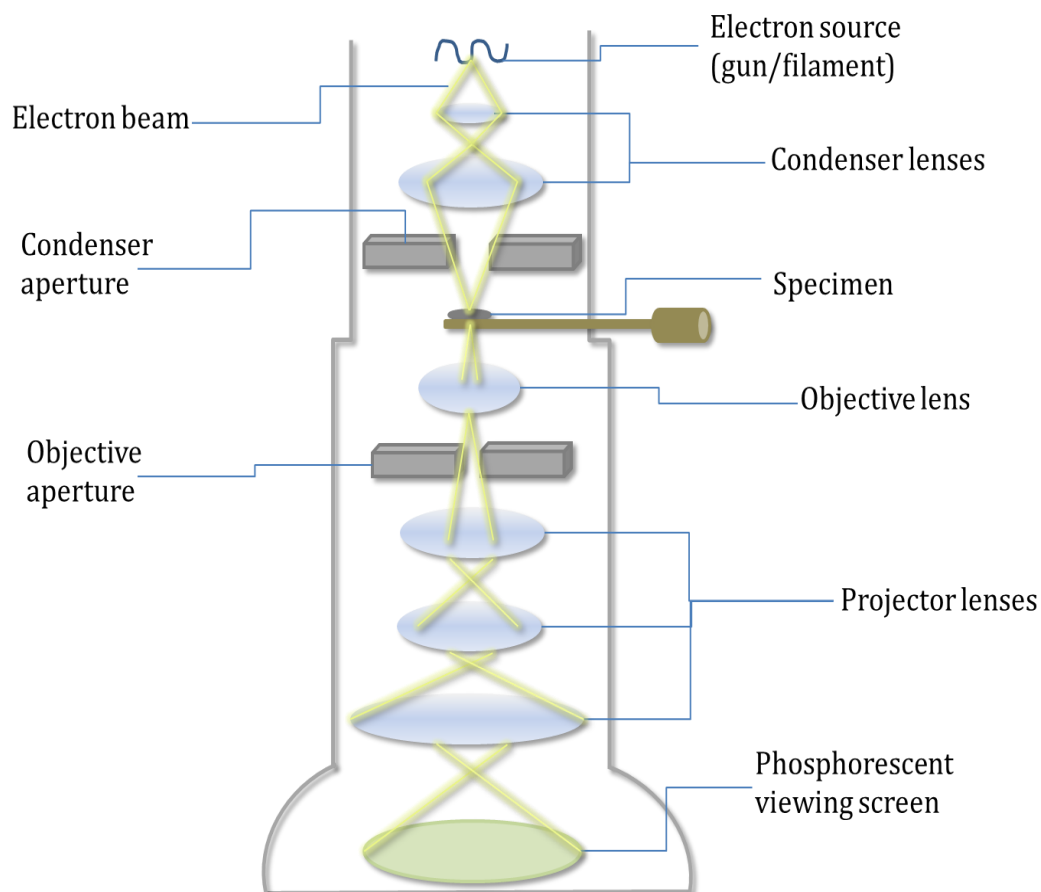


**Figure 2.7:** Schematic of a transmission electron microscope as described in Section 2.7.1.1.

### 2.7.1.2 CRYOGENIC TRANSMISSION ELECTRON MICROSCOPY

Greater detail and accuracy with regards to vesicle structure can be achieved by cryogenically freezing the sample before electron microscopic analysis. Freezing the sample conserves its structure which is often lost when dried on to a conventional TEM grid. For a vesicle, this is analogous to popping a balloon or deflating a beach ball, and then attempting to analyse its structure. Samples are prepared for cryo TEM by freezing in liquid ethane. Essential to cryo TEM is the absence of cubic water ice, for this reason instrumentation involved in grid preparation must be kept under liquid N<sub>2</sub>, cooled and dried before introducing the grid.<sup>177</sup>

Cubic ice can absorb the electron beam leaving the grid obsolete as the beam can no longer penetrate the sample. Liquid ethane is used for sample freezing due to it having a higher boiling point at -188°C when compared to -195°C of liquid nitrogen. Liquid ethane is cold enough to freeze the aqueous solution on the grid without the formation of cubic ice and without being so cold that it will boil upon the introduction of the grid; as in the case of liquid nitrogen. Samples are prepared for cryo EM using a Vitrobot (Series 2 and 3). The sample is loaded on to a holey carbon grid (~5 µl), unlike conventional TEM there is no need for dilution. The Vitrobot automatically blots the sample (3-6 seconds at blot force 3) to remove excess sample and achieve an optimum thickness of ice for imaging. The grid is then plunged into the liquid ethane and stored under liquid nitrogen until use. Grids are loaded into the microscope (in this case a Phillips CM200 or a Tecnai F20) and imaged in low dose mode, to avoid damaging the solvent ice. In addition to this, there are three separate modes which must be used to obtain the final image: 1) search mode is used at low magnification to move around the grid and identify areas of interest. The microscope is then switched into 2) focus mode, these are two areas on either side of the region of interest, each area is adjusted to absolute focus, which in turn should bring in to focus the area to be imaged, an element of defocus is then applied (~ -1 µm) to enhance contrast. Finally the microscope is switched to 3) exposure mode and the image is taken, this can be taken only once as the effect of exposing an area essentially melts it.

### 2.7.1.3 DYNAMIC LIGHT SCATTERING

Dynamic light scattering (DLS) was utilised to explore vesicle size distribution and aggregation properties.<sup>178</sup> DLS is the measurement of fluctuations observed in light scattered from a vesicle or particle sample. These fluctuations are related to diffusion within the sample, and used to calculate particle size, the intensity of light scattered is measured with respect to time.<sup>178</sup> Due to Brownian motion occurring within the sample, there is constructive and destructive interference which has an effect on the light intensity and scattering over time; called the translational diffusion coefficient ( $D$ ) (Equation 2.1). This takes into account solution viscosity ( $\eta$ ), Boltzmann's constant at absolute temperature ( $kT$ ), and the hydrodynamic diameter ( $D_H$ ) of the particle; which assumes that all of the particles are solid spheres:<sup>178</sup>

$$D = \frac{kT}{3\pi\eta D_H} \quad (2.1)$$

Smaller particles diffuse faster through the solution causing more fluctuations than bigger particles that have slower diffusion. The technique works by way of a polarised beam which is scattered by density and concentration fluctuations in the sample. A detector picks up speckling caused by scattered light interfering with the sample. The time dependence of this scattering at a specified angle is used to form an autocorrelation function, which describes the spot intensity over time. For monodisperse samples, this comes from the exponential decay arising from the diffusion within the sample. This in turn is related to the hydrodynamic diameter of the particle. If a sample is polydisperse, the correlation function is based upon a distribution of decay rates, due to the variation in particle motion in the sample.

For vesicle samples, a dilution of 400  $\mu\text{l}$  in 1 ml was analysed in a disposable DLS cuvette with a scattering angle of  $173^\circ$  on a Zetasizer Nano (Malvern Instruments).

Samples were scanned three times at a standard temperature of 25°C, with each scan having 10-14 runs, the sample is scanned using the refractive index and viscosity settings for a sample of liposomes in water, as these most closely match the sample properties. Data is analysed using Malvern Zetasizer software, and replotted using GraphPad Prism. It is also possible to estimate the polydispersity index (PDI) (Equation 2.2) of the sample which relates to the standard deviation ( $\sigma$ ) of a Gaussian distribution applied to the data ( $Z_D^2$ ).

$$PDI = \frac{\sigma^2}{Z_D^2} \quad (2.2)$$

#### 2.7.1.4 GEL PERMEATION CHROMATOGRAPHY

To determine polymer concentration following dilution during clean up, gel permeation chromatography (GPC) is employed. GPC separates compounds in a solution by size. An aqueous column is used to analyse the polymer molecular weight, size and concentration. The system is first pumped with PBS buffer; which also acts as a baseline for polymer samples. Samples of polymer (1ml) at known concentrations, in PBS buffer are then injected into the column. A constant supply of fresh buffer is pumped along the column. As the polymer sample moves along the column it interacts with porous beads in the column akin to SEC (section 2.2.4), the samples retention time in the column is dependent on its size and molecular weight, as bigger/heavier particles move down the column faster resulting in a shorter retention time. For this reason different polymer sizes and weights have different retention times. A detector analyses the solution leaving the column, giving rise to a chromatogram, displaying the species present at a given retention time. In the case of the polymer, two peaks were observed (one peak representing each polymer block). The peak areas can be integrated to give an approximate polymer concentration, therefore each peak is integrated to create a standard curve for polymer concentration (from samples with a known concentration). Polymer samples of unknown concentration are then injected, and the peak area is again integrated. These values are then extrapolated against the standard curve to estimate polymer concentration.

### 2.7.1.5 FLUORESCENCE MICROSCOPY

Vesicles with the addition of fluorescently tagged lipids are analysed using a fluorescence microscope.<sup>179</sup> Excitation of electrons in the fluorescently tagged lipids by radiation of light at a specific wavelength causes emission of light by the fluorophore upon electron relaxation. Vesicles are labelled with the fluorescent lipophilic dye Bodipy (Life technologies,  $\lambda_{em}$  503 nm  $\lambda_{ex}$  512 nm). This allows for initial analysis on the formation of vesicles, and measurement of the approximate size (to a resolution of approximately 500 nm).

## 2.7.2 SPECTROGRAPHIC TECHNIQUES

### 2.7.2.1 UV-VISIBLE SPECTROSCOPY

An electrons transition from the highest occupied molecular orbital (HOMO) to the lowest unoccupied molecular orbital (LUMO) can have an energy which corresponds to the UV/visible region of the electromagnetic spectrum (200-900 nm) depending on the orbital structure of the molecule. This HOMO/LUMO transition occurs when light energy ( $\Delta E$ ) is absorbed by the molecule. A broad absorption is observed due to a range of  $\Delta E$  values, which correspond to the multiple vibration and rotation states within the molecule.<sup>179</sup> The expected absorbance of a material is given by the Beer-Lambert law (Equation 2.8). This relates the absorbance of a molecule ( $A$ ) to either the relationship between the incident light ( $I_0$ ) and transmitted light ( $I$ ), or its molar extinction coefficient ( $\epsilon$ ), given by the molecules attenuation of light at a specific wavelength, the sample concentration ( $c$ ) and the path length of the light through the sample ( $l$ ).

$$A = \log_{10} \frac{I_0}{I} = \epsilon cl \quad (2.3)$$

A sample is exposed to a light source of known wavelength in a spectroscope (Cary 50 probe).

Before hitting the sample, wavelengths in the light are then separated by either a monochromator, which uses diffraction grating for the separation, or splitting with a prism. The absorbance by the sample is then detected. Standard curves of each sample analysed by UV-Vis spectroscopy are first compiled by serial dilution of a sample of known concentration. Spectra of samples are then recorded at a concentration below the saturation concentration, as determined by calibration. The UV-Vis spectra of relevant vesicle samples were collected using a Lambda 35 (Perkin Elmer) or a 50 probe (Cary) UV-Vis Spectrometer. Samples concentrations were optimised by serial dilution of the initial vesicle concentration (generally unknown), 1 ml of sample at the appropriate dilution were measured in disposable UV-Vis cuvettes with a path length of 0.45 cm. Spectra were run between 200 and 900 nm initially for detection of an absorbance peak and analysis of the overall sample. Secondary measurements were then taken to obtain spectra of the specific absorbance of the UV active material present, which were as follows; Ferene  $\lambda = 593$  nm, Prussian blue with ferrous iron  $\lambda = 740$  nm and ferric iron  $\lambda = 492$  nm, Resazurin at pH 2  $\lambda = 530$  nm and at pH 10  $\lambda = 610$  nm.

### 2.7.2.2 FLUORIMETRY

A fluorimeter can offer quantitative analysis on the fluorescence emitted from a sample. Two electron beams pass through two monochromators, one each for excitation and emission.<sup>179</sup> The signal then hits a detector and is outputted graphically. Fluorimetry was used to confirm encapsulation of a fluorescent dye within a vesicle, which subsequently confirmed the presence of the vesicles following clean up *via* SEC (Section 2.2.4) to remove background fluorescence. A LS55 Fluorescence spectrometer (Perkin Elmer MA, USA) for the detection of fluorescently labelled vesicles. A maximum sample volume of 1 ml was added to a disposable fluorimetry cuvette. Spectra were collected for both excitation and emission of the fluorescent dye carboxyfluorescein appropriate scanning wavelengths were chosen to ensure that  $\lambda_{em}$  of 492 nm and  $\lambda_{ex}$  of 517 nm were collected. Samples were diluted 10 fold (for a 1 mg/ml vesicle sample) to avoid saturation.

### 2.7.2.3 ENERGY DISPERSIVE X-RAY SPECTROSCOPY

Energy Dispersive X-ray (EDX) elemental analysis is carried out on vesicle samples which appear to have a dark crystalline encapsulant during TEM imaging, in order to determine the elemental composition of the vesicle contents. In EDX, the incident electron beam focussed on the sample ejects electrons from the core of the elements encountered. A higher energy electron fills this vacancy, emitting an X-ray of a characteristic wavelength to allow it to fill this lower energy level. Therefore, the energy of the emitted X-ray can be used to identify the element it came from. Every element has unique X-ray emission pattern, the intensities of which are detected by a spectrometer. Plotting the spectrum allows peaks to be identified that correlate to the element(s) that emitted the X-rays. Fitting of the peaks in the spectrum includes a correction factor based on the intensity of the X-ray from that element. In general, heavier elements are easier to detect. Thus, fitting of the spectrum allows the user to quantitatively confirm the relative elemental composition of the specimen.<sup>180</sup> EDX analysis is performed on the whole samples (i.e. the vesicle containing nanoparticles) in addition to individual particles within the vesicle. The spectra are recorded using a UWT Oxford Instruments EDXS detector and processed using the ISIS software during TEM analysis (Section 2.6.1.1) by focusing of the beam on to a sample after insertion of an X-ray emission detector mounted on to the side of the microscope.

### 2.7.2.4 INDUCTIVELY COUPLED PLASMA MASS SPECTROMETRY

Inductively coupled plasma mass spectrometry, (ICP-MS) is used to determine iron concentrations in magneto-vesicle samples. ICP uses ionisation of samples followed by mass spectrometry to detect the presence of specific elements down to a concentration of part per billion (PPB).<sup>179</sup> The sample is nebulised into an argon gas phase to form electrically conductive plasma, by heating with an electromagnetic coil. Heating the plasma causes the formation of positive ions; by loss of an electron. The plasma is then introduced to a mass spectrometer and ions are separated based in their mass/charge ratio by acceleration in an electric or magnetic field. The mass/charge ratio causes a certain amount of deflection in the spectrometer, and it is this deflection that is detected.

A quadrupole mass spectrometer scans the mass ranges present in the sample, and only allows samples with a specific mass/charge ratio to hit the detector. The detected intensity is then compared to a standard curve for that element, to determine the concentration of a specific element in the sample. ICP samples are prepared for detection of the iron concentration, by dissolving a known volume of magneto-vesicle sample into nitric acid (concentrated) to a total volume of 5 ml (4 parts water to 1 part acid). This was done to dissolve magneto-vesicles so that any iron ions present are in solution. Samples were analysed using a Spectro-Ciros-Vision Inductively Coupled Plasma Optical Emission Spectrometer, in which the iron content was detected by measurement at optical emission lines (usually at least 2 per element) this is then compared to a previously measured calibration standards of known concentrations which the instrument uses to calculate a calibration graph for each line and subsequently displays the calculated element concentration in the sample.

#### **2.7.2.5 RAMAN SPECTROSCOPY**

Raman spectroscopy analyses the vibrational and rotational modes of a molecule which causes inelastic scattering and can be detected spectroscopically to determine the identity of a molecule, by analysis of its chemical fingerprint. Raman spectroscopy were carried out on artificial magnetosome samples to identify a chemical fingerprint for both magnetite and the surround bilayer. Raman spectra were obtained with a confocal-Raman spectrometer (Jobin Yvon LABRAM) equipped with a Nd-YAG laser (100 mW, 532.2 nm) and diffraction gratings of 1800 grooves  $\text{mm}^{-1}$ . Detection was performed using a Peltier-cooled, slow-scan, CCD matrix detector

## 2.7.3 MAGNETIC MEASUREMENTS

### 2.7.3.1 SUPER QUANTUM INTERFERENCE CONDUCTION DEVICE (SQUID) SAMPLE PREPARATION

A SQUID is an extremely sensitive magnetometer, able to detect magnetisation between  $1 \times 10^{-17}$  and 5 Tesla. A SQUID measures the voltage from a sample when it is placed in a magnetic field.

At a critical electric current, a voltage will be given out; this voltage is affected by the applied magnetic field. The SQUID consists of two superconductors separated by an insulator, which form a Josephson junction. When this is exposed a magnetic field, current flows through the superconductor loop. Any change in the magnetic field induced by the sample has a direct effect on the current and the overall flux in the coil. This change in flux is then translated into magnetisation of the sample.<sup>181</sup> Hysteresis loops of the magneto-vesicle samples are recorded by applying and reversing a field between 1000 and -1000 Oe at 300 K to create an M/H curve (Section 1.3.1, Figure 1.2). These measurements were performed by either Miss Wala Dizayee (Department of Physics) or Dr Paul Southern (UCL Healthcare Biomagnetics Laboratory). Samples are prepared for analysis by drying a known volume or weight of solution into a small eppendorf under vacuum. Data are analysed by first plotting the paramagnetic contribution from the eppendorf. The paramagnetic signal is then subtracted from the sample data and the M/H curve plotted.

## 2.7.4 PROTEIN CHARACTERISATION

### 2.7.4.1 GEL ELECTROPHORESIS

The success of gene cloning can be assessed by gel electrophoresis.<sup>182</sup> Running the purified DNA through gel separates the DNA by size. A 1 % agarose gel is made up by dissolving 0.5 g of agarose into 50 ml of TAE conducting buffer (Table 2.2). The dissolved gel is poured into a mould and 3  $\mu$ l of SYBRsafe™ (Life Technologies) is added to the molten gel. SYBRsafe™ is an aromatic compound which interacts with the DNA product *via*  $\pi$ - $\pi$  stacking, known as intercalation, which then makes the DNA visible under UV light.<sup>183</sup> For this reason, the dye can be incorporated into the agarose gel, but is only visible after intercalation with DNA. The negative charges on the phosphate backbone of the DNA; due to the structure of the nucleotide building blocks (Figure 2.8) are the basis of DNA gel electrophoresis.<sup>182</sup> These negative charges cause the DNA products to move towards the positive electrode once a potential difference is applied.

The distance the DNA migrates is dependent on its size; the larger the DNA product the less distance it will travel towards the positive electrode compared to a smaller DNA molecule. Each DNA sample is combined with loading dye (Mass Ruler) to a total volume of 6  $\mu$ l (5 parts DNA to 1 part dye), a voltage of 200 V is applied and the sample is electrophoresed for 20 minutes. Once separated, the gel is visualised under UV Light and compared to a DNA ladder with bands of a known size (kDa) (Mass Ruler, Life Technologies).

### 2.7.4.2 SODIUM DODECYL SULPHATE-POLY-ACRYLAMIDE GEL ELECTROPHORESIS (SDS-PAGE)

Gels were prepared according to the recipes in table 2.2, with the resolving gel below the stacking gel and a comb to provide appropriately sized gels. The re-suspended cell pellet and/or the purified protein is combined with sodium dodecyl sulphate (SDS) loading dye in a 1:1 ratio (20  $\mu$ l total volume) which is heated to 95°C.

This denatures the protein into a linear peptide chain so that movement through the gel is dependent on molecular weight alone. The protein is also coated in SDS detergent, which provides an  $\text{SO}_4^{2-}$  charge. This negative charge allows the protein to travel through the poly-acrylamide gel matrix in response to an applied electric field. 5  $\mu\text{l}$  of the protein/loading dye solution is loaded into the gel along with a molecular weight ladder (Page Ruler, Life Technologies); the gel is then electrophoresed at 200 V for 40 minutes (Figure 2.8). The gel consists of a stacking gel on top of a resolving gel (Table 2.2). These gels are at different pH depending on whether the glycine is protonated or not. The stacking gel maintains the denatured protein as a tight band. This band then enters the resolving gel and each protein migrates depending on its molecular, with smaller molecular weight species travelling further (Figure 2.8). The proteins can be visualised by addition of Coomassie blue staining or subsequent electro-blotting (Section 2.7.4.3).

#### 2.7.4.3 BLOTTING

Specific proteins analysed by SDS-PAGE can be visualised using a technique termed Western blotting.<sup>182</sup> This involves electrophoretically transferring the protein contents of a gel to a nitrocellulose membrane. The membrane is then incubated with a protein which blocks nonspecific binding of antibodies to the membrane surface. The protein of interest is detected by incubation with a primary antibody which can bind specifically to the target protein (usually the antibody is for an affinity tag, such as the His tag or strepII tag used in this study). The antibody is also conjugated to a Horseradish peroxidase enzyme (HRP) which can break down hydrogen peroxide and is also able to interact with luminol.

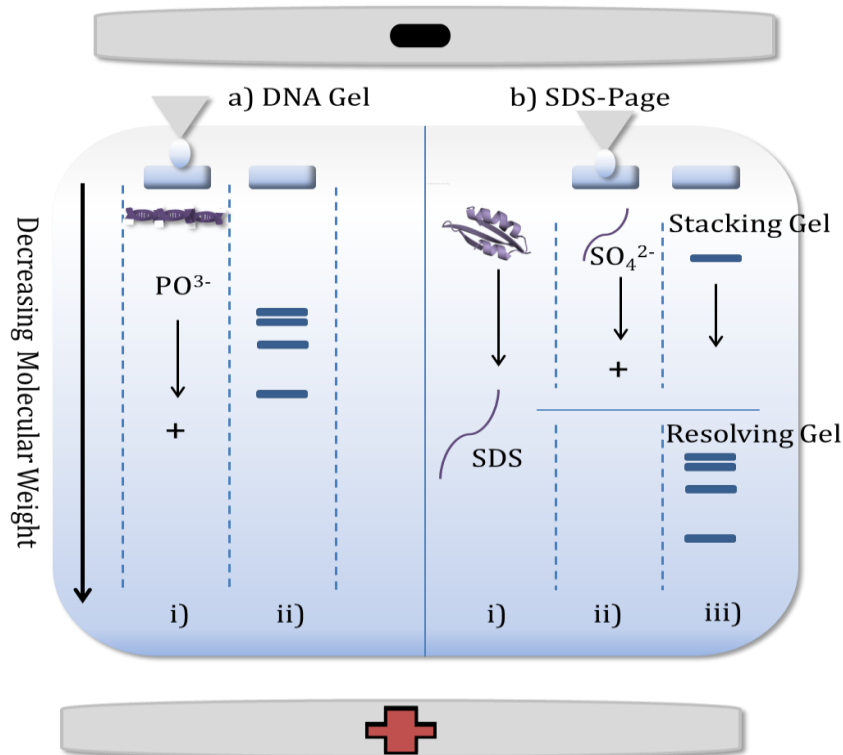


**Figure 2.8:** Gel Electrophoresis ai) DNA gels are run using the DNA product as a whole mixed with mass ruler loading dye to visualise the DNA bands. The  $PO_3^-$  on the backbone of the DNA drags the DNA through a 1 % agarose gel towards the positive electrode. ii) The products in the DNA separate by size as they move toward the positive electrode; with bigger products travelling slower and so producing bands higher up the gel. b) SDS-PAGE protein gels work in similar way, i) proteins are first denatured with SDS to produce long chain peptide so that proteins are compared by molecular weight alone. The SDS also coats the peptide with charge in the form of  $SO_4^{2-}$  ions. ii) This charge then forces the peptide to move towards the positive electrode during the electrophoresis. iii) An SDS-PAGE gel is made of a stacking gel and a resolving gel. The protein first moves through the stacking gel as a tightly stacked band, a pH change in the resolving gel then separates bands by size in the same way as DNA gel electrophoresis (aii).

The HRP oxidises the luminol, which emits light at 425 nm in this excited state. As the HRP is affixed to the antibody, which is attached to the protein of interest on the nitrocellulose membrane, the chemo-luminescence is localised to only those areas that contain the protein of interest. The gel, nitrocellulose membrane, and filter papers are soaked in transfer buffer (Table 2.2) for 5 minutes and then assembled into a stack before loading into a Transblot Turbo (Bio-rad). Semi-dry electroblotting for 30 minutes transfers the protein bands from the gel onto the nitrocellulose membrane. The membrane is then blocked for one hour using 45 ml of PBST (Table 2.1) and 5 ml of 10 x concentrated blocking buffer (Sigma) to prevent nonspecific antibody binding.

The primary antibody (Strep-Mab classic HRP) is added at a ratio of 1:4000 and left to bind to StrepII tag containing protein sites for one hour. The membrane is then washed three times for ten minutes with PBST. Finally, a detection reagent (Clarity Western ECL, Bio-rad) is added to the membrane which was visualised using the Bio-rad Chemi-doc. Dot blotting of expression trial time points are prepared using the same method, however protein samples are dotted directly on the nitrocellulose membrane before the blocking of non-specific binding sites.

#### **2.7.4.4 CIRCULAR DICHROISM**

Circular dichroism (CD) was used to analyse the secondary structure of protein samples to ensure successful protein folding upon purification. CD measures the difference between left and right circularly polarised light. In the case of optically active protein samples (due to the presence of chiral centres in the protein structure), the secondary structure can be analysed, as the presence of  $\alpha$ -helices and  $\beta$ -sheets have distinctive CD spectrum traces. Purified protein samples were diluted with ultrapure water to give a concentration of 0.1 mg/mL based on the A at 280 nm. A Jasco J810 CD instrument was used to acquire spectra using a 2-mm path-length cuvette. Wavelength scans of 260 nm to 190 nm were collected using a 1-nm slit width and 1<sup>-s</sup> intervals. Each sample was analysed three times, and data were averaged before subtracting a blank water spectrum. For thermal stability, the A at 222 nm (a marker of helical content) was monitored as the temperature of the sample was ramped from 20–85 °C. Data analysis was performed using DichroWeb (20).<sup>5</sup>

#### **2.7.5 MAGNETIC HYPERTHERMIA MEASUREMENTS**

Magnetic nanoparticles can induce a temperature increase in an alternating magnetic field (Section 1.2.2). Magneto-vesicle samples were tested for their ability to induce similar effects. Samples are tested on a Magnetherm (Nanotherics). The heating ability of samples in a predefined alternating field was tested.

The magnetherm consists of a coil (with 9 or 17 turns) around which a specified current flows to generate a magnetic field. This coil is connected to a recirculating water bath set at 10 °C to prevent non-specific heating from the coil. The sample is placed in the centre of the coil to experience an even magnetic field, and a temperature probe is then placed into the sample (T-type thermocouple). Once the temperature of the sample has equilibrated, the voltage is turned up to the maximum resonant peak-to-peak voltage for the coil/capacitor combination being used.

This generates a magnetic field (of strength  $H$ ) alternating at a specific frequency. The voltage must first be tuned to resonance for the coil/capacitor combination to prevent excess heating. Once the current is flowing and the sample is exposed to the alternating magnetic field, the temperature is recorded every one second over a 30 minute period. Control samples of the sample buffer solution are also measured over a 30 minute period. The control sample measurements are then subtracted from magneto-vesicle sample to obtain the heating from the vesicles alone. Data is plotted of the change in temperature over time, and an intrinsic loss parameter (ILP) (Equation 2.4) for the sample is extracted. The ILP is calculated from the specific absorption rate (SAR) (Equation 2.5) of the sample at a specific magnetic field ( $H^2$ ) and frequency ( $f$ ), after normalisation, so the ILP value is independent of sample vessel, magnetic field and alternating frequency. The specific absorption rate of the system measures the initial heating of the sample ( $\Delta T/\Delta t$ ) with respect to the specific heat capacity of the material ( $c$ ) and its concentration ( $M_{Fe}$ ).

$$ILP = \frac{SAR}{H^2 f} \quad (2.4)$$

$$SAR = \frac{\Delta T}{\Delta t} \frac{c}{M_{Fe}} \quad (2.5)$$

# CHAPTER 3:

---

## MAGNETITE FORMATION AND QUANTIFICATION OF IRON ION TRANSPORT

### 3.1 INTRODUCTION

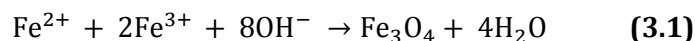
In order to use a vesicle as a nanoreactor as outlined in section 1, the reaction that the vesicle encapsulates must first be optimised. For this system, the intended purpose is the incorporation of a magnetite precipitation reaction into the core of the vesicle. The vesicle itself must of course be optimised; in terms of both size and chemical composition, before consideration of the vesicle optimisation, an appropriate magnetite precipitation route must be chosen and optimised.

Many published routes for magnetite precipitation were disregarded due to the nature of methodology (see section 1.3.3). For example, if the method requires harsh chemical solvents<sup>20g</sup> or high temperatures<sup>20f, 20g</sup> such conditions could degrade the nanoreactor vesicles, either before or during mineralisation. Also, extremely tight control over the reaction conditions is required for the precipitation reaction to yield magnetite rather than other iron oxide or oxyhydroxide species. This is particularly crucial in the case of room temperature reaction routes, in which small changes in reaction condition can alter the product(s) formed. These changes can include altering the iron salt used, or variations in the strength of the alkali, and the rate of addition of the base used (Section 1.2, figure 1.5). However, perhaps the most difficult to control is the potential for oxidation from external sources, which could significantly shift the redox potential of the system away from the formation of magnetite. A change in any one of these parameters could divert the course of the reaction away from the intended route to the precipitation of magnetite. These deviations, particularly in pH or Eh, would result in changes in the iron oxide formed. For this reason, all solutions used have been deoxygenated, and reactions were carried out under an inert atmosphere wherever possible. Three synthesis routes to magnetite precipitation were explored, as outlined below. These synthesis routes were chosen from a range of published methods<sup>20b, 20d-f</sup> based on their suitability for eventual incorporation into a vesicle nanoreactor for *in situ* magnetite precipitation reactions. Three routes were selected for vesicular incorporation (Section 3.2) due to their expected suitability for integration into a lipid or polymer vesicle.

It is important to be able to monitor and quantify intra and inter-vesicle activity, particularly with respect to mimicking iron transport across the vesicle membrane. In an attempt to extract more information from the process of magnetite precipitation, and the consequent iron ion cross-membrane transport, a number of assays were designed and tested on the bulk magnetite syntheses described in this chapter. These have later been adapted to assay the efficiency of iron transport across vesicle membranes. The success of the assays both as a general method and their effectiveness in the core of a vesicle are also outlined (Section 3.3). The three most appropriate routes to magnetite synthesis identified in the literature were explored for their effectiveness in producing good quality MNPs of a narrow polydispersity and the ability of the synthesis route to translate to a liposome or polymersome nanoreactor platform. The results were analysed with the pretext of being able to carry out the reaction in the core of a vesicle.

## 3.2 ROUTES TO MAGNETITE FORMATION

The general mechanism for the formation of magnetite is the combination of ferric and ferrous ions at the stoichiometric ratio for the formation of magnetite; namely 2 Fe<sup>3+</sup>: 1 Fe<sup>2+</sup>. The pH of this solution is then raised by the addition of NaOH or thermal decomposition to create a hydroxyl ion source. This leads to the formation of iron oxyhydroxide intermediates.<sup>3, 20f</sup> A further increase of the pH by slow addition of the OH<sup>-</sup> ion source, or as the result of oxidation, results in precipitation of magnetite nanoparticles with a water by-product (Equation 3.1).<sup>20f</sup>



The mechanism by which the magnetite forms is by conversion of ferric iron salts into magnetite (and other iron oxides) by the introduction of hydroxyl ions (or oxidation). This in turn raises the reaction pH causing the precipitation of magnetite (or other iron oxides) (Figure 3.1).

There is a balance between the levels of ferric ions and the increasing pH, which is demonstrated in figure 3.1 a). The mass/balance diagram shows how the species in a magnetite reaction can be predicted as the reaction progresses. For example in the absence of ferric iron and at a OH/Fe ratio of 2 the reaction would contain 100 % ferrous hydroxide. As the ferric ion concentration in the reaction then begins to increase, the percentage of ferrous hydroxide present drops as it is converted, until 100 % green rust ( $\text{Fe}_6(\text{OH})_{12}\text{SO}_4 \cdot x\text{H}_2\text{O}$ ) is obtained of a ratio 0.33 ferric to total iron in the reaction.<sup>3</sup>

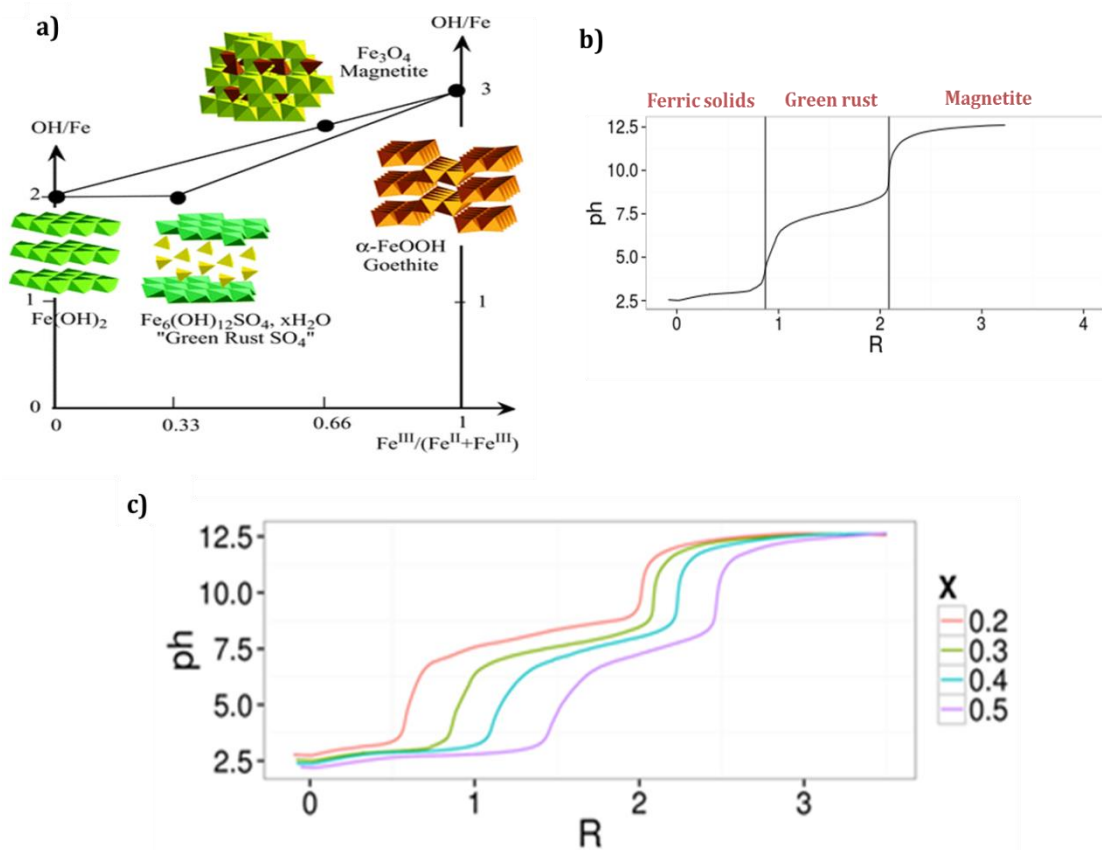


**Figure 3.1:** a) Shows the relationship- between magnetite and its iron oxide species ( $\text{Fe}_x\text{O}_y$ ) as formed at varying ferric to total iron ratios, with the increased addition of the hydroxyl ion source. b) A pH profile shows the relationship between magnetite formation and pH as a function of total iron:  $\text{OH}^-$  (R). The point at which these intermediates are formed can be controlled as demonstrated in c) by variation of the ferric : total iron ratio (x).<sup>10</sup> Figure adapted from unpublished data collected by J. Bramble.

Figure 3.1 a) shows that magnetite forms at an iron ratio of 0.66 ferric iron and an OH/Fe ratio of approximately 2.6:1. If either of these parameters then changes, i.e. the addition of excess hydroxyl and ferric iron (until the ratio is 1) magnetite is further converted to the entirely ferric iron oxide Goethite.<sup>10</sup>

There are multiple routes that this reaction can take depending on the type of reaction and the iron salts used (Section 1.3.3). More generally the magnetite formation pathway first goes *via* formation of green rust intermediates, which form at a 1:1 ratio of OH/Fe (R). The pH profile then plateaus, (Figure 3.1 b) indicating that additional OH<sup>-</sup> can be added and these intermediates remain stable until a critical point (R ~ 2) at which point the green rusts are converted to magnetite.

The formation of both the intermediate(s) and the eventual magnetite crystal can occur earlier by fine adjustment of the ferric to total iron ratio (Figure 3.1 c). The intermediates can form at a lower OH<sup>-</sup> to iron ratio. This means that they are essentially forming at a slightly lower pH when the amount of ferric iron to total iron is decreased. For example, figure 3.1 c) shows that at a ratio of 0.2 ferric iron to 0.8 total iron in solution, the green coloured magnetite precursor/intermediate is made at a much lower concentration of OH<sup>-</sup> compared to a ratio of 0.5 ferric iron to 0.5 total iron, due to the higher acidity of Fe<sup>3+</sup>. These slight changes can have a huge impact on the final species formed. While this makes conversion between iron oxides easy, this easy interconversion also results in mixed heterogeneous assemblies forming, when a single species (magnetite) is required. This interchange is the reason all magnetite precipitation must be performed under an inert atmosphere, with slow hydroxyl addition, as uncontrolled oxidation can result in the precipitation of mixed iron oxides.<sup>10</sup> The optimum ratio of ferric and ferrous iron has been determined by previous group members,<sup>62</sup> who used a 2:1 ratio of ferrous to ferric iron respectively, to account for uncontrolled oxidation during the reaction. This excess ferrous ratio was suitable for magnetite formation when using just chloride salts, and when using a combination of iron sulphate and chloride. Despite this, it was decided that the best ratio to use for intra-vesicular precipitation would be to use the stoichiometric ratio of ferrous to ferric iron for magnetite formation. It is unlikely that the same level of oxidation would be experienced upon precipitation within a vesicle, as the interior of the vesicle itself is a controlled environment.

Therefore; it would be more beneficial to begin with the stoichiometric ratio of iron for magnetite formation, thus increasing the probability of eventually forming magnetite within a vesicle nanoreactor.

### 3.2.1 THERMAL DECOMPOSITION OF UREA

Magnetite precipitation was carried out using the thermal decomposition of urea as the alkali source (method in section 2.1.2). Figure 3.2 shows a representative TEM image of the nanoparticles formed *via* this route. The TEM image shows that the particles have an aspect ratio of about 1, and the particles are euhedral (i.e. have sharp, well defined edges), and appear hexagonal in shape in these transmission images. The grainsize analysis (Figure 3.1 b) shows the particles have an average size of  $83 \text{ nm} \pm 6 \text{ nm}$ , which is a very uniform size distribution. A uniform size distribution is desirable because this should mean that the particles also have a uniform magnetic behaviour (see section 1.1.1 for more information on magnetic nanoparticle size and magnetic behaviour).

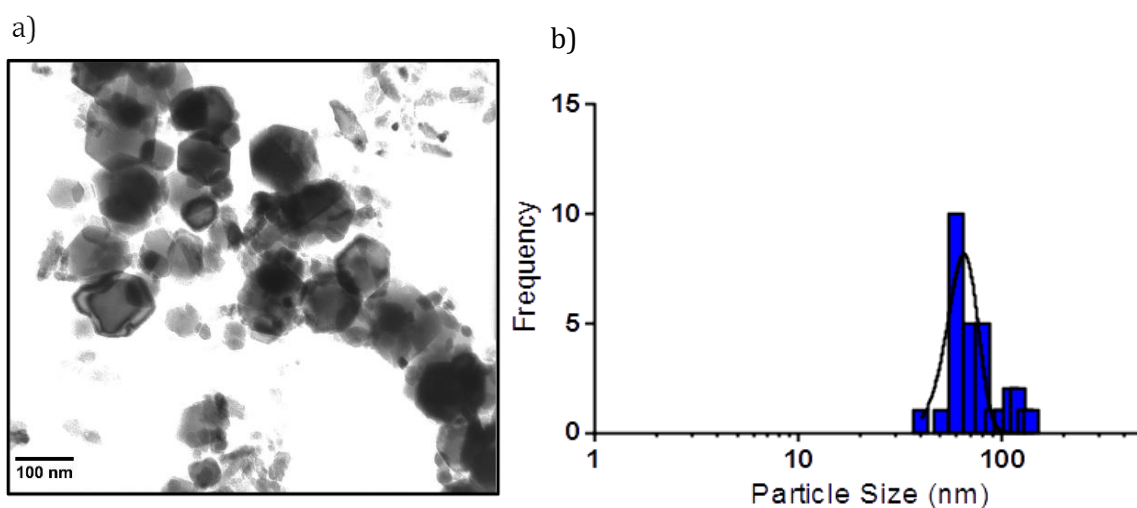
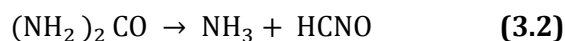


**Figure 3.2:** a) TEM micrograph of magnetite nanoparticles synthesised by thermal decomposition of urea b) Particle grainsizing from TEM micrographs confirmed that the method produced the biggest nanoparticles, with Gaussian distribution analysis giving an average particle size of  $65 \pm 11.17 \text{ nm}$  with respect to the spherical particles only.

Co-precipitation using urea maintains a neutral pH until the decomposition of  $\text{CO}(\text{NH}_2)_2$  to  $\text{NH}_3$  (Equation 3.2) at temperatures greater than  $85^\circ\text{C}$ . This release of ammonia to solution induces a pH rise (pH 2 up to 6 or 7) as aqueous ammonium hydroxide is formed. As a result minimal by-product oxidation occurs.



Particles of this size are within the size range of ferrimagnetic nanoparticles as opposed to superparamagnetic for the room temperature co-precipitation route (see section 1.1.1 for theory on magnetism of MNPs). The experiments which utilised precipitation with urea (Figure 3.2 a) show higher purity with respect to particles size and morphology when compared to other magnetite precipitation reactions. This is likely to be because of the greater control over oxidation when using these precipitants, which consequently provides improved magnetite crystallisation.

These ferrimagnetic particles are within the single domain size range, and they closely resemble the particles synthesised within magnetosomes of MTB. The main disadvantage of this method is that heating to  $90^\circ\text{C}$  for four hours is required. This limits the composition of the vesicle in which the reaction could be incorporated, due to most vesicle forming lipids and polymers being unlikely to be able to withstand these extreme temperature conditions. Therefore, whilst this method will be tested for incorporation into vesicles (Chapter 4), it is likely that the disadvantages of using the method will outweigh the superior quality of the particles it produces.

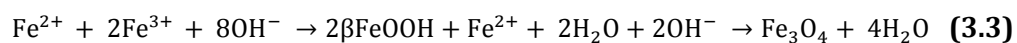
### 3.2.2 COMBINED UREA/AMMONIA DECOMPOSITION

A second method of magnetite formation was explored with the intention of decreasing the heating period needed for magnetite precipitation. It was hoped that introduction of ammonia into the reaction may decrease the volume of urea needed to decompose to initiate magnetite precipitation. This should lead to the reaction reaching completion earlier (i.e. with less heating necessary as less decomposition of urea is needed).

In turn, this should make the method more appropriate for incorporation into a vesicle interior. This method was adapted from Jeong *et al.*,<sup>20e</sup> as they find that improved particles are as the result of tight pH control. To explore the effect of the addition of ammonia on particle formation, with the intention of creating superior particles using shorter heating times, the ratio of urea to ammonia was varied starting from 100 % v/v urea; needing four hours heating for thermal decomposition, up to 100 % ammonia which is closer in mechanism to a room temperature co-precipitation (i.e. no heating should be required). Multiple iron salts were tested using ferric and ferrous iron chloride (10 mM) and iron sulphate (10 mM) and a combination of both. The reaction volume (8 ml), heating temperature (80-100°C) and the iron to hydroxide ratio (2:1) were kept constant. Some of the precipitates showed signs of magnetism on separation with a magnet; this did not follow a particular trend. Furthermore all samples appeared much browner in colour than those produced by other methods, the brown colour of the majority of the samples produced suggests that the reaction was lacking ferrous ion, instead forming ferric oxyhydroxide FeO(OH). This is likely to be due to oxidation of the ferrous ion present in the sample, either due to oxidation by undesired influx of air, or fast addition of the high pH ammonia solution, based on the visual quality of the sample following clean-up, no further measurements were carried out. In conclusion it was determined that to incorporate this into a vesicle would be an over-complication of an already successful method (Section 3.2.1), and so was not taken forward for testing as a compartmentalised vesicle reaction.

### 3.2.3 ROOM TEMPERATURE CO-PRECIPIATION OF MAGNETITE

Magnetic nanoparticles were synthesised using room temperature co-precipitation from ferrous and ferric iron ions (in a 1:2 ratio respectively) as described in section 2.1.1, using slow addition of NaOH *via* syringe driver (20  $\mu\text{l min}^{-1}$ ) as shown by equation 3.3.



The resulting precipitate was washed 3-5 times before imaging using TEM. The TEM micrographs show relatively monodisperse nanoparticles of an average size of  $10 \pm 2$  nm (Figure 3.3) Particle morphology was extremely consistent, with the particles appearing pseudo-spherical. It is envisioned that the incorporation of this method within a vesicle will result in rapid nucleation of magnetite as iron ions cross the vesicle membrane. This could have both advantages and disadvantages. For example, faster nucleation may result in higher quality crystals without allowing time for a) oxidation or b) unwanted intermediates. Rapid nucleation may also lead to the formation of many small magnetite nanoparticles within the vesicle, rather than a magnetosome-mimetic single MNP. Conversely this fast nucleation may also have huge disadvantages, in that successful precipitation of magnetite would depend on the kinetics of the diffusion across the membrane, i.e. whether a high enough concentration of iron ions are able to cross the membrane fast enough for all the desired precipitation mechanisms to occur.

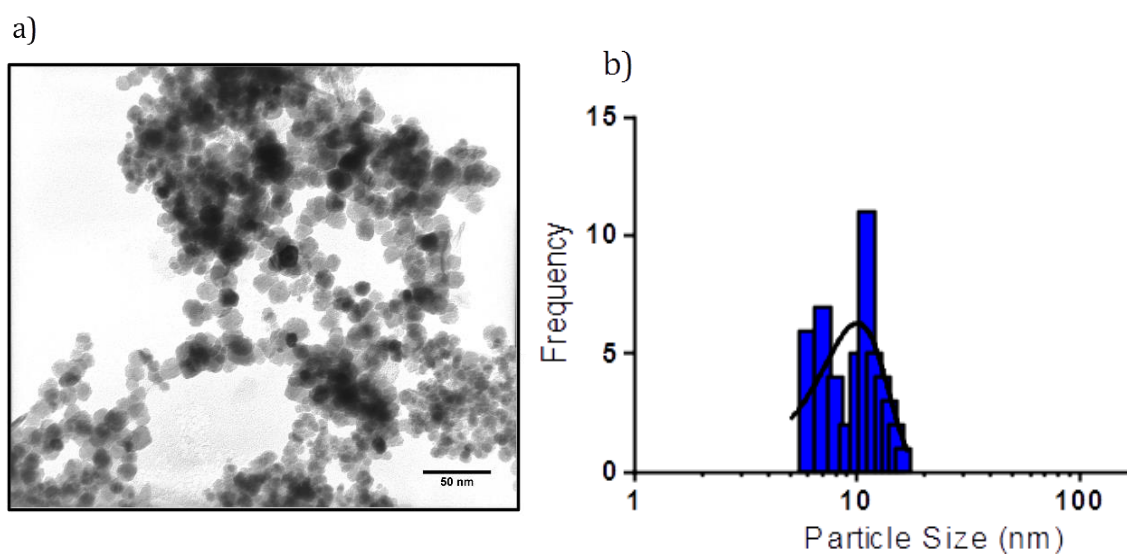


**Figure 3.3:** a) TEM micrographs of room temperature co-precipitated nanoparticles with 10 mM NaOH shows particles relatively spherical in shape, this is observed across the entire sample b) with the relatively monodisperse in size and shape. c) Particle grainsizing from TEM micrographs confirmed that particles had low polydispersity with Gaussian distribution analysis giving an average particle size of  $10.1 \pm 2.8$  nm.

The reaction was repeated at three different NaOH concentrations to determine the optimum concentration for the encapsulated nanoreactor precipitation reaction. Each sample was prepared from a single batch of ferrous and ferric iron chloride salt solution at the stoichiometric ratio for magnetite formation. NaOH was added at a rate of  $50 \mu\text{l min}^{-1}$  in which the only variable was increasing NaOH concentration. It was found, that as the concentration was increased from 1 mM to 5 mM, 10 mM and finally 50 mM a visible colour change from brown to black in the reaction solution was observed. After magnetic separation and washing with MilliQ water 3-5 times, each nanoparticle sample was analysed using TEM. The particulate samples with the lowest base concentration appeared dark orange to brown in colour indicative of the formation ferric-oxy-hydroxide. It is likely that the pH was not raised high enough to drive the reaction to completion, with the most likely product in this case being goethite.<sup>3</sup> As the concentration of hydroxyl ions in solution increases to 50 mM, the solution becomes brown green in colour, suggesting the presence of green rusts in the solution. After aging for 12-16 hours, this sample turned brown suggesting uncontrolled oxidation as a result of post formation aging.

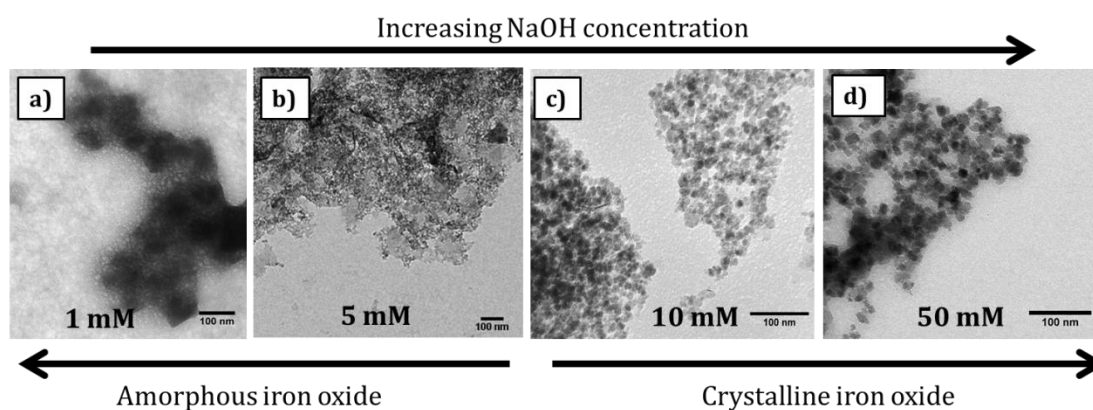


**Figure 3.4:** Optimisation of hydroxide concentration: TEM micrographs of iron oxide formation at increasing NaOH concentrations added to a room temperature co-precipitation reaction (a-d). The iron oxide products produced changed from an amorphous to crystalline phase. The crossover point of this transition is at around 5 mM where more structure is observed in the images. Fully crystalline particles are observed at 10 mM and above. Adapted from Bain *et al.*<sup>7</sup>

At NaOH concentrations of 10 mM and above, the presence of magnetic nanoparticles is observed. The TEM analysis confirmed this; figure 3.4 (a-d) shows TEM micrographs of particles synthesised at the four different alkali concentrations. Figure 3.4 a) made at 1 mM NaOH clearly shows the presence of amorphous material; most likely to be  $\text{Fe}(\text{OH})_2$ , based on the colour of the precipitate and correlation with the Eh/pH phase diagram for iron oxide precipitation (Figure 1.5). Figure 3.4 b) could be described as being in an intermediate phase,<sup>3, 20f</sup> whilst still largely amorphous there is a noted difference between 1mM and 5 mM, with the formation of some plate-like material; possibly “green rusts” or iron oxy-hydroxide.<sup>3</sup> Between Figure 3.4 c) and d) there is a marked difference in the particle quality, with 50 mM NaOH producing larger more monodisperse nanoparticles than 10 mM NaOH. Although the 50 mM sample was clearly superior in the quality of the particles produced, in terms of eventual *in vivo* application, the lower the concentration of base that can be used the more biocompatible the end vesicle is likely to be. Therefore, there needs to be a trade-off between particle quality and minimising potential toxicity. With this in mind, the optimum concentration was chosen to be 10 mM, as it was deemed to be relatively low toxicity (as confirmed in section 6.2.2) but also resulted in the successful precipitation of MNPs. It is also hoped that any loss of quality with respect to the particle morphology due to this lower base concentration would be compensated for during compartmentalisation of the reaction and the eventual incorporation of MTB biomineralisation proteins.

### 3.3 MAGNETITE FORMATION SUMMARY AND FURTHER WORK

There were multiple syntheses that could have been explored in determining the best magnetite precipitation route (Table 3.1). Not all methods could be tested either for practical reasons (temperatures required too high) or lack of time. This means that only the most promising methods were picked to be carried out, the resulting precipitate was analysed with respect to particle size, morphology and polydispersity of the population.

Synthesis Route	Fe <sup>2+</sup> /Fe <sup>3+</sup> ratio used	Reaction temperature (°C)	Average particle size (nm)	Vesicular Incorporation
Room Temperature Co-precipitation	2:1	20-25 (Ambient )	10±2	Yes
Thermal Decomposition	2:1	90	83 ±6	Yes
Urea/Ammonia decomposition	2:1	80-100	Not Measured	Unsuitable

**Table 3.1** Summary of magnetite precipitation routes tested

Three methods have been tested and the results presented above, (summarised in table 3.1) precipitation of magnetite. Summary of magnetite precipitation route *via* partial oxidation had been previously tested by Lays Gierakowski (previous student in the Staniland group) and the particles using this method were inferior to the particle produced using thermal decomposition of urea. Therefore the high temperatures and harsh conditions needed to make these particles did not justify its use and thus it was deemed unsuitable for incorporation into a vesicle. Similarly precipitation using a combination of urea and ammonia was judged to be an over-complication of the standard urea precipitation route. The samples produced were of poor quality visually, appearing brown in colour and with very little magnetism. Therefore no further experiments were performed using this method. For the two methods which produced suitable particles X-ray diffraction (XRD) was performed (again by L. Gierakowski). The diffraction pattern (Figure 3.5 ) for both thermal decomposition of urea and room temperature NaOH co-precipitated particles confirmed the presence of magnetite nanoparticles, by the presence of peaks representative of the faces that are found in the magnetite crystal structure, particularly the 111, 311, 511 and 440 miller indices. The ease with which these particles are made is a huge advantage for this system.

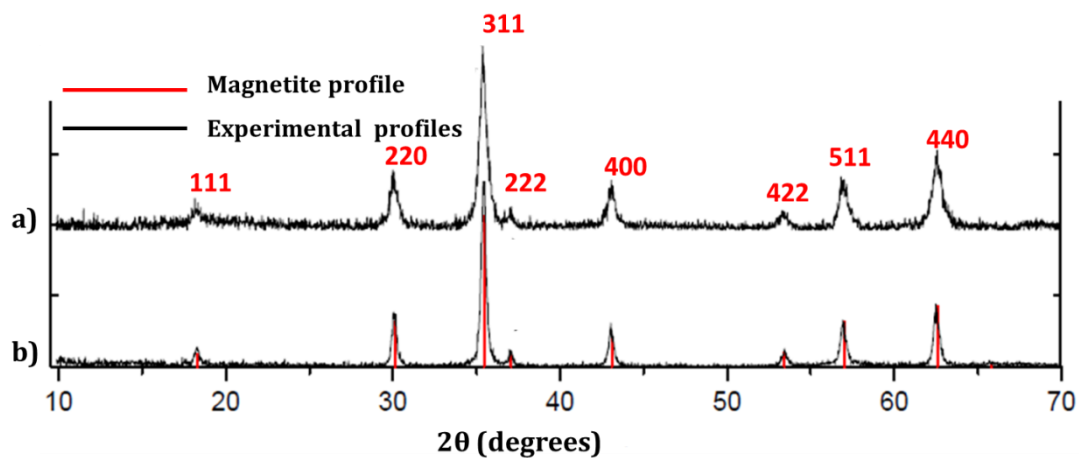


**Figure 3.5:** X-ray diffraction patterns of magnetic nanoparticles produced *via* a) thermal decomposition of urea and b) room temperature co-precipitation by NaOH. Experimental data (traces in black) have been compared to a literature profile for pure magnetite (red trace). Noise in the trace decreases from a) to b) which corresponds with TEM micrographs of the samples (Data collected and plotted by L. Gierakowski, adapted for this thesis).

For incorporation into a vesicle, both co-precipitation routes could be considered superior to other routes explored, largely due to the ambient conditions (NaOH) and delayed pH increase (urea) make these interesting routes to explore when compartmentalised within a vesicle core. Thermal decomposition of urea is perhaps the most suitable route for iron ion encapsulation and crystallisation of magnetite inside a vesicle as it prevents magnetite formation prior to the encapsulation of reagents. This means that membrane transport of the iron ions can be completed before the heating stage to induce precipitation. Furthermore heating the sample to induce precipitation on the whole produced larger magnetite nanoparticles with an average diameter of  $83 \pm 6$  nm compared to the room temperature co-precipitation which produced particles with an average size of  $10 \pm 2$  nm.

There is a wealth of further work which could be carried out on optimisation of an appropriate route if time permitted. This could include further variation of the ferric to ferrous ratio used, although this would then have to be translated to measurements on the intra-vesicular ratio to ensure that the ratio added to the extra-vesicular media is effectively transported into the vesicle core.

This is highly unlikely, and therefore fine tuning of the ratio (outside of the vesicle) would likely be required to achieve an optimum intra-vesicle ratio. Similarly, oxidation could be more closely monitored. The stoichiometric ratio of ferric to ferrous iron in magnetite has also been used in the solutions as it seems the logical place to begin for the compartmentalisation of the precipitation of magnetite on the assumption that oxidation will be negligible in the vesicle core. However, this has not yet been tested and should oxidation occur within the vesicle, it may be necessary for the ratios to be adjusted accordingly for optimisation of magnetite formation.

### 3.4 MEMBRANE TRANSPORT ASSAYS

The results of membrane transport for the formation of magnetite can qualitatively analysed visually (ideally the intra-vesicular precipitation of magnetite should yield a black/brown precipitate) and using electron microscopy. This is both time consuming and expensive. Furthermore, TEM alone cannot provide any quantitative analysis of, a) how much of the iron ion solution is crossing the membrane, b) whether one iron species is preferentially crossing the membrane over the other and c) what effect this is having on the internal pH. Therefore, the design of an assay is required to be able to quantify this transmembrane activity. This assay was designed so that encapsulation of a detection agent (for the detection of changes in pH, redox potential, iron ion chelation or vesicle leakage) was incorporated into the vesicle core.

The transmembrane transport of iron ions can then be both detected and quantified by measurement of changes to the UV-vis absorption or fluorescence spectrum due to changes in the encapsulated indicator. In each case, the solutions of the detection agents were made up at varying concentrations and the absorption or fluorescence spectra of standard non-encapsulated solutions were recorded to create a calibration curve. This could then be used to quantify the concentration of the detection agent inside the vesicle. Background spectra of blank vesicles were also recorded so any contribution from the lipid or polymer can be subtracted. In each case, the solution at maximum concentration (i.e. 100 % iron chelation) was encapsulated.

### 3.4.1 MEASUREMENT OF INTER-VESICULAR REDOX POTENTIAL

An assay was designed to detect changes in the redox potential of the system. As iron crosses the vesicle bilayer, there will be an increase in acidity which in turn will reduce the pH. This is because, as the reaction proceeds, the hydroxyl ions will be used up by reacting with the iron, further increasing the internal vesicular pH. This will change the redox potential of the solution in the vesicle interior. In an attempt to detect these changes, and consequently quantify iron ion membrane transport, a redox sensing dye was encapsulated along with the basic solution in the vesicle core. The dye used is the aromatic complex Resazurin (7-hydroxy-3*H*-phenoxazin-3-one 10-oxide). Due to its aromaticity, the dye is both UV-active and weakly fluorescent. A colour change is observed from blue to pink as the aromatic nitrogen in the complex is reduced (Figure 2.5). In the vesicular system, this reduction will occur as a consequence of iron ions entering the vesicle core and reducing the internal pH. The colour change that corresponds to decreasing pH can be seen in figure 3.6 a), with solution changing from blue to pink as the pH decreases from six to three. The UV-Vis spectra for these solutions at decreasing pH are plotted in figure 3.6 b). This shows an overall shift from 500 nm to 600 nm as the solution changes from pH 3.8 to 6.8. A calibration curve was constructed from the maximum absorbance in the UV-Vis spectrum of each sample (Figure 3.6 c). Measurements of the emission were taken at 5 nm intervals; and a biphasic calibration curve was obtained, which jumps between phases at approximately pH 5.4. This corresponds to the point at which the solution becomes distinctly blue; it is assumed that this switch corresponds with the reduction of the Resazurin complex.

While this is useful in measuring the increase in pH from 4 to 5 or vice versa (which would indicate incorporation of iron ions), it cannot give an accurate measurement of the specific pH at a given point as iron ions cross the membrane. However, Resazurin can also be monitored visually by a change from pink to blue, therefore rendering these measurements obsolete. After obtaining the necessary control data, the assay was incorporated into polymer vesicles (as optimised in chapter 4) for determination of trans-membrane iron ion transport.

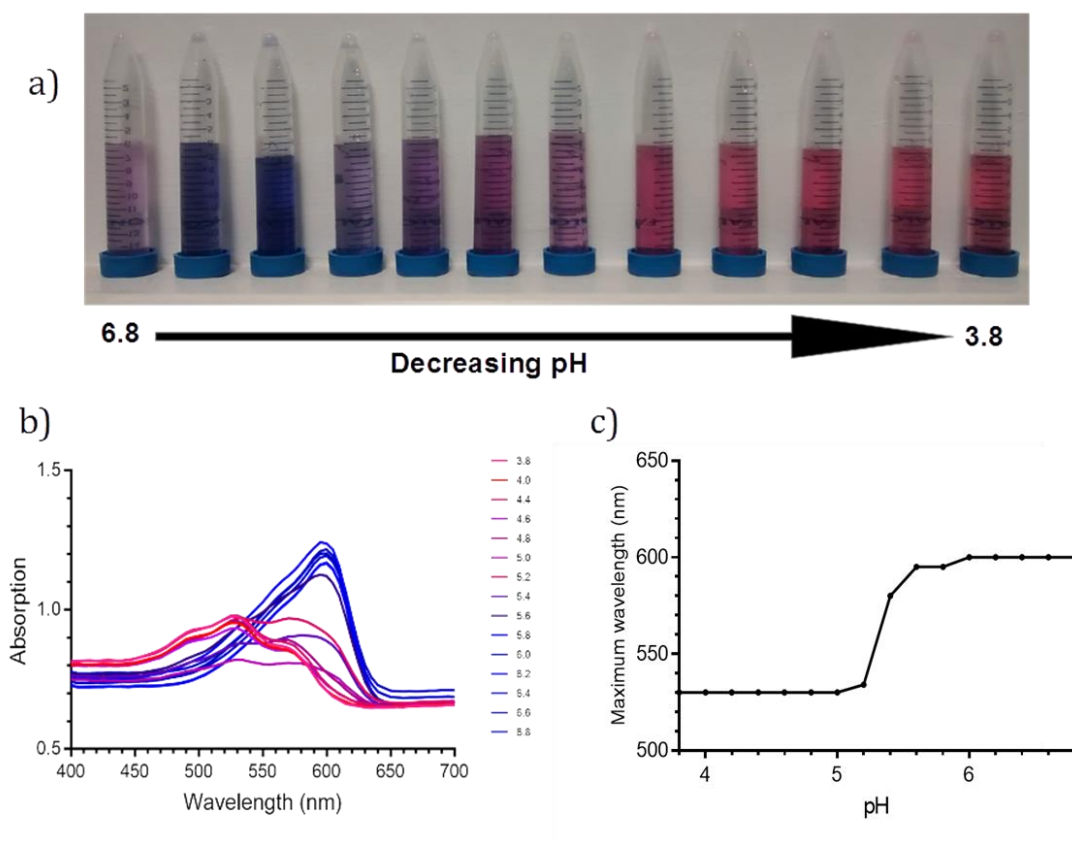


**Figure 3.6:** a) Shows the colour change observed as the pH of the solution is decreased. b) UV-Vis spectrum of the corresponding absorbance's at each pH, showing a shift from 500-600 nm. c) Calibration curve of Resazurin absorbance as a function of solution pH, experimental data is shown in black.

On incorporation into the vesicles, the absorption signal of the Resazurin was lost. This test was repeated multiple times at increasing concentrations of indicator before incorporation, and on each occasion the spectrum saturated. For the control sample, the signal was lost each time it was incorporated into the vesicle. There are a number of explanations as to why no absorbance was observed, such as the internal volume of the vesicles act to limit the ability to encapsulate volumes and concentrations of Resazurin that can be detected. Conversely, this may mean that the small molecule Resazurin; is able to leak out of the vesicle interior and be subsequently removed during clean-up. Furthermore, the vesicle interior is so small compared to the volume of the bulk solution that the amount of Resazurin remaining in the sample post-clean-up may be too low to detect even if it were successfully encapsulated. Although highly unlikely, it cannot be ruled out that the Resazurin was never encapsulated to begin with. It is more likely that scattering from the surrounding polymer/lipid is preventing detection of the absorbance of Resazurin.

Scattering from the polymer; which is visible in solution, is likely to impede the ability to measure the absorbance of the encapsulated indicator.

### 3.4.2 QUANTIFICATION OF FERRIC/FERROUS ION TRANSPORT

Two further approaches to quantify of trans-membrane iron ion transport were explored. These routes focussed not on change in internal vesicle condition (i.e. redox and pH), but instead on measurement of the ferrous iron concentration within the vesicle core. Again, calibration curves for each assay were obtained, to aid intra-vesicle iron ion concentration measurements.

#### 3.4.2.1 FERENE

Focussing on the ferrous ion concentration within the vesicle, control of ferrous iron ions chelated to the ferene complex (5,5'-[3-(2-Pyridyl)-1,2,4-triazine-5,6-diyl]difuran-2-sulfonic acid disodium salt), upon chelation of the ferrous ions a colour change from clear to deep blue is observed. Samples were measured by UV-vis spectroscopy, and again these control samples showed a maximum absorbance at around 520 nm, the intensity of which decreased as a function of concentration (Figure 3.7 a).

These data were plotted (Figure 3.7 b) for the determination of the internal vesicle iron concentration; with a darker blue solution and higher intensity of absorbance being related to increased trans-membrane movement of ferrous iron. This plot revealed a step-wise change when ferrous ion became chelated to the ferene molecule, which as with Resazurin is detectable by eye. It did not reveal any information with regard to the concentration of the ferene, from which the ferrous ion concentration could then be determined. Moreover, as in section 3.3.1, the absorption of the ferene species could not be detected following incorporation into a vesicle (Figure 3.7 c).

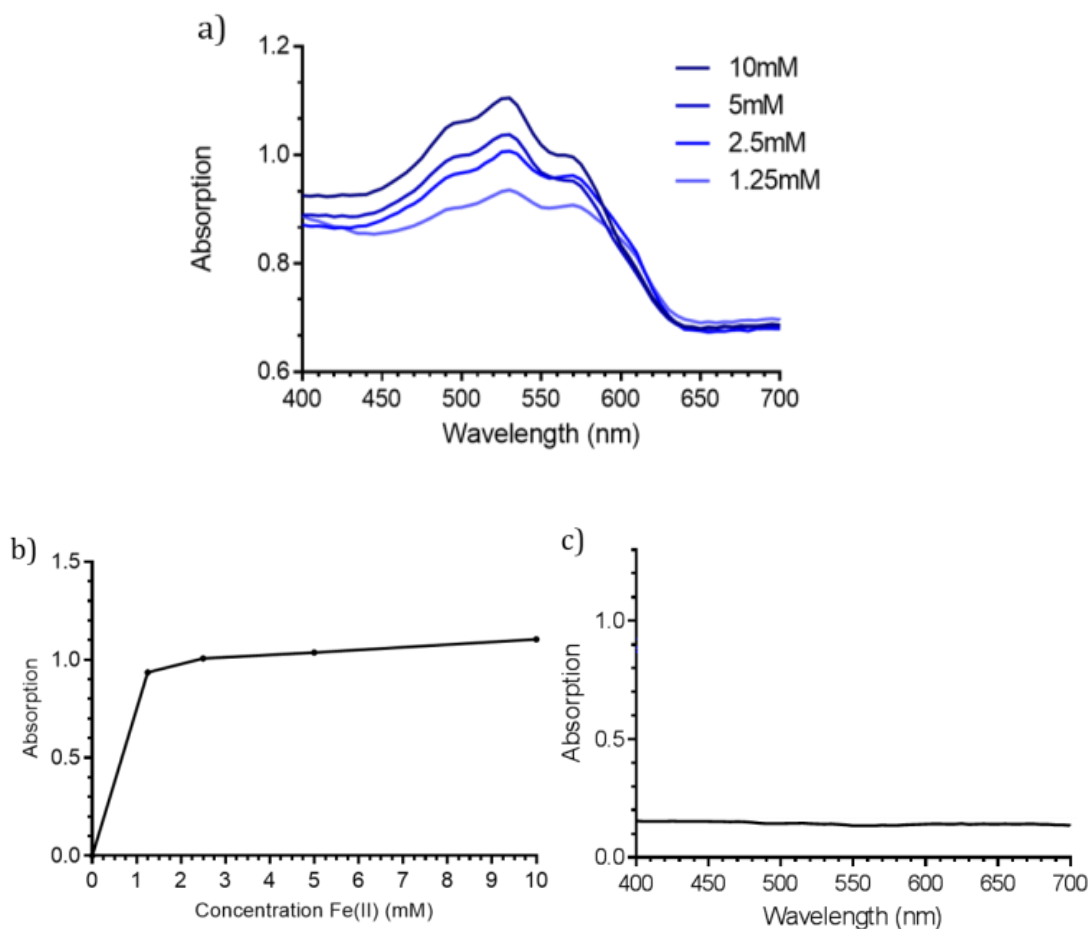


**Figure 3.7:** a) UV-Vis absorption of ferrous chelated ferene as a function of ferrous iron concentration, showing a maximum absorbance at 520 nm. b) Calibration curve of absorption vs. ferrous iron concentration. c) UV-Vis spectrum of ferrous chelated ferene after encapsulation in vesicles showing no absorption.

UV-Vis spectra taken of vesicles which should have the chelated ferene encapsulated showed no characteristic absorbance profile as observed in control, unencapsulated samples. The possible reasons for this are multiple, and relate to encapsulated volume/concentration of indicator and scattering from the polymer shielding preventing detection of the ferene complex.

### 3.4.2.2 PRUSSIAN BLUE

To determine whether leakage caused the failure of the ferene assay, a larger complex that can indicate the presence of iron in solution was investigated. Potassium ferrocyanide (Prussian blue) was deemed to be more suitable; particularly due to its wide-spread use as a detection agent of cell viability and cell death. On this basis, the same experiments (unencapsulated calibration curve determination and detection post encapsulation of known concentrations) were performed using the Prussian blue ligand complex. As before, Prussian blue was chelated to iron ions, although in this case ferric ions were used for the chelation. On introduction to a ferric ion solution, an extremely deep blue colour is observed due to the chelation of the ferric ions by Prussian blue, which after serially diluting multiple times still resulted in saturation when the UV-Vis spectrum was measured.

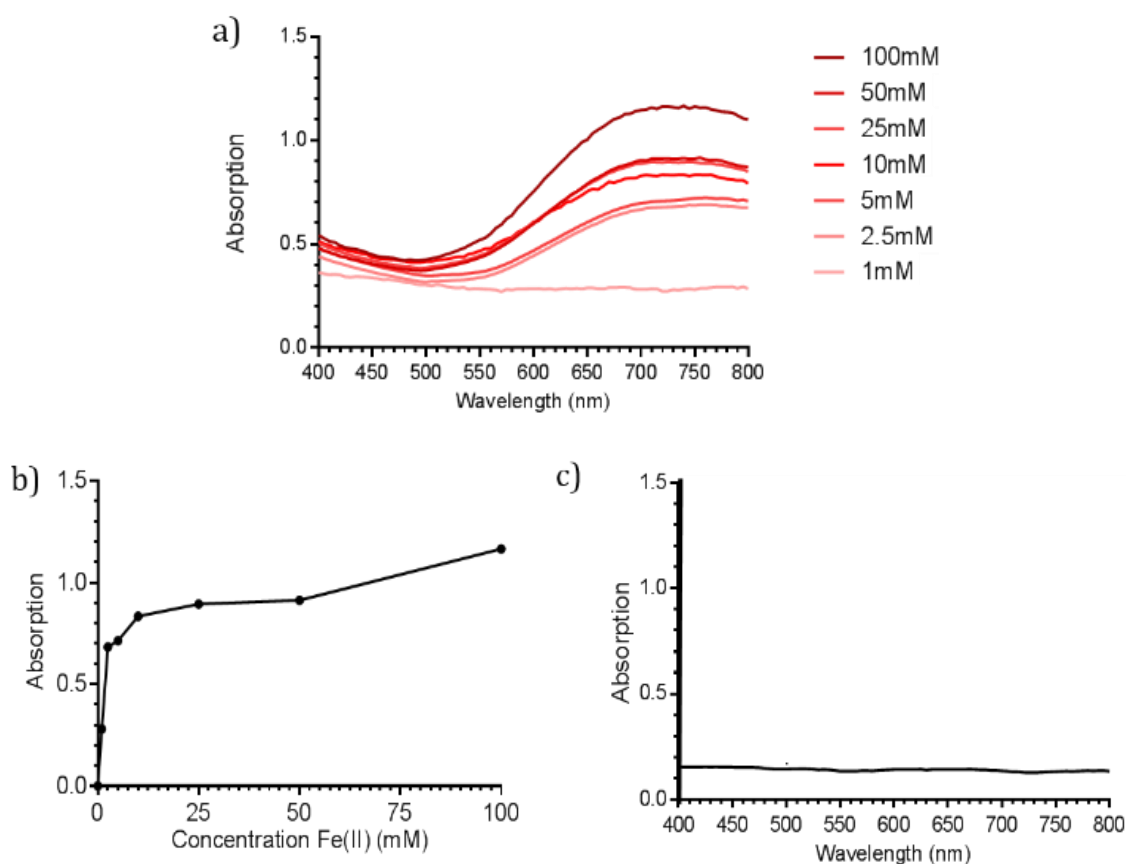


**Figure 3.8:** a) UV-Vis absorption of ferrous chelated potassium ferrocyanide as a function of ferrous iron concentration showing a maximum absorbance at 730 nm. b) Calibration curve of absorption vs. ferrous iron concentration. c) UV-Vis spectrum of ferrous chelated potassium ferrocyanide after encapsulation in vesicles showing no absorption.

To alleviate these issues, the control experiments were repeated with a ferrous ion solution, which formed a less intense red solution upon chelation. Each solution gave a maximum absorbance at 730 nm, with the intensity changing as a function of concentration; (Figure 3.8 a). When the absorption with ferrous iron chelated was plotted as a function of iron concentration, it is again not possible to estimate iron concentration as required. Instead, a step-wise change is observed upon chelation of iron ions, which can be detected by eye. However, on encapsulation of both the ferrous and ferric chelated solutions within a vesicle core, it was not possible to detect the absorbance of either species. It is unlikely that the Prussian blue chelated complex could leak across the vesicle bilayer, based on the complex size; therefore it is more likely that issues with scattering are responsible for the failure of this colourimetric assay.

### 3.4.3 VESICLES LEAKAGE ASSAY

Carboxyfluorescein is a fluorescent dye which is self-quenching at concentrations of 100  $\mu\text{M}$  and above.<sup>168</sup> Therefore, it can be used to monitor leakage from vesicles, by encapsulation at high (quenched) concentrations. Upon poration of a membrane (leakage) the dye will be diluted, and the fluorescence will be “switched on”. This fluorescence intensity can then be quantified, and related to the concentration that has leaked from the vesicle. PBD-PEO polymersomes were prepared that encapsulated carboxyfluorescein (10 % w/v at 100  $\mu\text{M}$ ), with the excess dye outside the vesicles being removed by SEC. Encapsulation of the dye in the core of the vesicles was confirmed by fluorescence microscopy (Figure 3.9 a). The resolution of this microscope is not high enough to allow us to see individual vesicles directly, but the discrete fluorescence observed can be attributed to the presence of the vesicles. Fluorescence spectroscopy was performed before and after electroporation. It was anticipated that electroporation would aid leakage and correspond to an increase in the fluorescent signal. The polymersomes were electroporated at increasing applied voltages (in parallel) to porate the membrane and aid leakage. It is expected that increased voltage will yield increase leakage, and therefore an increase in the fluorescence intensity (Figure 3.9 b).

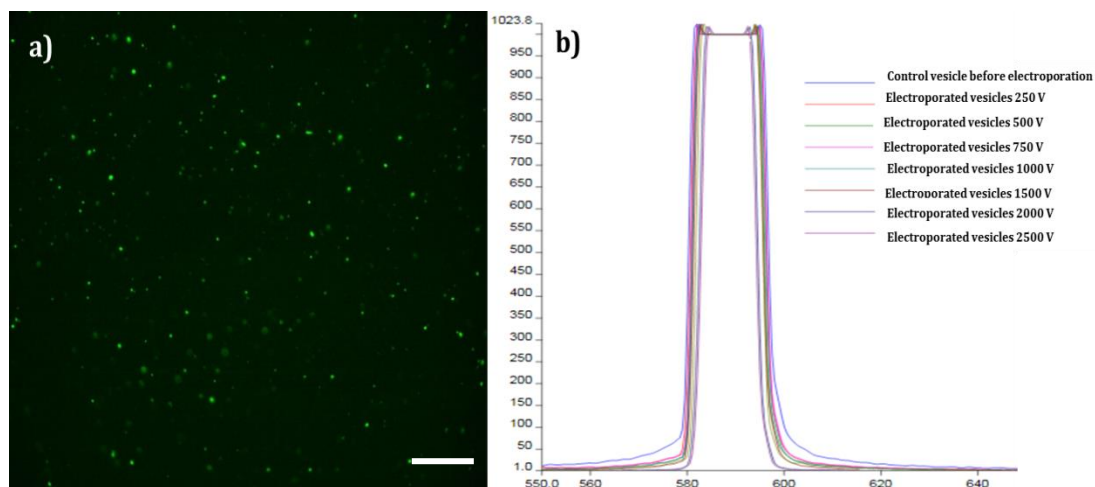


**Figure 3.9:** a) Fluorescence microscopy image of PBD-PEO polymersomes containing 10 % w/v 100  $\mu\text{m}$  Carboxyfluorescein. Scale bar is equal to 1  $\mu\text{m}$  b) Fluorimetry data on the carboxyfluorescein encapsulated polymersomes, electroporated at different voltages to detect fluorescence "switch on" following poration.

On poration of the polymer membrane, no change in the fluorescence signal intensity was observed. This is likely to be because the fluorescence signal was saturated before electroporation, and therefore any change was undetectable. Serial dilutions of the sample were unsuccessful. It is probable that there was a problem with the carboxyfluorescein concentration, as the microscopy image shows relatively strong fluorescence when the fluorophore should have been at a self-quenching concentration. The experiment was repeated at both lower (1  $\mu\text{m}$ ) and higher concentrations (100  $\mu\text{m}$ ) of carboxyfluorescein with the same result. Therefore it was not possible to optimise the method to obtain useable data.

### 3.5 WAYS FORWARD AND CONCLUSIONS

It was found that, in choosing an appropriate route to magnetite precipitation, there is a trade-off. This is between achieving high quality nanoparticles, while avoiding harsh reaction conditions and complicated synthesis routes which cannot be easily incorporated into a vesicle.

This is demonstrated by direct comparison between the room temperature co-precipitation and co-precipitation from the thermal decomposition of urea. While the particles produced by oxidation as a result of decomposition of urea appear to be of a better quality; as they show increased monodispersity and producing particles of a size which are comfortably in the region of a single domain ferrimagnetic nanoparticle. It can be argued that the urea based method is less suitable than co-precipitation at room temperature with NaOH method. This is because the urea method requires a long period of heating, which the vesicle may not withstand. Therefore, it may not be prudent to use the method which produces the most monodisperse nanoparticles, as the synthesis process may destroy the nanoreactor. Instead, it seems logical to choose a method which, although it produces nanoparticles of a lower size, distribution and quality, is more amenable for vesicular incorporation. It may also be that compartmentalisation of the room temperature reaction is able to control the size and morphology of the encapsulated precipitate. The urea/ammonia decomposition (Section 3.2.4) method was not selected for further study either. This is because many of the reaction attempts were unsuccessful, and the combined encapsulation of both urea and ammonia was overcomplicating the precipitation. Unfortunately, if only urea was encapsulated as the reactive base inferior particles were also produced.

Two methods were used for incorporation into a vesicle (Section 4.4); these are the decomposition of urea (Section 3.2.1) room temperature co-precipitation, (Section 3.2.3). Room temperature co-precipitation was chosen for encapsulation due to both the simplicity of the method and the ambient temperature at which the reaction occurs. The thermal decomposition of urea appeals mainly due to the delayed introduction of the high pH environment. This allows external control over the point at which precipitation occurs by altering the temperature. This means that the pH increase can be induced at an optimum time in the reaction, either during or post trans-membrane transport of iron ions (Section 3.2.1). The factor determining the quality of the particles in each case appears to be control of the rate of the pH increase, which induces precipitation. In the cases where high quality particles were produced, the introduction of the OH<sup>-</sup> was done in a gradual and controlled manner.

This control was exerted either by using a steady rate of addition controlled by syringe driver (NaOH), or by controlling the point at which precipitation can occur induced by heating the sample ( $\text{CO}(\text{NH}_2)_2$ ). In the cases where magnetite was not formed (combined urea/ammonia route), the high pH solution was added *en masse* at the beginning of the reaction. This rapid addition results in the formation of brown, non-magnetic nanoparticles (presumed to be  $\text{FeO}(\text{OH})$ ). Each of these routes to magnetite synthesis was tested for its effectiveness in both the lipid and polymer vesicles, and the optimisation is discussed in chapter 4.

Unfortunately, efforts to quantify the iron ion transport across both a lipid and polymer membrane were unsuccessful. Each iron and redox potential quantification assay was only able to indicate the point at which there was colour/pH switch, causing a change in the absorption spectra. This is ineffective, as each of these changes can be detected by visual inspection of the sample. Confirmation of successful encapsulation within a vesicle was also not achieved. As discussed above, this could be due to a number of reasons (Section 3.3). One reason being the low volume/concentration of the encapsulated assay reagent, this is unlikely as the concentration in each case was increased and the sample concentrated with no improvement in the ability to detect the encapsulated solution. The encapsulated volume is extremely small, but the absorption should still be detectable; as it saturated the spectrum in each case when measuring the control solution. Therefore the most likely reason for the undetectable emission/absorption from the vesicle contents is scattering from the polymer/lipid shielding the solution. This scattering would therefore make any change undiscernible, both by eye and in UV-Vis absorption analysis. Across all assays explored, it was not possible to determine whether scattering was the reason for failure in vesicles. In all cases the vesicle solution was cloudy before UV-Vis detection due to the scattering of light. It is therefore likely that this scattering effect, due to the vesicle bilayer, masks any absorbance from the dye, rendering encapsulated assay solution undetectable. The outcomes of this chapter have formed the basis for all other experiments throughout this work. The now optimised precipitation reactions were applied throughout all of the proceeding chapters to create a vesicle nanoreactor and eventually a fully artificial magnetosome. The failure to establish an effective assay has resulted in the iron transport in all subsequent experiments being estimated from TEM, elemental and magnetic measurements.

# CHAPTER 4:

---

## VESICLE FORMATION: OPTIMISATION OF THE FORMATION OF LIPOSOMES AND POLYMERSOMES

## 4.1 INTRODUCTION TO VESICLE FORMATION

The simultaneous iron uptake and pH increase for magnetite formation inside an artificial magnetosome requires an optimised composition of the nanoreactor vesicle. A pH gradient is required for successful magnetite precipitation, and this must be established and maintained across the membrane. The lipid or polymer system must therefore be able to remain assembled in the presence of this pH gradient. The magnetite precipitation route must also be considered, due to the possibility of sustained periods at high temperatures, as this is required as part of some magnetite precipitation reactions.<sup>20e, 20f</sup> Precipitation routes of this nature are known to make more homogeneous nanoparticles when compared to room temperature precipitation,<sup>2b, 3, 20f</sup> but are not necessarily suitable to be carried out within a vesicle core. Therefore, following the results presented in chapter 3, it was decided, that only two magnetite precipitation routes would be incorporated into vesicles. The room temperature co-precipitation route with NaOH, due to the mild synthesis conditions used, and the thermal decomposition of  $\text{CO}(\text{NH}_2)_2$ . Although thermal decomposition does require high temperatures (90 °C), the advantage of being able to remotely induce precipitation (using heating) may outweigh the drawback of needing to use elevated temperatures. This is providing a suitable vesicle can be found to withstand the temperature and pH conditions. With this in mind, the vesicle itself must of course be optimised; in terms of both size and chemical composition. The vesicle must be an appropriate size to contain the formation of an MNP of an appropriate size for application. The internal environment of the vesicle must also have suitable conditions for the reaction to be able to occur successfully. It is not feasible to develop a working vesicle nanoreactor without first knowing the reaction requirements; such as the pH and temperature range that the vesicle will have to withstand.

This chapter documents the formation of vesicles, trialling both phospholipids and amphiphilic di- and tri-block copolymers, as artificial magnetosome nanoreactors. Multiple formation routes, such as simple film rehydration, sonication techniques, extrusion and preparation of asymmetric liposomes, were investigated.

These techniques were assessed with reference to their ability to encapsulate a solution of high pH, and the vesicle monodispersity, to ensure uniform particle precipitation within the core. Monodisperse vesicle samples were taken forward for further study as the candidate nanoreactor vesicle for incorporation of magnetite co-precipitation optimised in chapter 3. Throughout this chapter, TEM of negatively stained vesicles shows the morphology, degree of aggregation, and sample homogeneity. However, staining and drying artefacts can result in distortions and an apparent shrinkage of the vesicles. Dynamic light scattering (DLS) was used to characterize both the vesicle size and the sample size distribution. While DLS offers analysis of the sample population, the measurement is based on the particles hydrodynamic size, which presumes a spherical, solid material. This can contribute to vesicles appearing larger than their true size, as they are not solid, may also not be perfectly spherical, and will also have a shell of water/solution around the exterior, all contributing to increasing the size measured in DLS. Therefore, it should be noted that there is a discrepancy (approximately two-fold) between the DLS and TEM sizing, but importantly the population distribution is in agreement.

This chapter is a summary of optimisation of vesicles formation therefore sections 4.2.1 and 4.3.1 are a discussion of the different properties of the lipids and polymers studied with respect to their applicability to use in a vesicle nanoreactor, and sections 4.2.2 and 4.3.2 explore the data that tests them.

## **4.2 LIPOSOMES**

### **4.2.1 PHOSPHOLIPID SELECTION**

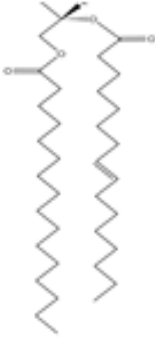
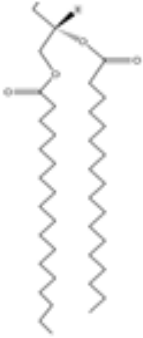
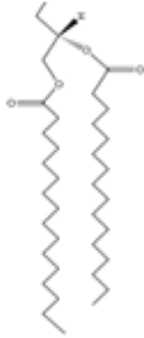
Naturally occurring phospholipids are an integral component of cell membranes; therefore making them well suited for use in *in vivo* biomedical applications. The properties of the phospholipids need particular consideration for functionality when designing a nanoreactor. Withstanding the pH gradient needed for magnetite precipitation is essential, but this has to be balanced with a capability for incorporation of biological components (e.g. transporter proteins) or for synthetic poration, to facilitate iron transport across the bilayer, and thus enable the magnetite precipitation reaction to proceed within the core.

The lipid properties that have been varied include; variations in charge (+/-) (which can affect vesicle formation), various hydrocarbon chain lengths, and degrees of hydrocarbon chain saturation, which dictates the flexibility, permeability and melting temperature ( $T_g$ ) of the lipids within a bilayer. The properties of the phospholipids selected are outlined in Table 4.1.

#### 4.2.1.1 SATURATED PHOSPHOCHOLINE (PC) BASED LIPIDS

Phosphocholine (PC) based phospholipids are zwitterionic molecules with an overall neutral charge. They are found in both the MTB bilayer<sup>39b</sup> and in the membranes of many mammalian cells, making them inherently biocompatible. PC lipids are also found in a wide variety of other organisms, including *Escherichia coli*. This should increase the likelihood of successful MTB membrane protein incorporation into synthetic liposomes, as they share similar properties to the native environment of the protein.

Phospholipids with mid-range  $T_g$ 's may represent materials that are ideal for magnetite nanoreactor formation. This is because they should be able to form a stable vesicle, which can also withstand the conditions needed for magnetite precipitation (pH 12 and possibly heating). As the  $T_g$  should not be too high, they should also not be too robust which would hinder membrane transport with respect to iron ion permeation of the vesicle membrane. For this reason, two lipids with  $T_g$ 's around 50°C were studied, as they may offer the ideal balance between stability and permeability required for magnetite nanoreactor formation. These are 1,2-distearoyl-sn-glycero-3-phosphocholine (DSPC) and Dipalmitoylphosphatidylcholine (DPPC) (Table 4.1). Both are phosphocholine lipids with entirely saturated hydrocarbon tails, which means there will be little fluidity in the bilayer. DSPC and DPPC will be in the gel phase at ambient temperatures, due to their relative  $T_g$ 's (55 and 41°C respectively), and so they should form relatively impermeable bilayers (to avoid OH<sup>-</sup> leakage) at room temperature. The only significant difference between these two lipids is the length of the stearic acid and palmitic acid non-polar chains. The stearic acid in DSPC is slightly longer, which should make DSPC vesicles slightly more robust and less prone to leakage.

Phospholipid	Structure	Molecular Weight (g/mol)	Glass transition temperature (T <sub>g</sub> )	Specific functionality
L- $\alpha$ -phosphatidylcholine (Egg PC)		770.12 (Average)	-10°C	Cost effective
1,2-distearoyl- <i>sn</i> -glycero-3-phosphocholine (DSPC)		790.14	55°C	High T <sub>g</sub>
1,2-dipalmitoyl- <i>sn</i> -glycero-3-phosphocholine (DPPC)		734.03	41°C	PC head group/ Biocompatibility
1,2-diphytanoyl- <i>sn</i> -glycero-3-phosphocholine (DPhPC)		846.25	~ 200°C	Thermal Stability

1,2-dioleoyl- <i>sn</i> -glycero-3-phosphocholine (DOPC)		786.11	-17°C	Unsaturated
1,2-dipalmitoyl- <i>sn</i> -glycero-3-phosphate (sodium salt) (DPPA)		670.87	67°C	PA head group
Dipalmitoylphosphatidylethanolamine-PEG 5000 (DPPE-PEG 5000)		5744.96	63°C	PE head group/High Molecular Weight
1,2-dioleoyl-3-trimethylammonium-propane (chloride salt) (DOTAP)		698.54	-11.9°C	Cationic
1,2-dioleoyl- <i>sn</i> -glycero-3-phospho-(1'- <i>rac</i> -glycerol) (sodium salt)		797.02	-18°C	Anionic

**Table 4.1:** Structure and properties of each phospholipid investigated for liposome formation.

The mid-range melting temperatures of DSPC and DPPC are above ambient temperature but below the temperature of co-precipitation using urea (90°C). This means that permeability to iron ions could be increased as the lipids are raised above the  $T_g$  as part of the precipitation reaction.

#### 4.2.1.2 UNSATURATED PHOSPHOCHOLINE (PC) LIPID

Egg-PC, as the name suggests, is isolated from chicken egg yolk, and is the most cost effective and widely studied of the PC lipids to be tested. The lipid has a comparable molecular weight to all of the other lipids investigated (770.12 g mol<sup>-1</sup>) (Table 4.1). The structure of the lipid is a simple phosphocholine, with a single unsaturated bond on one of the hydrocarbon. This means that egg-PC bilayers are relatively fluidic, which gives rise to its low  $T_g$  (-10 °C) (Table 4.1). If this is effective in encapsulating the necessary base for magnetite precipitation, it is likely that this lipid will provide a cheap (\$200 per gram, Avanti polar lipids) and easy method for formation of an artificial magnetosome. In terms of forming easily adapted liposomes, the chemistry of which does not interfere with its nanoreactor functionality, egg-PC may not be a good candidate.

Offering increased fluidity in a bilayer is, 2-dioleoyl-sn-glycero-3-phosphocholine (DOPC),<sup>8</sup> with a transition temperature of -20 °C<sup>7</sup> (Table 4.1). This was investigated due to its easy handling as a result of being in the liquid phase at ambient temperatures, when compared to other lipids used with much higher  $T_g$  (DSPC and DPPC discussed above) which are in the gel phase at low temperatures and therefore can precipitate easily. The low transition temperature of DOPC is the result of unsaturation in the hydrocarbon tail. The double bonds cause kinks in the backbone, which generates disorder in the bilayer upon self-assembly, resulting in space between adjacent phospholipids. This has a direct effect on both phase behaviour and bilayer elasticity.<sup>63</sup> Therefore, permeation of the bilayer with iron ions may be easier with DOPC but the flexibility may result in the encapsulated base being lost.

#### 4.2.1.3 THERMALLY STABLE LIPID

With liposome stability in mind, the more robust phospholipid 1,2-Diphytanoyl-*sn*-glycero-3-phosphocholine (DPhPC) was also investigated. It is the other extreme in properties when compared to DOPC, offering heightened thermal stability due to a  $T_g$  of 200°C. The lipid is known to be extremely robust in high pH environments, which arises from the methyl groups on the hydrocarbon backbone causing an interlocking effect when packed into a bilayer, stabilising the vesicle. This means that a higher temperature is required for DPhPC to transition to a fluid phase, making this lipid ideal for encapsulating high pH solution and withstanding the high temperatures involved in the thermal decomposition co-precipitation discussed in chapter 3. Conversely, it must not be ignored that the high  $T_g$ , and thus its rigidity, may hinder the transport of iron across the membrane. It should be noted that this study is novel, with such high temperature reactions never being compartmentalised within a vesicle, therefore it is now known yet known which lipids will react in what way during mineralisation. Furthermore, the high stability also dictates high cost (\$1,100 per gram, Avanti polar lipids), therefore DPhPC may not be a viable option for widespread testing and scale-up of artificial magnetosome synthesis.

#### 4.2.1.4 PHOSPHATIDIC (PA) LIPID

All phospholipids mentioned so far have phosphocholine head groups. There are other types of phospholipid that are also available and present in cell membranes, therefore present viable options for exploration as potential vesicle membranes as part on this thesis. The effect of changing the lipids polar headgroup was tested with vesicle formation using, 1,2-dipalmitoyl-*sn*-glycero-3-phosphate  $\text{Na}^+$ , (DPPA). DPPA (Table 4.1) has the same dipalmitoyl hydrocarbon backbone as DPPC, but with a smaller PA headgroup when compared to PC. The PA head group size means that it is much closer to the backbone than PC lipids, which is likely to affect the packing of a PA bilayer. It has been shown that the presence of PA lipids in a membrane has an effect on the curvature of the membrane,<sup>106b, 153</sup> presumably as result of the smaller head group leading to closer packing in the bilayer.

The closer packing may impact the overall vesicle size and its permeability as bilayer lipids move closer to one another. It is not yet known whether or not this will be advantageous in this nanoreactor system.

#### 4.2.1.5 PHOSPHATIDYLETHANOLAMINE (PE) LIPID

On the other hand, a larger head group may serve to increase fluidity and permeability across the lipid vesicle. Dipalmitoylphosphatidylethanolamine-polyethyleneglycol 5000 (DPPE-PEG 5000) has a larger phosphatidylethanolamine (PE) head group than phosphocholine, due to an extra ethyl group between the phosphorous and nitrogen. Again, this is likely to affect bilayer packing by increasing space between lipids in the membrane.<sup>104, 153, 184</sup> The increased membrane fluidity may affect both vesicle size and membrane permeability. The DPPE lipid investigated also has a large polyethylene glycol (PEG) chain attached to the polar head group, with a molecular weight of 5000 g mol<sup>-1</sup>. The presence of this PEG group may have both advantages and disadvantages, on the properties of the resulting vesicle. The PEG could add potentially useful properties for *in vivo* application, such as prolonging the vesicles' *in vivo* lifetime.<sup>71c</sup> On the other hand, the size of the PEG molecule on the inner leaflet will significantly reduce the inner diameter of the vesicle. On the outer leaflet; the size of the PEG molecule could sterically hinder the transport of ions across the membrane.

#### 4.2.1.6 CHARGED LIPIDS

Using a charged lipid for bilayer formation may help to prevent aggregation, essential for *in vivo* application, and possibly increase stability through entropic effects.<sup>185</sup> Charged lipids include the cationic lipid 1,2-dioleoyl-3-trimethylammonium-propane (chloride salt) (DOTAP) or the anionic lipid 1,2-dioleoyl-*sn*-glycero-3-phospho-(1'-*rac*-glycerol) Na<sup>+</sup> (DOPG), (Table 4.1). These lipids may also improve drug lifetimes through electrostatic bonding of the drug to the lipid,<sup>186</sup> although charged lipids can also increase vesicle toxicity.<sup>71c</sup> A charge on the outer leaflet of the vesicle may also affect ion uptake.<sup>71c</sup> Cationic lipids will likely lead to the repulsion of iron ions, whereas with anionic DOPG, uptake of the cationic iron could be improved.<sup>152, 187</sup>

Although one potential problem of using anionic lipids is electrostatic binding of the positively charged iron ions to the anionic polar heads.

#### 4.2.2 LIPOSOME FORMATION

The nine phospholipids outlined in table 4.1 were previously investigated as part of undergraduate projects in the Staniland group. They were screened using DLS for a high throughput approach to analyse the ability of each lipid to encapsulate basic solution (both NaOH and  $\text{CO}(\text{NH}_2)_2$  were tested), vesicle size and sample polydispersity following formation *via* bath sonication. The bath sonicated liposomes were then sequentially subjected to either tip sonication or extrusion to investigate their effect on sample polydispersity (again using DLS). The high throughput nature of the experiments meant that lipids which did not show a suitable peak in the DLS spectrum (i.e. a relatively monodisperse population in the region of 1  $\mu\text{m}$ ) were not taken forward. The results of this screening are shown in table 4.2. Here, lipid(s) egg-PC, DPPA, DOTAP and DOPG are shown to be the least suitable for further study, as a vesicle population could not be detected in DLS analysis. Lipid(s) DSPC, DPPC, DPhPC, DOPC and DPPE-PEG 5000 were found to have a vesicle population in the nanometer range (as measured by DLS), so were deemed suitable for further investigation.

The lipids revealed to be the most suitable in the screening were then optimised with respect to vesicle formation for the creation of a synthetic magnetosome nanoreactor. As NaOH represents the highest pH solution that would need to be encapsulated, it was assumed with respect to pH that if the vesicle was capable of encapsulating NaOH (pH 12) then encapsulation of  $\text{CO}(\text{NH}_2)_2$  would also be possible. For each of the three formation methods (bath sonication, tip sonication and extrusion) bath sonication was used to rehydrate the lipid film followed by parallel studies of either tip sonication or extrusion being applied to the vesicle samples.

<b>Phospholipid</b>	<b>Selected (Yes/No)</b>	<b>Formation method chosen</b>
Egg PC	No	N/A
DSPC	Yes	Tip sonication
DPPC	Yes	Tip sonication
DPhPC	Yes	Bath sonication
DOPC	Yes	Extrusion
DPPA	No	N/A
DPPE-PEG 5000	Yes	Tip sonication
DOTAP	No	N/A
DOPG	No	N/A

**Table 4.2:** Outcomes of high-throughput screening of phospholipids, which identifies the best vesicle formation method for each lipid tested.

The methods offer differing degrees of size and population control, with control increasing from bath sonication, to tip sonication, and the most control exerted by extrusion. TEM imaging was performed on the sample for each lipid which gave the best results in DLS screening to check vesicle morphology. Bath sonication was performed for approximately 30 minutes from a lipid film rehydrated with NaOH (10 mM). Tip sonication was then applied for 30 minutes at 70 % amplitude. This was carried out at 4°C during the high throughput test, however in cases where the  $T_g$  was above 4°C, the lipid precipitated. Thus, to avoid this, all subsequent tip sonication was performed at temperatures above the lipid  $T_g$  (Table 4.1). Using this combination of bath and tip sonication successively should give a higher propensity to produce unilamellar vesicles, when compared to film rehydration or bath sonication alone.<sup>6</sup>

In parallel to this samples were also extruded through a polycarbonate membrane with 100 nm pores, which should exert extremely tight control over the vesicle population size. Sizing was obtained from DLS measurements, which was compared to TEM grainsizing distributions. All concentrations used were determined from the high throughput screening which were based on literature values for successful vesicle formation above the lipid CMC.

#### 4.2.2.1 DSPC

For DSPC, the high throughput screening suggested that the most suitable vesicles were prepared by bath sonication followed by tip sonication. When this test was repeated, the results were again promising producing an average vesicle size of  $192 \pm 39$  nm (Figure 4.1). This is a huge improvement in the sample vesicle size distribution when compared to the two other vesicle formation methods which were applied. The samples produced by bath sonication were entirely unsuitable, with bath sonication generating species in the  $\mu\text{m}$  range ( $1.28 \pm 325$   $\mu\text{m}$ ). Extrusion does not appear to produce vesicles, due to the absence of a peak in the DLS spectrum (Figure 4.1).

The reason for the success of the tip sonication in comparison to the other two methods is likely to be due to the  $T_g$  of the lipid. Bath sonication may have a limited effect on the vesicle size, as the lipid will be in the gel phase. Therefore, the low frequency sonication of the water bath isn't likely to affect the DSPC assembly. This suggests relatively low stability of the DSPC lipid with which bath sonication is sufficient. However, when a more localised higher frequency is applied (in the case of tip sonication), a large change is observed in the DLS spectrum, which confirms a large decrease in vesicle size to  $192 \pm 39$  nm (Figure 4.1).

This higher frequency is expected to be more detrimental to the vesicles, and therefore the lipid  $T_g$  will not be an issue in the same way. The DSPC vesicles are presumed to be lost when extruded through a 100 nm membrane (after bath sonication), as no peak was observed in DLS analysis.

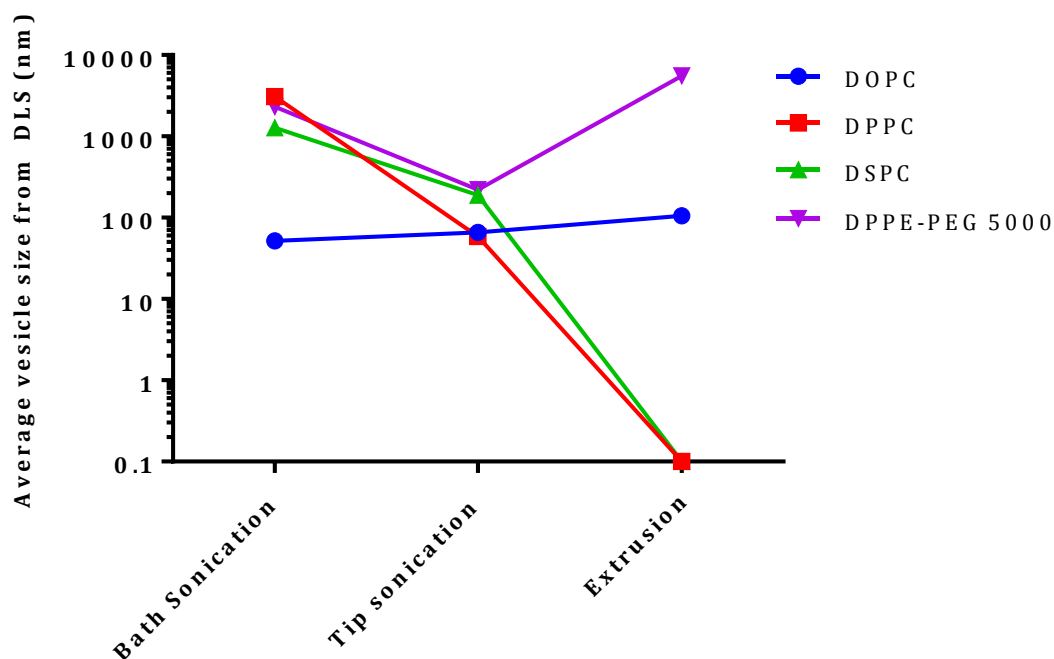


**Figure 4.1:** a) Plot of the average vesicle size (from DLS analysis) for the vesicle sample produced with each formation method (bath sonication, tip sonication and extrusion).

Again, due to the lipid being in the gel state, forcing 1.28  $\mu\text{m}$  liposomes through a 100 nm polycarbonate membrane in the gel state is unlikely to be effective. The reason for the loss of the peak in the DLS spectrum is probably due to precipitation of the lipid which then sediments in the cuvette during DLS scanning. This precipitation is visible when the lipid is below the transition temperature.

TEM imaging of DSPC vesicles produced using tip sonication at 60  $^{\circ}\text{C}$  with encapsulation of NaOH revealed a dual population (Figure 4.2 c). The images show vesicles at  $309 \pm 187$  nm. The bigger vesicles are not required, and the two populations can be separated using SEC, due to the large difference in size. The vesicles do show a consistently spherical morphology, with no sign of aggregation. However, this lipid was difficult to work with. For example, precipitation of the lipid below the  $T_g$  raised particular problems with extrusion and DLS analysis.

Therefore DSPC may not be a suitable for nanoreactor functionality, particularly with the room temperature co-precipitation. But the lipid does have greater potential with the higher temperature thermal decomposition method, and so was taken forward for further testing.

#### 4.2.2.2 DPPC

DPPC gave very similar results to DSPC (Figure 4.1), with bath sonication producing vesicles in the micrometre range (3  $\mu\text{m}$ ) and extruded samples showing no apparent vesicle structures in the DLS spectrum. Again, this is likely due to the  $T_g$  of the lipid hindering the effectiveness of these methods. The application of the higher frequency tip sonication produced vesicles with an average hydrodynamic radius  $59 \pm 17$  nm. This suggests that, as with DSPC, the localised higher frequency is enough to reduce the average vesicle size considerably. Subsequent TEM analysis (Figure 4.2 b) confirmed that vesicles formed in the presence NaOH were had a good average size of  $83 \pm 18$  nm, but also revealed a large amount of lipid residue in the sample. It is possible that this is the result of degradation of the lipid during the tip sonication, which could be optimised (in terms of applied amplitude and sonication time) to avoid the destruction of the liposomes.

#### 4.2.2.3 DPhPC

DPhPC produced the most monodisperse liposomes by bath sonication alone. The DLS of the bath sonicated sample showed the average vesicle size to be  $124 \pm 12$  nm. This corresponds well to the TEM micrograph shown in figure 4.2 d), in which liposomes are had an average size of  $77 \pm 35$  nm. TEM also reveals consistent vesicle morphology throughout the sample, with all vesicles appearing highly spherical with a constant bilayer thickness of 3-4 nm. No further size control measures were performed on the DPhPC liposomes, as the sample produced by bath sonication was of a good enough standard. The major disadvantage of using this lipid for large scale artificial magnetosome synthesis is the high cost (\$1,100 per gram, Avanti polar lipids).

Whilst the liposomes produced were of a suitable size and morphology when compared to the other lipids tested, more of the cost effective lipids screened produced suitable vesicles than was expected (although perhaps with the addition of tip sonication/extrusion). Therefore the good monodispersity of DPhPC samples did not justify the high cost of using the lipid for large scale testing and synthesis.

Therefore this particular lipid was only used when the requirement for extremely stable vesicles with minimal processing is the case. This is the case when vesicles were required to incorporate proteins, where high quality vesicles are required with minimal post-formation modification to avoid displacing the bilayer proteins, or if other lipids fail in permeation of soluble iron.

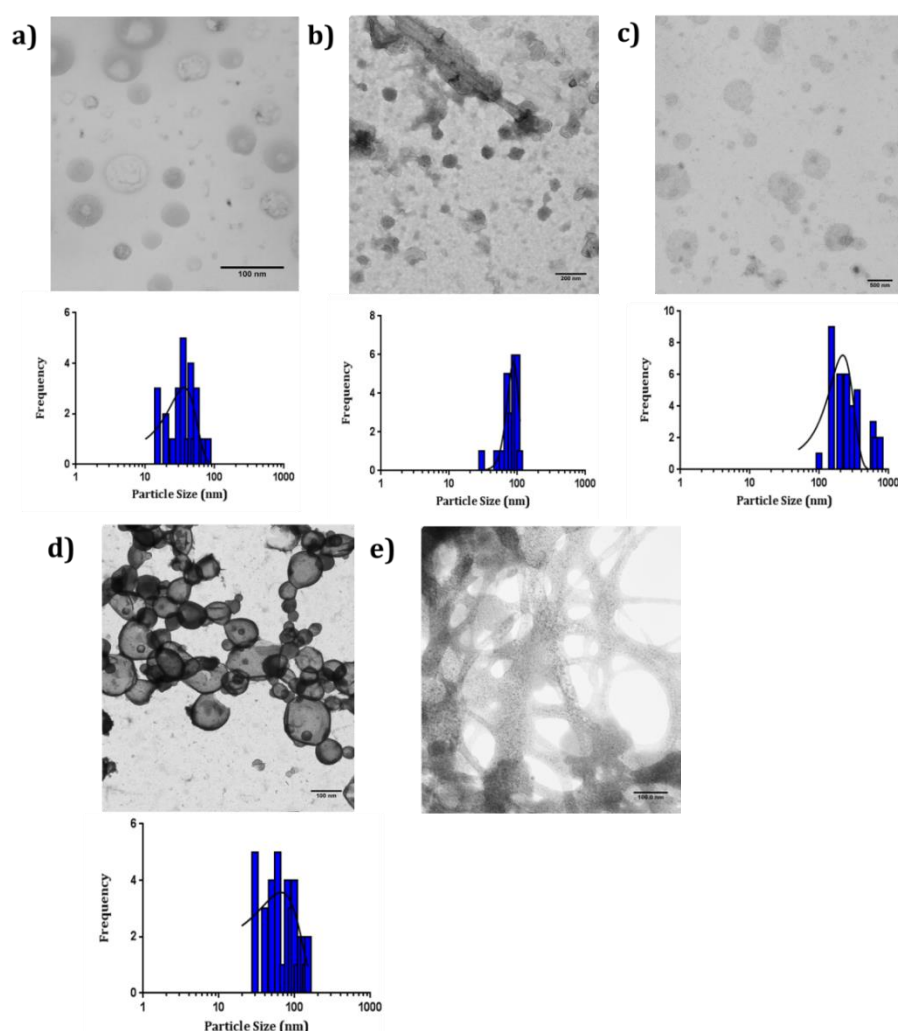


**Figure 4.2:** TEM micrograph of each liposome sample following formation with the best method as determined *via* the high throughput screening and the corresponding TEM grainsize analysis. a) DOPC liposomes *via* extrusion, b) DPPC liposomes *via* tip sonication c) DSPC d) DPhPC liposomes *via* bath sonication e) DPPE-PEG 5000 liposomes *via* tip sonication.

#### 4.2.2.4 DOPC

DLS analysis of DOPC vesicles formed using extrusion showed an average size of  $90 \pm 13$  nm, which is the most suitable vesicle size of all of the lipids tested. DOPC showed consistency in size of the species formed across all three formation methods: bath and tip sonication producing vesicle sizes of  $68 \pm 6$  nm and  $38 \pm 7$  nm respectively (Figure 4.1). DOPC may form vesicles more easily with all three methods, due to the high fluidity of the lipid bilayer. DOPCs low  $T_g$  proved much easier to work with overall, and it likely that this amenability made modification of the vesicle size with each technique easier. Whereas the higher  $T_g$  lipids, such as DSPC, were less responsive at ambient temperature, with a noticeable precipitate developing. TEM of the DOPC vesicles after extrusion showed a relatively monodisperse population with most vesicles between  $39 \pm 17$  nm (Figure 4.2 a). The vesicle morphology was highly consistent across the samples imaged, showing consistently spherical vesicles, particularly when compared to other lipids screened such as DPPC (Figure 4.2 b).

#### 4.2.2.5 DPPE-PEG 5000

DPPE-PEG 5000 vesicles formed *via* tip sonication gave the largest average vesicle size (as measured by DLS) to be  $252 \pm 27$  nm. This is not surprising, due to the attached PEG molecule which will affect bilayer packing and increase the overall vesicle diameter. As with DPPC and DSPC, bath sonication and extrusion had a detrimental effect on the vesicle size, with both showing much larger vesicle species, as  $2.7 \pm 0.9$   $\mu\text{m}$  and  $5 \pm 0.5$   $\mu\text{m}$  respectively. The PEG moiety is expected to be responsible for this, with bath sonication again not being a high enough frequency to affect the natural assembly size of the decorated lipid. Extrusion with a 100 nm membrane was probably not appropriate for such large vesicles, and appears to have had a detrimental effect on the vesicle size, with DLS analysis suggesting vesicles have increased in size. This peak in DLS spectrum is likely to be caused by large aggregations of lipid, as extrusion would not increase the overall vesicle size. TEM imaging of DPPE-PEG 5000 liposomes, revealed the formation of a lipid network (Figure 4.2 e).

The formation of this network is possibly the result of DPPE's high  $T_g$ . In order to verify if the sonication temperature could affect the formation of this network, DPPE was tip sonicated at a temperature of 65°C. TEM and DLS analyses indicate that vesicles were formed, suggesting that creation of vesicles at temperatures above the  $T_g$  is sufficient to prevent network formation.

### 4.2.3 LIPOSOME FORMATION DISCUSSION

All the lipids on which the formation and size control tests were repeated with NaOH as the encapsulant following the high throughput screen were successful to a relative degree. Each size control method defined as the most appropriate in these data presented in this section correlates with previous data obtained in the undergraduate project (see contributions page XV). Vesicles of a relatively monodisperse size distribution were obtained with all lipids, except for DPPE-PEG 5000. It was unexpected that TEM imaging would reveal such a high number of useable vesicle materials, therefore the DPhPC, which was predicted to be the most appropriate material was not cost effective enough to be used in in high throughput testing and high yield production of artificial magnetosomes. For the phospholipids, the majority of the DLS spectra indicated the presence of species at around the desired 100 nm size. There were a number of more cost effective materials to take forward, particularly with respect to high throughput synthesis. All lipids with the exception of DPhPC were further explored (in chapter 6) for their appropriateness as a nanoreactor for the precipitation of magnetite within the vesicle core.

## 4.3 POLYMERSOMES

Work in this section is taken from the publication Bain *et al*<sup>7</sup>

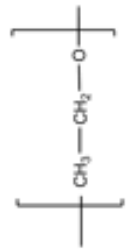
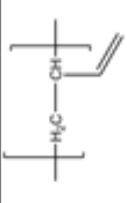
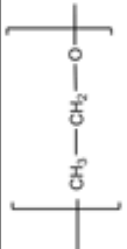
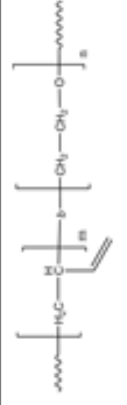
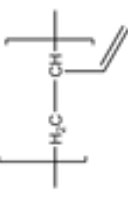
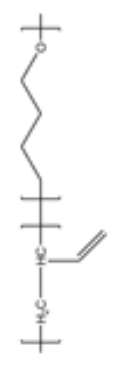
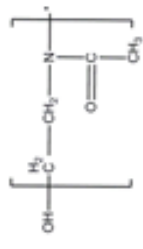
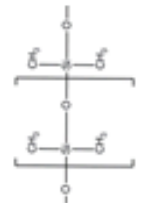
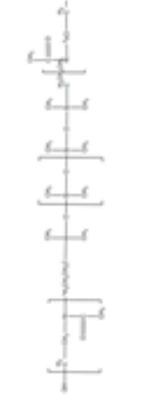
### 4.3.1 POLYMER PROPERTIES

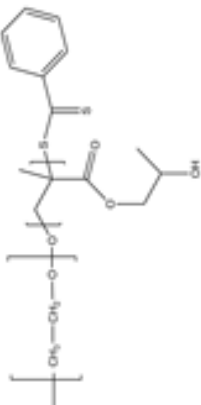
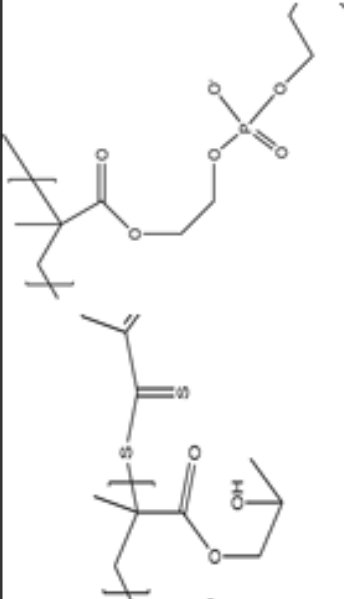
Section 1.4.3 describes how the use of polymers for vesicle engineering allows the incorporation of a wider range of properties appropriate for use in diverse applications. To address some of the issues encountered with lipids in section 4.2, such as robustness and stability, particularly with the DPPC and DSPC lipids which proved difficult to work with, a variety of polymers with a range of molecular weights, structures and functional groups were investigated.

These polymers are outlined in Table 4.3, with their selection explained throughout this section. Further reasoning includes the point that most of the polymers have their own distinct functionality to explore such as di-block versus tri-block structure, carboxylic acid end groups, and large variations in the polymer molecular weight.

The first polymer to be investigated was the amphiphilic A-B block copolymer, synthesised by the polymerization of ethylene oxide (PEO) and butadiene (PBD) monomers in separate block length of 2500 g mol<sup>-1</sup> and 1300 g mol<sup>-1</sup> respectively (low molecular weight) or 35,000 (PBD) and 15,000 (PEO) at high molecular weight. PBD-PEO was chosen as previous studies had shown the production of monodisperse unilamellar vesicles within the desired size range (50-200 nm) for this polymer system.<sup>99b, 108, 188</sup> PBD-PEO is a relatively simple polymer, with an unreactive non-polar block, which is unlikely to interfere with the transport of iron ions.

The polar block in the polymer is ideally suited for use in biomedical applications, where it could double up as a stealth coating, as it is already widely used in liposome engineering, delaying recognition *in vivo*<sup>71c</sup> without the need for functionalisation post formation. Two versions of this polymer were tested, each with varying block lengths. Block lengths has a direct effect on the overall packing factor of the polymer and the subsequent vesicle architecture (Section 1.4.3). Therefore, two extremes of both high (35,000-*b*-15,000) and low (2500-*b*-1300) molecular weight were investigated.

Polymer	Hydrophobic block	Hydrophilic block	Structure	Molecular Weight/Degree of polymerisation	Specific Functionality
Polybutadiene- <i>b</i> -Polyethylene oxide (PBD-PEO)				2500- <i>b</i> -1300	Low Mol. Weight
Polybutadiene- <i>b</i> -Polyethylene oxide (PBD-PEO)				35,000- <i>b</i> -15,000	High Mol. Weight
Polybutadiene- <i>b</i> -Polybutylene oxide (PBD-PBO)				16- <i>b</i> -22	Variation of head group
Poly(2-methyloxazoline- <i>b</i> -Poly(dimethylsiloxane)- <i>b</i> -Poly(2-methyloxazoline) (PMOXA-PDMA-PMOXA)				1700- <i>b</i> -4000- <i>b</i> -1700	Tri-block

<p>Polyethylene Glycol-<i>b</i>-Poly-2-hydroxypropyl methacrylate (PEG/PEO-PHPMA)</p>		113- <i>b</i> -400	Mms6 mimic
<p>Poly(2-methacryloyloxy)ethyl phosphorylcholine-<i>b</i>-Poly-2-hydroxypropyl methacrylate (PMPC-PHPMA)</p>		28- <i>b</i> -400	Mms6 mimic

**Table 4.3:** Shows the structure and properties of each polymer investigated for polymersome formation.

The packing factor of the low molecular weight polymer is on the theoretical boundary between the formation of vesicles and tubes (Figure 1.10). Therefore, by lengthening the hydrophobic block in particular, it is predicted that self-assembly will be driven towards the exclusive formation of vesicles. Another factor affecting the packing of the amphiphilic block co-polymers in the head group size (Section 1.4.1), therefore increasing the polar block of polyethylene oxide to polybutylene oxide (PBO) should affect polymersome size and possibly morphology. Thus, a PBD-PBO polymer was also selected for comparison. The PBD polymers tested were chosen following the work of Professors Antony Ryan, Stephen Armes and Giuseppe Battaglia who have extensively studied the chemistry, assembly and morphological behaviours of these polymers.<sup>20c</sup>

119

The other polymers were chosen because of their differing structures and specific functionalities, particularly the *A-b-B-b-A* tri-block polymer poly(2-methyloxazoline)-poly(dimethylsiloxane)-poly(2-methyloxazoline) (PMOXA-PDMS-PMOXA). This polymer has been extensively studied, largely by the group of Wolfgang Meier,<sup>9, 89a, 100</sup> due to its tri-block (*A-b-B-b-A*) composition. They have assessed polymersome formation, the polymer's permeability and polymerization properties. Several studies have provided proof of concept data for the use of the PMOXA-PDMS-PMOXA polymersomes as nanoreactors.<sup>9, 89a, 100, 189</sup> The discrete PMOXA-PDMS-PMOXA polymersomes has proven to be biocompatible and are thus the focus of research for exploitation in biomedical applications,<sup>98</sup> making them excellent vehicles for future theranostic applications.

70% PEG<sub>113</sub>-PHPMA<sub>400</sub>/30% PMPC<sub>28</sub>-PHPMA<sub>400</sub> polymersomes offers a different polymer assembly system for investigation. This polymer is produced through reversible addition fragmentation chain transfer (RAFT) synthesis, which is polymerisation induced by self-assembly (PISA). This work was performed in collaboration with Prof. Steven Armes group (University of Sheffield). The polymer system has been chosen to incorporate carboxylic acid groups exclusively on the inside of polymersomes (Figure 4.3). This acts as a mimic for the carboxylic acid rich magnetosome membrane protein Mms6 from magnetotactic bacteria,<sup>61</sup> which is believed to biotemplate magnetite nucleation and/or growth.

This system was designed so that the carboxylic acids would be preferentially displayed on the inside of the vesicle by control of the polymer lengths, with the smaller length acidic PMPC-PPMA chains favouring the inner bilayer leaflet (Figure 4.3).

Again, two variations of the polymersomes were investigated, with and without the addition of an ethylene glycol dimethylacrylate (EGDMA) cross-linker. Cross-linking should prevent trans-bilayer rearrangement (“flip-flop”); essentially ‘locking’ the chains in place to keep COOH groups on the inner leaflet of the polymersome.

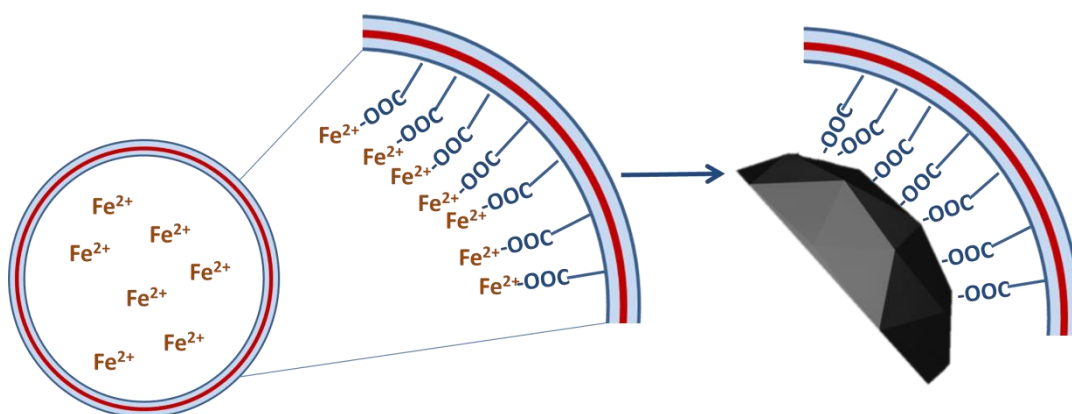


**Figure 4.3:** Schematic of the 70% PEG<sub>113</sub>-PPMA<sub>400</sub>/30% PMPC<sub>28</sub>-PPMA<sub>400</sub> system designed to mimic the nucleation of iron ions by Mms6 in the MTB magnetosome. The 70% PEG<sub>113</sub>-PPMA<sub>400</sub>/30% PMPC<sub>28</sub>-PPMA<sub>400</sub> polymersomes have been cross-linked with ethylene glycol dimethylacrylate (EGDMA) to promote the assembly of carboxylic acid terminated PMPC-PPMA exclusively on the inside of the polymersome. This assembly should then act as a mimic for acidic amino acids in Mms6, which are believed to bind ferrous iron and nucleate the controlled precipitation of magnetite.

### 4.3.2 POLYMERSOME FORMATION

A similar methodology to the lipid vesicle formation was applied (as described in section 4.2.2). Here generation of polymersomes encapsulating first neutral PBS and then secondly NaOH was used to test the formation method and then subsequently the ability to encapsulate high pH solution.

NaOH represents the highest pH that would need to be initially encapsulated, and therefore the most extreme conditions vesicle formation would have to withstand. As with the phospholipids, each of these polymer samples were formed using extrusion, bath and tip sonication. The outcome of this screening is outlined below (Figure 4.4).

#### 4.3.2.1 DI-BLOCK POLYMERSOMES

The di-block polymersomes were produced by rehydration and swelling of a polymer film. Although likely to have already formed, the polymersomes were then subjected to tip sonication to explore vesicle size control. For the three polymersomes; PBD<sub>2500</sub>-PEO<sub>1300</sub>, PBD<sub>35,000</sub>-PEO<sub>15,000</sub>, and PBD<sub>16</sub>-PBO<sub>22</sub>, polymer films were rehydrated with 10 mM NaOH, and initially stirred for 12 hours.

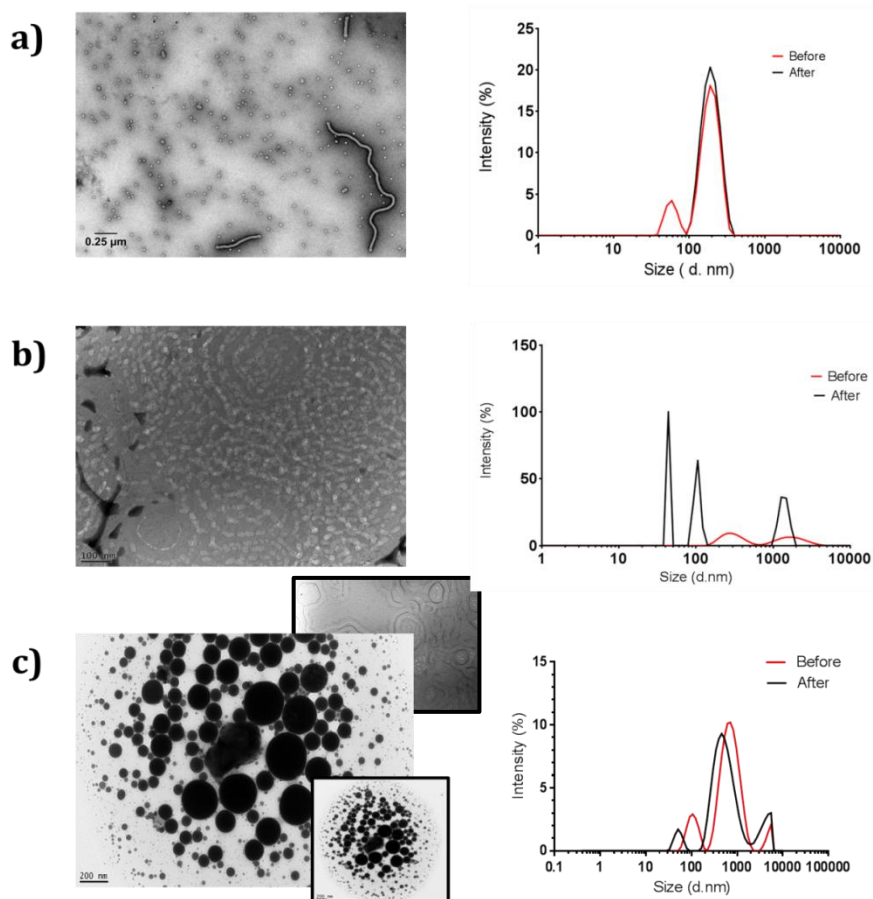


**Figure 4.4:** TEM micrographs for a) PBD<sub>2500</sub>-PEO<sub>1300</sub>, b) PBD<sub>35,000</sub>-PEO<sub>15,000</sub> and c) PBD<sub>16</sub>-PBO<sub>22</sub> polymersomes formed by tip sonication and the corresponding DLS population analysis taken before (red) and after (black) modification by tip sonication.

Following stirring, the polymersome samples were tip sonicated at 70 % amplitude for 30 minutes. The DLS analysis before and after sonication, and TEM images of the tip sonicated polymersomes are shown in figure 4.4. The low molecular weight PBD-PEO, produced the most discrete, monodisperse polymersomes with an average size of  $203 \pm 55$  nm (Figure 4.4 a). The sonication of the polymer sample had very little effect on the size of the polymersomes, with the only difference being a slight decrease in polydispersity, with an average size of  $203 \pm 45$  nm. This was not the case with the high molecular weight PBD-PEO, in which the tip sonication failed to produce discrete vesicles, instead forming a mixture of tubes and conjoined vesicles/micelles (Figure 4.4 b) These mixed morphologies are reflected in the DLS spectrum, with multiple species being detected giving an average size  $1.3 \pm 0.6$   $\mu\text{m}$ . The effect of tip sonication on the population was a general decrease in the size of the assemblies, but little improvement; or perhaps an increase of the population dispersity (Figure 4.3 b) but giving an average size of  $1.7 \pm 0.9$   $\mu\text{m}$ . Similarly, the third and final di-block polymer showed little improvement, although the TEM confirms the presence of only vesicle morphology (Figure 4.4 c). The DLS also showed multiple species are present with high polydispersity. The general populations in both the TEM and DLS analysis are much larger than desired, with an average size of  $893 \pm 353$  nm. Due to the poor quality of the high molecular weight PBD-PEO and PBD-PBO vesicles (Figure 4.3 b) and c), no further investigation was carried out on these polymers. Instead PBD<sub>2500</sub>-PEO<sub>1300</sub> was taken forward, due to its ability to form uniform, monodisperse vesicles, within the desired size-range produced by the simple film swelling and tip sonication techniques.

PBD<sub>2500</sub>-PEO<sub>1300</sub> polymersomes formed by film rehydration/swelling were compared to samples which had been further modified by extrusion through a 100 nm polycarbonate membrane. It was found that while extrusion produced a close to homogeneous population of  $41 \pm 6$  nm shown by TEM figure 4.5 a), and  $123 \pm 26$  nm by DLS (Figure 4.4. b). However, as this does require an extra processing step, which may not be necessary as simple stirring yields two populations of polymersomes. This first population is of  $100 \pm 9$  nm by TEM (Figure 4.5 a) and  $203 \pm 55$  nm by DLS, with the second population around  $43 \pm 4$  nm by TEM and  $58 \pm 6$  nm by DLS (Figure 4.5 b).

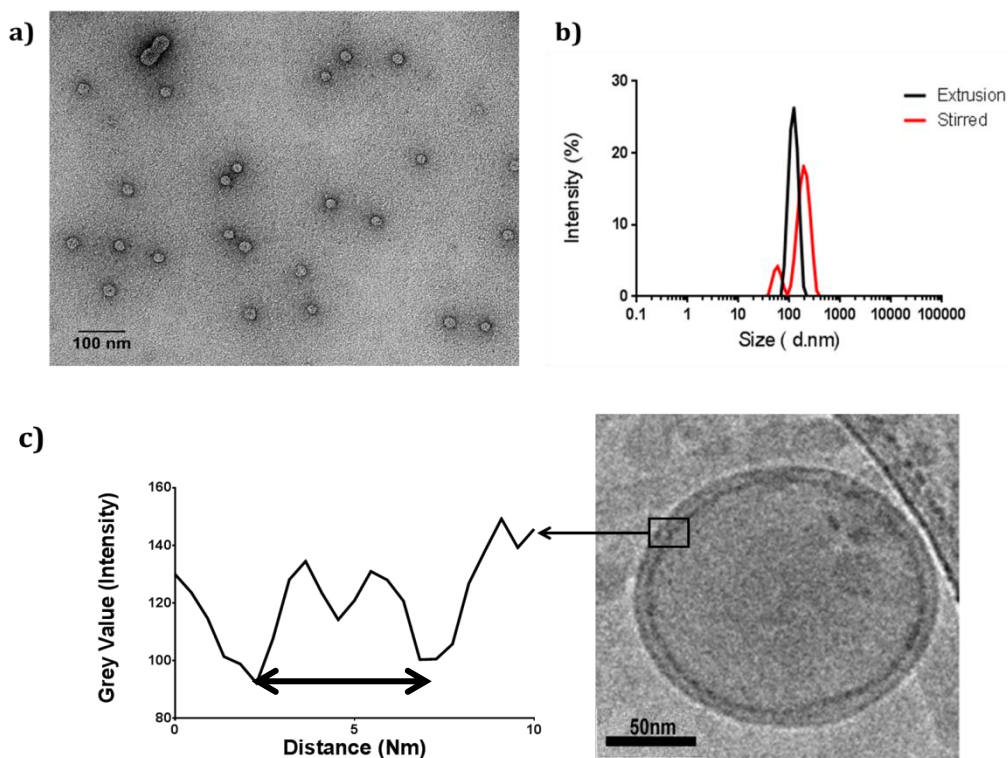


**Figure 4.5:** a) TEM micrograph of PBD2500-PEO1300 polymersomes after extrusion b) the corresponding DLS size analysis comparing the polymersome population difference between the stirred and extruded samples c) Polymersome bilayer measurement. Greyscale measurement of polymersome bilayer showing a thickness of 4-5nm, as measured on a cryo-EM image of the stirred polymersome sample.

The similar vesicle distribution achieved by stirring alone is indicative of the ease of processing possible with PBD<sub>2500</sub>-PEO<sub>1300</sub>. To fully confirm the PBD-PEO polymersome size, cryo-EM was also performed (Figure 4.5 c). This analysis doesn't generate the same deformations from staining and drying, showing a preserved membrane bilayer and a true size slightly larger than the corresponding stained TEM. However, cryo-EM is not a routine analysis, due to the time consuming and expensive nature required to prepare samples for this method. Therefore, cryo-EM cannot be performed on a large number of samples to produce accurate size distributions. Importantly, this analysis also revealed a polymer bilayer thickness of 4-5 nm (Figure 4.5 c) comparable to a naturally occurring lipid bilayers (approximately 5 nm).<sup>84</sup> Encapsulation of CO(NH<sub>2</sub>)<sub>2</sub> was also tested, which also produced polymersomes of an appropriate size distribution in the 100-200 nm range as shown in figure 4.6.

As PBD<sub>2500</sub>-PEO<sub>1300</sub> performed the best in the above experiments, all further tests on di-block polymersomes throughout this thesis were performed on PBD<sub>2500</sub>-PEO<sub>1300</sub>, and this polymer was the di-block example taken forward for further study and the main focus for the creation of a polymeric synthetic magnetosome.

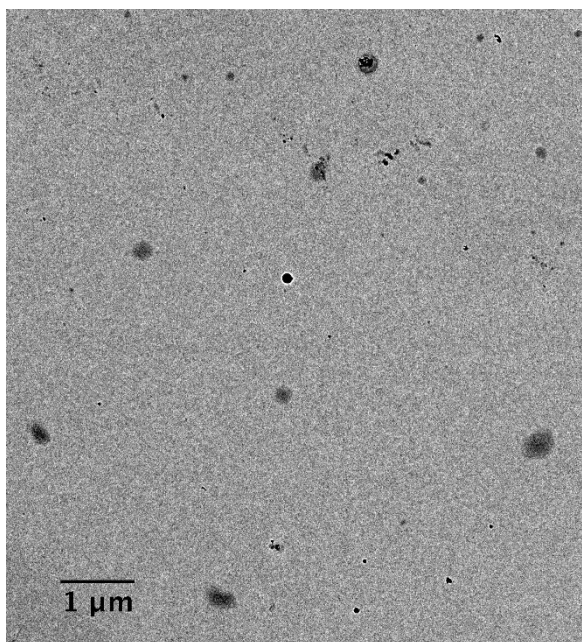


**Figure 4.6:** Negative stained TEM image of PBD<sub>2500</sub>-PEO<sub>1300</sub> polymersomes following encapsulation of CO(NH<sub>2</sub>)<sub>2</sub>.

#### 4.3.2.2 TRI-BLOCK POLYMERSOMES

Initially, PMOXA-PDMS-PMOXA polymersome formation was devised from the published method by Meier *et al.*<sup>9b, 89a</sup> In this method, the polymer is dissolved in ethanol at a concentration of 17 % by weight, followed by dilution to the critical aggregation concentration (CAC). Low solubility of the polymer and low volumes of the solvent made this method difficult to replicate. Therefore, the published method was adapted by dissolving the polymer in chloroform at a final concentration above the CAC of  $0.15 \times 10^{-3} \text{ g ml}^{-1}$  in water.<sup>9b</sup> Addition of aqueous solution at a rate of  $5 \mu\text{l min}^{-1}$  yielded phase separation between the aqueous solution and original solvent.

Isolation of the aqueous layer *via* centrifugation yielded a polymersome solution with an average size of  $45 \pm 6$  nm as imaged by TEM, (Figure 4.7 a) with the presence of some tubular structures (not included in the TEM grainsizing). The corresponding DLS data shows an average size of  $33 \pm 8$  nm and a polydispersity index of 0.5 (Figure 4.7 b) in agreement with the TEM data, and yielded a narrower dispersity than those previously published.<sup>9b</sup>

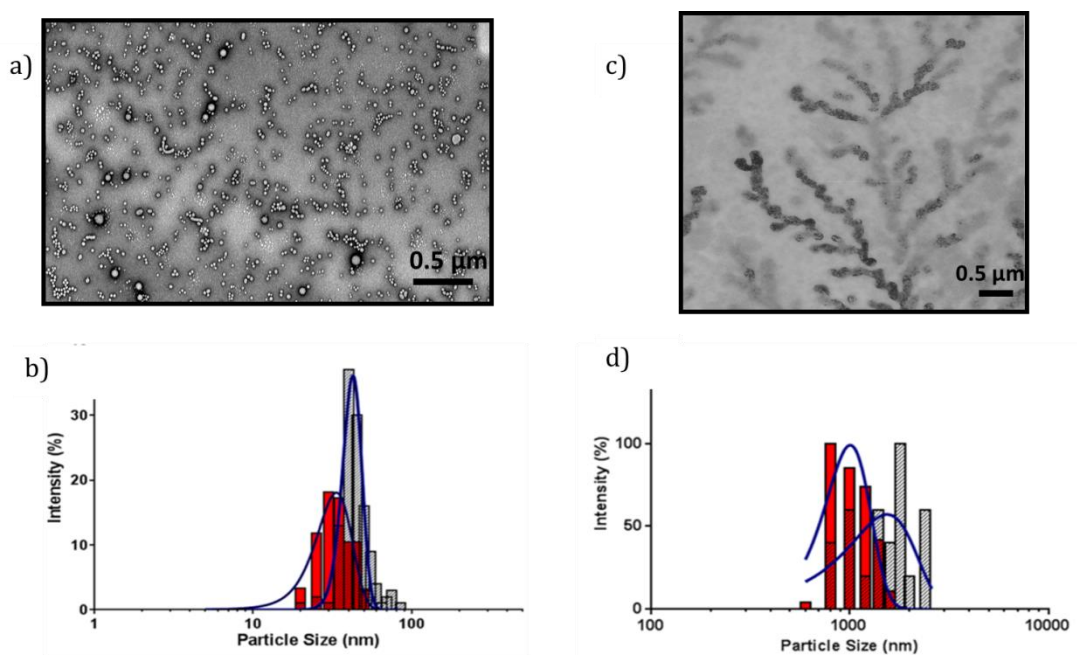


**Figure 4.7:** a) TEM of PMOXA-PDMS-PMOXA polymersomes sample produced *via* the adapted slow aqueous addition method. b) TEM of PMOXA-PDMS-PMOXA polymersomes produced *via* the previously published method<sup>9</sup> shows the presence of polymer networks c) Comparison of TEM (Grey bars) grainsizing and DLS (Red bars) sizing data show an average size of 45 nm compared to 32 nm respectively and a polydispersity index of 0.5. d) the corresponding TEM (Grey bars) and DLS (Red Bars) grainsizing showing an average size of 1.8  $\mu$ m and 800nm respectively.

When polymersomes were produced using method published by Nardin,<sup>9b</sup> (in which 17 % w/v polymer was dissolved in ethanol and which is the added dropwise to water whilst stirring) TEM analysis reveals large networks of interconnected polymer of approximately 1800 nm in length (Figure 4.7 b) or 800 nm as measured by DLS (Figure 4.7 d).

It is possible that the narrower dispersity obtained by the adapted formation route presented in this work, is a result of the slow addition of the aqueous solution. It is evident from figure 4.7 b) that the original synthesis route shows an extensive polymerisation of the polymer into a network.

This network formation is not observed with my novel method of PMOXA-PDMS-PMOXA polymersome formation, as the TEM images clearly show the presence of discrete vesicles (Figure 4.7 a). The biggest difference between the two synthesis routes was: firstly, the choice and volume of solvent used, and secondly the rate of addition of the aqueous solution. With a rate as slow as  $5 \mu\text{l min}^{-1}$  it is possible that vesicles are forming and being stabilised in dilute solutions, and so avoiding the further polymerisation or aggregation effects. Variation of the rate of addition from 5 to  $50 \mu\text{l min}^{-1}$  made very little difference to the overall quality of polymersomes. However, when the aqueous solution is added as one volume to rapidly dilute the sample, the large scale networks observed with Nardin's published method are again present. (Figure 4.7 c) <sup>87</sup> The PMOXA-PDMS-PMOXA concentration was varied from 5 mg to 10 mg but this did not appear to affect polymersome assembly.

#### 4.3.2.3 RAFT SYNTHESISED POLYMERSOMES

70% PEG<sub>113</sub>-PHPMA<sub>400</sub>/30% PMPC<sub>28</sub>-PHPMA<sub>400</sub> polymersomes were produced using RAFT polymerisation (reaction scheme in figure 4.8). This is the polymerisation of 2-hydroxypropyl methacrylate (HPMA) using a 4,4'-azobis (4-cyanopentanoic acid) (V-501) initiator and a 4-cyanopentanoic acid dithiobenzanoate (CADB) chain transfer agent.<sup>2</sup> The synthesis was carried out in water at 70 °C, with the HPMA block further polymerised by 2-(methacryloyloxy) ethylphosphorylcholine (PMPC). PMPC acts as both a macro chain transfer agent in the second polymerisation step and the zwitterionic, solvated hydrophilic block.<sup>2</sup>

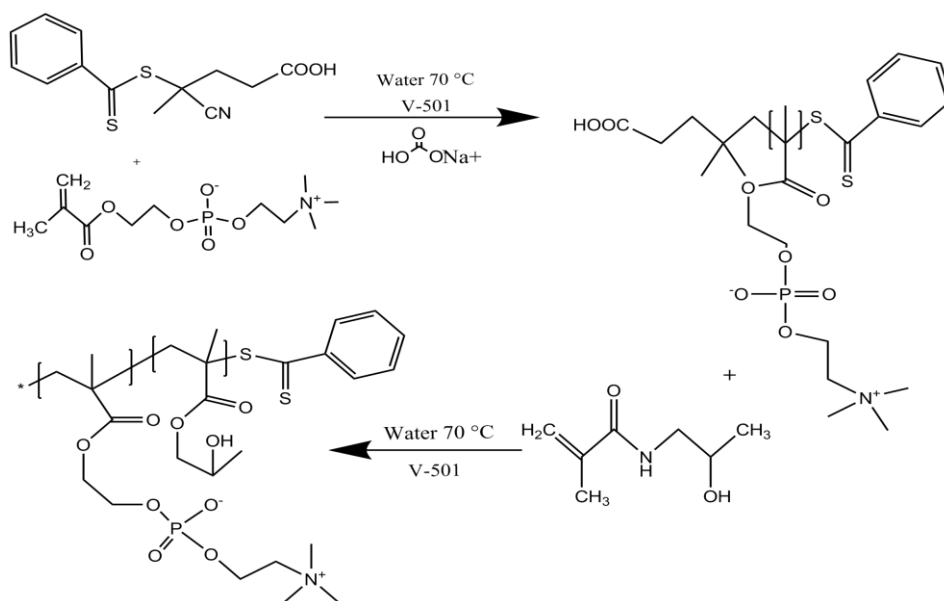


**Figure 4.8:** Synthesis route for the reversible addition fragmentation chain transfer (RAFT) polymerisation of PMPC<sub>28</sub>-PHPMA<sub>400</sub> in water at 70 °C using a 4,4'-azobis(4-cyanopentanoic acid) (V-501) initiator and 4-cyanopentanoic acid dithiobenzoate (CADB) chain transfer agent.<sup>2</sup>

It is this chain extension with PMPC that drives the self-assembly of the polymer, with PHPMA's degree of polymerisation dictating the eventual morphology. The nature of this synthesis, in which polymersomes are formed directly in the reaction, means the scheme is not open to modification, making it overall less flexible than other approaches. Therefore, polymersome size and quality is controlled by adaptation of the polymer synthesis conditions. To explore changes in morphology, two different PMPC polymers with varying degrees of polymerisation with respect to the PMPC blocks, were investigated. After formation both PMPC<sub>28</sub> and PMPC<sub>32</sub> polymersomes were soaked in NaOH to account for any shrinkage/swelling that may occur, so that the size can be accurately assessed.

The overall appearance of the vesicles with the PMPC<sub>32</sub> displays a more monodisperse size and consistent morphology (Figure 4.9 a). Whilst PMPC<sub>28</sub> still forms vesicles, there is a mixed population with the obvious presence of both vesicles and tubes of varying size (Figure 4.9 a). This is reflected in grainsize analysis of the polymersomes, giving high polydispersity with sizes ranging from  $246 \pm 137$  nm, compared to a narrow size distribution of  $79 \pm 24$  nm observed with PMPC<sub>32</sub> polymersomes (Figure 4.9 b).

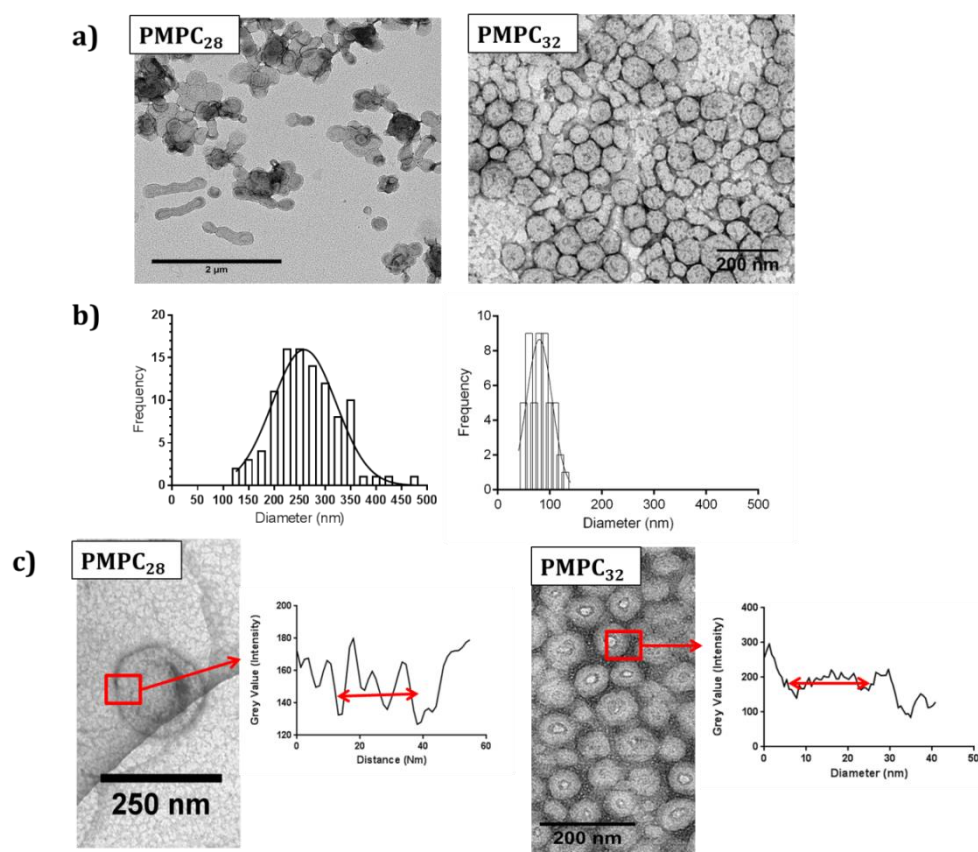


**Figure 4.9:** a) Comparison of the effect of variation of PMPC block length in PEG<sub>113</sub>-PHPMA<sub>400</sub>/30% PMPC<sub>28</sub>-PHPMA<sub>400</sub> polymersomes between PMPC<sub>28</sub> and PMPC<sub>32</sub>. b) The corresponding TEM grainsize analysis of polymersomes at the different block lengths. c) Highlight of the difference in bilayer thickness as a result of changing the PMPC block length.

However, when the structure of the polymersomes formed with both block lengths are more closely analysed with respect to bilayer thickness, the PMPC<sub>32</sub> block appears less suitable. Measurement of the thickness of the polymersome bilayer membrane reveals PMPC<sub>28</sub> is approximately 10 nm, two times thicker than a traditional lipid bilayer. Nevertheless, it is still comparative, having a similar hydrophobic/hydrophilic composition (Figure 4.9 c). The boundary layer of the PMPC<sub>32</sub> is a much wider, at 25 nm (Figure 4.9 c). This is likely to have a profound effect on iron ion transmembrane transport, decreasing the likelihood of full bilayer penetration by the iron ions. It is likely that the thicker the boundary layer, the less successful full penetration is likely to be. Furthermore, the increased thickness of the bilayer has the direct effect of reducing the inner core diameter.

This smaller core would result in a smaller MNP forming, even if the core is filled in the case of PMPC<sub>32</sub>. Therefore, although the appearance of the PMPC<sub>32</sub> block appears to make vesicles with the desired size and morphological characteristics, its bilayer thickness could hinder membrane transport, which is a major limitation for the creation of the nanoreactor. All subsequent investigations were carried out exclusively on polymersomes with a PMPC<sub>28</sub> block length, particularly as modification of the vesicle size and morphology is easier to control than bilayer thickness.

Synthesis of PEG<sub>113</sub>-PHPMA<sub>400</sub>/30% PMPC<sub>28</sub>-PHPMA<sub>400</sub> polymersomes is generally carried out at a pH of 3.5. As encapsulation of NaOH (pH 12) is required, polymersome synthesis was also carried out at pH 6.5, to minimise the impact of a pH switch by uptake of NaOH. Another alteration to the polymer synthesis was the introduction of an ethylene glycol dimethylacrylate (EGDMA) crosslinker, with the aim of locking the COOH end groups on the inner leaflet of the polymersome, to aid magnetite mineralisation. Finally, the samples prepared under each condition were tip sonicated, with the aim of further narrowing the dispersity of the sample population. The TEM micrographs of vesicles formed under each condition are shown in figure 4.10, negatively stained TEM images were analysed qualitatively to establish which methods are likely to produce vesicles with the most promising vesicle size and size distributions. Under the usual pH 3.5 polymersome formation conditions, tip sonication has a detrimental effect on the polymersomes, both with and without cross-linker. In this case, a network is formed, or polymerisation with the loss of discrete vesicles. On addition of the cross-linker at pH 3.5, the vesicle population is marginally improved with a decrease in the presence of tubes. Negatively stained TEM images were analysed qualitatively to establish which methods are likely to produce vesicles with the most promising vesicle size and size distributions (see figure 4.10).

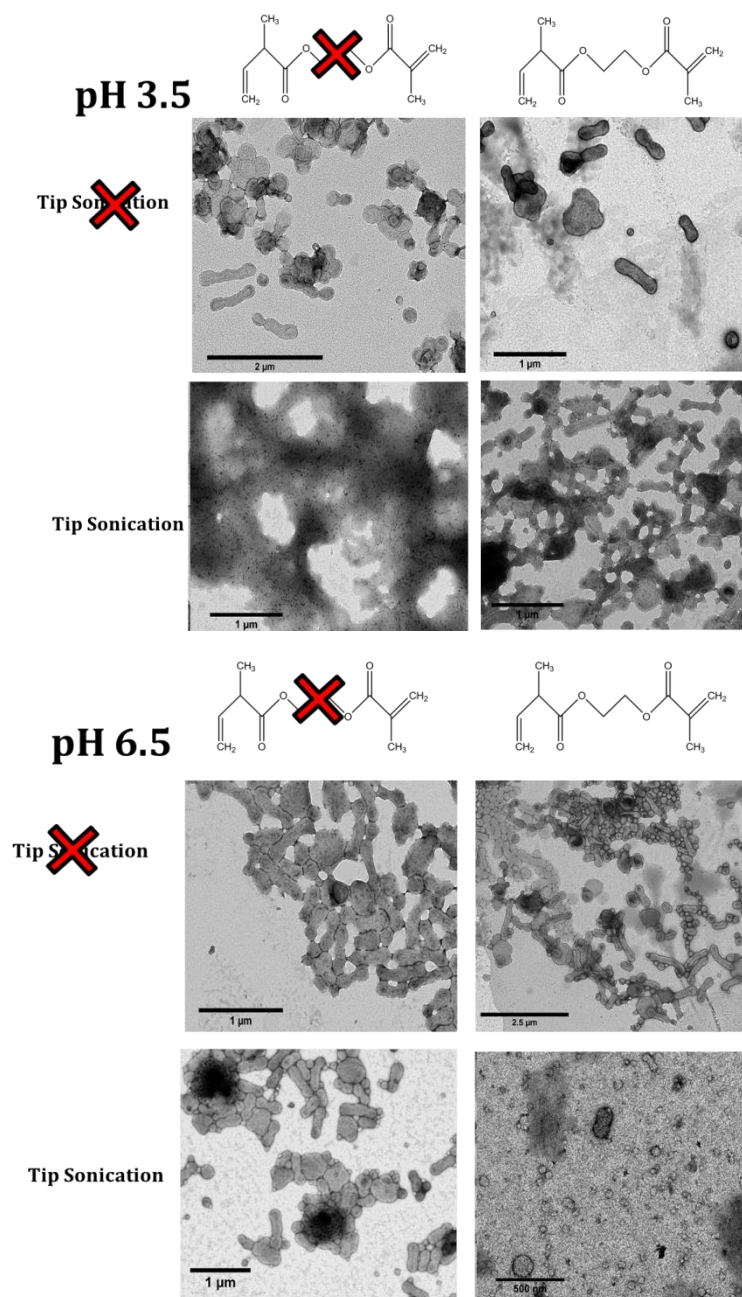


**Figure 4.10:** TEM micrographs of PEG<sub>113</sub>-PPHMA<sub>400</sub>/30% PMPC<sub>28</sub>-PPHMA<sub>400</sub> produced under different conditions. Top; pH 3.5 and bottom; pH 6.5. Under each pH condition polymersome morphology was compared between tip sonicated (Top row) and non-tip sonicated (Bottom row) samples. The polymersomes at each pH without (left column) and with (right column) the addition of a cross-linker are also compared.

In the absence of cross-linker, tip sonication significantly reduces the vesicle size; and again the presence of the EGDMA cross-linker changes the vesicle size, seemingly producing larger vesicles. This suggests that the cross-linker has a stabilising effect on the vesicles, allowing it to withstand the high frequency applied during tip sonication.

When the cross-linker is not present, the vesicles appear to be more easily broken up. This leads to a reduction in size upon re-assembly after sonication due the high frequency applied. Interestingly, the tip sonication does not seem to affect the presence of polymeric worms in the sample, as their formation arises from the hydrophobic/hydrophilic ratio in the polymer composition. Therefore, avoidance of tube formation would require further optimisation of the block lengths, rather than the formation method. Overall, the vesicles produced at pH 6.5 were much higher quality, particularly with the presence of the cross-linker.

At pH 6.5, discrete vesicles are observed in the TEM micrographs under each set of conditions (Figure 4.10). This was not the case for polymersomes synthesised at pH 3.5. Although, discrete vesicles can be seen in the unmodified polymer when tip sonication is applied, polymerisation or aggregation of the vesicles occurs. At low pH, the carboxylic acid groups on the end of the polymer will be protonated. This lack of charge repulsion may now promote polymer aggregation, which is further encouraged by the dis-assembly and re-assembly of polymersomes during tip sonication. Whereas, in the polymersome sample produced at pH 6.5, the carboxylic acids will be deprotonated, and so electrostatic repulsion between polymers occurs. Therefore all future experiments with respect to exploring membrane transport were carried out with polymersomes synthesised at pH 6.5, both with and without the EGDMA cross-linker.

### 4.3.3 POLYMERSOME FORMATION DISCUSSION

A wide variety of potential phospholipids and polymers are available. Thus, a systematic approach was taken to trial a range of polymer and lipid materials to assess their suitability for use as magnetite nanoreactors. Vesicle size, polydispersity and morphology were assessed at each stage, and materials were disregarded based on their results at each stage. The challenging nature of the magnetite precipitation reaction in addition to an ability to encapsulate basic solution and permit transmembrane transport of iron ions, either synthetically or *via* incorporation of MTB transporter proteins into its membrane is essential.

This means that a wide range of materials with varying composition, chemical properties (i.e. pH tolerance,  $T_g$ ) and molecular weight were investigated to obtain a suitable composition for design of a synthetic magnetosome.

All polymers tested were successful in that they are able to form polymersomes, although certain samples simultaneously formed worm-like tubular structures. The three di-block polymers tested formed polymersomes by basic film rehydration and further modification by tip sonication, to obtain low vesicle dispersion, without too much modification. Of the three di-block polymers tested, the low molecular weight PBD-PEO formed superior vesicles, of a much more appropriate size and polydispersity range  $101 \pm 9$  nm (TEM) and  $203 \pm 55$  nm (DLS), with the second population around  $43 \pm 4$  nm by TEM and  $58 \pm 6$  nm by DLS (Figure 4.5 b). The other two di-block polymers formed mixed morphologies and vesicles in the  $\mu\text{m}$  range, ( $1.7 \pm 0.9$   $\mu\text{m}$  for high Mw PBD-PEO and  $893 \pm 353$  nm for PBD-PBO) which are too large for the artificial magnetosome system.

The tri-block polymersome synthesis initially proved much more difficult to use to make appropriate polymersomes for nanoreactor formation. However, adaptation of the method produced appropriately sized vesicles with promising properties for use as a nanoreactor, particularly with respect to the mechanisms of transmembrane transport. The PEG<sub>113</sub>-PHPMA<sub>400</sub>/30% PMPC<sub>28</sub>-PHPMA<sub>400</sub> system proved extremely promising, particularly when synthesised at the higher pH of 6.5. This synthesis also provides less of a pH jump during the subsequent encapsulation of a basic solution. Therefore, only certain polymers were selected for further investigation, these being the low molecular weight PBD-PEO di-block polymer, as it formed robust monodisperse vesicles, with inherent biocompatibility (for the PEG molecule). The tri-block polymer also has potential following the development of an adapted formation method. It will be of particular interest to see how this polymer transports soluble iron, when compared to the more typical di-block bilayer compositions. Finally PEG<sub>113</sub>-PHPMA<sub>400</sub>/30% PMPC<sub>28</sub>-PHPMA<sub>400</sub> polymers, form well defined discrete vesicles of a good size and morphology under optimised conditions (formation at pH 6.5). These are also of particular interest due to their carboxylic acid functionality which should mimic the nucleation properties of biomineralisation proteins found within the MTB magnetosomes.

# **CHAPTER 5:**

---

## **BIOMIMETIC TRANSPORT SYSTEMS**

## 5.1 INTRODUCTION TO BIOMIMETIC TRANSPORT SYSTEMS

The proteins encoded in the Magnetosome Island (MAI) are pivotal to the successful formation of the MTB magnetosome (Section 1.3.2.1).<sup>42, 47, 190</sup> These proteins control each step of magnetosome formation: their size, shape, arrangement, the recruitment of iron, and the subsequent controlled precipitation of magnetite.<sup>47</sup> This chapter focuses on the proteins whose function is believed to be to the transport of iron across the magnetosome membrane and into the magnetosome lumen. The nucleation of the particle is controlled by proteins encoded within a specific gene cluster.<sup>42, 190</sup> These proteins are responsible for the high levels of homogeneity and distinct morphology of the particles, these proteins and their effects will be investigated in chapter 8.<sup>42, 47, 190</sup> The transport proteins outlined in table 5.1 are believed to act as antiporters, transporting ferrous ions into the core of the magnetosome, while pumping protons back out. As the protons are transported out of the core, the internal pH slowly increases. This increase facilitates the precipitation of a single magnetite crystal, which is mimicked in the artificial system by the encapsulation of solution at pH 10.

The functions of these proteins have been investigated by gene deletion experiments. Uebe *et al*<sup>52</sup> discovered, by gene deletion of *mamB* and *mamM* genes, that cross-membrane transport of iron is by way of a complex dimer. They believe that the transport protein MamB can only function in the presence of another protein, MamM. Deletion of both these genes together caused the  $\Delta mamB\text{-}\Delta mamM$  double mutant to exhibit a phenotypic loss of the magnetosome vesicle. This study is an excellent example of the control exerted by the proteins genetically encoded in the MAI. The structures of many of these proteins have been predicted from sequence analysis,<sup>47</sup> or the structure of soluble portions of the proteins have been determined by X-ray crystallography.<sup>47</sup>

As yet, the purification of these intact membrane proteins has not been achieved, which is probably due to their hydrophobic and water insoluble nature making the synthesis and purification of these membrane proteins extremely challenging. Membrane proteins require purification into detergent micelles, before reconstitution into a synthetic membrane, i.e. a vesicle.

The success rate of membrane protein purification in general is relatively low, due to the difficulty isolating the proteins from their native membranes and problems relating to protein mis-folding and low yields.<sup>173</sup> The successful cloning and expression of these genes will be invaluable for both the experimental confirmation of their predicted function and the formation of a fully mimetic artificial magnetosome. Incorporation of these proteins into the bilayers of the vesicles optimised in chapter 4 will confirm their function and allow for the selective and continuous transport of iron ions into the vesicle core. Due to the difficulty of their purification, it was decided that to investigate proteins exclusively from the magnetosome would further limit the experiments success. Therefore, this chapter looks at both MTB proteins believed to act as transporters in the magnetosome, but also homologues of these proteins from elsewhere in the MTB genome believed to have iron transporting function (Table 5.1).

## 5.2 BACTERIAL IRON TRANSPORTERS

Seven membrane proteins were chosen for investigation, (table 5.1) as previous studies have identified these proteins as potential iron transporters.<sup>47, 52, 53b</sup> Antiporters are a group of proteins which generally span a membrane; allowing movement of ions and protons across the membrane to maintain the osmotic pressure and dissolved ion concentration. In the case of MTB transporters, they are believed to take up iron ion from the magnetosome exterior and carry them across the membrane, subsequently collecting a proton and transporting it out of the magnetosome.<sup>39d</sup>

In the case of MTB transporters they are believed to take up iron ions from the magnetosome exterior and carry them across the membrane, while simultaneously transporting a proton out of the magnetosome. Mutagenesis studies have been carried out on some of these genes to determine their function. Mutagenesis experiments have suggested that the proteins act as antiporters, and in the case of MamMB and FeOA/B functioning as dimer complexes.<sup>52, 191</sup>

<b>Protein</b>	<b>Size (aa)</b>	<b>Isoelectric point</b>	<b>Transmembrane Helices</b>	<b>Effect of gene deletion</b>
FeOA	106	9.68	2	No Iron transport
MamB	296	5.35	3	No Magnetosome
MamM	318	5.88	3	No Crystal formed
MamO	637	6.50	8	Empty magnetosome
MagA	434	9.86	11	Empty magnetosome
MamN	437	6.59	11	Empty magnetosome
FeOB	706	5.12	15	No Iron transport

**Table 5:** Transporters investigated in this chapter and the associated properties of each protein<sup>47</sup>

With the exception of FeOA and FeOB (which are found in the cell membrane), all other transporters investigated here are believed to sit in the magnetosome membrane.<sup>47,53</sup> In all cases however, they show high hydrophobic content and the presence of multiple transmembrane helices (as shown in the hydropathy plots in figure 5.1). The presence of a high number of transmembrane helices (with proteins MamN, MagA and FeOB having 11-15 helices);<sup>47</sup> will likely make them highly insoluble and a challenge to successfully purify. It is likely that the high number of transmembrane helices will mean correct insertion into a synthetic bilayer extremely difficult, relying on both correct folding of all helices and simultaneous insertion of up to 11 transmembrane helices into a bilayer in the correct orientation for the protein to function.

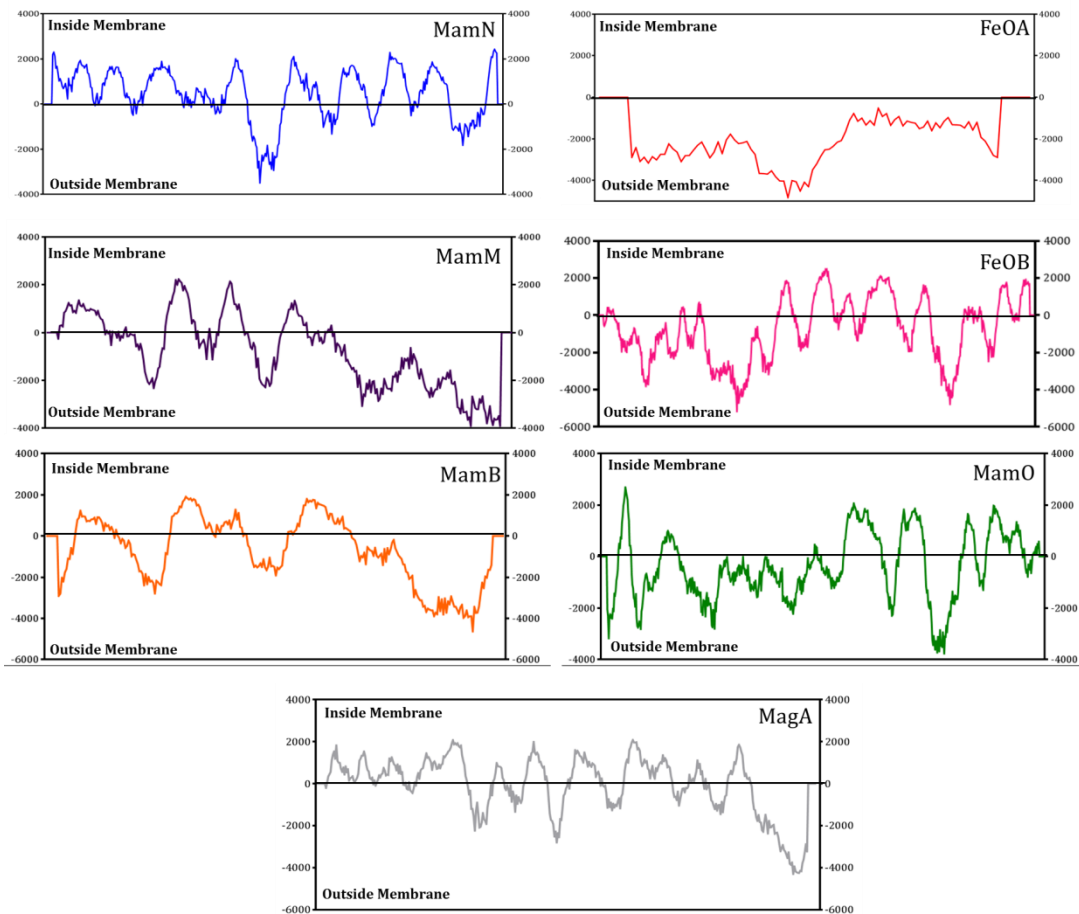


**Figure 5.1:** Hydropathy plots for each of the seven MTB transporters investigated throughout this chapter indicating the number of transmembrane helices and associated insolubility in each membrane protein structure.

Also, the proteins investigated that have been shown to function as heterodimers will likely need both partners present to be stable and active. MamMB and FeOAB form dimer complexes<sup>47, 52, 191</sup> and so must be co-expressed. This means that the genes (which will be cloned in separate PCR reactions) must then be ligated into the same vector in the correct order and orientation for successful dimer production.

## 5.2.1 CLONING OF IRON TRANSPORTERS

Genes encoding the various iron transporters were amplified from *Magnetospirillum magneticum* AMB-1 DNA by PCR using site specific primers (see section 2.6.1.1) into XL10 gold *E. Coli* cells. Cells colonies were harvested and incorporation of the desired target gene was confirmed by DNA sequencing (Beckman Coulter).

### 5.2.1.1 MAGA

MagA has previously been characterised by Nakamura *et al*<sup>53</sup> and was found to have iron transport functionality in the formation of the MTB magnetosome. The found that MagA possesses a sequence homologous to a potassium transporter (KefC) found in *E. Coli*.<sup>53</sup> The *magA* gene was amplified by PCR and subsequently digested using restriction enzymes *NheI* and *PstI* (N terminal) or *AvrII* and *SbfI* (C-terminal) depending on the required destination vector (encoding either an N or C terminal His<sub>8</sub> tag).

Analysis by gel electrophoresis (section 2.7.4.1) revealed that *AvrII* was unsuccessful in digesting the DNA (Figure 5,2). Therefore, sequential digestions with the enzymes were performed. This product (and the *NheI/PstI* digested product) was ligated into pBRNHT or pBRCHT vectors previously cut with the same restriction enzymes. These ligated plasmids were introduced into XL10 *E. coli* cells and colonies were allowed to develop overnight on LB-Agar in the presence of carbenicillin. When colonies were subject to DNA sequencing, the *magA* gene was not present. This result suggested that the colonies comprised empty vector only. The molecular cloning process was then repeated with alternative primers encoding *BsaI* restriction enzyme sites for insertion into pPRIBA1 vector. The outcome of this optimised PCR is shown in figure 5.2 a), and shows a DNA product of approximately 2000 base pairs when compared to the molecular weight marker (Massruler (Life Technologies) believed to be the MagA gene (as shown by the band in the right hand lane of the gel electrophoresis). After digestion with *BsaI*, the *magA* gene was ligated into the pPRIBA1 vector (previously cut with *BsaI*) and transformed into XL10 gold cells.

Ten colonies were selected and their plasmid DNA extracted. Colony PCR with the *magA* specific primers was used to confirm to presence of the *magA* gene. DNA gel electrophoresis analysis of these products showed that six of the ten colonies contained the desired gene. (figure 5.2 b). Colony ten (figure 5.2 b) which gave the most intense band was subsequently transformed into BL21 (DE3) *E. coli* cells for protein production (section 5.2.2).

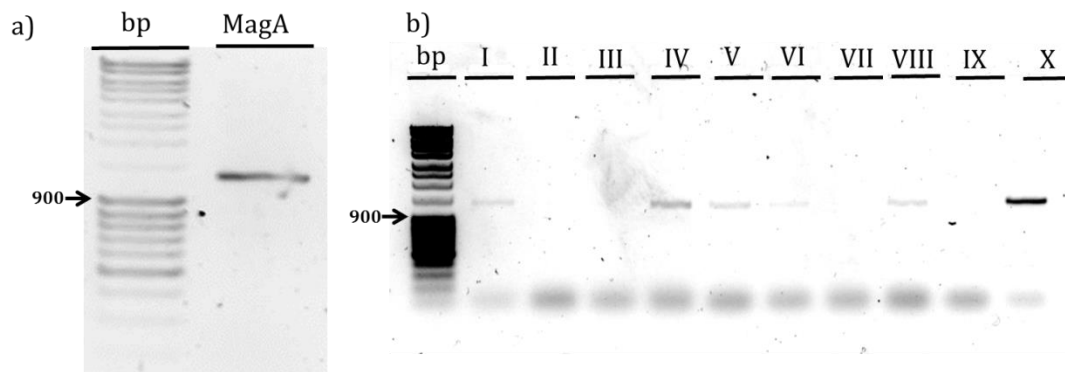


**Figure 5.2:** a) Gel electrophoresis of *magA* PCR product showing a single band at approximately 2000 base pairs. b) Colony PCR results of the same DNA product with 6 of the 10 colonies showing DNA present, again at 2000 base pairs; the colonies have varying concentrations (indicated by band intensity), with colony 10 being the highest, and therefore used in protein expression trials.

### 5.2.1.2 MAMMB

The magnetosome proteins MamM and MamB have been shown to form a heterodimer, present and highly conserved in all MTB.<sup>52</sup> MamB facilitates iron transport and magnetite mineralisation, and is stabilised by the presence of MamM.<sup>52</sup> MamB has been shown to play a pivotal role in MTB biomineralisation, functioning as an iron transporter, but also interacting with other magnetosome proteins.<sup>52</sup> Uebe *et al.* have reported the unusual interplay in this dimer complex, particularly how the deletion of MamB results in the complete loss of the magnetosome.<sup>52</sup>

Whereas the deletion of MamM results in only loss of the magnetosome crystals homogenous crystallinity, instead forming polycrystalline particles.<sup>52</sup> Two hypotheses are presented for the role of MamM in the dimer; the first being to protect it from proteolytic degradation, while the second suggests a role in MamB folding to ensure functionality.<sup>52</sup>

A different approach to that described in section 5.2.1.1 was taken to the production of the MamMB complex. In this instance, a synthetic gene sequence was used based on the combined sequences of MamM and MamB. It was thought that expressing a single gene product, which allows co-translation of the two proteins simultaneously, would be more likely to lead to a successful protein complex. The synthetic gene was designed so as to read the sequence of MamM followed by the MamB sequence, with production of each indicated by the usual start and stop codons found in the natural genes. Between the two open reading frames is a ribosome binding site to allow efficient translation of the second sequence. The *mamM* sequence also encodes a C-terminal His<sub>6</sub> tag, and the *mamB* sequence encodes a C-terminal StrepII tag. This differential tagging allows for separate detection of each protein of the complex individually. The synthetic gene was amplified by PCR. The PCR product was then digested with *BsaI*, the sites for which had been previously engineered into the synthetic gene. The cut PCR product was then ligated into a similarly cut pPRIBA1 vector and then introduced into XL10-Gold cells.

Digestions and ligation were repeated several times and, despite optimisation of the various steps, introducing a heat inactivating step into the ligation process and using different preparations of vector, no colonies formed following transformation into XL10 Gold cells. To circumvent these issues, blunt end ligation was used to insert the PCR product into pCR Blunt vector (Life technologies, in which the lack of insert yields a toxic gene preventing cell growth). This generated colonies containing the DNA product represented by the bands in figure 5.3 a), confirming the presence of a DNA product at 3000 base pairs presumed to be MamMB.

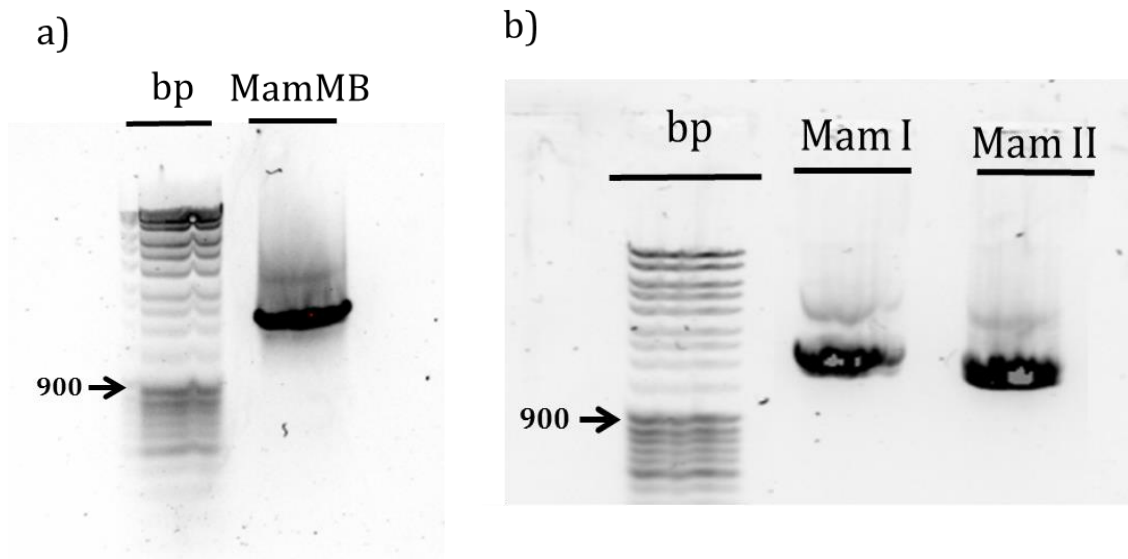


**Figure 5.3:** a) Gel electrophoresis of *MamB* cloning PCR product from a synthetic gene showing two bands at approximately 2000 and 3000 base pairs, believed to be *mamB* and *mamM* respectively. b) Shows the consequent colony PCR results of the same DNA product for the two colonies chosen with DNA products present again at 2000 and 3000 base pairs; the bands have varying intensities indicating that MamB is in relative excess.

A colony PCR of the *MamMB* product gave limited success, with only one of the four colonies collected giving a protein band which by the size (given by the band position on the gel) is deemed to be *MamMB*, following characterisation of the DNA by gel electrophoresis (Figure 5.3 b). Two bands at approximately 2000-3000 base pairs and 3000-4000 base pairs were observed, the exact size of the bands are hard to distinguish due to poor separation of the mass ruler bands. The presence of two bands confirms that that both pieces of DNA have been successfully cloned, with *mamB* at a much higher concentration (bottom band) than *mamM*. Again, sequencing of the colony PCR given by the band in lane I of Figure 5.3 b) confirmed that the plasmids did in fact contain the *mamMB* construct.

## 5.2.2 EXPRESSION OF IRON TRANSPORTERS

The seven transporters in table 5.1 were included in an expression trial to obtain optimised conditions for maximum expression of the membrane proteins. In the case of MagA, MamM and MamB, the DNA plasmids obtained in section 5.2.1 were used.

The other targets were provided already cloned into expression vectors by Dr. Andrea Rawlings (Staniland group). MamN was not included in the expression trial as several attempts to generate colonies in BL21 (DE3) cells were unsuccessful, with no colonies being present after 18 hour plate incubation at 37°C. This could be due to degradation of the DNA stock, or potential toxicity to *E. coli* from the encoded gene. The success of the other six did not warrant repeating the cloning of MamN from bacterial DNA. In the case of each of the other proteins, the plasmid DNA was extracted from XL10 Gold cells and introduced into BL21 (DE3) *E. coli* cells following clean-up. Colonies were grown on agar plates and added to starter cultures which were grown for 6-8 hours. These starter cultures were used to inoculate LB, 2YT, TB (Terrific broth) and SB (super broth) media cultures and grown for 24, 40 and 48 hours at 37 °C. Following incubation, cells were chemically lysed to degrade the cell wall and the proteins denatured using guanidine.

Protein detection using dot blot analysis was used to determine the presence of the correct protein (by antibody/tag recognition) and qualitative determination of the relative protein concentration produced under each condition. Each target protein was detected using HRP labelled anti-Strep tag antibodies as described in section 2.7.4.2. The results of expression for each target under each condition are shown in the dot blot in figure 5.4. a). All six proteins expressed under at least one of the conditions tested, although the concentration of the proteins (given by the intensity of each spot) differed quite significantly.

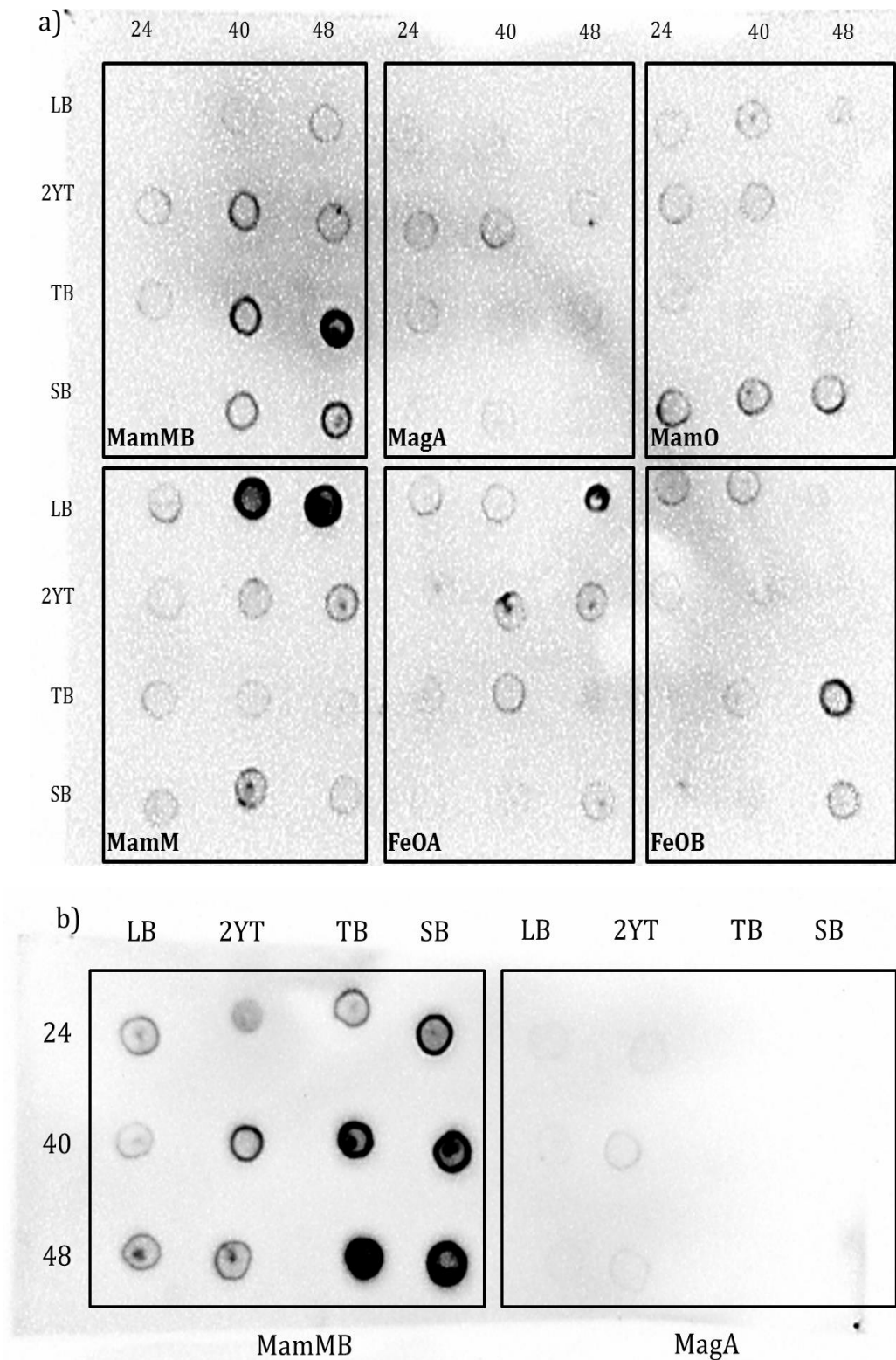


**Figure 5.4:** a) A dot blot for optimisation of each the growth condition of each of the six transporters (MamN was omitted) expression levels were analysed from growth in four different media ( LB, 2YT, TB and SB ) with protein concentration analysed after 24, 40 and 48 hour growth periods, detection of the proteins was using a strep tag specific antibody. b) Both MagA and MamMB both have His6 tags, therefore detection was carried out for these two samples using a His6 tag specific antibody.

While FeOA produced relatively high protein concentrations in LB auto inducing medium after 48 hours its counterpart FeOB did not give the same levels of expression. As the literature demonstrates these proteins need to be used in conjunction with one another<sup>191</sup> as FeOB is believed to be the transporter in the FeOA/FeOB complex analogous to MamMB, therefore it can be deemed inadequate to express and purify FeOA if the same levels of production cannot be reached by FeOB. On this basis, neither protein was carried further. The highest expressing targets in figure 5,4 b) are MamM and MamMB (synthetic gene), with MamM the highest in LB after 40-48 hours incubation and MamMB in TB after a 48 hour growth period. Although it was interesting to confirm that MamM can be produced without its partner MamB, it was not possible to singularly clone MamB to fully confirm the findings presented in Uebe *et al.*<sup>52</sup> MamMB produced extremely high intensity spots in multiple conditions (possible due to its codon optimisation) and therefore was the priority target for purification.

The least abundant protein was MagA, which (section 5.2.1.1) had low or undetectable expression levels with each growth medium, even after the maximum time point of 48 hours. In 2YT medium after 40 hours, there was a detectable signal; however it was not high enough compared to the other targets to warrant further investigation. MagA also has an octa-histidine tag sequence, modified sequence which can then be detected using an antibody which recognises a His<sub>5</sub> sequence. Protein expression using His<sub>5</sub>-tag detection are shown in figure 5.4 b). The dot blots showed the presence of protein but at extremely low levels, therefore it was decided not to try and purify MagA. This was also the case for MamO, again protein was detected at extremely low concentrations, although grown in super broth this concentration was higher, it was determined to be too low compared to the expression levels of other proteins tested.

### 5.2.3 TRANSPORTER PURIFICATION

MamMB was produced in TB for 48 hours in a larger volume (2.4 L) to ensure a sufficient yield for membrane harvesting. Cells were harvested by centrifugation at 4,000 x *g*. Membranes were isolated from the cell pellet by first disrupting the cells (using a cell disrupter to lyse the *E. coli*).

The cells were subjected to centrifugation to pellet the cell debris. The supernatant was collected and the cell membranes isolated by ultra-centrifugation (100,000 x *g*, for 1 hour). The membranes were then suspended in resuspension buffer (PBS + 20 % glycerol) and frozen at -80°C. The isolated membranes were then thawed and dissolved in PBS supplemented with 1% DDM detergent, before insoluble material was removed by ultracentrifugation as before. The solubilised membranes were mixed with streptactin resin and purified *via* the StrepII tag on MamM. Following competitive elution by desthiobiotin, the protein was applied to a nickel resin and purified *via* the His<sub>8</sub> tag on MamB. The presence of the complex in the eluent following both purification steps was confirmed by detection on a Western blot using both streptactin-HRP (for MamM) and anti His<sub>5</sub> antibody (for MamB) in parallel (Figure 5.5). The blot shows that MamB (figure 5.5, left) and MamM (figure 5.5, right) are both present confirming that they have assembled into a complex.

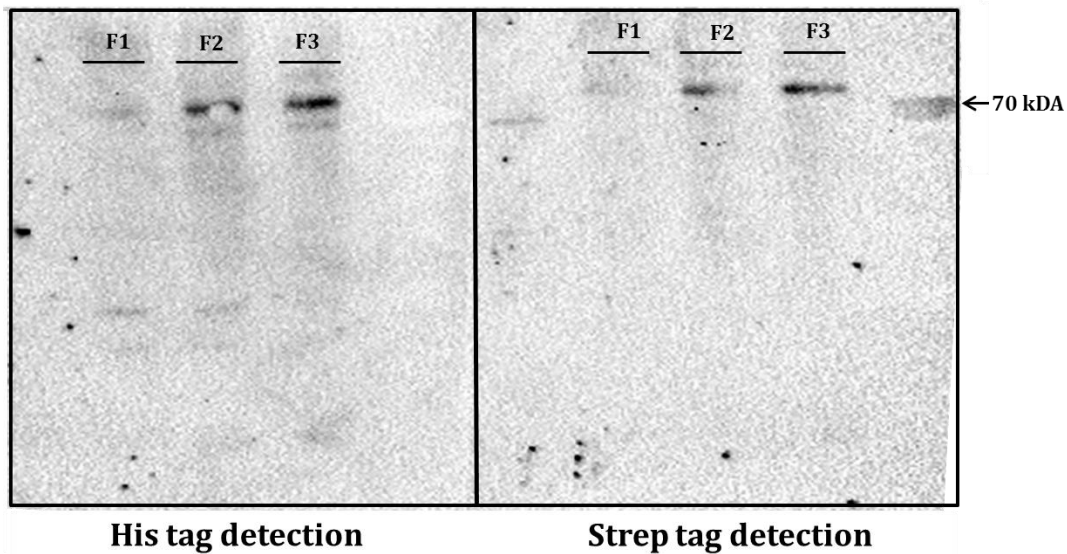


**Figure 5.5:** MamMB protein after affinity purification was analysed using a Western blot. The presence of protein was detected using a histidine specific antibody for detection of MamB (left) and a streptactin specific antibody for detection of MamM (right). This individual tagging made detection of both proteins possible from a single column fraction.

## 5.2.4 INCORPORATION INTO VESICLES

The detergent micelles containing MamMB were combined with pre-formed DPhPC lipid vesicles with the addition of Bio-beads. The presence of the Bio-bead in the solution should disrupt the detergent micelles, causing their dissolution and subsequent incorporation of MamMB into the DPhPC lipid membrane. To aid incorporation, the system was incubated for 12 hours at 4°C. Following removal of the Bio-beads (by centrifugation) the DPhPC liposomes were mixed with a ferrous and ferric iron solution combined at the stoichiometric ratio to investigate iron transport into the vesicle. This would serve to both confirm incorporation of the protein into the lipid membrane and its activity as a transporter. Unstained TEM micrographs of the liposomes after the incubation period (Figure 5.6) did suggest the presence of iron oxide in and around what is presumed to be the DPhPC liposomes (due to their highly spherical morphology).

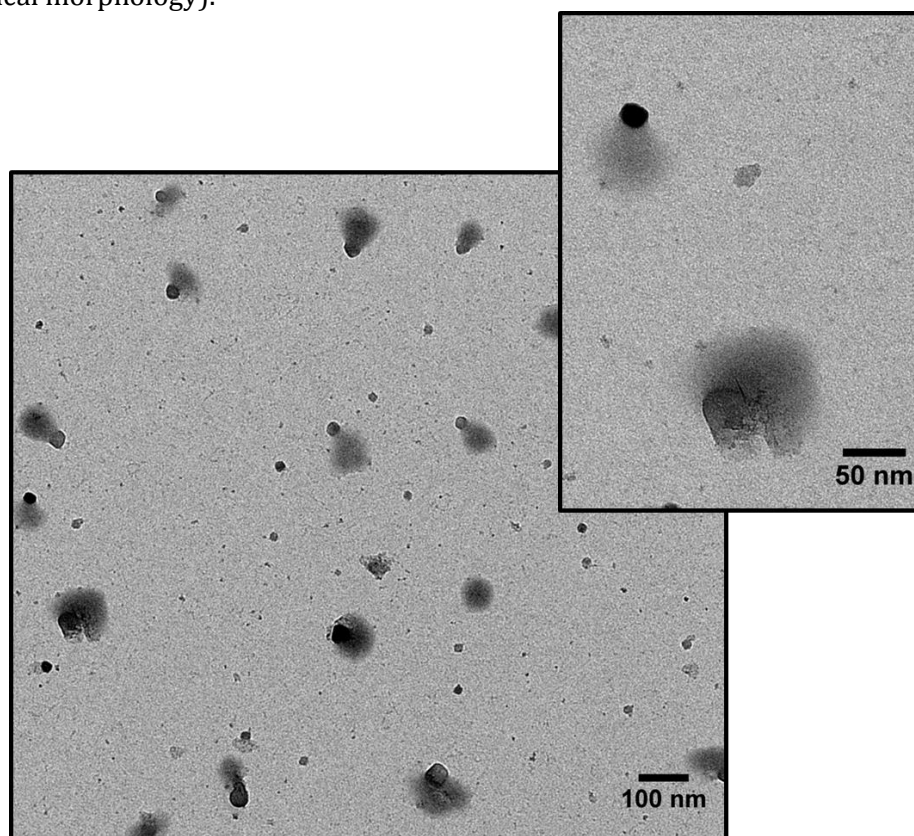


**Figure 5.6:** TEM micrographs of DPhPC/MamMB liposomes mixtures after incubation in a ferrous and ferric ion mix solution (At the stoichiometric ratio for magnetite precipitation).

A unique feature on many of the liposomes looks to be iron ion accumulation, suggesting the localisation of the transporter on or in the liposomes. However it is clear that this accumulation is not in the core of each vesicle, looking to be located in or on the bilayer (which cannot be seen due to poor contrast). This is common between all species in the sample, appearing to all have a single accumulation (presumed to be of iron) on one side of the vesicle. This suggests that the transporter is accumulating soluble iron but is failing to transport it into the vesicle. Other micrographs (not shown) suggested disruption of the DPhPC liposomes by the detergent, suggesting that both the type of detergent and the detergent removal process needs to be better optimised. From the analysis conducted so far it is difficult to ascertain if the MamMB complex has been incorporated in a functional state within the vesicle membrane. Some of the vesicle species within the micrographs do suggest some localisation of the protein to the liposome bilayer, as shown by the accumulation of metal ions. However, further confirmation is required. An ideal method would be to introduce a fluorescent label onto the protein to visualise any potential co-localisation of the protein to the vesicle.

### **5.3 IONOPHORE IRON TRANSPORT**

Ionophores are lipid-soluble molecules synthesised by microorganisms for the transport of ions across a cell membrane. These come under two classifications: compounds that bind to a particular ion, shielding its charge and facilitating its crossing of the lipid membrane, and ionophores which form channels or hydrophilic pores in the membrane, to allow ion transport. Ionophores can increase membrane permeability to certain ions.

#### **5.3.1 A23187 INCORPORATION INTO POLYMERSOMES**

The divalent cation ionophore, A23187, is a carboxylic acid known to carry ferrous ions across a bilayer membrane.<sup>167a</sup> This was used to test polymer membrane permeability to biological moieties and transport of iron ions in to the polymersome core.

The ionophore can carry various divalent ions, having been shown to transport both calcium and magnesium from an aqueous to an organic phase.<sup>167</sup> *In vivo* this is used to maintain divalent concentration across membranes in rat liver mitochondria. A23187 works *via* exchanging carboxylic acid protons for cations, by dissociation of the proton associated to the molecules carboxylic acid groups. Two ionophore molecules are required for the complexing of a single divalent cation, (i.e. a carboxylic acid group for each charge on the cation).<sup>167b</sup>

Three polymers were screened which had previously been shown to be effective as a nanoreactor (Chapter 4). These were the di-block polymers PBD-PEO and PEG<sub>113</sub>-PHPMA<sub>400</sub> / PMPC<sub>28</sub>-PHPMA<sub>400</sub>, and the tri-block polymer PMOXA-PDMA-PMOXA. 1 % (v/v) of A23187 was added to each of the polymersome solutions and left for 24 hours in the presence of a ferrous ion solution. This should cause the transport of the ions across the membrane. Each polymer had a basic interior by encapsulation of NaOH ions prior to incubation with A23187. Incorporation of A23187 into a PBD-PEO membrane resulted in the production of amorphous polymer with no discrete polymersomes present under TEM analysis. Entrapped within the polymer appears to be iron oxide nanoparticles, which suggests that the ionophore is chelating iron but has disrupted the polymer membrane.

Unstained TEM micrographs (Figure 5.7) of the PMOXA-PDMA-PMOXA samples show beam damage to the polymersome, but also the presence of electron dense material in the vesicle core, suggesting precipitation of iron oxide. However this electron dense material looks to be both amorphous and limited. This could be due to the low concentration of the ionophore in the solution, resulting in a finite concentration of ferrous ion to be transported across the membrane. This is akin to the problems experienced by Mann *et al.*<sup>4</sup> in their earlier artificial magnetosome study. This could be due to the increased thickness of the polymer membrane (~10 nm) when compared to a biological membrane of 4-5 nm, hindering the penetration of the full membrane by of the ionophore.

Finally, the A23187 was used with polymersomes prepared from PEG<sub>113</sub>-PHPMA<sub>400</sub> / PMPC<sub>28</sub>-PHPMA<sub>400</sub> without cross-linker. As with other polymers tested, after addition of the ionophore, the polymer was soaked in ferrous ion solution.

TEM and cryo-TEM micrographs analysis (figure 5.7) shows that an electron dense species has accumulated within the core of the polymersomes. This is likely to be due to the formation of an iron oxide. The polymersomes appear distorted in the TEM micrographs, which could be attributed to the presence of the ionophore in the membrane. To confirm this, the vesicles were further analysed by cryo-TEM, which showed the presence of spherical polymersomes (Figure 5.7 inset), which shows the distortion of the membrane in the room temperature TEM images is likely to be a drying artefact during TEM grid preparation.

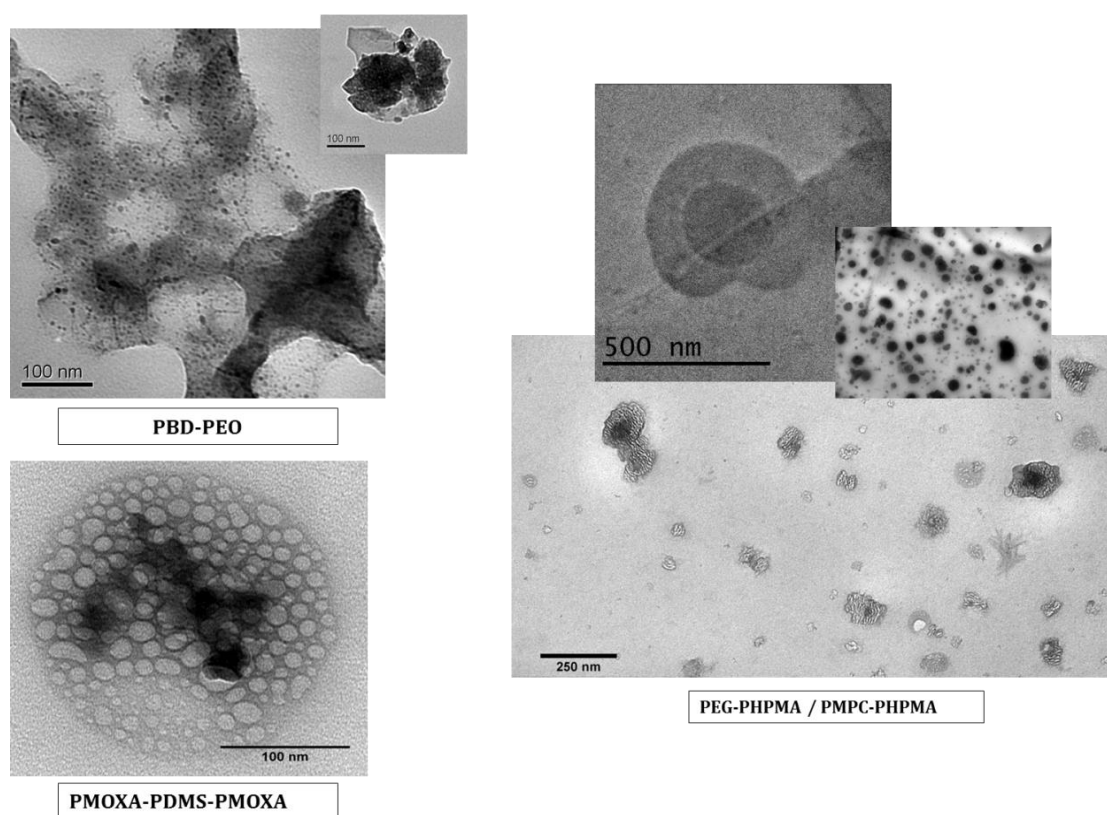


**Figure 5.7:** Clockwise from top left: TEM micrographs of PBD-PEO, PEG<sub>113</sub>-PHPMA<sub>400</sub> / PMPC<sub>28</sub>-PHPMA<sub>400</sub> and PMOXA-PDMS-PMOXA polymersomes after incubation with 10 mM ferrous chloride solution containing 1 % (v/v) A23187 to facilitate ferrous ion transport into the polymersome cores.

The cores of PEG<sub>113</sub>-PHPMA<sub>400</sub> / PMPC<sub>28</sub>-PHPMA<sub>400</sub> polymersomes appear to have the highest electron density of all the other polymers investigated (figure 5.7 inset). Despite having the thickest membrane, it is possible that the difference in the polymer chain lengths adds to the fluidity of the membrane, making the transport of iron across the membrane by the ionophores easier.

Increased iron oxide precipitation could also be improved by the chemistry of the polymersome membrane, namely the presence of carboxylic acids lining the vesicle core which could aid precipitation once A23187 has successfully transported the ferrous ion across the membrane. It has not yet been possible to detect the presence of A23187 in the membrane, for this a marker such as a fluorescent tag would be needed for direct visualisation of the molecule in the membrane. However, control samples (shown in chapter 6) have proven that ferrous and ferric ions cannot cross any of these polymer membranes unaided. Therefore the presence of iron oxide in the vesicle core can be confidently attributed to ionophore activity.

## 5.4 BIOMIMETIC TRANSPORT SYSTEMS DISCUSSION

Membrane proteins are notoriously difficult to work with, with their cloning, expression, purification and incorporate into artificial vesicles extremely difficult to perform. Furthermore, confirmation of the proteins' orientation is also extremely difficult to determine. The orientation is under thermodynamic control, and is dependent on the hydrophobic interactions in the bilayer.<sup>76</sup> Minimal control of this can be achieved during addition of the protein to the vesicle.<sup>107b</sup> Only one of the six transporter targets was successfully cloned, expressed and purified, which was the MamMB complex. Previous work had shown MamMB is extremely difficult to work with, due to the need for co-expression to make a stable complex of the two proteins.<sup>52</sup> Therefore, the decision was taken to clone the two genes *mamM* and *mamB* from a synthetic gene which encodes the expression of both proteins in series from a single piece of DNA. This had surprising success, with both proteins being co-expressed with less optimisation than expected. This was confirmed by the identification of the two different tags on each protein. A major issue with the production of membrane proteins is that, due to their function, they sit in a membrane, making them largely hydrophobic and highly insoluble. Therefore, extracting the proteins from their native membrane is extremely difficult. For this reason, multiple MTB transporter targets were chosen, and a large scale expression trial was carried out to determine optimum production condition for each protein. Despite the majority of the transporter targets expressing protein in expression trials at detectable concentrations, it was not feasible to attempt to purify all targets within the timeframe of this PhD.

Therefore, targets that were expressing at low levels were dismissed. Only MamMB was successfully purified within the time constraints after solubilisation of the proteins with detergent micelles. Co-purification of both proteins was confirmed by Western blotting, showing two bands of varying sizes detected by their respective tags in the same column fractions. Unfortunately, testing of the protein complex for iron transport in a vesicle system was largely inconclusive, mainly due to limited characterisation and a lack of time for thorough optimisation. The TEM analysis revealed localised precipitation to DPhPC liposomes; it was not possible to detect the presence of the protein, so at this stage analysis was restricted to detection of morphological changes only.

It would also be of advantage to fluorescently label the proteins to determine localisation to differentially labelled liposomes (either spectroscopically or using fluorescence microscopy). However, to perform this efficiently it would require mutagenesis of the protein sequence to incorporate a cysteine residue for the specific addition of a fluorescent tag.

Transmembrane transport of iron ions by ionophore proved successful. Positive results were not seen across the board for all polymers tested, for example, A23187 was unsuccessful in incorporation into PBD-PEO. Limited incorporation was observed with PMOXA-PDMS-PMOXA, but the ionophore did appear to transport ferrous iron into the membrane. However, this transport was limited, meaning optimisation of the ionophore concentration, which would have to be increased four-fold to double the iron ion concentration transported, this would likely yield increased precipitation. PEG<sub>113</sub>-PHPMA<sub>400</sub> / PMPC<sub>28</sub>-PHPMA<sub>400</sub> yielded much better results, appearing to have electron dense material filling the vesicle cores. Although TEM analysis indicates that the ionophore has produced a change in the contents of the vesicle core, specific detection of the ionophore within the vesicle has not been confirmed. Similar to the future approach set out above for the MamMB complex this would ideally be *via* addition of a fluorophore.

Although at this point analysis has been limited to TEM characterisation and observation of morphological changes to the vesicle structure and core. Results have been positive and indicated some successful incorporation and functionality of A23187 and possible ferrous localisation to the MTB transporters.

Detailed studies of the other transporter targets investigated would not only help characterise multiple MTB proteins, but may yield formation of fully functioning artificial magnetosomes. However, in its present state, biological transporters cannot be considered a feasible route to iron transporter in a synthetic magnetosome, due to difficulty of the proteins production and the low yields expressed. From an academic point of view further work will be carried out on this protein to fully confirm incorporation and functionality as a transport, but from the context of scale-up for biomedical application it does not represent a practical option, therefore through the rest of this thesis, synthetic transport routes will be explored.

# **CHAPTER 6:**

---

## **SYNTHETIC TRANSPORT SYSTEMS**

## 6.1 INTRODUCTION TO SYNTHETIC REAGENT TRANSPORT

The natural transport system used in MTB uses protein antiporters, which both transport ferrous iron into the magnetosomes whilst also slowly increasing the internal pH by removal of H<sup>+</sup>. However, expression and purification of the antiporters has proven difficult; as demonstrated in chapter 5. Their inherent hydrophobic nature means that isolation of *E. Coli* membranes and later reconstitution in synthetic vesicles has proven challenging, and therefore impractical. Whilst their incorporation would have created a fully artificial magnetosome, other artificial and more practical synthetic methods of membrane permeation are possible, and so are investigated throughout this chapter. The primary method of transmembrane iron transport explored here is the use of electroporation. As discussed in chapter 1, electroporation is the use of an electric field to open temporary hydrophilic nanoscopic pores in a membrane to allow reagents to cross that membrane.<sup>159a, 161, 164, 192</sup> The potential generated across the membrane is dependent on: the membrane composition, the vesicle size, and the extracellular medium; and is widely used in the field of molecular biology to deliver DNA into cells.<sup>164</sup> In this chapter, electroporation is used as a completely synthetic method of membrane permeation. During electroporation, the reagents should be able to cross the vesicle membrane to precipitate magnetite within the vesicles, which is a novel use of this technique. In each case, the vesicles have a high pH aqueous core. These are suspended in an iron solution (low pH) with the membrane providing a barrier to mixing, and therefore to reacting. Control of the electroporation parameters can control the pore size, and thus the reactant flow. This should allow control over the size of the nanoreactor bounded MNP, as *in situ* electroporation could offer a magnetic response remotely activated by the application of an electric field. In these experiments, vesicles encapsulating an OH<sup>-</sup> source (optimised in chapter 3) are electroporated in the presence of mixed valence iron salts. This technique has been applied to all lipid and polymer vesicles which have produced high quality vesicles in the presence of basic solution in chapter 4. As with other studies in this project, many lipids/polymers were trialled initially, due to the large number of potentially suitable materials. Of those materials, those that appeared promising were then investigated more thoroughly to determine the type of iron oxide present.

## 6.2 ELECTROPORATION OF VESICLE MEMBRANES

### 6.2.1 ELECTROPORATION OF LIPOSOMES

The two different routes to magnetite precipitation discussed in chapter 3, were incorporated into the most promising liposomes, from the results presented in chapter 4. In each case, iron chloride salt solutions were used, made up of iron (II) chloride tetrahydrate ( $\text{FeCl}_2 \cdot 4\text{H}_2\text{O}$ , 10mM) and iron (III) chloride hexahydrate ( $\text{FeCl}_3 \cdot 6\text{H}_2\text{O}$ , 10 mM) in a 1:2 ratio. For DOPC samples, 3ml of the 1:2  $\text{FeCl}_2/\text{FeCl}_3$  solutions were added to vesicles encapsulating either NaOH (10 mM) or urea (10 mM). Electroporation was used to porate the lipid membrane and allow iron ions to enter the vesicle core. These short lived and reversible pores, allow the non-specific exchange of solution across the vesicle membrane.<sup>8</sup> Transport across the membrane is the result of a difference in chemical potential as the result of a concentration and pH gradient between the inner and outer solution.

#### 6.2.1.1 ELECTROPORATION FOR ROOM TEMPERATURE CO-PRECIPIATION.

Following electroporation, room temperature co-precipitation vesicle samples (encapsulating NaOH) were kept at 4 °C. This is because the co-precipitation reaction using sodium hydroxide and iron salts is virtually instantaneous, precipitating magnetite at room temperature. TEM analysis of electroporated 1,2-dioleoyl-sn-glycero-3-phosphocholine (DOPC) encapsulating NaOH, shows vesicles with an average size of  $396 \pm 77$  nm, (Figure 6.1 a). Vesicles appear to be filled with electron dense material, presumed to be iron oxide, but this needs to be confirmed using a technique such as single-axis electron diffraction as part of further work. The TEM analysis suggests that DOPC vesicles containing NaOH do produce iron oxide, possibly in the vesicle core. Overall, there are very few distinguishing factors with regards to the nature of the iron oxide precipitated such as a distinct crystal facets or the obvious presence of the bilayer (which should be visible at low contrast).

Generally, the DOPC vesicles are homogeneously electron dense, and it is apparent that the entire vesicle structure (core and bilayer) contain the same electron dense species with very little distinction.

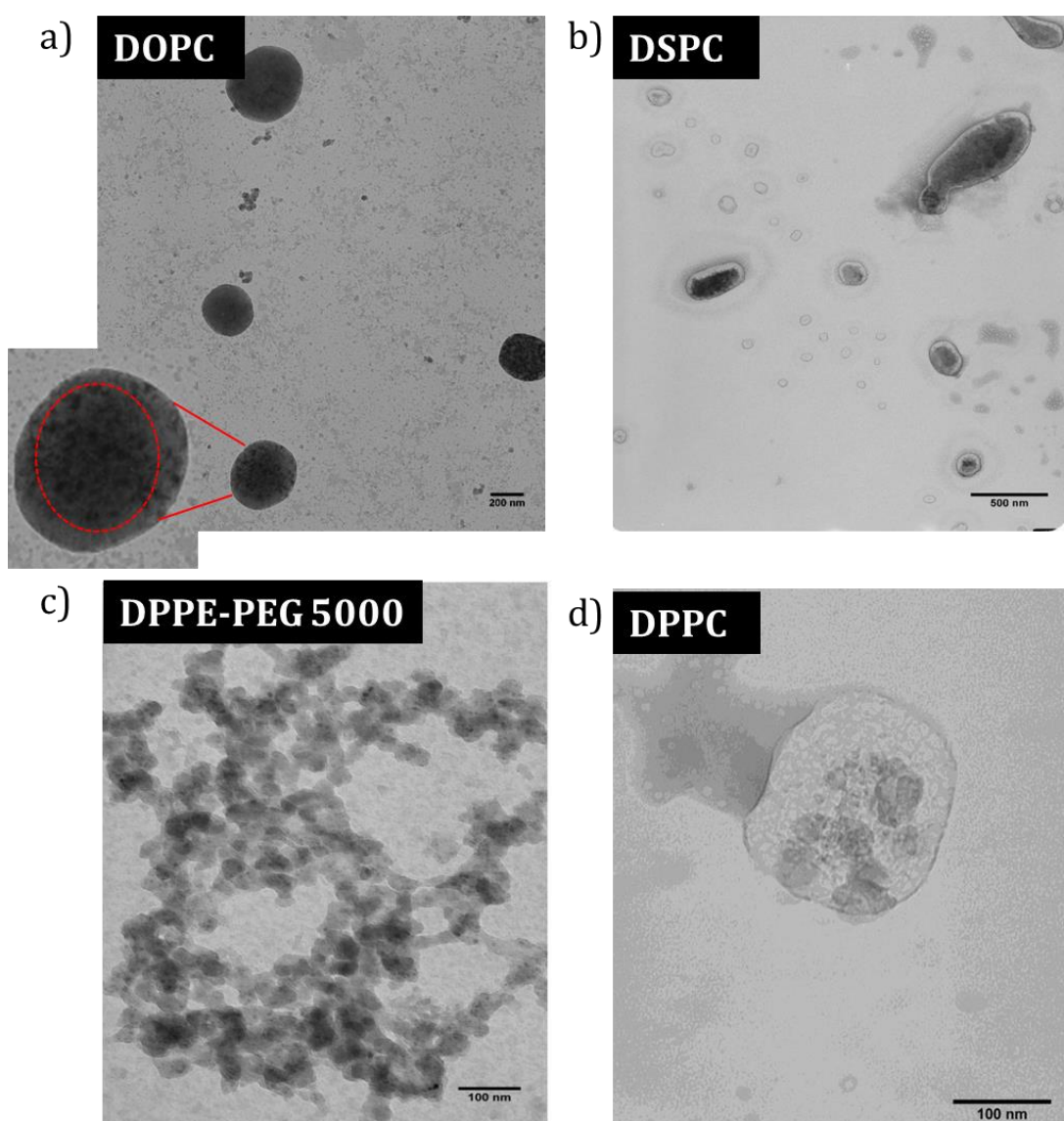


**Figure 6.3:** TEM micrographs of liposomes made from a) DOPC lipid, Inset highlights electron density difference between what is believed to be the vesicle bilayer and the darker core b) DSPC lipid c) DPPE-PEG 5000 lipid and d) DPPC lipid after electroporation. In each case the liposomes containing NaOH, were electroporated in the presence of iron ion solution for the room temperature co-precipitation of magnetite.

This was not what was expected, as soluble iron should have passed through the membrane into the vesicle core during electroporation, leaving the bilayer free of electron dense material. This suggests that the vesicle membrane has been flooded with the soluble iron, which may be in an amorphous phase. It is possible that this is due to the concentration of NaOH in the core being too low (either through leakage or too low concentration at encapsulation).

There is some heterogeneity with respect to the electron density in some of the vesicles imaged, as distinct particles can be seen. These vesicles still have the homogenous dark core as seen in other examples, which is distinct from the smaller darker areas. This suggests that these darker spots are made of a different, denser material, with the smaller particles perhaps being in the membrane or stuck to the outer surface. Overall, it is clear that electroporation has been successful, as unstained DOPC vesicles now have dark (electron dense) material within them, which is presumed to consist of iron oxide species. This homogeneity with respect to the presumed vesicles encapsulation of iron oxide is possibly due to the high fluidity of the DOPC bilayer. However, it can also be seen in the sample shown in figure 6.1 a), that the applied voltage does not have a uniform effect, with the outcome of the precipitation differing both within and between vesicles.

When the vesicle material is changed to 1,2-distearoyl-sn-glycero-3-phosphocholine (DSPC) but still incorporating NaOH, more definition can be observed in the TEM micrographs, with a visible bilayer surrounding the electron dense cores (Figure 6.1 b). There is a distinct difference in the sizes and shapes of the vesicles following electroporation. Before electroporation, vesicles are  $192 \pm 39$  nm in size. After, there is a mixture of morphologies: spherical vesicles with an average size of  $188 \pm 49$  nm but also elongated vesicles  $597 \pm 237$  nm occurring after electroporation. It is possible that these larger structures are the result of vesicle fusion during electroporation, especially as some of the samples appear to have budding vesicles on the end of the elongated structures. Both the larger and smaller vesicles appear to have a distinct, electron dense core, and look to be partially fused. These larger structures were also present in the DSPC vesicles pre-electroporation (Figure 4.2), and so can be assumed to be a product of the formation method as opposed to an effect of the electroporation.

All of the vesicles in the DSPC sample have an electron dense core, which look to be particulate. As these particulates have a rounded morphology rather than a faceted one, it is unlikely that they are salt crystals from the PBS buffer. Their spherical nature suggests the presence of a smaller vesicle population on which electroporation has been unsuccessful at generating an electron dense mineralised core. More analysis would need to be performed on this sample to determine if this is in fact a smaller vesicle population.

For example, dilution of the sample would solubilise the structures if they are salt crystals and they would no longer be visible in TEM. In vesicles where the electroporation appears to have been successful, evident by the dark, electron dense vesicle core, the contents of the interior appear to be much more heterogeneous than within the DOPC vesicles. Furthermore, in most cases, this precipitate does not fill the vesicle core. Instead, the precipitate exhibits varying density, with distinct smaller particles in the core again having higher density when compared to the rest of the vesicle core. This suggests the presence of mixed species in the core, and is likely due to heterogeneous nucleation within the vesicle.

In the case of NaOH filled Dipalmitoylphosphatidylethanolamine-poly(ethylene glycol) (DPPE-PEG 5000) vesicles, the TEM images show a lipid network rather than vesicles after electroporation (figure 6.1 c). Whilst individual spherical structures could be vesicles of <50 nm, they are entirely embedded in the network and. Also, no distinct features of a vesicle (i.e. a bilayer) can be identified. Despite this, there is a clear difference in density between these structures and smaller darker particles. These particles are presumed to be iron oxide nanoparticles, and are associated with or embedded in larger and paler formations (presumed to be liposomes) (Figure 6.1 c). Unfortunately, as with the other liposome examples, while nanoparticles may be present they are not filling the interior of a vesicle. It is possible that this is again due to a shortage of iron ions that are able to penetrate the liposomes and the network, or loss of the basic solution due to the network formation. On the whole, the DPPE-PEG 5000 sample is highly unsuitable for further investigation, and more exploration of the formation method to obtain discrete vesicles would have to be carried out. In this project, this is unjustified due to a large number of more successful combinations of materials, with the only advantage to this lipid being the PEG functionalisation.

However, this lipid could be re-visited in future work, if PEG attachment for biomedical application proves difficult with other materials.

Liposomes prepared with Dipalmitoylphosphatidylcholine (DPPC) prepared above the lipid  $T_g$ . Figure 6.1 d) shows what appears to be a vesicle with a diameter of 230 nm, although no typical vesicular features are observed. The presence of only one vesicle in the TEM micrograph (Figure 6.1 d) is reflective of the poor quality of the sample. Although the size of the vesicle before and after electroporation is comparable, there is a distinct difference in the shape. Before electroporation (figure 4.2 c), vesicles appear extremely spherical, the vesicle in figure 6.1 d) is highly distorted (although too round to be a salt crystal). There is the presence of sparse electron dense material inside the possible vesicle; however this is much less dense than in the other electroporated lipid samples (Figure 6.1). It is unlikely that this electron dense material is magnetic, crystalline iron oxide, but is more likely to be an amorphous iron intermediate species. It is not clear whether this poor precipitation is the result of poor iron uptake, as DPPC has a  $T_g$  above the ambient temperature at which the mineralisation reaction is performed. Therefore, the DPPC lipid will be in the gel state, which could result in poor permeability even when using electroporation. However, this is unlikely as the same effects are not observed in DSPC (which has a similar  $T_g$  to DPPC), so it may be another property of this system that is responsible for the differences observed.

The limited mineral precipitation may also be due to loss of the basic encapsulant, which will limit the precipitation reaction, meaning the reaction is likely to stall at an amorphous intermediate phase. There is no clear reason, from analysis of the DPPCs composition, as to why it should be more “leaky” to NaOH than the other lipids tested. However, in the absence of an effective leakage assay, it is impossible to say conclusively. Despite beam damage to the sample, it is still clear that DPPC does not respond well to electroporation. Only limited transport into the vesicle core has been achieved, evident by the limited nucleation within the core.

### 6.2.1.2 ELECTROPORATION FOR THERMAL DECOMPOSITION CO-PRECIIPITATION

Samples encapsulating urea were electroporated and then subsequently heated to 90°C in an oil bath for four hours. During this time, the decomposition of urea occurs, yielding ammonium hydroxide (an aqueous solution of ammonia). This increases pH and is able to induce the co-precipitation reaction, and should yield a single magnetite particle within the vesicle core. Electroporated DOPC vesicles containing urea show a large amount of lipid residue, and the presence of electron dense material (presumed to be iron oxide) (Figure 6.2 a). The presence of an electron dense precipitate confirms that all of the reagents of the precipitation reaction were present during the heating step after electroporation, and the thermal decomposition of urea was successful to yield a mineral precipitate. However this precipitate is not nanoparticles as expected, but looked to be large aggregates of electron dense material of mixed morphologies. Furthermore, this precipitation has not occurred within vesicles, evident by a large amount of lipid residue on the grid.

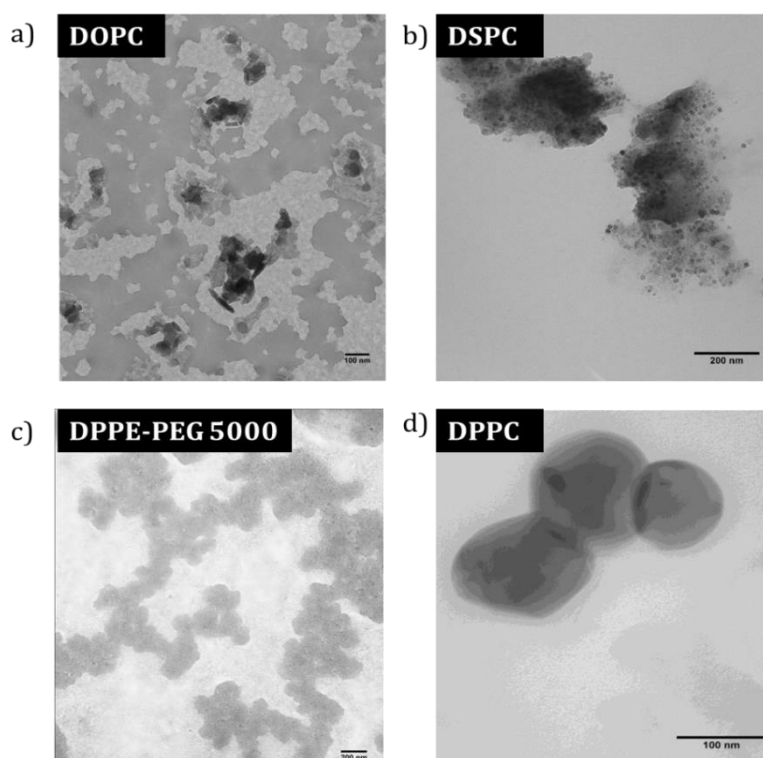


**Figure 6.4:** TEM micrographs of liposomes made from a) DOPC lipid b) DSPC lipid c) DPPE-PEG 5000 lipid and d) DPPC lipid. In each case the liposomes containing urea, were electroporated in the presence of an iron ion solution for the room temperature co-precipitation of magnetite.

As the DOPC vesicle in the room temperature experiments (section 6.2.1.1) were of a much higher quality, this degradation of the lipids cannot be attributed to the lipid. Instead, this suggests that DOPC is unable to withstand the heating step required to decompose  $\text{CO}(\text{NH}_2)_2$ .

When the DOPC lipid is changed to DSPC and encapsulating urea (Figure 6.2 b), only the presence of electron dense material (likely to be iron oxide) can be determined. Again, this is coupled with a large amount of lipid residue. DSPC lipid again appears unable to withstand the sustained period of heating, as the electron dense material appears to be suspended in a lipid agglomeration, rather than precipitated within vesicles. It is of note that the particles are extremely well defined; possibly suggesting that DSPC has incorporated and better retained the precipitation reactants when compared to the DOPC lipid, possibly due to the reduced flexibility of DSPC.

DPPE-PEG 5000, (Figure 6.2 c) appears to be equally poor when using the urea magnetite precipitation route. DPPE-PEG 5000 samples still have a large amount of agglomeration. Contrast is greater than with unstained lipid, the liposome core is of a much lower electron density than with the other samples, suggesting poor encapsulation or permeation of reactants. This may be due to steric hindrance from the PEG groups on the outer leaflet of the DPPE-PEG 5000 vesicles. The heat looks to have disrupted the vesicle membrane, causing fusion and aggregation of the lipid, again likely promoted by the presence of the large outer PEG groups. When this experiment was repeated but with liposomes prepared above the  $T_g$  of DPPE-PEG 5000, there is better formation of vesicles but still no presence of iron oxide after electroporation and heating. These data show that vesicles cannot form when the lipid is in the gel state. Furthermore, the apparent agglomeration of the below  $T_g$  formed liposomes during heating, suggests that the liposomes are unstable upon heating. However, when liposome formation was repeated above the lipid  $T_g$ , liposomes are successfully formed. Presumably, as these liposomes drop below the  $T_g$  they return to the gel state, they are presumed to be stabilised, essentially “locked” in this conformation. It is likely that this gel state is responsible for the unsuccessful electroporation as the “locked” lipids are not likely to rearrange as easily upon electroporation.

As in the case of the NaOH sample, and to avoid the same pitfalls observed with DPPE-PEG 5000, liposomes made with DPPC lipid were formed above the lipid  $T_g$ . When incorporating urea into these liposomes, very round vesicles with a distinctive electron density formed after electroporation and heating. These were found in small aggregates ((Figure 6.2 d), and their size and shape indicates that all vesicles in this sample have similar characteristics. The contrast that can be seen between the vesicles and the unstained TEM grid suggests permeation of the membrane with the iron ion solutions.

## 6.3 ELECTROPORATION OF POLYMERSOMES

Work in this section is taken from the publication Bain *et al*<sup>7</sup>

### 6.3.1 DI-BLOCK POLYMERSOMES

The di-block copolymer PBD-PEO, formed vesicles of an appropriate size, with the narrowest size distribution from the results presented in chapter 4. Therefore, PBD-PEO was chosen for trial experiments on the electroporation of polymersomes. An initial electroporation voltage of 2500 V was chosen due to a recommendation from collaborators (Battaglia group, UCL) who had previously optimised these conditions for PBD-PEO polymersomes. Furthermore, due to the increased robustness of the polymersomes, it was thought that a larger voltage would be required than for the liposomes. This is because increasing the voltage applied to the vesicle should form bigger pores, and hence allow for higher volumes of iron to be transported into the polymersomes.

### 6.3.1.1 TEM OF PBD-PEO POLYMERSOMES

When the PBD-PEO polymersomes were subjected to electroporation (2500 V, 5 pulses), reagents were able to diffuse through the resulting membrane pores. This was first carried out on polymersomes pre-loaded with the iron ion solution and incubated in the presence of the either NaOH or  $\text{CO}(\text{NH}_2)_2$  (both 10 mM) and heated if required as per the conditions outlined in section 2.1.3. These polymersomes appear to be filled with an electron dense material that is presumed to be iron oxide. In each case, a bilayer of approximately 5 nm can be observed around the electron dense core (Figure 6.3). This experiment was performed initially to ensure that the polymer could behave in the way that was hypothesised. This is also how Mann *et al*<sup>4</sup> tried to mineralise their phospholipid artificial magnetosomes (i.e. encapsulation of iron and base to yield the precipitation of iron oxide). However, the iron oxide is not homogenous across the core of the vesicle, presumably due to the same issues encountered in the original Mann work.<sup>4, 121a</sup> The finite concentration of iron encapsulated within the polymersomes core during formation is not sufficient to crystallise a single homogenous nanoparticle. Therefore the system was switched back to that used within section 6.2.1, i.e. the encapsulation of base and the transport of iron into the core which should continually grow the nanoparticle precipitating in the core.

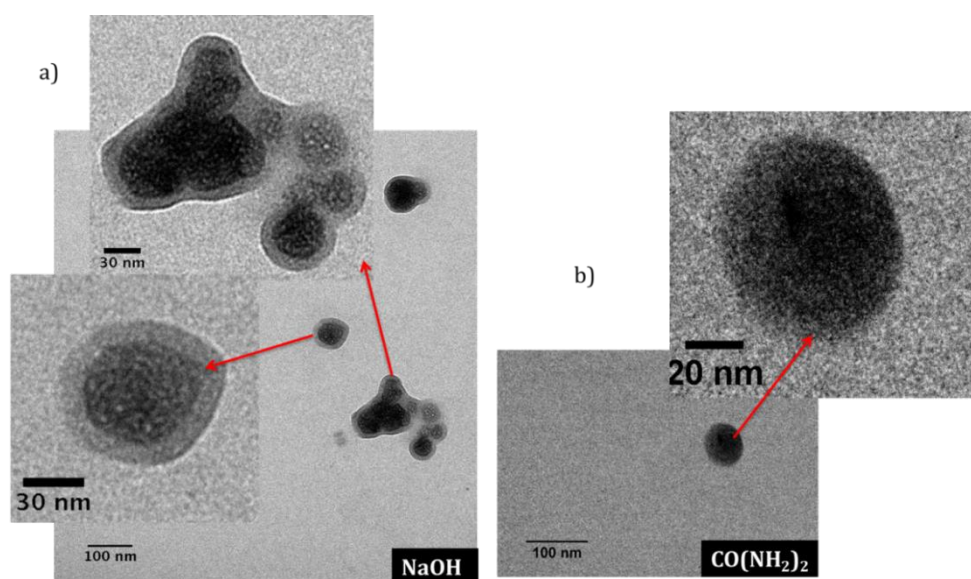


**Figure 6.3:** a) Shows TEM micrographs of iron solution loaded PBD-PEO polymersomes which have then been electroporated in the presence of NaOH. Typical vesicular features, such as the bilayer is visible in addition to a heterogeneous electron dense core. There is also evidence of some membrane breakage. B) Similarly shows the same system but electroporated in the presence of  $\text{CO}(\text{NH}_2)_2$  and heated at 90°C for four hours. The polymersomes have remained intact throughout this period and appear again to be filled with heterogeneous but electron dense material.

The system was reversed (base on the inside) and electroporated under identical conditions. The PBD-PEO polymersomes now appear as membranes decorated with much smaller discrete particles (Figure 6.4 b) and c). A control sample of base (NaOH) filled polymersomes were suspended in an iron solution, and left to incubate for 48 hours. After this time, MNPs did not form, showing that the natural permeability of the PBD-PEO membrane was not sufficient to allow the reagents to penetrate the membrane (i.e. the base cannot leak out and the iron ions cannot leak in) (Figure 6.4 a). Figure 6.4 b) shows some MNPs associated with the external vesicle membrane; this is likely due to some degradation of the sample. The charged and magnetic nature of the mineralised PBD-PEO polymersomes appears to result in free iron oxide MNPs concentrating in the outer leaflet of the magneto-polymersomes.

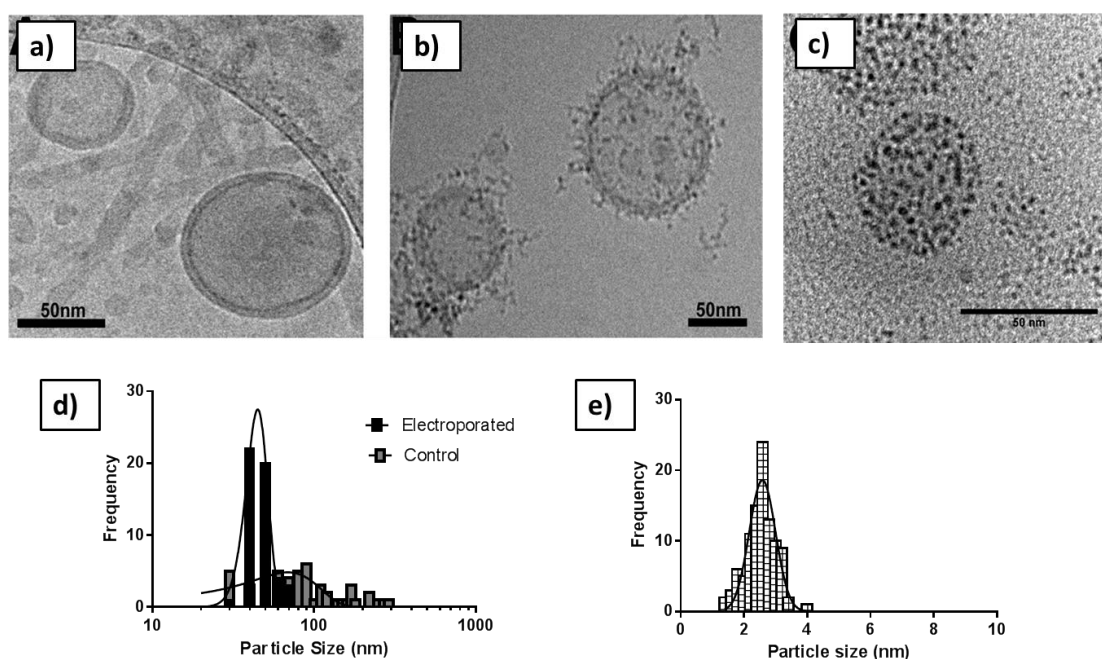


**Figure 6.4:** Cryo-EM images of extruded PBD-PEO polymersomes before a) and after b) electroporation, with the latter displaying a high density of electron dense particles around the membrane (presumed to be iron oxide). c) Shows the same sample as in b) but imaged after drying down by regular TEM. d) Grainsize distributions from TEM images of a control sample (unelectroporated PBD-PEO polymersomes incubated in an identical iron solution) and an electroporated sample after SEC clean-up. This shows a narrower size distribution in the electroporated sample as a result of size separation during column clean-up e) Magnetic nanoparticle grainsizing taken from TEM images shows the particles to have an average diameter of 2.5 nm (SD  $\pm$  0.5 nm).

In order to determine how the MNPs are associated with the membrane, Cryo-EM was employed (Figure 6.4 b) to ensure far fewer sample preparation artefacts.<sup>193</sup> Cryo-EM images of unelectroporated polymersomes (Figure 6.4 a) and electroporated PBD-PEO magneto-polymersomes (Figure 6.4 b) showed particles present within and associated with the membrane only in cases where electroporation had been applied with negligible free particles in the background. This is because any unbound external precipitate is removed, due to difference in size when run down the SEC column. Size analysis of the PBD-PEO magneto-polymersomes based on the room temperature TEM data showed them to be  $47 \pm 9$  nm (Figure 6.4 d). To further characterize the vesicles and their associated MNPs, a tomographic tilt series of the polymersome sample was generated. This allows for a clearer analysis of both the polymersome membrane and its interior (see video in the appendix). A few PBD-PEO magneto-polymersomes can be seen to have smaller polymersomes encapsulated within them. From analysis of the entire sample, it is clear that precipitation of MNPs is localised to within the outer membrane of the PBD-PEO magneto-polymersomes. This is evident by the lack of MNPs within the membrane of the inner polymersomes (see appendix video). The MNP size analysis shows that they have a small size and a tight size distribution of  $2.5 \pm 0.5$  nm in diameter (Figure 6.4 e) when electroporated at this voltage. The extremely small size of the particles is likely to be controlled by the elasticity of the polymer limiting particle growth. The nanoparticle size could be limited by the stretching range of the polymer membrane. Also, because of the position of the nanoparticles within in the membrane, it is likely that they can only propagate within the confines of the pore in the membrane.

It is of particular interest that the Cryo-EM images (Figure 6.4 a and b) were obtained 10 months after the sample was prepared, as opposed to the regular TEM image in Figure 6.4 c) which was obtained two months after preparation. This confirms the stability of the magneto-polymersomes against degradation over a long time period, which is promising for their potential future use in biomedical applications. It can be confirmed that the particles appear to be coming out of the polymersome membrane are still tightly bound, to either the MNPs within the membrane or the membrane itself, as they were not removed during SEC clean-up.

Although this was an unexpected result (as precipitation was expected to occur in the polymersome core), it is highly advantageous as it leaves the core of the vesicle completely free for further functionalization, such as the encapsulation of therapeutics during formation or post formation.

### 6.3.1.2 PORE FORMATION IN *DI-BLOCK* POLYMERS

A hypothesis for the mechanism of MNP formation within the membrane during electroporation is that pores open allowing ion-transport across the polymer membrane upon application of a voltage. This would result in an iron ion / base interface within the poration channels. The membrane acts as a nucleation site, and the pore acts as a template to restrict the size of the growing MNPs within the membrane (Figure 6.5). Upon poration, the interface between the two reagents within the membrane is the point at which precipitation is likely to occur. The size of these particles is controlled by the pore width, i.e. the particle cannot grow outside of the dimensions of the membrane core. Furthermore, according to current literature,<sup>160,164</sup> the pores created during electroporation are presumed to be reversible. It is unlikely that these pores will be able to re-close with the newly precipitated particle now sat inside it. Therefore, it is likely that the pore remains partially open (although filled with the MNP) and this gives rise to the “feathering” effect observed around the polymersomes (Figure 6.4 b). This hypothesis also supports that, because the pores are not entirely closed, continued nucleation and precipitation can occur in the pore which effectively then spills out.

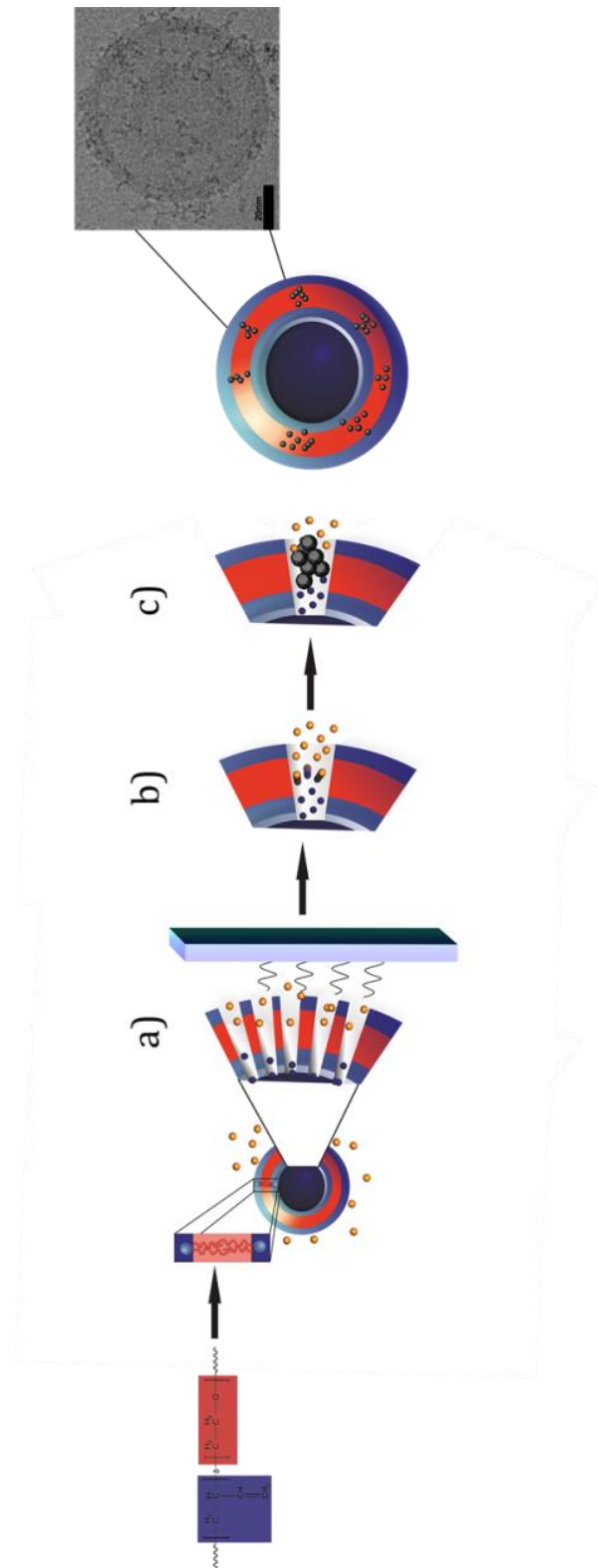


**Figure 6.5:** Schematic of the proposed mechanism for nanoparticle synthesis within polymersomes using electroporation. (a) Electroporation opens pores within the membrane at which point influx of iron ions occurs in parallel with efflux of NaOH (encapsulated) (b). (c) Shows the *in situ* room temperature coprecipitation that then occurs at the interface between the reactant solutions within the membrane. To the right of this is a diagram and a Cryo-EM image of a PDB-PEO magneto-polymersome.<sup>7</sup>

### 6.3.1.1 ELEMENTAL ANALYSIS OF PBD-PEO POLYMERSOMES

Energy dispersive X-ray (EDX) elemental analysis showed the particles within the polymersome membrane were an iron-oxide species by the presence of characteristic peaks for Fe and O (although of course oxygen will always be present) (Figure 6.6). Other peaks in the spectrum arise from polymersomes (e.g. C, O), the buffer (e.g. P, Na, Cl & K in PBS) or the instrument itself and the formvar-carbon coated copper grid on which the sample has been dried down (e.g. C & Cu). Unfortunately, EDX cannot give any information about the redox species or amount of iron oxide present. Therefore, to determine the amount of iron oxide present, induced coupled plasma emission spectroscopy (ICP-MS) mass spectrometry was applied to the sample.

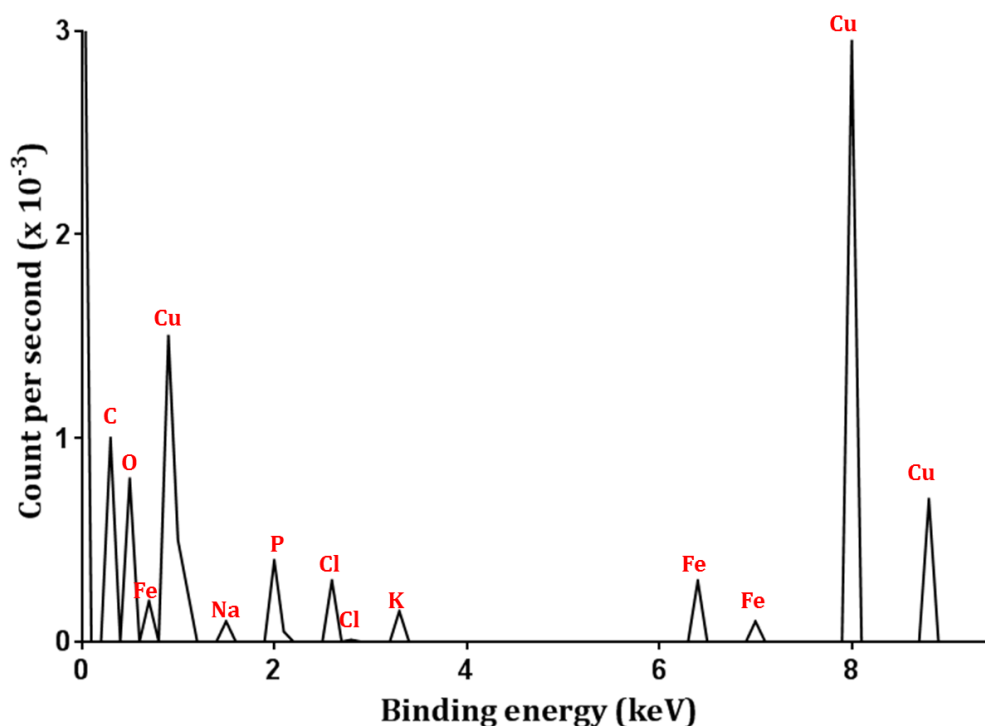


**Figure 6.6:** Energy dispersive X-ray spectrum of an MNP within the bilayer of a PDB-PEO magnetopolymersome. Spectra show peaks for copper ( $\text{CuK}\alpha$  at 8.05 keV,  $\text{CuK}\beta$  at 8.90 keV and  $\text{CuL}\alpha$  at 0.93 keV) as a result of the copper mesh TEM grids. Presence of iron oxide is indicated by peaks for both iron ( $\text{FeK}\alpha$  at 6.40 keV and  $\text{FeK}\beta$  at 7.06 keV, and  $\text{FeL}\alpha$  at 0.71 keV) and oxygen ( $\text{OK}\alpha$  at 0.53 keV). Other peaks are likely to be due to the buffer used in the reaction and the carbon coating on the TEM grid.

ICP-MS revealed that iron compounds make up approximately 1.40-1.42% of the sample (dependent on oxide type) of the PDB-PEO magneto-polymerosome (iron concentration: polymer concentration ratio (as measured by ICP-MS and gas chromatography), (Appendix calculation 1). This value was calculated using the approximate polymer concentration, as estimated from gas chromatography (see Appendix for GC polymer weight calibration) and the polymerosome size (from TEM micrographs). This was used to calculate the internal volume of the polymer and the total volume occupied. Weighing the PDB-PEO polymerosome used to form the magneto-polymerosome film was done by drying a known volume of polymer solution at a known concentration under vacuum into a pre-weight Eppendorf. This was compared to the polymer theoretical weight (as measured by GC, see appendix), a ratio of polymer to iron oxide (by mass and ICP-MS ppm values) was established; in ppm.

#### **6.3.1.2 MAGNETIC MEASUREMENTS OF PBD-PEO POLYMERSOMES**

Magnetic hysteresis measurements (Figure 6.7) reveal that the particles behave superparamagnetically. This corresponds to the expected magnetic behaviour of the  $2.5 \pm 0.5$  nm sized magnetite MNPs, as they should be smaller than the single domain size for magnetite (which is about 30 nm)<sup>3</sup>. Magnetic measurements have been quoted as ranges to accommodate for the formation of either magnetite or maghemite, which have different molecular weights. It is not possible to tell from the magnetic measurements alone which of the two magnetic iron oxides have formed. To confirm this, further analysis would be required in the form of Mössbauer spectroscopy or powder X-ray diffraction (XRD). However, these techniques require large amounts of particles as a powder, which it has not been possible to synthesise at this time. It may be possible to do these measurements once scale-up of the magneto-polymerosome process is begun.

Magnetic analysis combined with the established ratio for polymer to iron oxide also reveals that MNP magnetic material makes up approximately 0.20-0.23 % of the magneto-polymerosome mass. There is a significant difference between the percentage of MNP and the total amount of iron present in the sample (1 to 1.4 %).

This means that not all of the particles (or all of each particle) observed in the TEM images is magnetic. It may be that other iron oxides, such as ferrihydrite,  $\text{FeO}(\text{OH})_2$ , goethite ( $\alpha\text{-FeO}(\text{OH})$ ), or other iron containing species that are not magnetic may have also formed in these PDB-PEO magneto-polymerosomes.

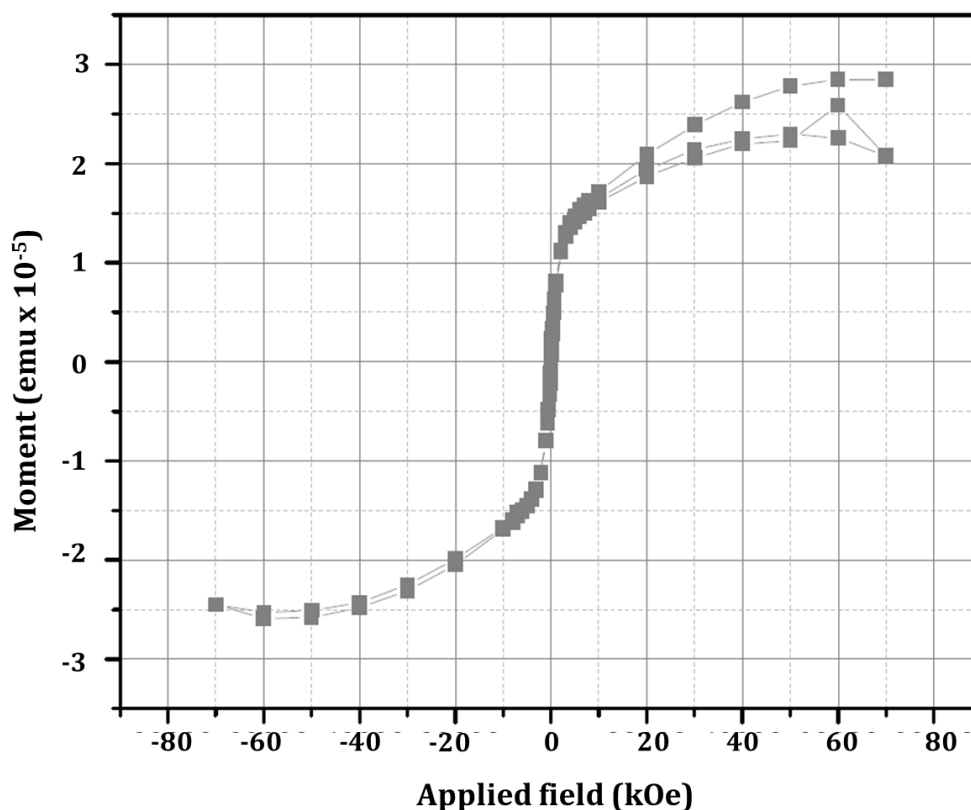


**Figure 6.7:** A superconducting quantum interference device (SQUID) was used to analyse the magnetic response of the magneto-polymerosomes at 300 K. The hysteresis indicates the presence of superparamagnetic nanoparticles in the magneto-polymerosomes. There is little to no coercivity in the hysteresis, which corresponds to the magnetic behaviour that is expected for magnetite particles that are likely to be present from the sizing analysis.

### 6.3.1.3 pH OF PBD-PEO POLYMERSONES

pH was measured at each stage of the magneto-polymerosome formation process. This shows minimal change in pH to the extravesicular solution before and after electroporation (Figure 6.8). Polymerosomes were also sonicated to disrupt the membranes before and after electroporation.

Disruption of base filled polymersomes that had not undergone MNP precipitation showed an increase in pH as the NaOH was released. This is contrary to the disruption of the magneto-polymersomes, which showed a small lowering of the pH. This is evidence that no NaOH remains on the interior of the magneto-polymersomes after electroporation. It also supports that the insertion of MNPs within the polymer membrane does not alter the integrity of the membranes. Importantly, the small pH changes seen are not significant enough to raise toxicity concerns for eventual *in vivo* applications, as this indicates that all NaOH is reacted and neutralised during the MNP formation process.

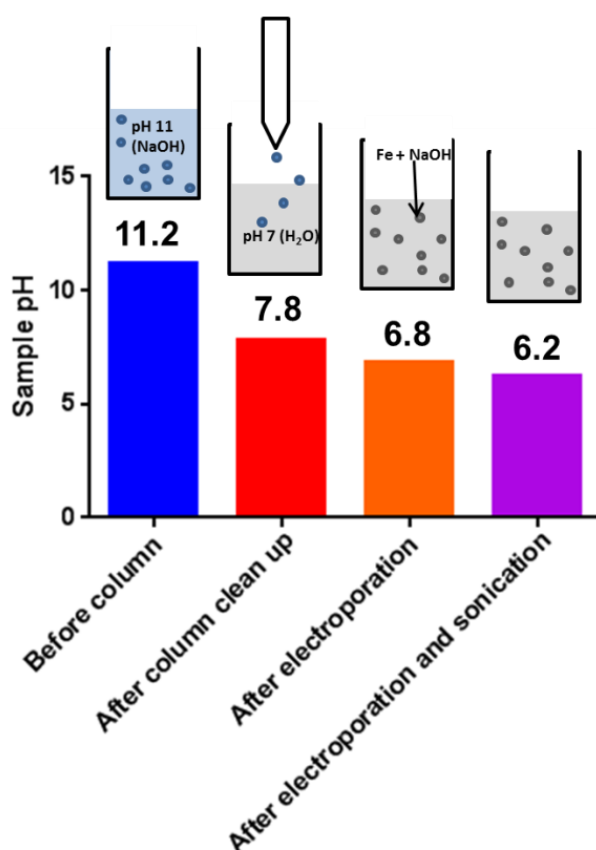


**Figure 6.8:** Assay of leakage of NaOH during polymersome preparation. The pH of a polymersome solution ( $10 \text{ mg ml}^{-1}$ ) was taken before (blue column) and after (red column) SEC clean up. The sample was then sonicated to break open the polymersome. The pH was then taken again to determine the effect of encapsulant (orange column). Finally a magneto-polymersome sample was sonicated to break them open and to release any unreacted NaOH and the pH taken a final time (purple column). Minimal and a lower change in pH after the magnetopolymersomes and cleaned up post electroporation, with a further minimal lowering of the pH post sonication indicating no NaOH remains post MNP production.

### 6.3.2 TRI-BLOCK POLYMERSOMES

Tri-block polymer membranes differ from conventional bilayer membranes in that the hydrophilic-hydrophobic-hydrophilic composition of a conventional membrane is now all part of one molecule. This forms a monolayer with the same hydrophilic/hydrophobic characteristics as a traditional bilayer. Therefore, it cannot be assumed that a *tri-block* membrane (essentially a monolayer) will react to the application of an electric field in an identical way to a di-block polymer membrane. Previous studies have shown that pores can form in a PMOXA-PDMS-PMOXA 2D suspended membrane by application of an electric field.<sup>100b</sup> Pores are able to form in the PMOXA-PDMS-PMOXA membrane behaving in a manner analogous to a phospholipid membrane. The difference in geometry and stability between a suspended membrane and a polymersome monolayer means that the two systems may not be directly comparable. However, the extended hydrophobic region of the polymer, as a consequence of its ABA type composition, results in reduced permeability due to an increased thickness of 10 nm,<sup>100b</sup> which is about double that of a lipid bilayer. This means that the incorporation of biological processes and biomembrane species into these polymersomes is unlikely, due to its synthetic nature and low permeability.

#### 6.3.2.1 TEM OF PMOXA-PDMS-PMOXA POLYMERSOMES

As with the other materials in this chapter PMOXA-PDMS-PMOXA polymersomes have been investigated as a nanoreactor for room temperature co-precipitation of magnetite. Again, an optimum concentration of NaOH (10 mM) was used as the aqueous solution for polymersome formation to create the high pH core environment needed for the precipitation. Similarly, electroporation was again used to facilitate synthetic iron ion transport across the PMOXA-PDMS-PMOXA membrane. The application of the electric potential across the membrane leads to poration. The presumed influx of the iron ion solution and efflux of NaOH induced precipitation, as with the other polymers investigated.

On meeting (presumably in the membrane as with PBD-PEO)<sup>7</sup> the precipitation of electron dense nanoparticles is observed (Figure 6.9). The electroporated magnetopolymersomes produced a paramagnetic response when placed in a magnetic field, which when combined with other data suggests a magnetic iron oxide has been precipitated within the polymersome, and that electroporation of tri-block polymersomes allows the permeation of reagents, resulting in MNP crystallisation in the polymersome membrane yielding magnetopolymersomes.

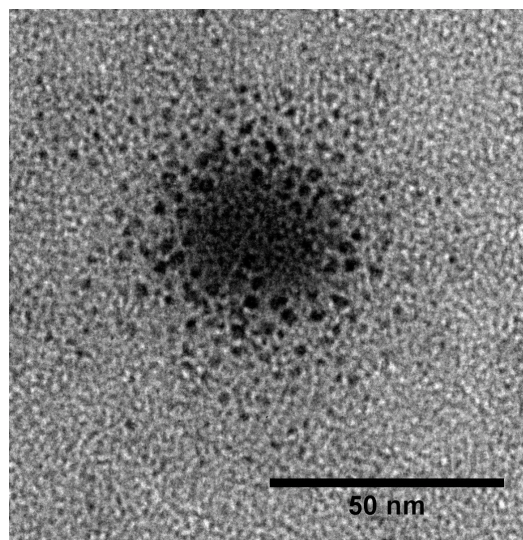


**Figure 6.9:** PMOXA-PDMS-PMOXA polymersome following electroporation at 5 x pulses at 750 V shows electron dense material presumed to be iron oxide MNPs within the polymersome, with higher density in the core when compared to the extremities.

Close inspection of the polymersomes (Figure 6.9) confirms the formation of electron dense nanoparticles within the polymersome membrane, almost analogous to the raisins in a plum pudding. The particles are presumed to be iron oxide, and are tightly associated to the membrane as they remain bound during the column clean-up process, as seen with PBD-PEO discussed above. The nanoparticles have an average size of  $2.7 \pm 0.9$  nm, (Figure 6.10 a) and show improved monodispersity with regards to particle size and shape when compared to a typical room temperature co-precipitation of magnetite (Figure 6.10 b) & c). This particle distribution is comparable with the NPs formed within the bilayer of the PBD-PEO discussed above.

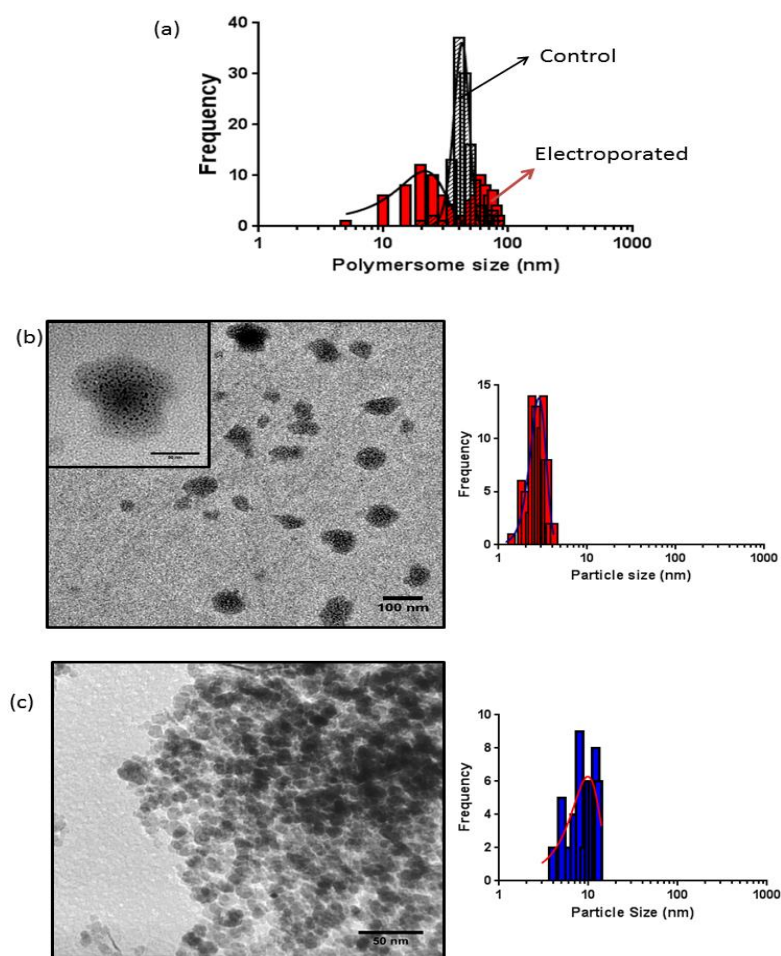


**Figure 6.10:** (a) Shows the change in polymersome size before and after electroporation. Unelectroporated control polymersomes (striped bars) have an average size of  $45 \pm 8$  nm, whereas after electroporation a dual polymersome population at 20 and 60 nm is observed giving an average polymersome size of  $43 \pm 2$  nm. (b) Shows the formation of iron oxide nanoparticles within tri-block PMOXA-PDMS-PMOXA polymersomes as the result of electroporation. Inset: an example of a magneto-polymersome, showing the distribution of nanoparticles within the polymersomes. On the right is the corresponding grainsizing from TEM, showing the average nanoparticle formed after electroporation to be  $3 \pm 1$  nm in diameter. This is in comparison to (c) a standard room temperature co-precipitation of magnetite, grainsizing from TEM images shows an average nanoparticle size of  $9 \pm 2$  nm.

In stark contrast to the di-block polymersomes (section 6.3.1.1), precipitation also appears to occur in the vesicle core. The core appears considerably more electron dense than previously seen in the TEM micrographs (Figure 6.4 c). This can be attributed to a higher particle yield in the membrane following electroporation, and greater influx of iron ions into the core of the polymersome. This would result in a proportion of NP precipitation within the core that is not seen the PBD-PEO magneto-polymersomes. This is most likely due to the difference in polymer composition and the effect this has on the electroporation mechanism.

It is possible that the tri-block polymer pores are more stable, due to polymerisation of the methacrylate groups, which can have a stabilising effect.<sup>9</sup> This stabilisation would allow increased iron influx to the vesicle core. It is also a possibility that the increased length of the hydrophobic region of the polymer (4000 when compared to 1300 of the PDB-PEO system) would lead to decreased permeability prior to electroporation. This would significantly reduce leakage of NaOH out of the polymersome. Leading to a higher concentration of reactant being present in the vesicle core during electroporation. This would support the observation of a slight increase in both vesicle size and polydispersity after electroporation.

Furthermore, the voltage the polymersomes are able to withstand is orders of magnitude higher than previously reported values for suspended membranes of PMOXA-PDMS-PMOXA. A voltage of 750 V was applied to the polymersomes five times, and this did not cause breakdown of the polymer membrane. This can be compared to a previously reported breakdown voltage  $1 \pm 0.2$  V and  $1.5 \pm 0.2$  V following polymerisation for a suspended membrane.<sup>100b</sup> Although there is not complete breakdown of the polymersomes following electroporation, there is a distinct change in their size distribution and morphology (figure 6.10 a & b). The polymersomes appear much more robust than previous membrane studies have demonstrated,<sup>100b</sup> with significant changes in the size and shape of the polymersomes. Post electroporation, polymersomes form a dual population at 20 and 60 nm, which give an average polymersome size of  $43 \pm 12$  nm.

### 6.3.2.2 PORE FORMATION IN *TRI-BLOCK* POLYMERS

Polymersomes also appear to be misshapen when compared to the non-electroporated control sample, (Figure 6.10 a) and to other di-block polymersomes. Di-block polymersomes are able to maintain their shape following the application of voltages up to 2500 V.<sup>7</sup> For these reasons, it is believed that the electroporation pore formation and molecular rearrangement of the membrane in a tri-block co-polymer differs substantially from bilayer arrangements previously reported.<sup>161</sup>

It is reasonable to believe that the generally accepted theories of electroporation, both the transient aqueous pore mechanism<sup>159a, 160b, 194</sup> and the water wire mechanism<sup>195</sup> could both cause membrane pore formation, as there is currently insufficient evidence to draw a firm conclusion. However, these mechanisms are based on bilayer membrane arrangements composed of molecules with a single hydrophobic and single hydrophilic region. The new single-layer membrane ABA tri-block polymersome differs from this model, and as such will likely yield significantly different results upon electroporation. This should be able to contribute to electroporation theory and the establishment of a conclusive mechanism.

It has previously been proposed by both Lomora<sup>196</sup> and IteI<sup>197</sup> that the *tri-block* polymers could completely double over on itself, in a configuration analogous to a “hairpin”, which would render them equivalent to a di-block or lipid, thus assembling to form a bilayer equivalent to a lipid bilayer (as shown by Figure 6.11 b). However further analysis would be required to investigate whether this is possible for a polymer with a molar mass as large as 4000 g/mol; such as the polymer used here, this could include more detailed studies on the polymersomes mechanical properties (such as the elasticity and bending modulus) or more involved and accurate techniques such as neutron scattering. More achievable measurements could come from Cryo-EM analysis, which should allow for more accurate bilayer thickness measurements, which may give an indication as to how the polymer is assembling.

While this may be the case, the *tri-block* magneto-polymersomes are distinctly different to those formed with lipids and di-block co-polymers, in that there is electron dense material also within the core of the vesicle which gradually lessens towards the vesicle extremities. Therefore, it is possible that a different mechanism is in play. One hypothesis is that because the membrane is one unit (a single polymer as opposed to 2 polymers forming a bilayer), this would mean that head group rearrangement to form a pore is restricted (Figure 6.11). A mechanism for the polymers rearrangement during electroporation may be due to the mechanical properties arising from the *tri-block* composition of PMOXA-PDMS-PMOXA. Flexibility within the tri-block polymer membrane could mean that the introduction of polar water molecules into the membrane by electroporation could cause the polymer to bend over on itself to shield the hydrophobic region of its structure (Figure 6.11 c).

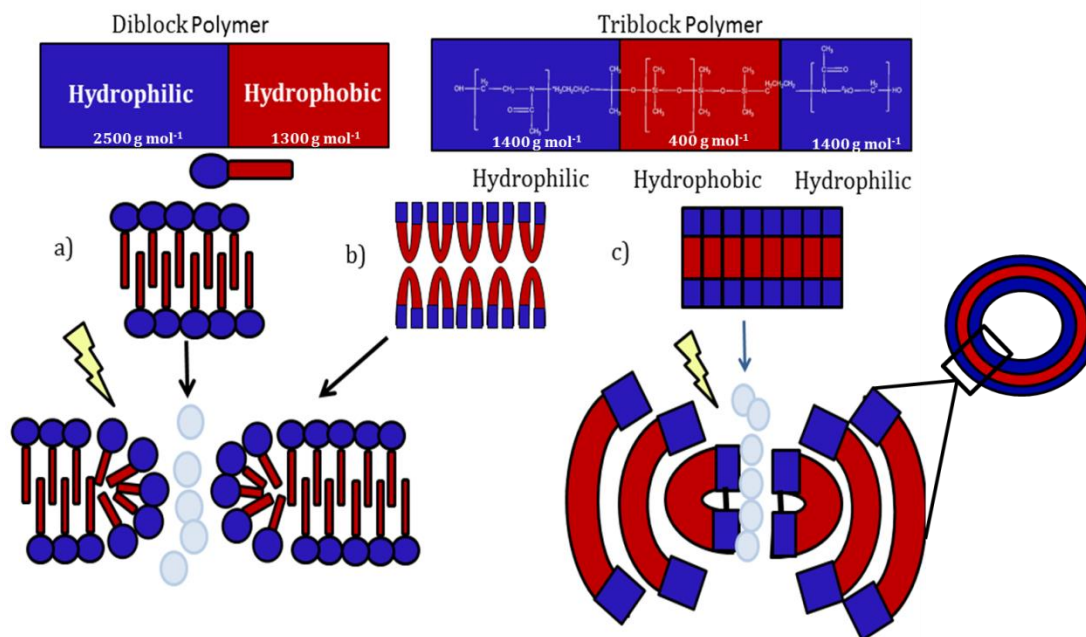


**Figure 6.11:** Schematic of our hypothesis of the formation of pores by electroporation. a) Shows the case for a lipid or di-block polymers. The PMOXA-PDMS-PMOXA tri-block membrane could self-assemble in one of two ways: b) shows a schematic of the completely fold over hairpin-like membrane form analogous to a more traditional bilayer, which can then follow the same mechanisms for electroporation as a), and c) shows the tri-block assembly as a monolayer and on electroporation bend over on it-self to shield the hydrophobic region of it structure.

This is possible due to both the length of the membrane and its high flexibility. The driving force of this rearrangement is that adopting a bent configuration would likely be more entropically favourable than interactions between the PDMS and water.

Furthermore, the distortion observed post electroporation (which has not been the case with other materials explored) suggests that electroporation and mineralisation is more destructive to the integrity of the polymersome morphology than for the di-block and phospholipid bilayer vesicles. It may be that, for the tri-block polymersomes, the electroporation process is not as reversible as with polar head rearrangement seen for di-block and lipid membranes. This may be due to interactions between the reactive PMOXA end groups on the polymer (Figure 6.11 c) maintaining the pores, or the extreme bending of the polymer damaging its structure. In each case this is likely to be the cause of both the change in polymersome morphology and increase in particles observed, as well as more MNP density in the core as the pore are retained.

This theory could be proven by applying the same method to tri-block polymer possessing a smaller hydrophobic region. Decreasing the hydrophobic region would reduce flexibility and ability to shield the hydrophobic region, possibly resulting in less poration or no poration, with high fields resulting in membrane breakdown.

### 6.3.3 CARBOXYLIC ACID TERMINATED RAFT SYNTHESISED POLYMERSOMES

PEG-PHPMA / PMPC-PHPMA polymersomes, have been designed by the group of Professor Stephen Armes, (University of Sheffield) to assemble so that the carboxylic acid groups of the PHPMA monomer are displayed on the inner membrane of the polymersome. This can be used to mimic the nucleation properties of the MTB biomineralisation proteins, which are rich in carboxylic acids. These polymersomes were electroporated with the same iron ion solution as used with other polymers tested. Unstained TEM images (Figure 6.12) suggests electroporation was successful for the PGMA polymersomes. This is the case for both those with the unprocessed polymer (Figure 6.12 a) and with the presence of an ethylene glycol dimethylacrylate (EGDMA) cross-linker (Figure 6.12 b), as all have dark, electron dense cores, which is expected to be iron oxide.

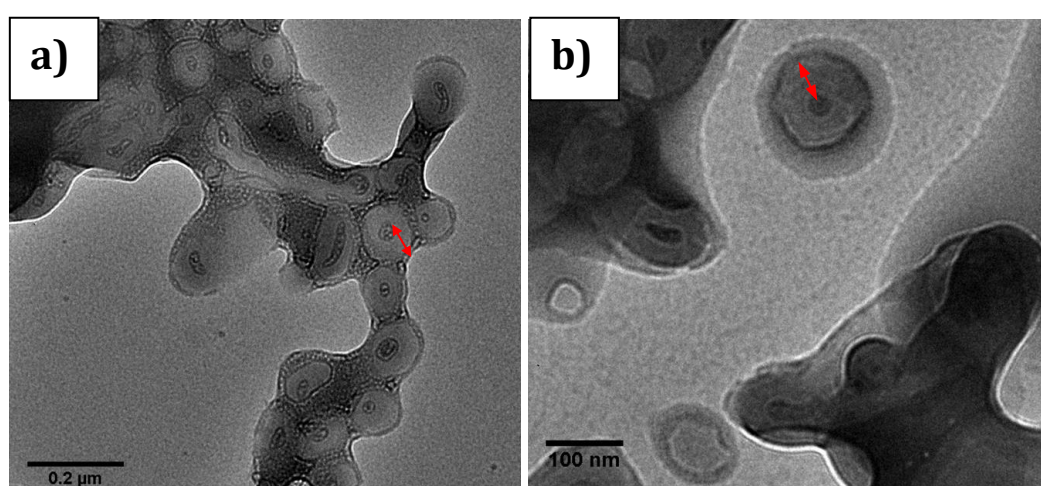


**Figure 6.12:** TEM micrographs of PEG-PHPMA / PMPC-PHPMA polymersomes encapsulating NaOH (10 mM) a) without and b) addition of EGDMA cross-linker. Polymersomes were electroporated (750 V, 5 times) in the presence of 1:2 Fe(II):Fe(III) solution. (Red arrows indicate polymersome membrane)

However these results differed from electroporation of the other polymersomes. In this case, electron dense material seems to fill the entire core of the polymersomes. TEM shows vesicle membranes which are much wider, at 50 nm, than those seen before (Figure 6.12). It has been shown by Warren *et al*<sup>2a</sup> that as the PHPMA molecular weight increases the polymersome membrane grows exclusively inwards, eventually leading to vesicle death.<sup>2a</sup> This increase in membrane width is likely to affect the polymersome properties, particularly under electroporation (to look more like the PMPC<sub>32</sub> sample (chapter 4)). More notably, there is a dark ring around the outside of each polymersome, which also seems to have caused aggregation of the vesicles. There is a dark vesicle core which is equally electron dense to the outer layer of the polymersomes (Figure 6.12 b), suggesting that incorporation of the carboxylic acids groups into the polymer are on both leaflets of the bilayer causing the additional nucleation of iron oxide around the outer rim of the polymersomes.

## 6.4 OPTIMISATION OF ELECTROPORATION

In an effort to optimise the electroporation process and understand the mechanisms of membrane rearrangement on application of the electric field, a varied voltage, reagent concentration and number of pulse were applied to the polymersome sample. These experiments were carried out on three examples of different types of membranes, a di-block polymer membrane (PBD-PEO), a tri-block membrane (PMOXA-PDMS-PMOXA), and a lipid membrane (DSPC). The amount of electron dense material present in the vesicles was analysed after the samples were cleaned using SEC, to remove any unreacted soluble iron precipitate or iron oxide that had not been successfully incorporated into or on the polymer. Vesicles were dissolved in nitric acid (5 ml total sample volume, 4 part water to 1 part acid) and analysed using ICP-MS.

When PBD-PEO polymersomes were electroporated between 250 and 2500 V, a general trend of increasing incorporation of iron is observed with increasing voltage, (measurement obtained from iron content in ICP-MS) (Figure 6.13). This is presumed to be due to a higher voltage being able to open larger pores in the membrane. It may also be that the higher voltage resulted in deeper penetration of the membrane, with pores having longer lifetimes, both of which could lead to the observed increased iron incorporation.

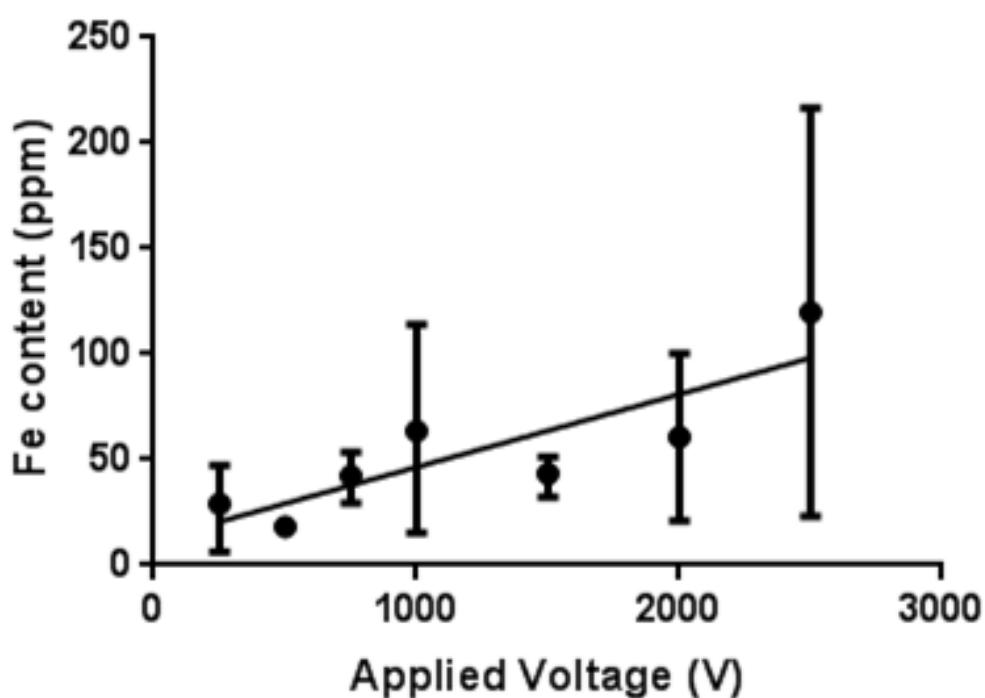


**FIGURE 6.13:** ICP-MS iron of PBD-PEO magneto-polymersomes content measured as a function of the voltage applied to the polymersomes during electroporation showing increasing iron incorporation with increased electroporation voltage.

It can be presumed that the iron in the ICP-MS sample (within error) is tightly associated with polymersomes, as they have been passed through the SEC column after electroporation. This means that any external iron precipitate in the sample should have been removed by a combination of SEC and centrifugation. When, at a low voltage of 200 V, the number of pulses applied to the sample is increased from 2 to 50 pulses, iron content as measured by ICP-MS also increases (Figure 6.14 a).

It is perhaps surprising that the polymersomes are able to withstand the application of 50 pulses. By applying a low voltage multiple times, it is expected that fewer, smaller pores will be opened each time. As more pulses are applied, this will slowly build up the number and/or size of particles precipitated in the membrane. This will depend on whether each pulse opens new pores in the membrane (more NPs) or if previous NP containing pores are re-opened (larger NPs). In either case, this will allow an increased mass of iron to precipitate within the membrane, with each pulse applied to the polymer (Figure 6.14 a).

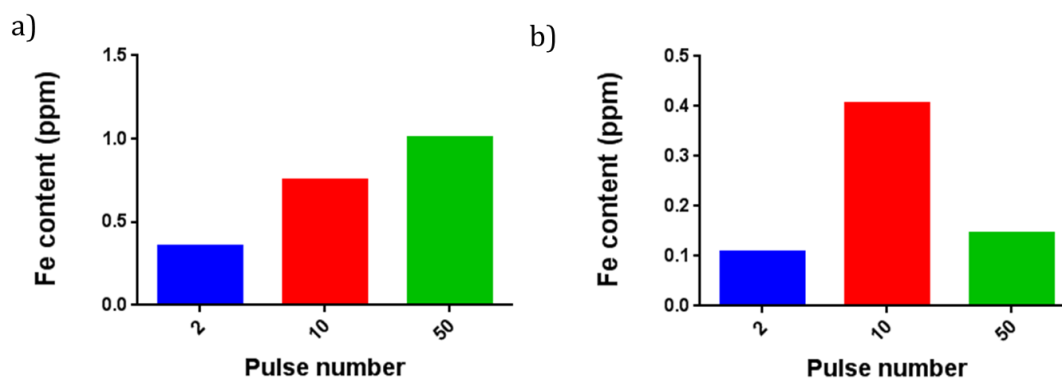


**Figure 6.14:** Iron content (ppm) in magnetopolymersome samples as a function of the number of pulses applied to the sample at a) 200 V and b) 1000 V.

This same trend is not observed when the pulse number is varied at higher voltages (1000 V) (Figure 6.14). In all cases, the Fe content is lower for these samples electroporated at higher applied voltages. A huge (4 fold) increase of iron content is observed when the number of pulses is increased from 2 to 10 pulses (the same pulse increase at 200 V for the same range is only 2 fold). However, the iron content at 50 pulses returns to a much lower level, similar to iron content seen at 2 pulses when the applied voltage is 1000 V. Whereas at 200 V a further increase occurs, at the higher voltage of 1000 V, a dramatic decrease in the polymersome iron content ensues, back down to a ppm level which is comparable to that obtained with just 2 pulses (Figure 6.14 b). The reason for this decrease is unclear, but one possible explanation could be that the vesicle structure is compromised after the large high number of voltage pulses.

Further analysis is required to confirm if vesicles are still present following electroporation under these most extreme conditions. It is likely that there are optimum critical values between 10 and 50 pulses, at which point maximum iron oxide precipitation is reached.

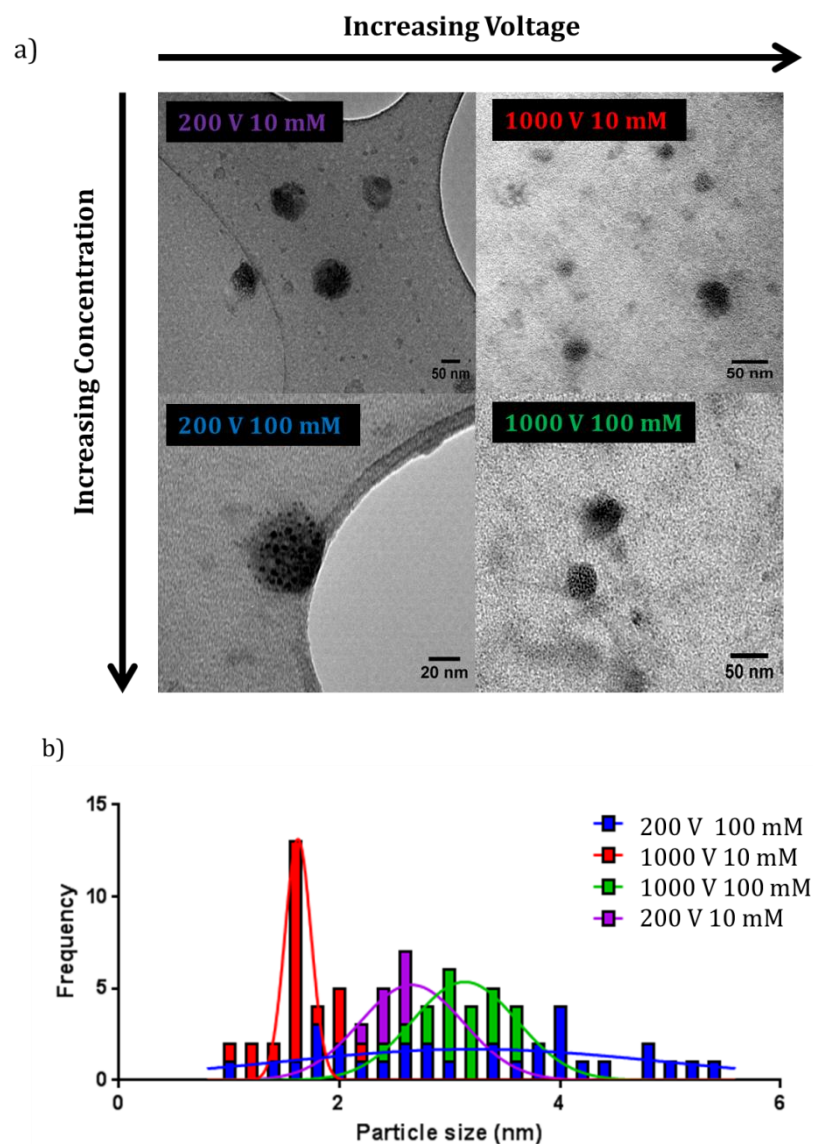


**Figure 6.15:** a) TEM micrographs of polymersomes after electroporation at different voltages and increasing NaOH concentration (as labelled). b) Shows the corresponding MNP grainsize analysis for each sample.

By exploration of this matrix, and by fine tuning of the number of pulses at each voltage, an optimum pulse number for maximum precipitation could be extrapolated for each applied voltage, by further work. The most telling results for the mechanisms of electroporation come from TEM micrographs electroporated at the two extreme voltages (200 V and 1000 V). As the voltage is increased five-fold, and NaOH concentration kept constant, the number of nanoparticles in each polymersome increases approximately three-fold (as determined by visual inspection), (Figure 6.15 a), but the particle size decreases dramatically (Figure 6.15 b).

Furthermore, applying a fixed voltage to samples containing increasing concentrations of NaOH and mixed valence iron solution increases the number of particles present but has less effect on the particle size. This suggests a mechanism where once the pore has been opened the more reagent there is present, the more the particle can grow; perhaps even sustaining the lifetime of the pore by continued precipitation. It is also possible that, at a lower voltage, the pores are wider or open for longer, either of which would also lead to increased particle size. Increasing voltage seems to also have an effect on cross-membrane transport and subsequent precipitation, by increasing the number of pores in the membrane per pulse applied. This therefore increases the number of opportunities for precipitation, hence increasing the number of particles per polymersome.

Electroporation of the PMOXA-PDMS-PMOXA membrane was also carried out at three different voltages: 200, 750 and 1500 V. ICP-MS was used to assess the iron content in each polymersome sample after electroporation (Figure 6.16).

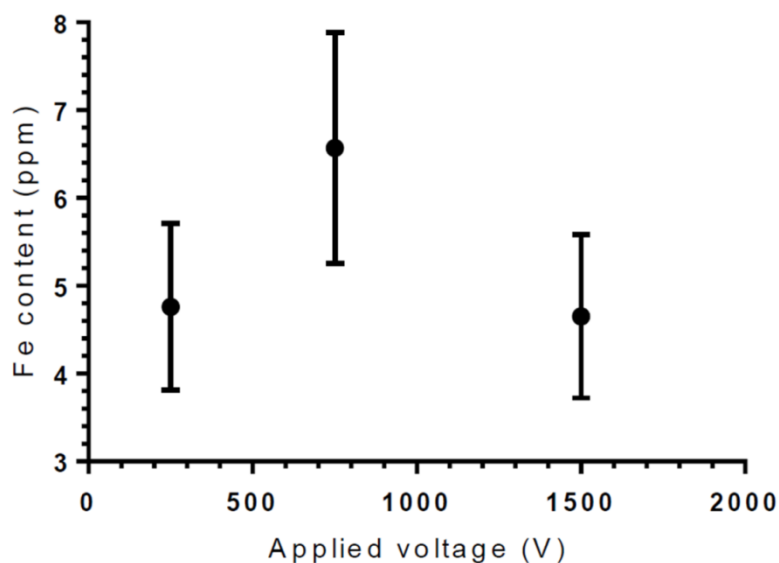


**Figure 6.16:** ICP-MS iron content (ppm) of magneto-polymersomes as a function of the voltage applied to tri-block polymersomes during electroporation with varied electroporation applied voltage.

The largest amount of iron was observed for 750 V (6.5 ppm), suggesting this is the optimal voltage to carry out electroporation at; this value is in agreement with studies presented in chapter 7.

The use of significantly lower voltages (200 V) may lead to poration which does not fully penetrate through the entire membrane, or fewer pores opening, limiting iron ion permeation into the vesicle. Conversely, larger voltages may lead to ions or base leaking through the pores before they are able to react. This forms the basis of working hypothesis that pores formed at lower electroporation voltages are either larger or more stable, allowing increased precipitation within the membrane. Whereas at higher voltage, pores may be smaller and/or close more quickly and therefore the resulting particles are much smaller. As with other studies in this chapter, more in depth investigation is required to confirm these results and further optimisation is required (e.g. temperature, ratio of iron ions in solution, type of polymersomes electroporated) which will likely affect the outcome of electroporation.

## **6.5 ROOM TEMPERATURE: INCORPORATION OF IRON INTO RAFT POLYMERSOMES**

PEG-PHMPA/PMPCA-PHPMA was of particular interest, due to the COOH group on the PHMPA monomer. It is hypothesised that the addition of these groups will mimic the ferrous ion binding sites of the Mms6 protein as a possible nucleation site on the inner leaflet of the polymersome for precipitation of magnetite in natural magnetsomes. Should it be possible to preferentially place all of these groups on the inner leaflet of the vesicle, this should create a synthetic mimic of the proteins incorporated into the MTB membrane. To attempt to achieve this, the EGDMA cross-linker was incorporated into some samples in an attempt to lock all of the COOH groups on the inside of the vesicle and avoid bilayer “flip-flop” turning these acidic moieties to the external surface of the vesicles.

These polymersomes assemble as part of the polymer synthesis process, and in some cases are pre-cross-linked. Therefore, the same method of encapsulation during rehydration could not be employed as was used with the other liposomes and polymersomes. Instead, these pre-formed polymersomes were left in solution with 10 mM  $\text{Fe}^{2+}$  solution for 4 days to ensure diffusion of iron into polymersomes.

This differs from the usual stoichiometric ratio of ferrous to ferric iron (1:2), as the carboxylic acid groups on the PHPMA polymer are expected to bind only ferrous iron (mimicking the biomineralisation proteins in MTB). These iron soaked samples were then cleaned using SEC before NaOH was added to mineralise these RAFT polymersomes. TEM images (Figure 6.17 a) obtained from the non-cross-linked PEG-PHPMA/PMPC-PHPMA polymersomes show a monodisperse vesicle population, with dark rings on the inner and outer leaflet of the polymersomes. This suggests chelation of electron dense material to the carboxylic acids on the polymersome membrane surfaces, but limited nucleation within the vesicle core. This is likely to be due to the concentration of iron ions being too low. There are multiple reasons for this low concentration such as: nucleation on the outer polymersome leaflet which could prevent permeation of the ferrous ions to the core, or low permeability of the ferrous ions through the membrane, independent of the concentration. However when this experiment was repeated on multiple occasions, unstained TEM images (Figure 6.17 b) showed polymersomes that do not have a dark core, indicating the membrane may be impermeable to ferrous ions, as suggested by the earlier experiment. Therefore mineralisation of these pre-formed polymersomes is unreliable and not reproducible, which is far from ideal for carrying forwards.

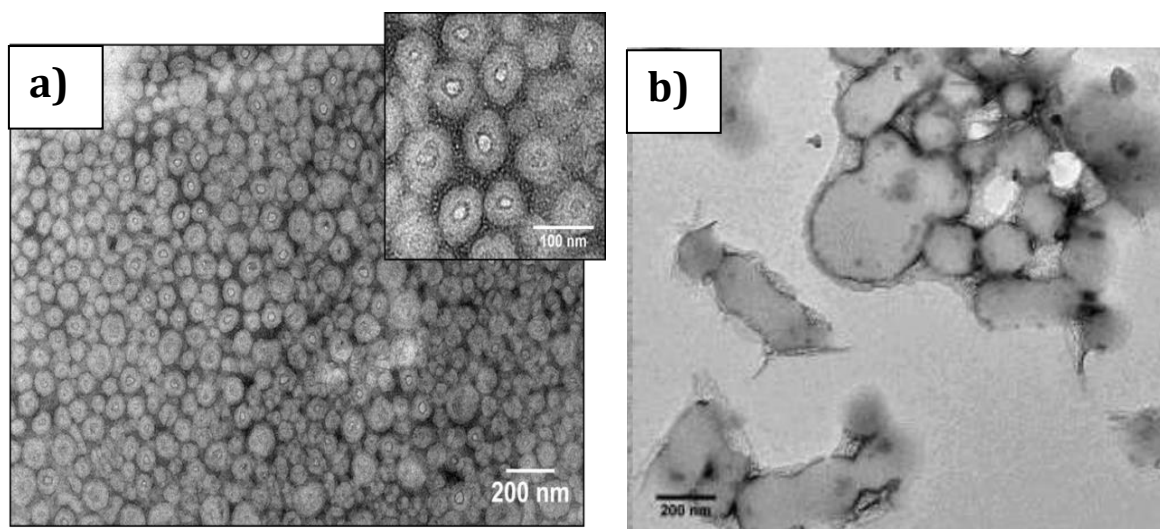


**Figure 5.17:** PEG-PHPMA / PMPC-PHPMA polymersomes, after being soaked in iron ion solution for 4 days. As can be seen in a) electron dense material is chelated to both the inner and outer leaflet, whereas compared to b) in which the electron dense material appears to chelate only to the outside of the polymersomes.

To assess the success of the iron oxide precipitation TEM images on cross linked and non-cross-linked polymer after clean up *via* SEC were taken (Figure 6.17). These dark areas remain attached, even after samples were cleaned up using SEC, and so should still be functional for ferrous ion binding. It appears overall that nanoparticles have formed both inside and outside these structures. This suggests that carboxylic acid groups are displayed on both sides of the polymersomes, in spite of efforts to orientate them exclusively on the inside. More investigation is required to understand exactly why there is intermittent uptake of iron (Figure 6.17 a) and b). Perhaps, more importantly, these groups do seem to be involved in coordinating the growing nanocrystal by mimicking the Mms6 nucleation site. This is certainly at least a proof of concept for the use of polymers and synthetic amino acid mimics such as these to carry out biomineralisation reactions inside vesicles.

A second and unique method to precipitate iron oxide inside the PGMA polymersomes was developed, in which polymersomes encapsulating NaOH were added to a room temperature co-precipitation (RTCP) magnetite synthesis (Figure 6.18). The reaction uses stoichiometric amounts of base and iron ions (outside of the polymersomes) to produce magnetite.

It was hypothesised that, by addition of the polymersomes to the reaction, some of the mineralisation reaction would occur within the polymersome by diffusion of the reactants. To allow full conversion to magnetite from other iron oxides, the reaction mixture was left overnight to mature.

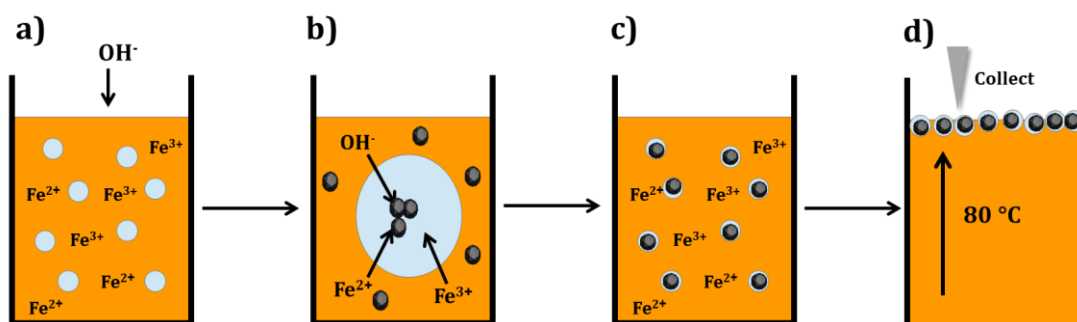


**Figure 6.18:** Schematic of room temperature precipitation incorporation into polymersomes a) pre-formed polymersomes are added to the mixed valence iron solution of a room temperature coprecipitation (section 2.1.1). b) As the precipitation reaction proceeds, it is anticipated that permeation of the reagents (iron and hydroxyl ions) through the vesicle membrane will result in c) precipitation of magnetite within the polymersomes core, d) polymersomes are collected by heating the solution to 80 °C, at which point the polymer flocculates to the top of the solution and can be collected.

After magnetic separation, two layers were observed: a bottom layer of black particles, and a top white layer of polymersomes. The polymersomes were speckled with orange and black, suggesting incorporation of iron oxide. To separate polymersomes from any external precipitate, samples were heated to 80°, the heating step causes the polymer to flocculate to the top of the reaction vessel. A dirty white layer, which is thought to contain polymersomes with encapsulated nanoparticles was subsequently removed from the rest of the solution. TEM images of this layer (Figure 6.19) suggest incorporation of iron oxide was successful in all samples, as a dark electron dense core can be seen in the polymersomes, although further characterisation and optimisation is required to demonstrate if it is magnetite, and if the nanoparticles are within the vesicle lumen.

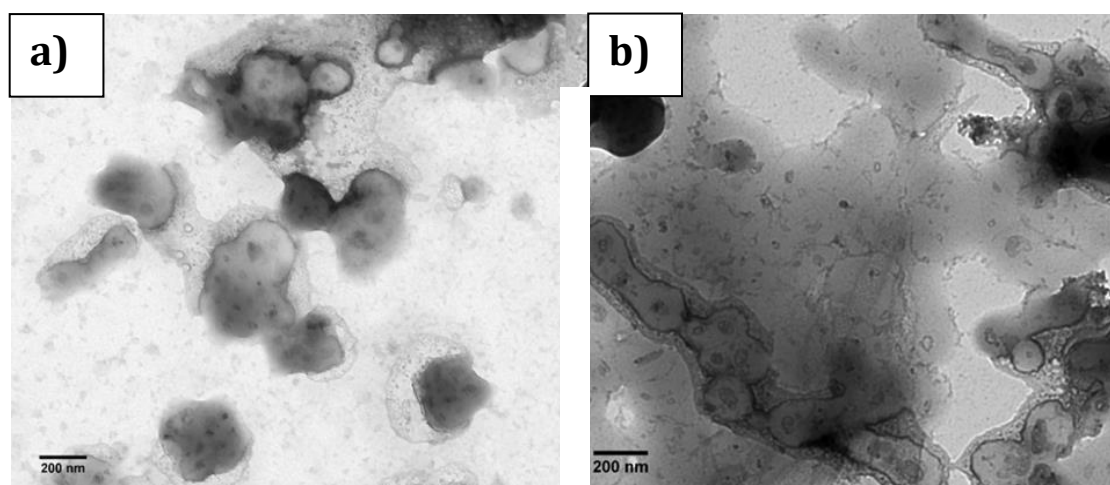


**Figure 6.19:** Incorporation of iron oxide by incubation of PEG-PHPMA / PMPC-PHPMA polymersomes, in a room temperature co-precipitation reaction a) without and b) with cross-linker. The mineralisation in this case was carried out with both iron salts and base on the exterior of the pre-made polymersomes.

## 6.6 DISCUSSION OF SYNTHETIC TRANSPORT SYSTEMS

This chapter documents the first time electroporation has been used to permeate synthetic vesicle biomineralisation nanoreactors. The advantage of this method is that it is a simple process (far less complex than incorporating biological trans-membrane transporters). With optimisation, electroporation may also offer greater templated control of the inorganic metal oxide precipitation reaction being encapsulated. This should allow the development of magnetically tuneable vesicles. The hypothesis for the mechanism of electroporation (Figure 6.5) is that it induces pore formation. In these vesicles, this should enable the simultaneous efflux of base and influx of iron through the pores to mix the reagents and equilibrate the pH gradient. It appears that this occurs at a mixing boundary within the membrane, yielding the crystallisation of multiple membrane embedded MNPs templated within the electroporated pores.

In the case of the lipids tested, the room temperature co-precipitation route appeared more amenable for use in conjunction with electroporation, although none of the lipid samples gave high amounts of monodispersed nanoparticles or a single nanoparticle in the vesicle core. All liposome samples appear to contain aggregated non-liposomally associated lipid residue.

Overall, the liposomes are able to maintain their structural integrity following electroporation for the room temperature route to precipitation, with the vesicles for the most part remaining intact and almost identical in size and morphology to those imaged before the voltage was applied. For DPPE-PEG 5000 and DPPC, precipitation was finite with limited precipitation in the core. It is unclear (due to lack of an appropriate assay) whether this is due to low base encapsulation or limited electroporation success. The resulting precipitate was relatively heterogeneous where encapsulation and uptake of iron ions appeared much more successful (DOPC/DSPC). There appears to be a homogenous amorphous species which fills the core, in addition there is also a suite of smaller more electron dense heterogeneous NPs. For DSPC, the amount of this precipitate also varies considerably between vesicles in the same sample. In the case of the  $\text{CO}(\text{NH}_2)_2$ , most lipids did not appear to withstand the four hour heating step necessary for the decomposition of urea to ammonium hydroxide, except in the case of DPPC liposomes. The DPPC liposomes were formed at temperatures above the  $T_g$  of the lipid, which appears to yield more stable liposomes. On the whole, liposomes do not fare well under the harsh heating conditions necessary to thermally decompose urea. For this reason, polymersomes were deemed to be possibly a more robust route to the formation of vesicle templated magnetic nanoparticles. As such, polymersomes were trialled in identical experiments.

Polymersomes were formed that encapsulate either NaOH or urea to be used in the two different magnetite precipitation routes. Once electroporated, they were then left to age (NaOH) or heated (urea) depending on the encapsulate, to induce magnetite precipitation. In the case of the PBD-PEO and PMOXA-PDMA-PMOXA polymersomes they were tested for the *in situ* formation of MNPs within a vesicle. The diameter of magneto-polymersomes was shown to be uniform by DLS and TEM, with no signs of aggregation. The mineralised polymersomes are embedded with electron dense NPs, presumed to be iron oxide. These NPs vary in size depending on the electroporation conditions used (Figure 6.15). Further optimisation of the reactant concentrations can alter the rate of influx and efflux of substances across the membrane, due to the basic principles of osmosis and diffusion. Figure 6.16 demonstrates the first steps towards a tuneable method of nanoreactor encapsulated magnetite synthesis, and offers flexibility with respect to designing the number and size of the MNPs within the membrane simply by altering the reagent concentration and/or the electroporation parameters.

Whilst these results are by no means conclusive with regards to explaining the mechanism of electroporation as applied to polymersomes, it does shed light on some of the theories in the literature. However, to truly understand the mechanism of electroporation and to obtain full control over the nanoreactor bounded mineralisation process is likely to be the subject of another full thesis.

Interesting results were gathered with the carboxylic acid terminated polymers PEG-PPHMA / PMPC-PPHMA. The addition of the carboxylic acid groups appeared to be effective in the nucleation of iron ions and precipitation of iron oxide. However, the electron dense material seems to be precipitating on both the inner and outer leaflet of the polymersomes, with the internal precipitation appearing more limited. Further investigation is required to determine whether this limited precipitation is due to an issue with reactant concentration, or if it is due to the location of a proportion of the carboxylic acid groups on the outer leaflet of the polymersomes. Despite this double edged mineralisation, these data are extremely promising, as the mineralisation method appears to have been effective. However, as with all of these methods, further optimisation is required with respect to maximising trans-membrane iron ion transport. Control over the arrangement of the carboxylic acids groups to exclusively display on the inner leaflet of the polymersomes (by modification of the polymer chain lengths), could well solve this issue and ensure that internal polymersome mineralisation is heavily favoured.

# CHAPTER 7:

---

## HIGH-THROUGHPUT SYNTHESIS AND ELECTROPORATION OF VESICLES

## 7.1 INTRODUCTION TO HIGH-THROUGHPUT SYNTHESIS USING ELECTROHYDRODYNAMIC ATOMISATION (EHDA)

Although monodisperse vesicle populations can be achieved using conventional processes such as tip sonication and extrusion (Section 4.2.2), for large-scale production of vesicles, they do not constitute feasible methods as they are time-consuming and difficult to scale above microgram quantities (particularly with regards to extrusion). To achieve commercially viable yields of monodisperse vesicles, other more high-throughput methods of production have been explored.

Taking an engineering approach to high-throughput synthesis of vesicle formation led to collaboration with the Edirisinghe group, at the Department of Mechanical Engineering University College London (UCL). The Edirisinghe group have designed multiple ways to synthesise vesicles based on a method termed Electrohydrodynamic Atomisation (EHDA). In EHDA, fluid is delivered through a needle under an electric field.<sup>113-114</sup> The technique has traditionally been used for the high-throughput production of microbubbles, solid nanoparticles and some forms of electrospinning.<sup>113-114</sup>

Briefly, EHDA comprises the lipid or polymer solution delivery at an optimised rate, *via* a syringe driver. The solution is then fed through a capillary needle of a specific length; this length depends on both the material used and the desired end morphology (Figure 7.1). The capillary can be single (EHDA), co-axial (CEHDA) or also multi-junction (for example, T-junctions). Each of which allow various methods of delivery to be explored with multiple solutions incorporated at varying points in the synthesis. The electric potential delivered across the end of the capillary causes the breakdown of the solution into monodisperse droplets; in the case of bubbles or droplets (Figure 7.1). This droplet size determines the size of the end particle, and is regulated by the voltage applied to the capillary; in the order of kV. The polydispersity of the population achieved *via* EHDA/CEHDA is controlled by the jetting mode used; which is again determined by the applied voltage. The various jetting modes achievable include, a single conejet; producing the most monodisperse populations. Bi-jet and multi-jetting is also possible, with the polydispersity of the sample gradually increasing as the jets multiply.

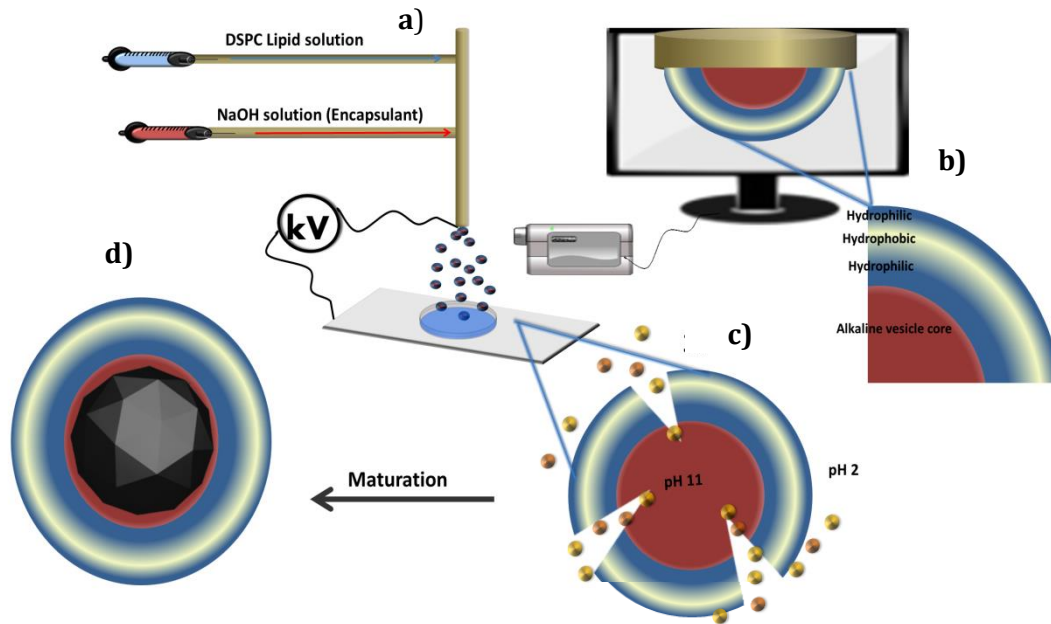


**Figure 7.1:** Schematic diagram showing experimental set-up for the electrohydrodynamic production of artificial magnetosomes. a) Encapsulation of NaOH within DSPC liposomes *via* the EHDA jetting system, b) showing the composition of the EHDA formed vesicles, c) before being introduced to mixed valence iron solution which is consequently electroporated at 750 V, d) to yield a magnetic nanoparticle within the vesicle core (artificial magnetosome).

The synthesis of vesicles *via* EHDA is a novel process jointly developed the Staniland/Edirisinghe groups, specifically between myself and Dr Poonam Kaushik Bakhshi from the Edirisinghe group, for the high-throughput synthesis of artificial magnetosomes. Throughout the optimisation of the EHDA magneto-vesicle synthesis, parameters such as needle length, flow rate and applied voltage were both explored and optimised, using both EHDA and CEHDA, for lipid and polymer systems. The successful synthesis of an artificial magnetosome lipid system was the aim of this work, but at a higher yield than other methods explored thus far. As with all other studies throughout this project, the system is designed to mimic the invagination of the cytoplasmic membrane in MTB to form an empty magnetosome. In this case with the DSPC assembly process, this occurs as the lipid is delivered to the end of the capillary, at the point where the lipid flow is broken down into monodisperse droplets, giving rise to self-assembly of the lipid into a vesicle.

The results and discussion throughout this chapter is based on the joint first author publication Bakshi/Bain *et al.*<sup>198</sup>

## 7.2 HIGH THROUGHPUT VESICLE FORMATION USING EHDA

The size and morphology of the MTB magnetosomes is a key advantage when compared to conventionally synthesised, non-biogenic MNPs. Therefore, an essential property of an artificial magnetosome system must be tight control.<sup>39b, 58a, 199</sup> Making artificial magnetosomes using EHDA offers a high-yield route to more adaptable functional MNPs, and represents an excellent model system for biomineralisation. Throughout the chapter this goal is achieved by the formation of lipid vesicles using the high-throughput electrohydrodynamic atomisation (EHDA) methodology. EHDA vesicles were porated by way of electroporation (as described in chapter 6), to transport iron into the vesicle core, to encourage magnetite crystallisation. A single-crystal iron oxide nanoparticle was precipitated within each liposome, forming a near-monodisperse population. The particles were assessed by TEM, Cryo-EM, fluorescence microscopy, DLS, Raman spectroscopy and magnetic susceptibility measurements. The results indicate the potential for a commercially viable route of producing very high-yields of artificial magnetosomes.

### 7.2.1 OPTIMISATION OF EHDA

Several of the materials discussed throughout chapter 4 were used to determine the ideal lipid or polymer material combinations in the optimisation of artificial magnetosome synthesis *via* EHDA. The results of previous vesicle formation experiments using these materials (chapter 4) differed considerably to the results presented throughout this chapter. This is presumably due to the introduction of the applied voltage during EHDA altering the assembly process.

Specifically, the synthesis of DSPC vesicle using the EHDA technique produces a much more monodisperse population when compared to synthesis *via* methods such as tip sonication and extrusion. Due to the large volumes of lipid and/or polymer needed to run the EHDA experiment, not all materials investigated in Chapter 4 were suitable for EHDA vesicle synthesis. For example, the expensive DPhPC produced possibly the best vesicles in chapter 4, however the large amount of lipid that would be required to repeat this experiment make the cost of using this lipid unfeasible. Initial experiments have been carried out using the EHDA equipment at the Erdisinghe lab (UCL) by Dr Poonam Bakshi, who optimised the needle length to be used. Experiments were performed on both the single and co-axial capillary systems using a wide variety of materials and material combinations. For the observation of the slurry during EHDA jetting, a high speed camera (Weinberger AG, Dietikon, Switzerland) was connected to a computer and a fibre optic light source was used for illumination. Data were recorded at 138 frame s<sup>-1</sup> and shutter control was 1/140 s. Samples were then analysed using both DLS sizing and conventional TEM images (performed by Dr. Bakshi)

### 7.2.1.1 SINGLE-AXIAL EXPERIMENTS

The conventional polymersome synthesis method requires up to 24 hours of stirring to fully rehydrate a polymer film, with regards to the polymer-base solutions tested. In the case of an EHDA polymer sample, the polymer film rehydration was not used. Instead, for single axial experiments, a 17% (w/v) polymer in ethanol solution was added to the appropriate base. It is possible that some polymersome self-assembly may occur prior to EHDA in the syringe pump, before being passed through the EHDA capillary. However, it is thought that any assembly that had occurred would disassemble and subsequently re-assemble, in a similar manner to that seen during extrusion (Section 4.2.2), or at the very least modified by the effects of passing the solution through the EHDA. In each case, the solution produced by the EHDA in various jetting modes<sup>115</sup> were collected in an iron solution (Fe<sup>2+</sup>/Fe<sup>3+</sup> 2:1) and subsequently electroporated. The distance between the needle tip and the iron solution bath was 120-150 mm.

Material	Solute	Applied Voltage (kV)	Flow rate	Jetting mode	Collection fluid	DLS (average size) (nm)
DSPC (10 mg/ml)	NaOH	15	15 $\mu$ l/min	Conejet	Iron	106 (Very broad)
DSPC (1 mg/ml)	EtOH/NaOH	17.7	20 $\mu$ l/min	Conejet	Water	295
DOPC (0.5 mg/ml)	NaOH	16.7	15 $\mu$ l/min	Conejet	Iron	220
DOPC (0.5 mg/ml)/ DSPC (1mg/ml)	NaOH/EtOH	15.6	15 $\mu$ l/min	Conejet	Water	712
Stearyl acetate/Ethyl Cellulose (40/60)	NaOH	14	15 $\mu$ l/min	Conejet	Iron	164/32
Stearyl acetate/Ethyl Cellulose (20/5)	NaOH	16.4	15 $\mu$ l/min	Conejet	Iron	78 (Broad)
Stearyl acetate/Ethyl Cellulose (20/5)	EtOH	16.4	15 $\mu$ l/min	Conejet	Water	58
PMOXA-PDMA-PMOXA (17% by weight)	EtOH	16.8	15 $\mu$ l/min	Conejet	Iron	1000
PEO-40 Stearate (5% solution)	EtOH	16.7	15 $\mu$ l/min	Conejet	Iron	1000-2000
PBD-PEO (10 mg/ml)	NaOH	15.3	15 $\mu$ l/min	Conejet	Iron	58
		15.6			Water	122

**Table 7.1:** Single axial experiments performed on various lipid and polymer material.

DSPC liposome formation was tested using the single axial EHDA system. The resulting TEM images (Figure 7.2 a) (i)) show much improved liposomes of a relatively monodisperse size of  $106 \pm 22$  nm when compared to liposomes synthesised *via* tip sonication ( $192 \pm 39$  nm). Experiments were also carried out using an A-B-A *tri-block* copolymer (PMOXA–PDMS–PMOXA, 17% w/v solution in ethanol) (Table 7.1).

Optical microscopy images (Figure 7.2 b) (i)) suggests that nanoscale vesicles were not present in solution, but more likely to be polymer micro-particles, produced by the EHDA system. The most likely composition of these particles is as a mixture of polymer and base that, due to variation in solute and solution, have remained stable.

TEM carried out on the PMOXA–PDMS–PMOXA EDHA produced particles showed only a small number of dark spots on the grid. As there is no distinct structure to the particles, they are unlikely to be vesicles. Also tested was an amphiphilic commercially available polymer (PEO-Stearate 40 5% w/v solution) purchased from Sigma Aldrich. Again, optical microscopy images suggested the presence of polymer particles on the microscale.

TEM imaging of the PEO-Stearate sample (Figure 7.2 c) (i)) show an electron dense material, which is likely to be crystalline iron oxide. This has precipitated due to the presence of un-encapsulated base during the atomisation process, which has led to uncontrolled precipitation in the iron solution.

The TEM micrographs also show what appears to be residual polymer in the solution, meaning assembly was largely unsuccessful. Although there seems to be vesicle-like species, it is more likely, when combined with the optical imaging, that these are polymer particles produced by the cone-jet of EHDA.

### 7.2.1.2 CO-AXIAL EXPERIMENTS

The experimental set-up for the coaxial needle EHDA jetting consists of a needle within a needle stainless steel coaxial device coupled to the high power voltage supply. In each case, the basic solution intended for the interior of the vesicle is delivered through the inner capillary. Simultaneously, the lipid or polymer encapsulating solution is delivered *via* the outer capillary. This method was developed based on the theory that the co-axial flow will induce vesicle formation as a droplet forms at the end of the capillary. The droplet then forms with the NaOH solution on the inside of the lipid or polymer solution, forming a droplet within a droplet. Optimisation of flow rate and voltage was conducted with a view to obtaining a stable cone jet.

Co-axial experiments in which polymers or lipids are dissolved in organic solvent was driven through the outer capillary, and a solution of aqueous NaOH through the inner capillary, creating “a-droplet-within-a-droplet” encapsulation system. These experiments proved to be unsuccessful in establishing a cone-jet. This is most likely because of a mismatch between the two solution spray rates, which meant they failed to establish a stable jetting mode. For this reason, there were fewer material combinations suitable for this methodology, with most failing to form a stable jet.

For the synthesis of artificial magnetosomes, the inner needle was fed with aqueous 0.1 M NaOH, and the outer needle was supplied with polymer or lipid vesicle solution (10 mM in ethanol). These solutions were subjected to EHDA jetting at different voltages. The flow rate of the vesicle solution and NaOH were varied between 10-50  $\mu\text{l min}^{-1}$  in a 1:1 ratio. The resultant jet spray was collected in double distilled water, which was deoxygenated by bubbling with nitrogen gas. The distance between the needle tip and the double distilled water bath was again 120-150 mm.

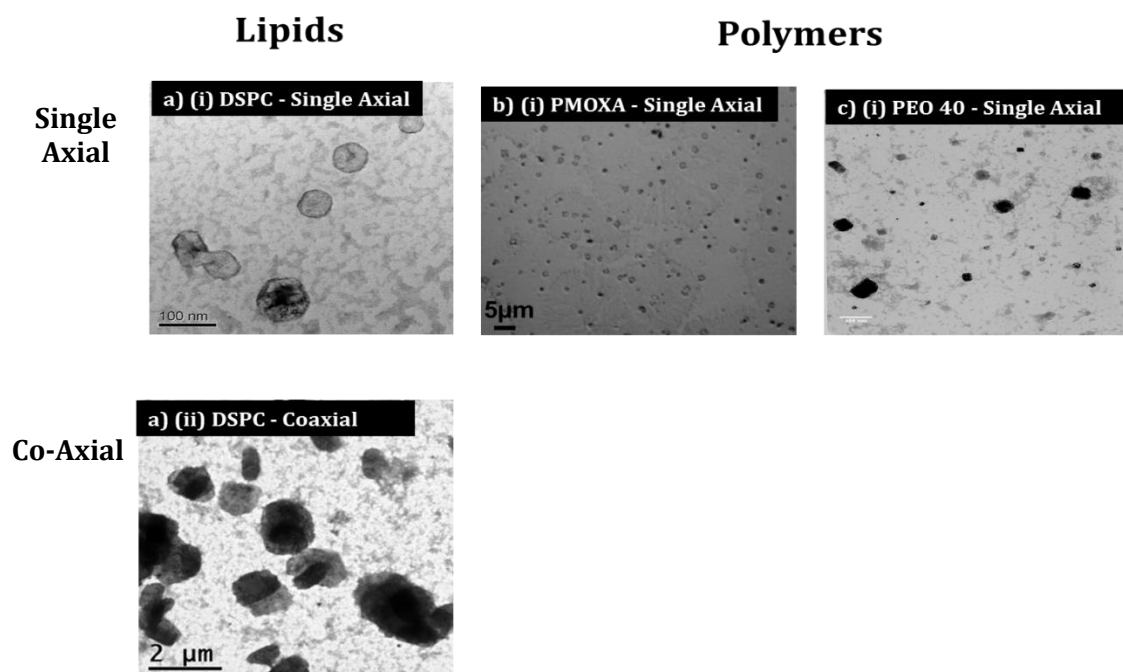


**Figure 7.2:** Shows TEM micrographs (stained with 2 % Uranyl acetate) representative results from the structures produced using the parameters outlined in table 7.1. For single axial experiments (upper), a) DSPC (10 mg  $\text{ml}^{-1}$ ), 15  $\mu\text{l min}^{-1}$ , 15 kV, b) PMOXA-PDMS-PMOXA, 15  $\mu\text{l min}^{-1}$ , 16.8 kV and c) PEO-40 stearate, 15  $\mu\text{l min}^{-1}$ , 16.7 kV). For co-axial experiments (lower) a) DSPC (1 mg  $\text{ml}^{-1}$ ), 15  $\mu\text{l min}^{-1}$ , 5.2 kV)

Three materials were tested under these conditions, these being DSPC lipid, PMOXA-PDMS –PMOXA tri-block polymer and the stearyl acetate/ethyl cellulose (20%:5% v/v respectively). In each case, the polymer or lipid material (in ethanol) was run through the capillary at a flow rate of 15  $\mu\text{l min}^{-1}$ .

The DSPC and the stearyl acetate/ethyl cellulose mixture produced a conejet, whereas the tri-block polymer formed a multijet. All three samples were analysed using DLS. These DLS data established that the only successful sample produced on the coaxial capillary system is the DSPC lipid, which shows a peak at 79 nm. However, this size information did not correspond well with the subsequent TEM analysis. TEM micrographs (Figure 7.2) show the presence of much larger structures (about 2-4  $\mu\text{m}$  in diameter). Therefore, further optimisation of the voltage and flow rate was needed to achieve smaller droplets upon atomisation. In the case of the stearyl acetate/ethyl cellulose system, no peak was observed in the DLS analysis. A broad peak at between about 2-3  $\mu\text{m}$  for the tri-block polymers suggests that the synthesis of vesicles in the nanometre range was unsuccessful.

Therefore no further tests were carried out on either of these materials. It is likely that the poor results achieved with the co-axial system when compared to the single axial system are largely due to imbalance in both the surface tensions and conductivities of the two different solutions. The concentration of the basic solution was increased by multiple orders of magnitude (from 100 mM to 1 M) in an attempt to bring the base solution conductivity in line with that of the polymer solution. Unfortunately, this resulted in the formation of a mutijet, which makes encapsulation impossible. Based on these data, it was decided that DSPC formed the best, most cost effective EHDA synthesised vesicles and this was the focus of the remaining studies in this chapter.

### **7.3 SYNTHESIS OF MAGNETO-LIPOSOME ‘ARTIFICIAL MAGNETOSOMES’**

The best lipid for the system was determined to be 1,2-distearoyl-sn-glycero-3-phosphocholine (DSPC) which was then further optimised to determine the optimum flow rate and applied voltage combination; as outlined in table 7.2.

The optimised conditions (Table 7.2) for the formation of the artificial magnetosome were found to be a combination using a single axial, bi-port needle (Schematic figure 7.1).

Flow rate ( $\mu\text{l}/\text{min}$ ) DSPC/NaOH	Applied Voltage(kV)	Spray and jetting mode
10/10	0-20	Too slow drop formation
20/20	0-3	No-effect
	4	Drop elongation
	5-9	Micro-dripping
	9-13	Unstable Cone-jet (fine particles)
	14	Occasional double- jet
	15	Unstable mode
	<b>16-18</b>	<b>Multi jet</b>
	19-20	Unstable mode
30/30	0-3	No effect
	3-6	Thinning and micro-dripping
	6-25	Unstable cone jet with thinning
40/40	0-3	No effect Dripping
	3-6	Thinning and micro-dripping
	6-25	Unstable cone jet with thinning
50/50	0-3	No effect Dripping
	3-6	Thinning and micro-dripping
	6-25	Unstable cone jet with thinning

**Table 7.2:** Table of EHDA optimisation all experiments were carried out at a concentration of 10 mM DSPC and 100 mM NaOH: Variation of flow-rate and applied voltage specific for generating DSPC nanovesicles using EHDA technology. For effective vesicle production a stable jetting mode must be achieved, the optimum conditions are highlighted in the table.

This is a single capillary featuring two separate inlets, meaning the solutions (DSPC and NaOH) remain separated until they enter the capillary, at an optimised rate of 20  $\mu\text{l min}^{-1}$ . This generates a steady flow of mixed lipid and base (NaOH 10 mM) solution, and it should be noted that DSPC lipid was delivered below its  $T_g$  (55°C). An optimised electrical potential difference of 16.8 -17.5 kV was delivered to the capillary as at this voltage the vesicle solution generated a continuous stable jet as it left the capillary.

Unlike the studies discussed in chapter 4 using DSPC, in which synthesis was difficult due to the  $T_g$  making polydisperse vesicles, the lipid self-assembles into a high quantity of near-monodisperse liposomes when accelerated by jetting through the EHDA needle outlet as  $20 \mu\text{l min}^{-1}$  with a capillary voltage of between 16-18 kV.

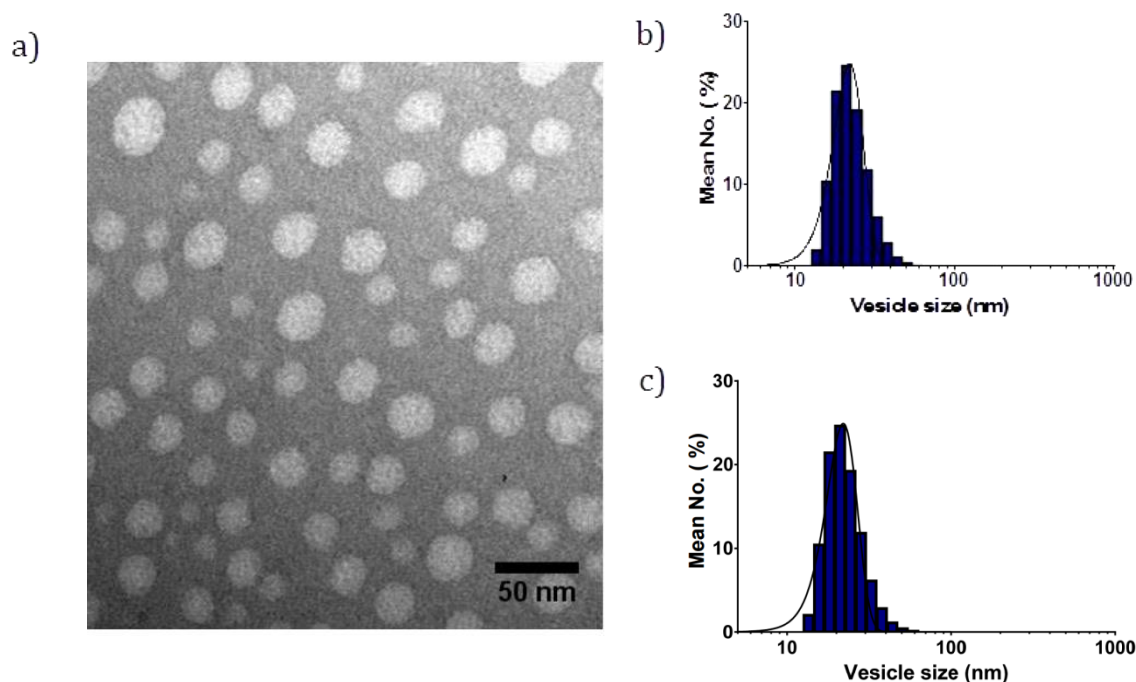


**Figure 7.3:** a) A stained TEM image of the NaOH encapsulated vesicles formed under optimised conditions ( $200 \mu\text{m}$  diameter, 96 mm needle length,  $20 \mu\text{l min}^{-1}$  flow rate, 16.8-17.5 kV voltage). b) The size distribution of non-electroporated liposomes obtained by DLS. c) Compared to the size distribution obtained *via* grainsizing from TEM images.

The size and size-distribution of the resulting liposomes were measured as  $22 \pm 4.8 \text{ nm}$  by both electron microscopy (TEM) and  $22 \pm 0.2 \text{ nm}$  using dynamic light scattering (DLS) analysis (Figure 7.3). The application of a localised high electric field during electroporation induces the reversible poration of the DSPC membrane. In the case of EHDA synthesised liposomes, this leads to the transport of iron ions across the membrane through these pores into the liposome core, hence mimicking the role of the transmembrane ion-transport proteins found in the MTB magnetosome. On this basis, DSPC was further investigated for the best conditions for incorporation of the magnetite synthesis routes optimised in chapter 3, particularly with respect to the voltage applied during electroporation. The findings of this investigation are summarised in table 7.3.

Jet	Voltage	Electroporation	TEM analysis
<b>Single Axial (200 <math>\mu\text{m}</math> needle)</b>			
<b>Multijet</b>	17-18kV	4 x 500-1000v	Polymer residue
	17.1kV	5 x 160V	No vesicles
		5 x 310V	Monodisperse vesicles
		5 x 460V	No vesicles
		5 x 600V	No vesicles
		5 X 750V	Monodisperse vesicles
<b>Conejet</b>	17.1kV	No	Monodisperse vesicles
		5 x 170V	
		5 x 320V	
		5 x 480V	
		5 x 630V	Large vesicles
		5 x 750V	Monodisperse vesicles
<b>Co-axial (207 <math>\mu\text{m}</math> inner and 396 <math>\mu\text{m}</math> outer needle)</b>			
<b>Conejet</b>	16.1kV	5 x 140V	No vesicles
		5 x 280V	Monodisperse vesicles
		5 x 420V	No vesicles
		5 x 570V	Lipid residue
		5 x 680V	
	17kV	5 x 860V	

**Table 7.3:** Optimisation of the EHDA DSPC liposomes. All Samples were made with DSPC at a concentration of 10 mM (unless otherwise stated) encapsulating NaOH at 100 mM, under single axial and co-axial conditions (as indicated). These EHDA generated vesicles were electroporated in the presence of mixed iron ion solution (in the stoichiometric ratio for magnetite formation).

Many of the samples looked to contain vesicles when investigated using TEM but confirmation of vesicles on the micrographs was inconclusive as to whether the electroporation step was successful; therefore DSPC liposomes samples were dismissed. Also, the majority of the coaxial samples showed only lipid residue in the TEM imaging. In terms of the electroporation, differing to the results presented in chapter 6, mid-range voltages around 200-300 V appear to be the most successful at inducing mineralisation. TEM images show some electron dense material in the vesicle core (Figure 7.4). The most promising conditions screened are shown in figure 7.4.

These were produced by both single and coaxial capillary systems, forming a multijet and a conejet respectively, and electroporated five times at 310 V in the case of the single axial sample and 280 V in the case of the coaxial sample.

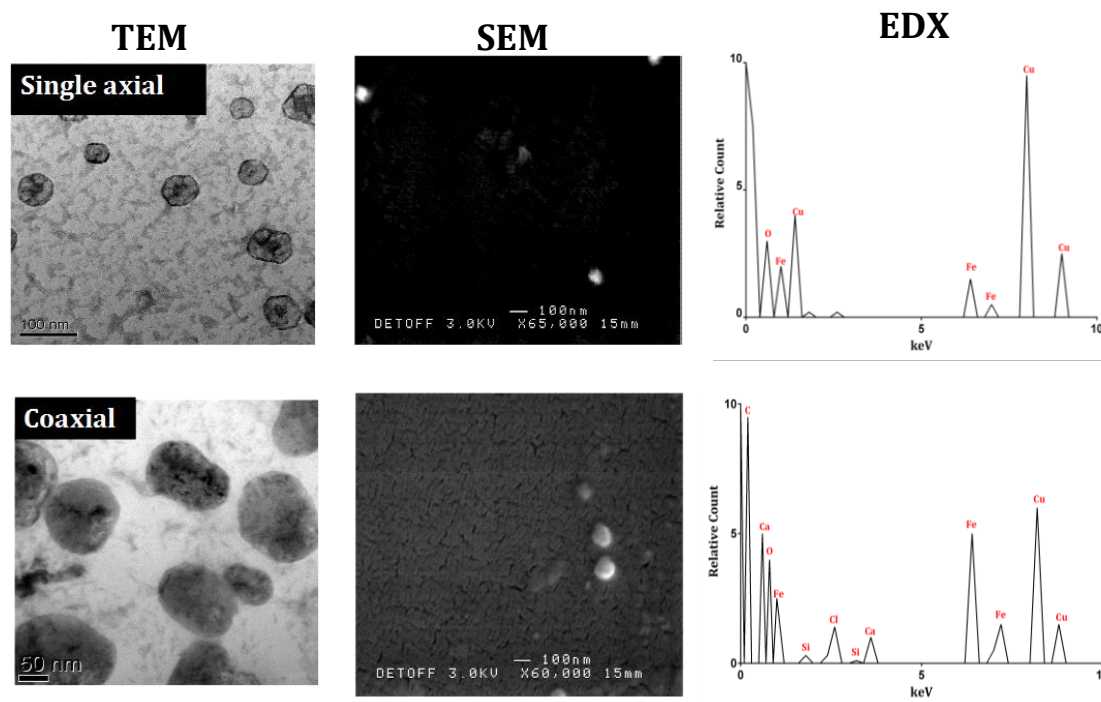


**Figure 7.4:** TEM, SEM and EDX data for the DSPC liposomes made *via* EHDA using the single axial (electroporated 5 times at 310 V) and coaxial (electroporated 5 times at 280 V) outlined in table 7.3 Cu, Ca, Cl, C and Si are probably from the grid and/or the buffer used to prepare the samples. Also, the spectra indicate the presence of iron (FeK $\alpha$  6.40 keV, FeK $\beta$  7.06 keV, FeL $\alpha$  0.71 keV) and oxygen (O $\alpha$  0.53 keV) indicating that the cores do contain iron oxide.

The samples were then analysed by TEM, SEM (performed at UCL) and EDX. These data show that the electron dense vesicle core contains iron and oxygen, suggesting the possible presence of iron oxide. This data was used as a basis for further analysis and fine tuning by Dr. Bakshi (UCL), in terms of needle length, flow rates and voltage applied to the capillary, to yield the optimised parameters outlined below (Section 7.2.1). Optimised electroporation conditions for maximum transport of iron ions into the EHDA synthesised liposomes were applied to the DSPC liposomes. These conditions used a voltage of 750 V, (optimised by the UCL team) with a pulse length of 100  $\mu$ s; a parameter determined automatically by the electroporator. This pulse was applied to liposome solution 9 times (Again optimised by the UCL team).

## **7.4 CHARACTERISATION OF MAGNETO-LIPOSOME 'ARTIFICIAL MAGNETOSOMES'**

### **7.4.1 ELECTRON MICROSCOPY OF MAGNETO-LIPOSOME 'ARTIFICIAL MAGNETOSOMES'**

Electroporation of EHDA synthesised DSPC liposomes results in the crystallisation of an electron dense material (presumed to be a magnetite MNP based on elemental and magnetic analyses) within the liposome core. This system comprises an artificial magnetosome, as shown in both standard (dried sample) and cryogenic TEM (figure 7.5). This TEM confirms that electroporation of EHDA synthesised DSPC liposomes according to these parameters, results in the successful formation of an electron dense material within the liposome core. TEM micrographs (figure 7.5) show clearly a dark material, around which membrane of approximately 8 nm is visible. Membranes were visualised using a 0.75 % uranyl formate stain. This negative stain pools around the objects, and is able to highlight electron sparse (organic) materials, such as the liposome bilayer.

To confirm that the presence of the apparent lipid bilayer around the nanoparticle is not simply an artefact of drying the sample down on to the TEM grid, Cryo-EM was employed. Cryo-EM maintains the liquid content of the vesicle, which means its structural integrity, is preserved, making the detection of the bilayer much more conclusive. This can be seen in the Cryo-EM images (Figure 7.5b). The vesicles appear to have swelled during the electroporation process, resulting in an increased average size when compared to the non-electroporated liposomes (Figure 7.5 c). This is likely due to the high fluidity of the lipid membrane; especially when compared to the polymer system (Chapter 6) which may account for this swelling. This, when combined with the voltage applied during electroporation, likely means that the lipid is still in the gel phase, which would give rise to movement of the phospholipids during the electroporation process.

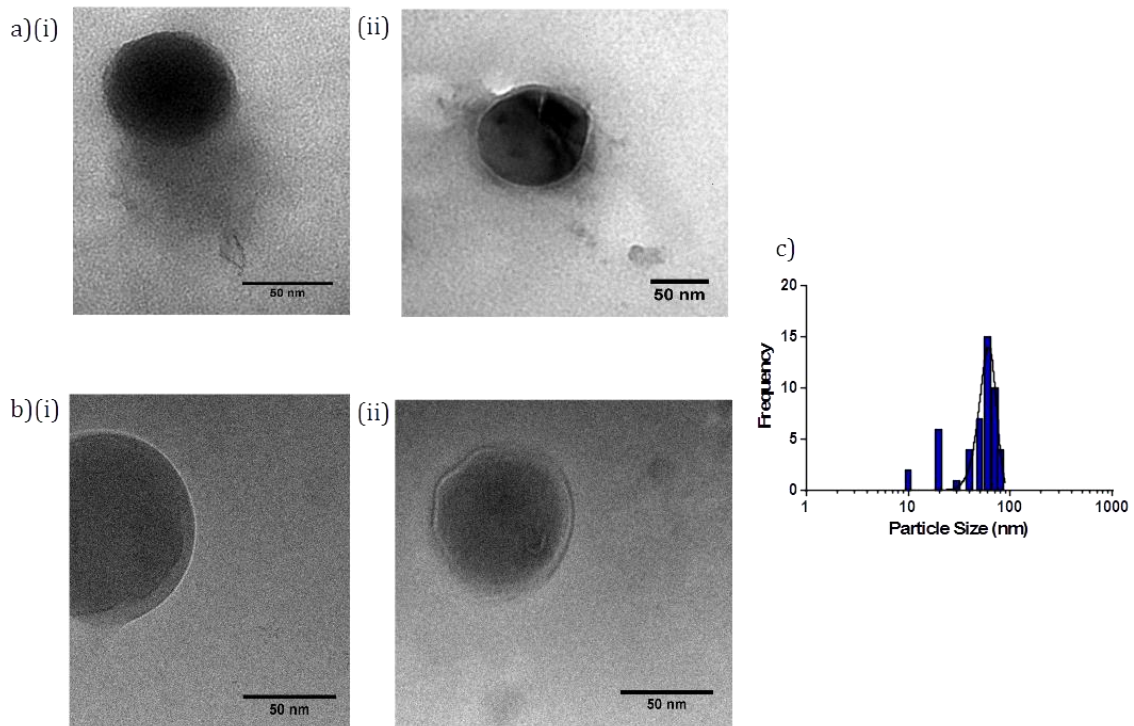


**Figure 7.5.** TEM images of unstained nano-liposomes subjected to optimised (100  $\mu$ s pulse duration, 9 pulses, 750 V) electroporation conditions show electron dense material in their core, assumed to be an MNP crystal. a) (i) and (ii) standard TEM micrographs b) (i) and (ii) Cryogenic-TEM images. c) Grainsizing from the TEM of the artificial magnetosomes, showing an average size of  $58 \pm 8$  nm.

If this is the case it is probable that, once the liposomes are within the iron solution and the ions cross the bilayer, the resulting formation iron-oxide within the interior can swell the vesicles, within the range of the phospholipids elasticity.

This gives rise to artificial magnetosomes closer in size to the native MTB structures. This is a particular point of interest, i.e. that the artificial magnetosomes are of comparable size ( $58 \pm 8$  nm) to natural magnetosomes. These are significantly larger than the average size of the non-electroporated liposomes (Figure 7.3). TEM analysis (performed by the UCL team) also confirms that EHDA formed electroporated magneto-liposomes remain stable for a minimum of 120 days, confirmed by TEM (performed at UCL). This stability could be due to stabilisation by the presence of the magnetite crystal within their core, and the likelihood that the lipid is now in a solid phase (below its  $T_g$ ).

## 7.4.2 RAMAN SPECTROSCOPY OF MAGNETO-LIPOSOME 'ARTIFICIAL MAGNETOSOMES'

As discussed earlier, TEM alone cannot confirm the elemental and material composition of the observed structures within the magneto-vesicles. Therefore Raman spectroscopy (performed at UCL) was used to analyse the artificial magnetosome sample, to confirm which materials are present. The spectrum contained significant peaks at 180-240 and 579  $\text{cm}^{-1}$  ( $T_{2g}$  shifts) 300-400  $\text{cm}^{-1}$  ( $E_g$  shift) and 668  $\text{cm}^{-1}$  ( $A_{1g}$  shift),<sup>76</sup> which are indicative of the presence of magnetite.<sup>19</sup>

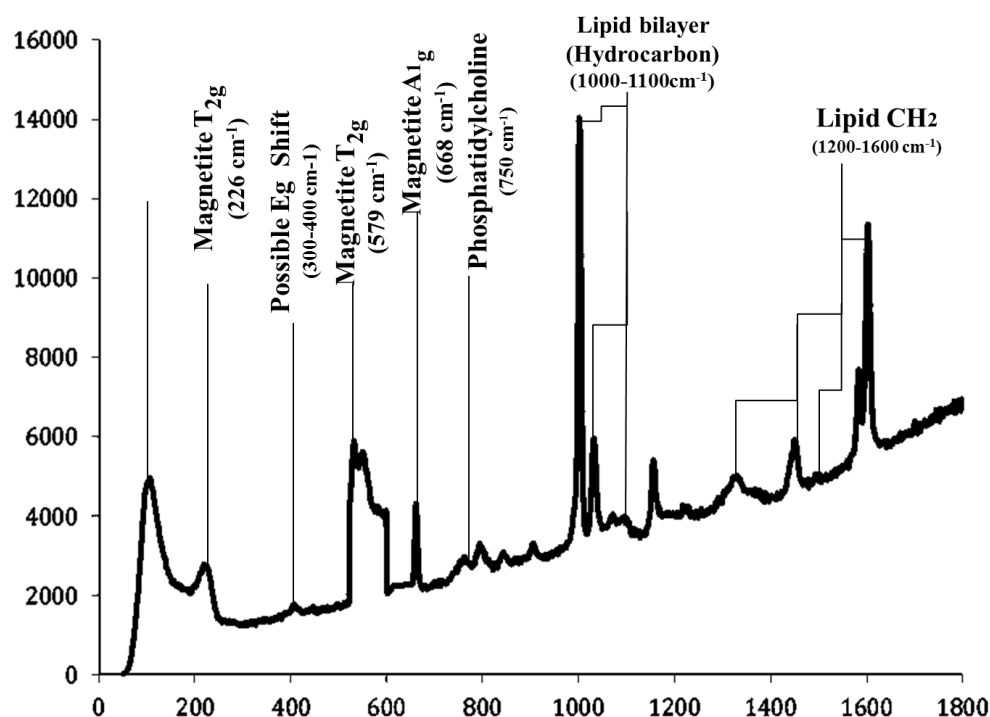


**Figure 7.6:** Raman spectrum of artificial magnetosomes (shows DSPC lipid encapsulating magnetite). Spectrum shows the presence of peaks representative of magnetite (at 180-240 and 579  $\text{cm}^{-1}$  ( $T_{2g}$  shifts) 300-400  $\text{cm}^{-1}$  ( $E_g$  shift) and 668  $\text{cm}^{-1}$  ( $A_{1g}$  shift)<sup>76</sup>) and a phosphatidylcholine lipid bilayer (peaks highlighted at 750  $\text{cm}^{-1}$  (Phosphocholine), 1000-1100  $\text{cm}^{-1}$  (Hydrocarbon tail) and 1200-1600  $\text{cm}^{-1}$  ( $\text{CH}_2$ )).<sup>76, 185, 200</sup>

This is assumed to come from the only electron dense material observed in the samples, i.e. from the dark vesicle core. As magnetite is a crystalline iron oxide, it can be extrapolated that the electron dense cores of the magneto-vesicles do consist of magnetite. Similarly, peaks at  $750\text{ cm}^{-1}$ ,  $1000\text{-}1100\text{ cm}^{-1}$  and  $1200\text{-}1600\text{ cm}^{-1}$  correspond to the presence of both a lipid bilayer, and more specifically a phosphocholine head group. This is assumed to be due to the DSPC lipid (Figure 7.6).<sup>185, 200</sup> It cannot be ruled out that these peaks are the result of segregated magnetite nanoparticles and vesicles. Similarly, it is possible that the lipid peaks are due to free lipid not incorporated into the vesicles. SEC clean up should have removed both free lipid and external iron oxide precipitate. However, as what appear to be co-assembled structures are consistently observed in standard and cryogenic TEM (see above), it is most likely that the lipid bilayer does surround a magnetite core. Therefore, it is assumed that the Raman spectra, TEM micrographs and more specifically the increase in the vesicle size before and after electroporation are extremely indicative of magnetite filled DSPC lipid vesicles, i.e. artificial magnetosomes.

### **7.4.3 FLUORESCENCE OF MAGNETO-LIPOSOME 'ARTIFICIAL MAGNETOSOMES'**

A fluorescence assay was employed to confirm that the MNPs are surrounded by DSPC liposomes. This was carried out by incorporation of the lipophilic dye BODIPY FL (C<sub>5</sub>-ceramide(*N*-(4,4-difluoro-5,7-dimethyl-4-bora-3a,4a-diaza-*s*-lidacene-3-pentanoyl)sphingosine, Life Technologies) which was simply mixed with the artificial magnetosome sample, with the excess dye subsequently being removed by SEC. The dye should only be visible if a lipid bilayer is present, and should be localised to the bilayer or lipid structure(s).<sup>201</sup> Analysis by fluorescence microscopy showed the presence of discrete fluorescent vesicles following magnetic separation and washing of the artificial magnetosome sample (Figure 7.7 a). These fluorescent vesicles were subjected to a magnetic field; by application of a magnet at the edge of the microscope slide. When the magnetic field is applied, movement of the discrete fluorescent vesicles was observed in the direction of the magnetic field (Figure 7.7 b). This was not the case for suspensions of uncoated MNPs, which were used as a control.

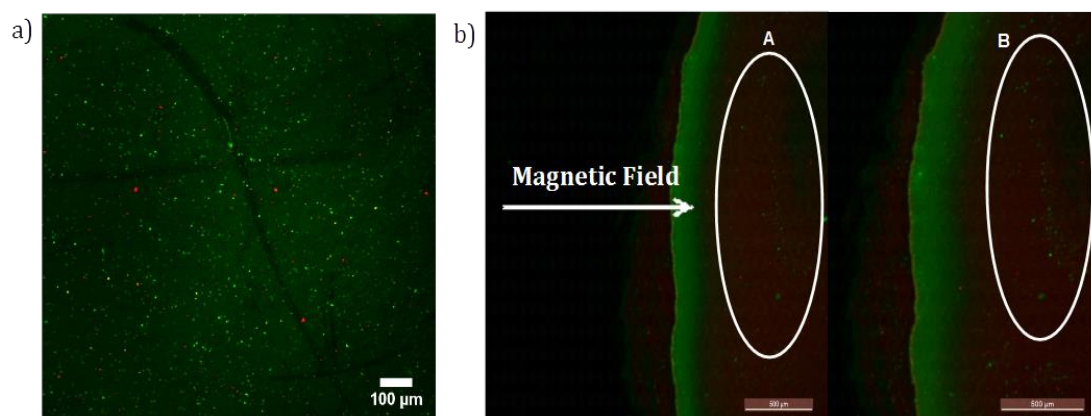


**Figure 7.7** a) Lipophilic fluorescent dye incorporation (Bodipy), showing the presence of fluorescently labelled DSPC liposomes. b) On application of a magnetic field (applied in the direction of the magnet) show the movement of the fluorescently tagged liposomes (circled).

#### 7.4.4 BULK MAGNETIC PROPERTIES OF MAGNETO-LIPOSOME ‘ARTIFICIAL MAGNETOSOMES’

Evidence so far has established that the system has been successfully optimised for the precipitation of a single magnetic iron oxide crystal within the core of a DSPC lipid vesicle. To confirm the composition of the magnetic material, magnetic hysteresis and field-cooled/zero-field-cooled magnetic susceptibility measurements as a function of temperature were performed using a SQUID (by the team at UCL). Particular attention was applied to the identification of the characteristic Verwey transition<sup>16</sup> of magnetite; and thus rule out the precipitation of significant amounts of maghemite. In the case of the room temperature magnetic analysis, a characteristic hysteresis of a soft magnetic material was observed (Figure 7.8). The magnetic particles within the DSPC liposomes align with the magnetic field as it was switched between 3000 and -3000 Oe. The magnetic particle switched easily, showing little or no coercivity. As magnetite is a soft magnetic material, this low coercivity is to be expected.

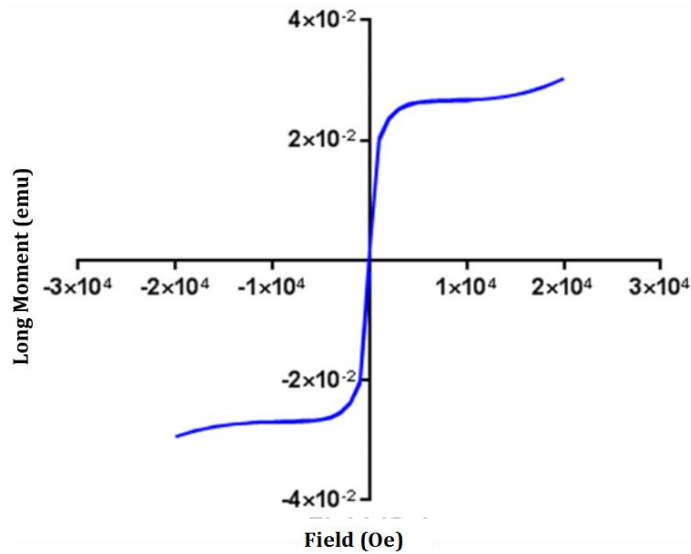


**Figure 7.8** Magnetisation vs Field hysteresis plot performed at 300 K using a SQUID. The plot shows typical hysteresis of soft magnetic material, and is characteristic of magnetite.

With respect to the zero-field cooled magnetic data, (Figure 7.9) despite the small sample size (maximum of  $1 \times 10^{-2}$  emu  $g^{-1}$ ), these data clearly show the presence of a magnetic material. More specifically, there is a change in magnetic behaviour at 118 K, where there is a change of slope in the zero field cooled (ZFC) plot. This is due to the Verwey transition, a structural re-ordering that is characteristic of bulk magnetite.<sup>16</sup> The re-ordering leads to a magnetic phase transition, i.e. the Verwey transition, as indicated by the slight plateau at 118 K.<sup>17</sup> This characteristic change along the cubic magnetocrystalline axis switching from the body diagonal to the cube edge results in a magnitude loss of magnetic remanence and provides a fingerprint for the presence of a magnetite nanoparticle. This is highly indicative of the presence of a pure magnetite nanoparticle, which in combination with both the Raman and fluorescence studies, can confidently be assumed to be precipitated within the core of the EHDA synthesised DSPC liposomes.

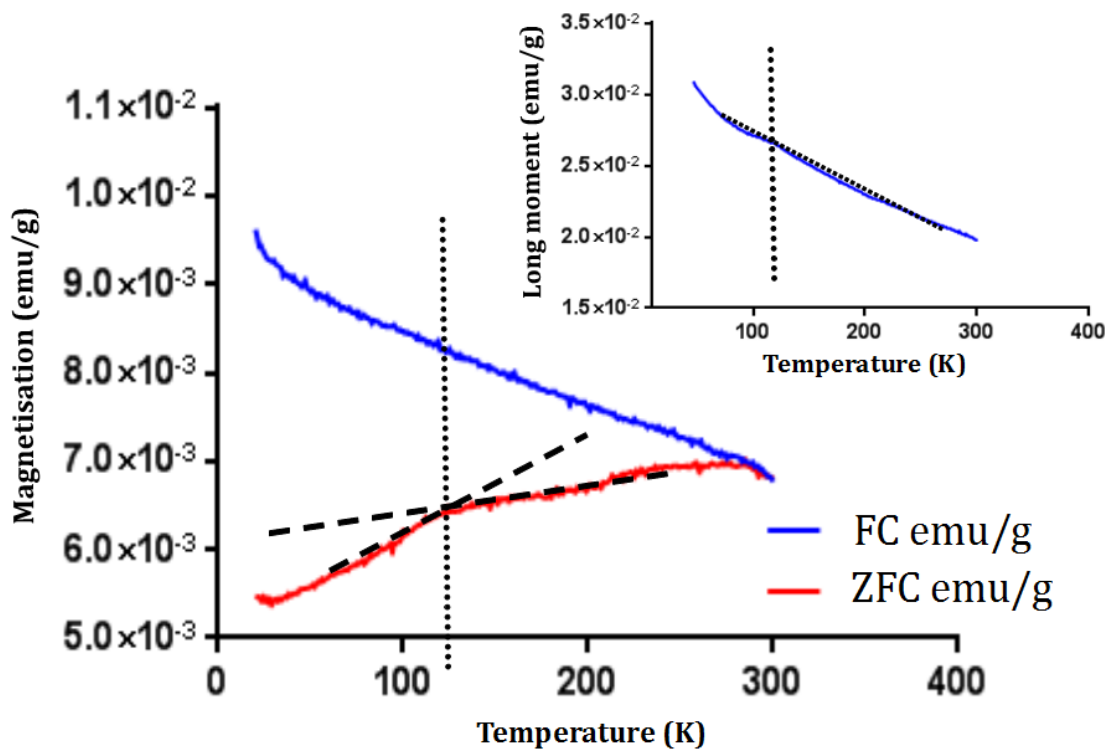


**Figure 7.9.** Zero field cooled and field cooled magnetisation vs temperature plots (applied field of 100 Oe). Inset shows remanence of the field cooled data. The Verwey transition is shown a dotted line (.....) marked on the plot to highlight the temperature it occurs at (118 K).

## 7.5 ADAPTABILITY OF EDHA FOR ARTIFICIAL MAGNETOSOME SYNTHESIS

### 7.5.1 DOPC MAGNETO-LIPOSOMES VIA EHDA

To determine the adaptability and robustness of the system, a methodology using the same synthesis route was applied to an alternative lipid material. In this case the phospholipid used was 1,2-dioleoyl-sn-glycero-3-phosphocholine (DOPC). When compared to DSPC, this lipid has increased fluidity, due to unsaturation in the hydrocarbon tail. DOPC has proven successful both in initial liposome formation tests (Chapter 4) and with the conventional electroporation method (Chapter 6).

As with the DSPC liposomes; at an initial lipid concentration of  $0.5 \text{ mg ml}^{-1}$ , single axial EHDA was used. This was run through the single axial capillary at a rate of  $15 \mu\text{l min}^{-1}$  under 16.7 kV. During delivery of the lipid solution a stable conejet was achieved and maintained which resulted in the formation of monodisperse liposomes.

### 7.5.2 MICROSCOPY OF DOPC MAGNETO-LIPOSOMES *VIA* EDHA

Although not characterised to the same extent, the DOPC magneto-liposomes synthesised by EHDA appear to produce a mono-disperse population compared to formation by tip sonication or extrusion. A dark, electron dense core and a bilayer (as observed by negative stain) are both visible in TEM. This can be seen in the TEM micrographs (Figure 7.10 a), although not as clear as in the DSPC lipid micrographs, a distinct difference in the density between the vesicle core and respective bilayer can be seen in figure 7.10 a) inset. Grainsizing of several TEM micrographs gave an average vesicle size of  $207 \pm 42 \text{ nm}$  (Figure 7.10 b). The increased size of the DOPC artificial magnetosomes demonstrates the adaptability of the methodology to produce mineralised vesicles of controlled sizes.

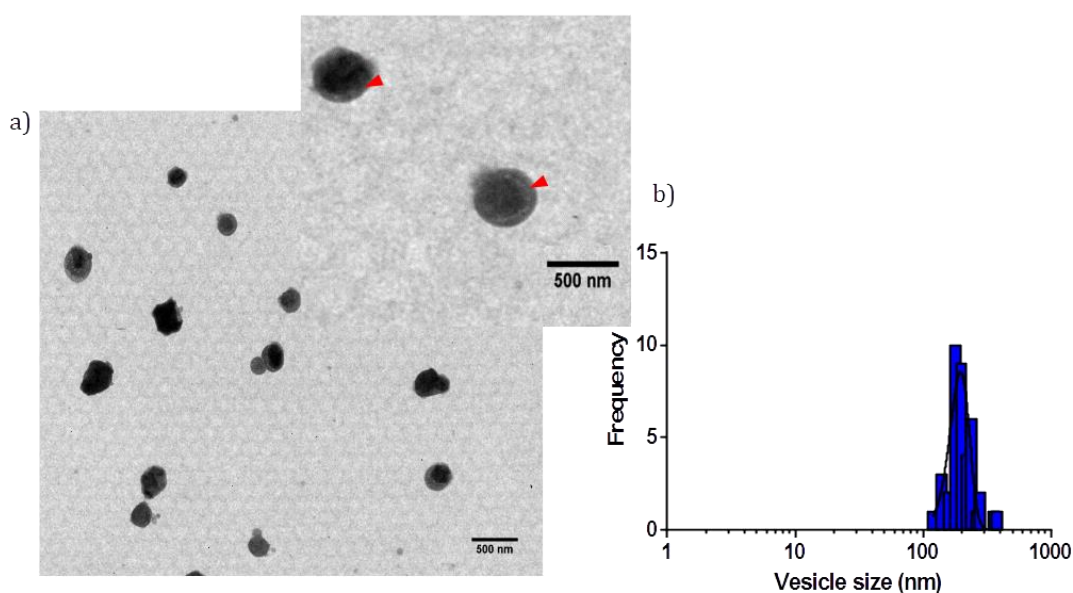


**Figure 7.10** a) TEM micrographs of DOPC lipid artificial magnetosomes showing both an electron dense core and lipid bilayer; as indicated by the red arrows (inset). b) Shows the corresponding TEM grainsizing which gives an average liposome size of  $207 \pm 42 \text{ nm}$ .

## 7.6 DISCUSSION OF EHDA MAGNETO-VESICLE SYNTHESIS

Many lipids, particularly DSPC, can be difficult to work with in more traditional liposome synthesis methods, such as sonication or extrusion<sup>71a</sup> owing to high glass transition temperature ( $T_g$ ) (Section 4.2.3). TEM analysis of liposomes prepared by both traditional and electrohydrodynamic methods show a distinct difference. Those prepared by EHDA show clear vesicles of a near monodisperse distribution, which are not observed in the DSPC control sample. (Chapter 4, section 4.2.3). It can be surmised that the negative effects of the DSPC lipid  $T_g$  are not observed in the EHDA prepared sample. This may be due to the application of substantially high voltages during the continuous flow and rapid formation process circumnavigating the fluidity issues seen below  $T_g$  in the non-electrically mediated syntheses. This ensures that the DSPC remains in the amorphous/gel phase throughout the self-assembly. During conventional liposome synthesis, the temperature must be kept above 55°C to maintain lipid fluidity, making processes like extrusion difficult. This is in stark contrast to the wet-chemistry formed DSPC liposome control sample in which vesicles appeared to be severely damaged by the preparation method (tip sonication), (Chapter 4, Section 4.2.3). The application of the electrical potential difference is not only responsible for the rapid formation of nano-vesicles, but also appears to assist in the formation of a vesicular structure, hugely increasing their stability, when compared with liposomes formed by e.g. tip sonication.

Room temperature magnetic analysis showed only little coercivity. As magnetite is a magnetically soft material, it was expected that the coercivity would be relatively low, and this is not the case in naturally biomineralised magnetosomes in MTB.<sup>144, 202</sup> Despite this the temperature versus moment magnetic measurements performed on the DSPC magneto-liposomes undoubtedly shows the characteristics of magnetite. Most convincingly, the Verwey transition was observed during ZFC measurements, which is a characteristic feature of stoichiometric magnetite. This is supported by EDX elemental analysis of the electron dense cores shown in TEM, which contain iron and oxygen, and Raman spectra that show peaks for magnetite. Thus, a simple, high-throughput method to producing precise single-domain sized magnetite nanoparticles *in situ* within liposomes has been demonstrated to create these magneto-liposome 'artificial magnetosomes'.

# CHAPTER 8:

---

## BIOMINERALISATION OF IRON OXIDES

## 8.1 INTRODUCTION TO THE BIOMINERALISATION OF IRON OXIDES

Biom mineralisation reactions in organisms are controlled by dedicated proteins.<sup>1b, 1c, 47</sup> It was briefly discussed in section 1.3.2.2 that precipitation of the magnetite crystal within the magnetosome is tightly controlled by specific proteins present in the magnetosome membrane.<sup>1a, 5, 29</sup> The transmembrane helices which span the magnetosome membrane can present the protein termini and/or hydrophilic loop regions to the magnetosome interior. These sequences displayed within the magnetosome core are believed to act as nucleation sites for precipitation of the magnetite crystal, or to direct the crystal growth and particle properties. Many of these proteins have previously been investigated *in vivo* (for instance phenotypes resulting from gene deletions, localisation of the protein within the cell).<sup>1a</sup> Studies *in vitro* have analysed their effects on synthetic magnetite formation in one pot precipitation reactions, as well as when anchored on to synthetic surfaces.<sup>1a, 62, 203</sup> There are believed to be a minimum of nine biomineralisation proteins essential for magnetosome synthesis, the details of which have been collated and reviewed by Nudelman *et al.*<sup>47</sup> Gene deletion experiments performed by various groups have found that this group of proteins has control over the number of crystals (MamR),<sup>47</sup> magnetic properties (MamS)<sup>47</sup> and crystal size and shape (MamD, MamG, Mms6, Mms13 and MmsF).<sup>47</sup> In general, all of these proteins are of low molecular weight, and comprise a high number of exposed charged residues, which are believed to give these proteins their nucleation properties in the magnetosome.<sup>1a, 5, 29a</sup> Large proportions of their sequences are made up of hydrophobic residues arranged into transmembrane helices, which allow them to insert into the magnetosome membrane. This chapter presents the first incorporation of MmsF proteins into a synthetic vesicle, and the first test of intra-vesicular function for the creation of an artificial magnetosome (for MmsF and Mms6). These proteins were produced and purified by Dr. A. Rawlings within the Staniland group. In addition, an artificial antiparallel coiled coil protein scaffold was used to display the loops connecting the transmembrane helices of these proteins in a stable and water soluble form in a conformation similar to that thought to be present in the native protein. The loops selected were the regions considered responsible for interacting with the *in vivo* MTB magnetite crystal. These proteins have also been incorporated into vesicles, as they offer a much more feasible alternative for future large scale production.

## 8.2 PROTEINS USED IN SYNTHETIC VESICLES

Three MTB biomineralisation proteins have been explored in the Staniland laboratory. These have been designated as biomineralisation proteins by way of genetic mutations, deletions and proteomic analyses *in vivo*. These proteins are Mms6,<sup>61</sup> MmsF<sup>5, 29b</sup> and Mms13.<sup>61</sup> Within the Staniland group, previous work has focussed on cloning, expressing and purifying each of these proteins to confirm their function and assess their effect on synthetic magnetite precipitation. Both Mms6<sup>1a, 29a</sup> and MmsF<sup>5</sup> (as part of this thesis) have been successfully expressed by Dr. A. Rawlings (Staniland group). It was found that, when these proteins were added to room temperature co-precipitation reactions to produce magnetite nanoparticles, significant differences in the morphology of the resulting nanoparticles were observed.<sup>1a, 5</sup> For this reason, this chapter explores their incorporation into synthetic magnetosomes to investigate their effect on intra-vesicular magnetite precipitation. In the case of Mms13, attempts to produce the protein in a soluble form (due to its highly hydrophobic content) were unsuccessful. Therefore tests on its biomineralisation functionality have thus far been limited to genetic analysis within MTB.<sup>204</sup>

Vesicular incorporation of artificial scaffolds has also been explored, as part of this chapter. Within the Staniland laboratory, coiled coil artificial scaffolds have been developed which display what is believed to be the active, magnetite interacting loop of the magnetite biomineralisation protein. The *in vitro* effect of these proteins on MNP precipitation has been investigated in room temperature co-precipitation reactions, (by other members of the Staniland group) and this chapter presents the first results of their incorporation into synthetic magnetosomes.

## 8.3 MAGNETITE BIOMINERALISATION PROTEIN PROPERTIES AND PURIFICATION

### 8.3.1 PROTEINS

#### 8.3.1.1 MmsF

MmsF is a small 20 kDa protein described in the literature as the master regulator protein of magnetite biomineralisation in the MTB magnetosome.<sup>29b</sup> The presence of MmsF in the magnetosome has been confirmed by the addition of a green fluorescent protein tag.<sup>29b</sup> This tag has indicated that the C terminal region of the protein is located on the inside of the magnetosome. Structural predictions and sequence analysis have suggested that there are three transmembrane regions, the sequences of which are highly conserved.<sup>5</sup> The helices sit in the magnetosome membrane (Figure 8.1), causing the formation of a loop between helices I and II, which is present in the magnetosome interior. This loop is highly conserved in MmsF, and various homologues; it's believed that this conservation is due to its function as the active site.<sup>5</sup>

Within this loop region there are a large number of acidic residues, believed to act as a nucleation site(s) for magnetite precipitation.<sup>5</sup> Mutagenesis studies *in vivo* have discovered that deletion of the *mmsF* gene causes defects in the magnetite biomineralisation process, resulting in smaller, misshapen particles, the effects of which are reversed when the *mmsF* gene is reintroduced.<sup>29b</sup> In fact, deletion of the entire gene cluster (containing *mmsF*) yields the same results as the single *mmsF* deletion, but morphological control is restored when just *mmsF* alone is reinstated.<sup>29b</sup> This provides an excellent indication that MmsF is the magnetite regulating protein in the gene cluster.

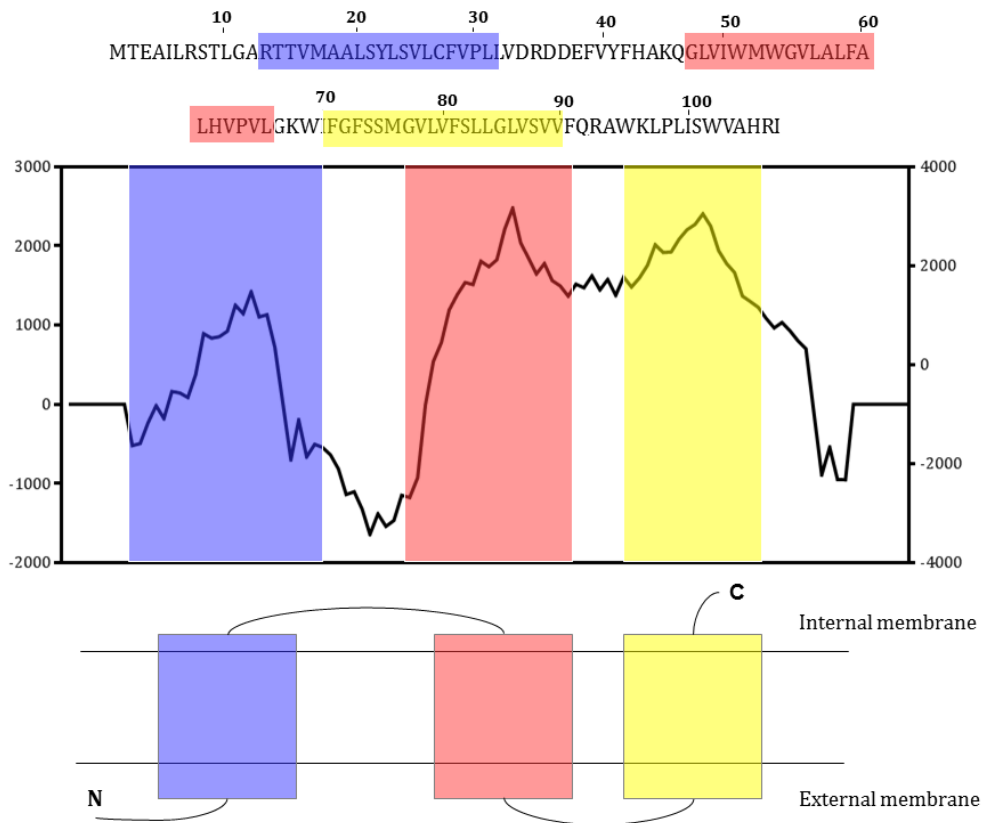


**Figure 8.1:** Sequence analysis of MmsF (top) reveals three transmembrane helices shown by the blue red and yellow regions in the sequence. These correspond to the same coloured regions in the hydropathy plot (middle). The arrangement of these regions results the structure shown (bottom left) which when in the membrane leads to the N terminus displaying on the exterior of the membrane with the C-terminal region presented on the magnetosome interior. There are additionally two intermembrane loops, one on the interior and one on the exterior of the magnetosome membrane, the internal loop is believed to give the protein its nucleation properties, (bottom). Figure created from hydropathy data provided by TMPred Server (Expasy).

### 8.3.1.2 Mms6

Mms6 is a small acidic protein which has previously been found to be bound to the magnetosome crystal on extraction from MTB.<sup>1a, 29a</sup> Deletion of the operon containing the *mms6* gene causes a decrease in the size and change in the geometry of the magnetite crystal.<sup>29a</sup> It is believed that Mms6 is functional in biomineralisation of magnetite due to its localisation on or near the magnetite crystal surface.

The structure and sequence composition of Mms6 is key to its function.<sup>61</sup> A high proportion of the Mms6 protein is thought to span the magnetosome membrane *via* a transmembrane helix. This topology means that the C-terminal region will be exposed to the magnetosome core, and able to make contact with the magnetite crystal (Figure 8.2). The residue character of the C-terminal region of Mms6 is highly acidic, having a pI of 4. This region has the ability to bind metal ions (in particular ferric iron) and the magnetite crystal face.<sup>61,205</sup> Wang *et al*<sup>205</sup> have devised a hypothesis by which Mms6 accumulates iron ions *via* acidic amino carboxylic acid side chains. This is believed to initiate magnetite nucleation in the magnetosome.<sup>205</sup> Again, Mms6 has been studied outside of its native environment in MTB to confirm its structure and function.

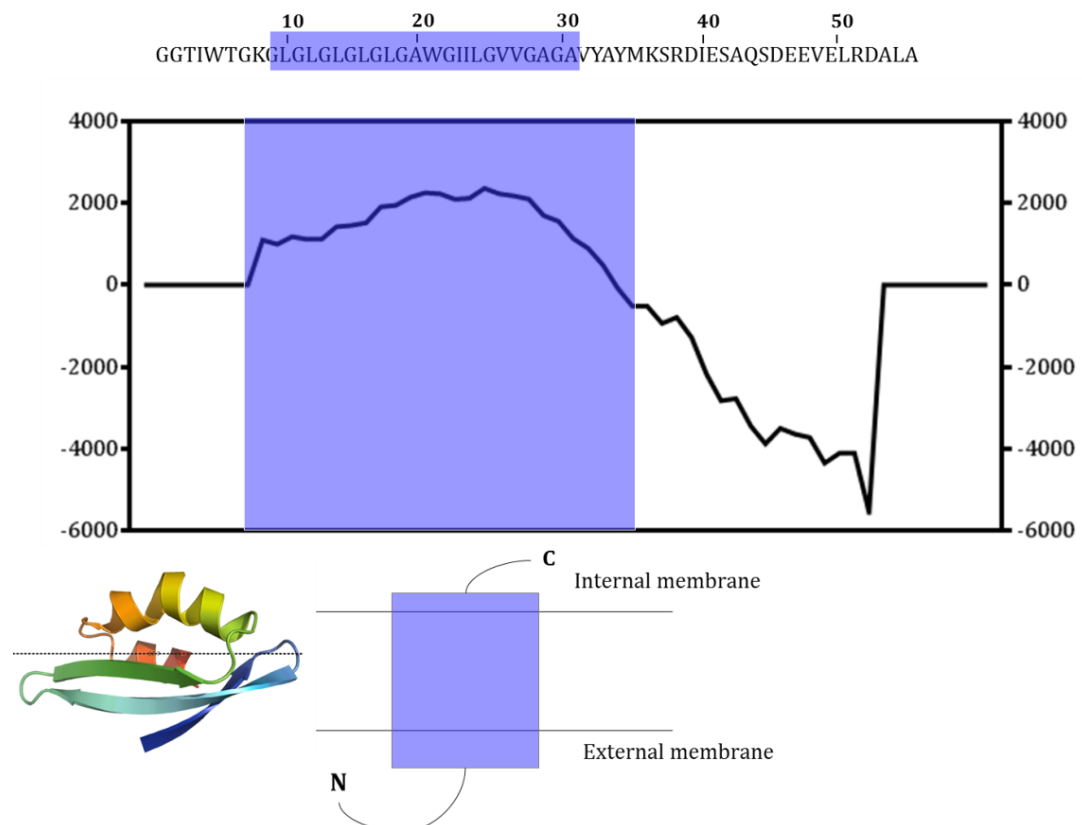
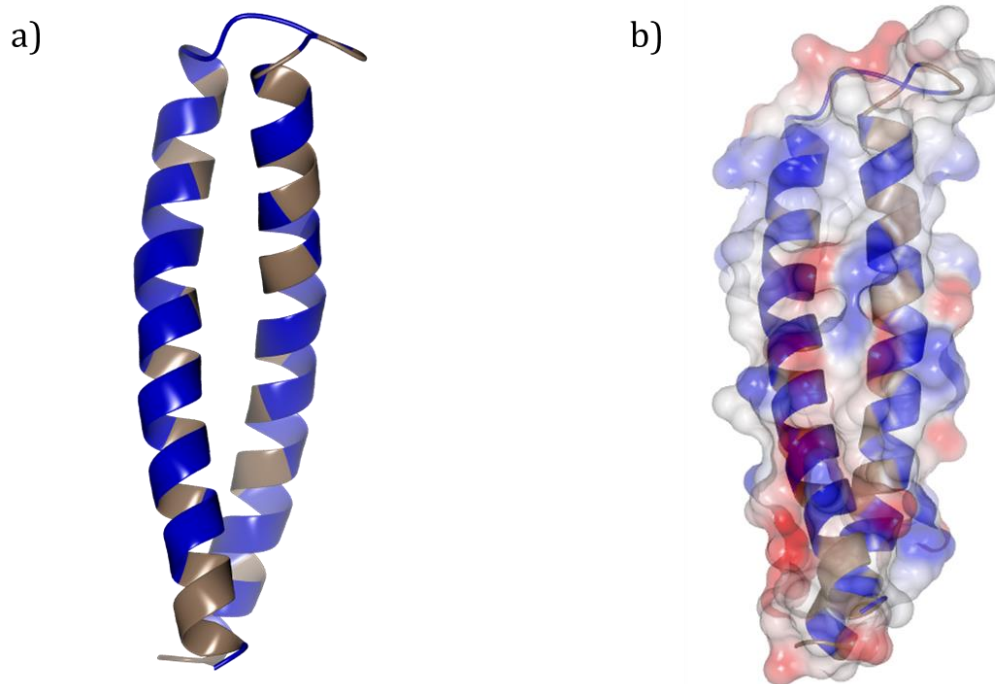


**Figure 8.2:** Sequence analysis of Mms6 (top) with a transmembrane helix shown by the region highlighted in blue in the sequence. This corresponds to the blue region in the hydropathy plot (middle). The predicted structure of Mms6 is shown (bottom left) and its arrangement in the membrane in which the single transmembrane helix spans the magnetosome membrane in a topology so that the N-terminus is on the exterior of the magnetosome and the C-terminus is presented to the interior. Figure created from hydropathy data provided by TMPred Server (Expasy).

### 8.3.1.3 BIOMIMETIC SCAFFOLD PROTEINS

The membrane associated nature of the Mms suite of proteins can cause difficulties in successful over expression in *E. coli* as well as in subsequent purification steps for *in vitro* use. To alleviate these problems, a coiled-coil peptide display scaffold was developed in the Staniland group based on previous work by Gurnon *et al.*<sup>206</sup> A coiled-coil is, as the name suggests, two  $\alpha$ -helices which can coil around one another, forming a stable and soluble “coiled-coil”.<sup>207</sup> In our case, the two helices are present within one protein molecule, and the region connecting these two coils forms a loop which is displayed as shown in figure 8.3. The loop region of the sequence (highlighted in black in figure 8.3) can be designed to display loop sequences of interest from other proteins. In this case, the coiled coil protein scaffolds have been mutated to display the active loop regions of MTB biomineralisation proteins.



```

MGSHHHHHHHGGSTENLYFQGPSMKQLEKELKQLEK
ELQAIEKQLAQLQWKAQARKKKLAQLKKKLQASRDDE
YVYFHAQKQGMKQLEKELKQLEKELQAIEKQLAQLQWK
AQARKKKLAQLKKKLQA

```

**Figure 8.3:** Top: Schematic of the stem loop coiled-coil incorporated into vesicles a) shows the region of hydrophobicity (gold) and hydrophilicity (blue) b) Overlay shows areas of electron density. Bottom: The protein sequence of the coiled-coil used.

This methodology has been applied to MmsF, to display the loop region between the two transmembrane helices which are displayed in the magnetosome core for nucleation of iron ions. This is designed to act as a soluble mimic of monomeric MmsF. Similarly the same approach has been applied to the loop connecting helices I and II in the MTB biomineralisation protein Mms13. Mms13 was found to be tightly bound to the magnetite crystal from magnetosomes from *M. magneticum* AMB-1. Although it is a larger protein, it is thought to have a similar function to Mms6 *in vivo*, being able to exert control over magnetite crystal morphology.<sup>1a</sup> Previous studies carried out in the Staniland group (unpublished) have proven unsuccessful in purification of Mms13; therefore it proved an excellent target for incorporation into the coiled-coil scaffold

#### 8.3.1.4 PROTEIN PURIFICATION

The proteins used in the following analyses were produced in *E. coli* and purified by Dr Andrea Rawlings.

MmsF was purified to assess its effect on the *in vitro* precipitation of magnetite, and for its incorporation into synthetic vesicles. It was hoped that the addition of MmsF into the artificial magnetosome would yield precipitation of particles analogous to those precipitated in naturally occurring magnetosomes. MmsF purification was expected to be challenging due to this protein's transmembrane regions. Unexpectedly, it was found that MmsF was produced in a soluble form in *E. coli*, and could be purified without the aid of detergents.<sup>5</sup> Circular dichroism was used to analyse the secondary structure of the protein and, as expected, it gave the characteristic peaks at 222 nm and 208 nm, confirming the presence of alpha helical secondary structure<sup>5</sup> (Figure 8.4 b). Thermal stability tests revealed that MmsF was stable up to 85 °C, at which point 50 % of the secondary structure was lost; this was measured by monitoring the change in absorbance at 222 nm.<sup>5</sup>

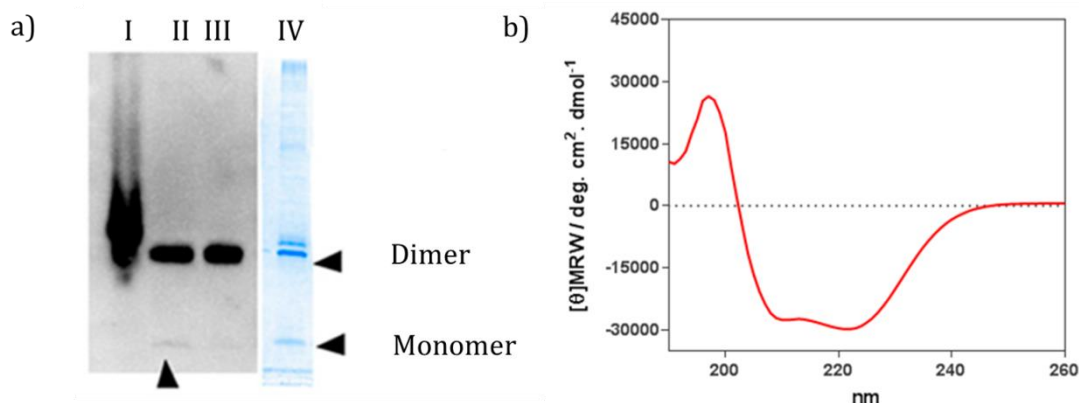


**Figure 8.4:** a) A Western blot of purified MmsF in which (I) is the total cell fraction (II) is the soluble fraction (III) is the unbound protein fraction following streptactin column purification. Arrow indicates the presence of the monomer in the western blot. (IV) shows a coomassie stain gel of the fully purified MmsF. Again arrows indicate the positions of the monomer and dimer species (as labelled). b) Circular dichroism spectrum of MmsF protein at 0.1 mg/ml at an absorbance of 280 nm collected using a 1-nm slit width cuvette and 1-s intervals, data shown is the average of three measurements with the subtraction of water blank. Adapted from Rawlings *et al.*<sup>5</sup>

Purification *via* a Streptactin resin column using the StrepII tag on the protein resulted in only a small amount of protein bound to the column, evident by the large amount of StrepII tagged material present in the unbound fraction (Figure 8.4 a). This indicates that the majority of the StrepII tags on over-expressed soluble MmsF protein is not accessible for immobilisation onto the Streptactin column. The high aqueous solubility and lack of binding to the Streptactin purification resin suggested that MmsF may be forming larger assemblies, similar to those observed for Mms6.<sup>205</sup> Due to this unexpected high solubility of MmsF it was hypothesised that self-assembly may be occurring to shield the transmembrane helices and hence improve the solubility of the protein.<sup>5</sup> This would also explain the lack of affinity for the Streptactin column, as it is likely that the tag could become buried in such an assembly.

The combination of these factors led to the decision to analyse the protein by DLS (section 2.7.1.3) to look for the presence of assembled structures.<sup>5</sup> The DLS showed the presence of species of  $100 \pm 25$  nm in diameter. This size meant that the assemblies would be visible by TEM (Section 2.7.1.1). Stained TEM micrographs revealed discrete and uniform vesicular-like assemblies now termed "proteinosomes" with an average size of 36 nm (Figure 8.5).

It was difficult to determine whether these structures were dense or hollow from TEM due to drying and staining artefacts. Therefore cryo-TEM was employed to better investigate the proteinosome structures (Figure 8.5). Under cryogenic conditions, the proteinosomes appear to be hollow due to uniform density across the structure.

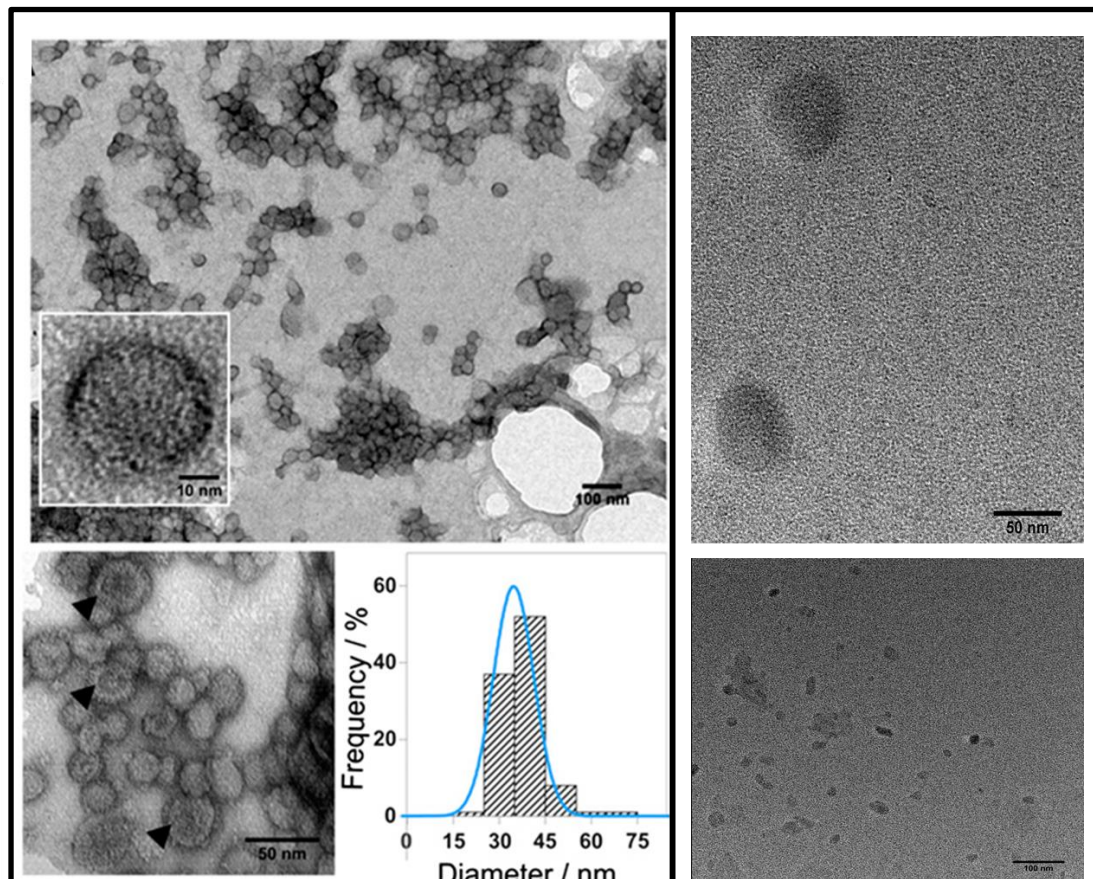


**Figure 8.5:** (Left) room temperature TEM of MmsF proteinosomes, showing protein assemblies with an average diameter of 40 nm. (Right) Cryo-TEM of MmsF proteinosomes in which they appear to be hollow protein assemblies. Adapted from Rawlings *et al.* <sup>5</sup>

It was presumed that these assemblies were composed entirely of protein. To confirm this, proteinase K was added. This should exclusively degrade the protein assemblies leaving any lipid present intact. This experiment revealed a large increase in species present in DLS studies, suggesting aggregation of the protein, and a white precipitate was observed in the sample.

TEM performed after the addition of the proteinase K confirmed degradation of the assemblies replaced by large amorphous protein aggregates.<sup>5</sup> This goes some way to confirming the hypothesis that proteinosomes are composed entirely of MmsF. Further analysis by electrospray ionisation mass spectrometry showed no lipid present in the sample.<sup>5</sup>

## 8.4 PROTEIN EFFECTS ON *IN VITRO* PRECIPITATION

### 8.4.1 MMSF IN MINERALISATION REACTIONS

The addition of purified MmsF has a significant effect on *in vitro* magnetite synthesis when added to a room temperature co-precipitation reaction. Much more consistent particle morphology was observed, with an absence of alternative iron oxide by-products when compared to control samples containing either no protein or MmsF homologue proteins (Figure 8.6).<sup>5</sup> Particles produced in the presence of MmsF were larger and with a more homologous morphology, much closer in appearance to the particles observed in MTB magnetosomes. Selected area electron diffraction revealed a higher degree of crystallinity in the MmsF sample with much more defined absorption which yielded the characteristic peaks for the presence of magnetite (Figure 8.6).

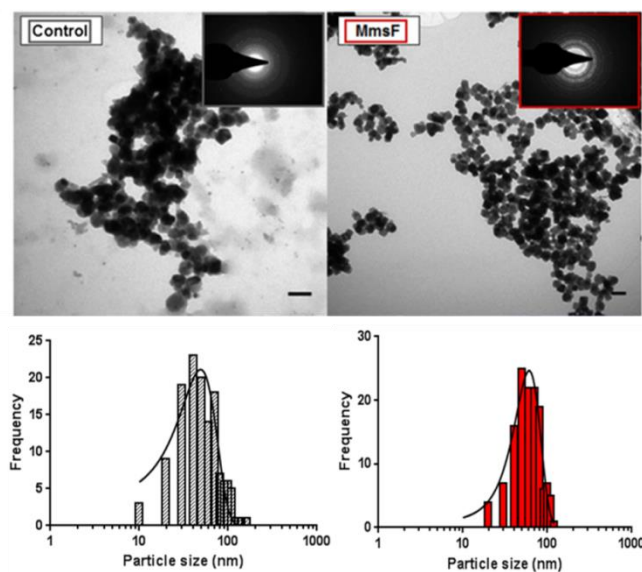


**Figure 8.6:** Left: Shows TEM (top) of room temperature co-precipitated magnetite nanoparticles, and the electron diffraction pattern collected from the TEM (inset) also shown is the particle grainsizing from the TEM (bottom). Right: shows the equivalent data for the particles produced *via* the same method with the addition of MmsF. Adapted from Rawlings *et al.*<sup>5</sup>

The control sample (which was produced in the absence of protein) electron diffraction confirmed that particles were much more amorphous, with more diffuse diffraction rings. Furthermore, particle grainsizing revealed a significantly narrower size distribution of the resulting particle population with the addition of MmsF to the reaction having an average size of  $56 \pm 22$  nm. The effects observed in the particles produced in the presence of MmsF indicate that, despite its assembly into a proteinosome-like structure in aqueous solution, it still has the ability to exert control over magnetite particle formation. This suggests that, in the proteinosome assembly, the active loops of the protein may be displayed on the outer shell of the proteinosome, for it to remain functional *in vitro* giving rise to the effects shown in figure 8.6.

### 8.4.2 Mms6

As with MmsF, addition of Mms6 to a room temperature co-precipitation reaction causes a significant change in the quality of the particles produced. Converting what would normally be a mixed population of iron oxides (Figure 8.7 a) to a homogenous particle population comparable to the morphology of MTB mineralised magnetite (Figure 8.7 b).<sup>1a, 61-62</sup> The particles are much larger in size, presumably becoming more ferrimagnetic, and appear to contain a single iron oxide species, unlike the control particles which contained needles and plates, indicating mixed iron oxides (Figure 8.7). This tight control is exerted despite relatively low concentrations of protein being used ( $5.6 \mu\text{g ml}^{-1}$ ).<sup>1a</sup> It has also been discovered that the same level of control can be achieved in partial oxidation routes to synthesis,<sup>1a, 62</sup> proving that the mechanisms of Mms6 control are not specific to synthesis route, iron salt or control of the intermediate oxide phases, as these vary between the two synthesis routes.

The mechanism by which the protein can control the magnetite precipitation is largely still unknown; however, as with MmsF, the presence of the hydrophobic region in Mms6 gives rise to the hypothesis of aggregation in aqueous solution.<sup>205</sup> The high hydrophobicity at the N-terminal region of Mms6 is believed to drive this assembly.<sup>205</sup>

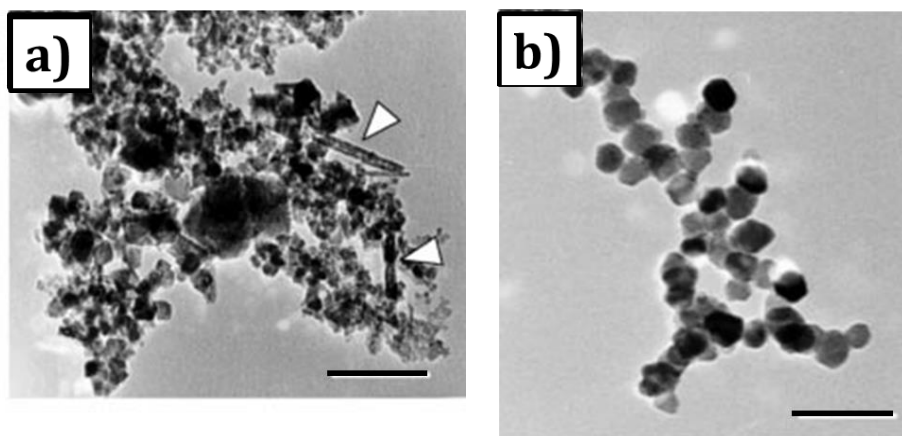


**Figure 8.7:** a) A standard room temperature co-precipitation of magnetite (arrows indicate needles) b) the particles produced *via* the same reaction route with the addition of Mms6. Adapted from Arakaki *et al.* (Scale bars = 100 nm).<sup>1</sup>

Zeta potential measurements of these aggregates have proven that they are negatively charged at neutral pH which suggests that the negative C-terminal chain of the protein must be covering the surface of the assembly. This surface may then act as a nucleation site for *in vitro* magnetite precipitation.<sup>205</sup> The aggregation of Mms6 may affect vesicular incorporation, in a similar way to MmsF, although incorporation into synthetic vesicles has not yet been tried, so the mechanisms can only be hypothesised.

### 8.4.3 COILED-COILS

The functionality of coiled-coil scaffolds displaying the active regions of MmsF and Mms13 have been tested previously by members of the Staniland group in room temperature co-precipitation reactions. Coiled-coil proteins were added at a concentration of 50  $\mu\text{g ml}^{-1}$ . TEM micrographs of the particles precipitated in the presence of the MmsF and Mms13 coiled-coils are shown in figure 8.8, along with control particles precipitated in the absence of a coiled-coil. A huge increase in the size of the resulting particles was observed as confirmed by particle grainsizing (Figure 8.8).

An increase from  $10 \pm 2$  nm (no protein) to  $74 \pm 12$  nm with the addition of MmsF coiled coil and  $41 \pm 24$  nm in the case of Mms13 coiled coil, which will have a direct effect on the magnetic properties of the particles, possibly improving their suitability for biomedical application. Particles precipitated in the presence of the coiled coils also had a much more defined morphology, appearing closer to the expected cubo-octahedral morphology seen in MTB magnetosome crystals.

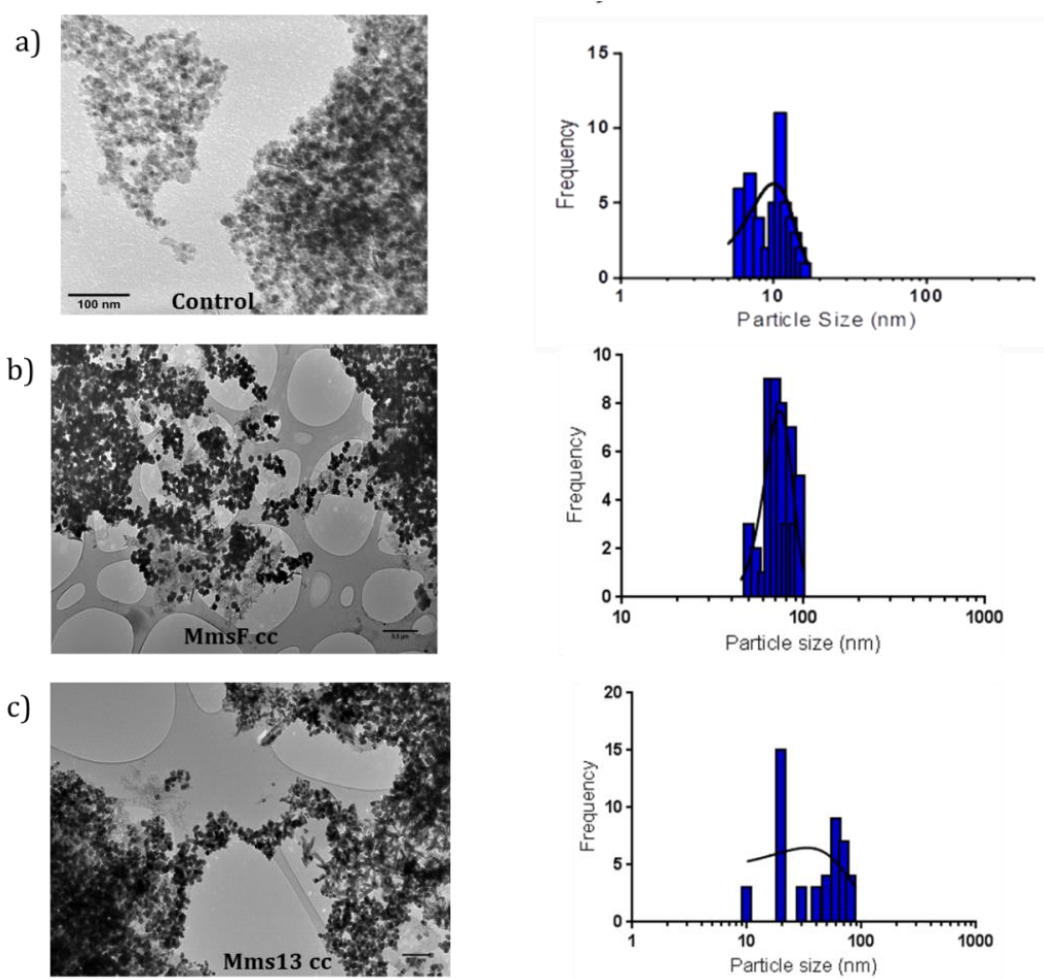


**Figure 8.8:** TEM micrographs of magnetic nanoparticles produced by a) standard room temperature precipitation conditions, with the addition of b) coiled-coil displaying the active region of MmsF and c) coiled-coil displaying the active region of Mms13, and their corresponding TEM particle grainsizing. Data provided by previous Staniland group members (TEM performed by me).

## 8.5 VESICLE INCORPORATION OF BIOMINERALISATION PROTEINS

Proteins were incorporated into DPhPC liposomes or PBD-PEO polymersomes on rehydration of a lipid/polymer film with 10 mM NaOH. The proteins should remain stable and folded after vesicular incorporation at pH 12, as they have all been previously used in room temperature co-precipitation with basic solution at higher concentrations and retained their activity. These data present morphological changes in the vesicle core following the incorporation of biomineralisation proteins into the vesicle.

### 8.5.1 LIPIDS AND PROTEINS

MmsF and Mms6 were added to a DPhPC film rehydrated with 10 mM NaOH, so that protein incorporation can occur during liposome assembly. The vesicles were then electroporated (Section 2.3.3) with an applied voltage of 750 V in the presence of ferrous and ferric chloride solution (at the stoichiometric ratio for magnetite). The nature of incorporation of the proteins is currently unknown, but is likely to proceed *via* disassembly of the aggregate or incorporation of the protein aggregates as a whole.

#### 8.5.1.1 MMSF INCORPORATION

It was hoped that the resulting vesicles would be filled with iron oxide as seen with previous vesicle samples (Chapter 6) but that the presence of MmsF would yield higher quality nanoparticles closer in morphology to those extracted from MTB. Due to its self-assembling properties it was unknown how MmsF would incorporate into the synthetic DPhPC liposomes. One hypothesis was that the proteinosome will remain assembled and sit within the liposome forming almost another leaflet. Incorporation *via* this mechanism would yield a complete nucleation surface on the inside of the liposome offering increased control over precipitation of the particle.

However incorporation of this type (which would essentially increase the bilayer thickness) may hinder transmembrane transport of iron. Another hypothesis is that the proteinosome will disassemble and incorporate into the membrane in the same way as monomeric membrane proteins. It is also possible that the MmsF protein may incorporate into the membrane not as single protein monomers, but instead form “islands of proteins” akin to lipid rafts observed in liposomes.<sup>208</sup> In both cases, the orientation of the protein upon incorporation will be crucial to the proteins functionality, and it is likely that incorporation *via* the second proposed mechanism has a higher probability of positioning the protein with the desired topology. TEM micrographs of the liposomes following electroporation show incorporation of what is presumed to be iron oxide (Figure 8.9).

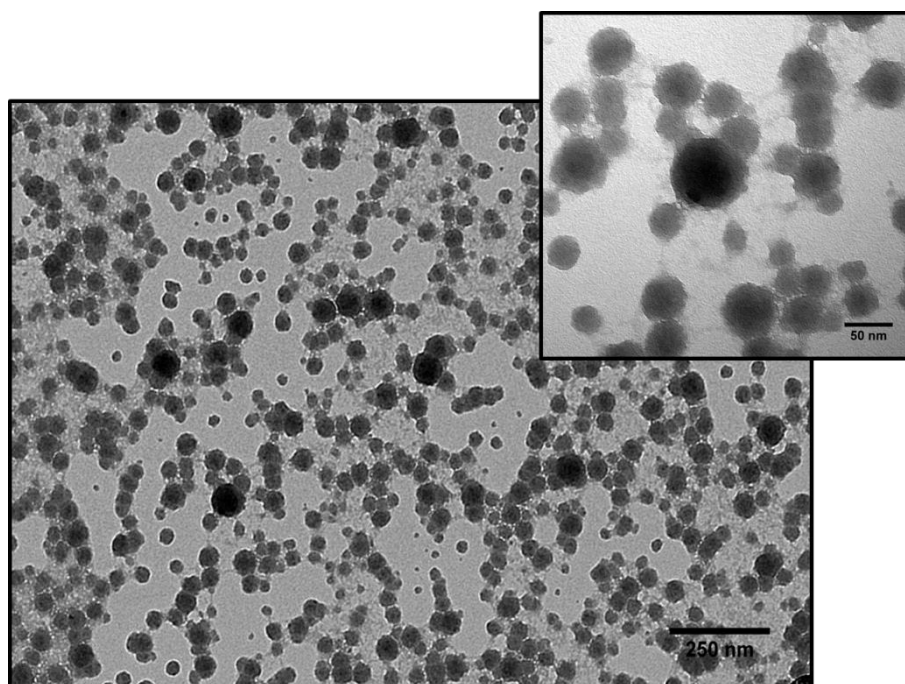


**Figure 8.9:** TEM micrograph (main picture and inset magnification) of MmsF incorporated into DPhPC liposomes after electroporation (5 x 750 v) in the presence of ferrous and ferric mixed iron chloride (10 mM) solution, Inset: magnification of negatively stained liposomes from the same sample that have not been electroporated in the presence of iron.

It is impossible to distinguish presence of the protein/proteinosome or any obvious difference in the morphology of the precipitate. What can be seen is a distinct density difference between the core of the liposome and the bilayer, suggesting increased penetration of the bilayer. There is an obvious presence of electron dense material in the liposome bilayer (as liposomes are otherwise unstained), (figure 8.9). This could be as the result of miss-orientation of the protein in the bilayer causing nucleation of iron oxide on and in the bilayer. As yet, this hypothesis remains inconclusive and confirmation would first require identifying the position and orientation of the protein in the bilayer, either by the addition of fluorescent tags to the protein or chemical composition analysis.

#### 8.5.1.2 Mms6 INCORPORATION

TEM micrographs of Mms6 incorporated vesicles post electroporation indicates encapsulation of iron oxide, by the appearance of electron dense material in the vesicles (see figure 8.10). Vesicles also appear much less discrete than in previously imaged samples. It is hard to determine whether the disrupted vesicle structure is as a result of Mms6 incorporation or degradation of the DPhPC lipid (Figure 8.10). However, as with MmsF, there is an increased density associated with the vesicle core. It is hoped that this is a consequence of increased nucleation of iron ions to encapsulated Mms6, but again would require analysis of the protein within the vesicle.

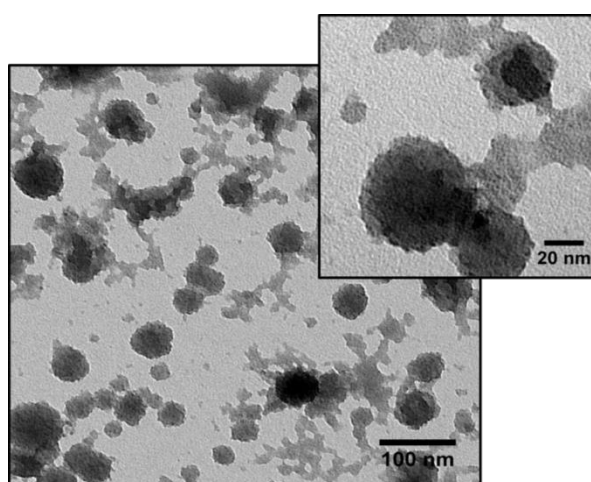


**Figure 8.10:** TEM micrograph (and inset magnification) of Mms6 incorporated into DPhPC liposomes and electroporated (5 x 750V) in the presence of ferrous and ferric mixed iron chloride (10 mM) solution, Inset: magnification of liposomes from the same sample.

## 8.5.2 POLYMERS AND COILED-COILS

As with the native biomineralisation proteins, the coiled-coil scaffold proteins were incorporated into PBD-PEO polymersomes during rehydration of the polymer film with 10 mM NaOH. Polymersomes were subsequently electroporated in the presence of ferrous and ferric chloride solution (mixed at the stoichiometric ratio for magnetite). The polymersomes were cleaned up by SEC to remove externally precipitated iron oxide (Section 2.2.3). The polymersome sample was analysed SDS-PAGE with Coomassie staining for detection of the coiled-coil in the sample. The resulting gel confirmed that coiled-coils are associated with the PBD-PEO polymersomes by the presence of the bands at 15 kDa (compared to PageRuler Life Technologies molecular weight marker) present for both Mms13 and MmsF coiled coils (Figure 8.11 a).

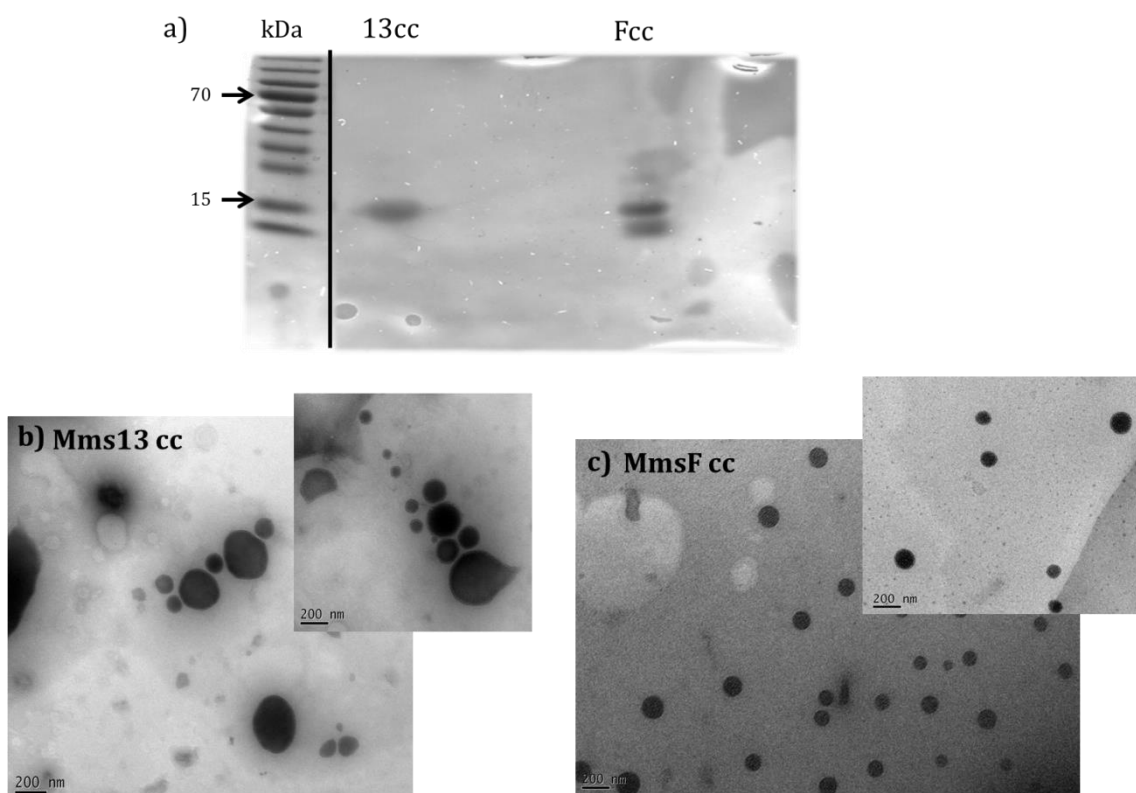


**Figure 8.11:** a) Western blot of polymersomes incorporating coiled coils (after clean up) confirmed the presence of the proteins associated with the polymersomes as shown by the bands at approximately 15 kDa. TEM micrographs of the same polymersome sample incorporating b) Mms13 coiled coil and c) MmsF coiled coil.

When these same samples are observed in TEM, the polymersomes appear to be of a high quality and relatively monodisperse polymersomes which have a consistent highly spherical morphology. A bilayer is visible on many of the PBD-PEO polymersomes (Figure 8.11 b). All polymersomes imaged had consistently filled electron dense cores, predicted to be iron oxide. They are significantly different in morphology to electroporated polymersomes without coiled coils, (Figure 6.4). Therefore, this change could be attributed to the presence of the coiled coil artificial proteins within the core.

The MmsF coiled-coil incorporated polymersomes were of a highly uniform morphology (Figure 8.11 c), when compared to polymersomes incorporating the Mms13 coiled-coil. In both polymersome samples, it is also possible to distinguish the presence of a bilayer. The reason for this may be the high homogeneity of the precipitate, more of which appears to have occurred within the core of the polymersome for the Mms13 coiled-coil when compared to the MmsF coiled-coil polymersome samples. For the MmsF sample, although the core is equally as dark, heterogeneity in the density of the core suggest the presence of a cluster smaller particles rather than a single MNP crystal. It is possible that these smaller particles reside in the polymersome membrane as with electroporated PBD-PEO in the absence of protein (Figure 6.4). It is possible that this is also why the bilayer is not as easily distinguished. This could be due to a difference in the position of the coiled-coil in the polymersomes, although this is impossible to confirm without further analysis. To answer this question this would first require labelling of the coiled coil proteins with a fluorescent tag or perhaps gold binding peptide to make its detection and analysis of its position possible.

## **8.6 BIOMINERALISATION WITHIN VESICLES: DISCUSSION**

This chapter presents the preliminary work on the incorporation of MTB proteins into synthetic magnetosomes, for the control of intra-vesicular magnetite precipitation. This is a difficult process, involving the expression and purification of the protein, incorporation into synthetic vesicles, identification of position and orientation of the incorporated proteins and confirmation that they are functioning successfully.

Not all of this work has been completed as part of this project, but the proof-of-concept data presented now allows for further modification of the proteins to confirm the successful incorporation that TEM analysis suggests. The chapter focussed on observation of morphological changes introduced by MTB biomineralisation proteins and their biomimetic scaffold counterparts.

Each of the MTB proteins in their native form (cloned from bacterial genomic DNA) are difficult to purify and work with due to their highly hydrophobic nature, expressing at low concentrations. Incorporation of both the proteins and the artificial scaffold proteins into synthetic vesicles will help to create an artificial magnetosome. Not only will this aid the formation of a fully functional synthetic magnetosome with the superior properties required for biomedical application, it is hoped that this would also contribute to understanding the function of the proteins in a close to native environment.

However confirmation of a) incorporation, b) position, c) orientation and d) functionality of the proteins and scaffolds is extremely difficult. It can be assumed that the incorporation has been successful and TEM micrographs and in some cases SDS-PAGE supports this hypothesis. For this premise to be conclusive detection of the protein must be confirmed *via* the routes discussed (such as addition of fluorescence tags, or other labels). Tagging the protein should also indicate its position in the vesicle, conclusive evidence of the proteins orientation and functionality are much harder to achieve. For these, multiple characterisations are required, which when combined should confirm the hypotheses drawn from the preliminary data shown throughout this chapter. For example, confirming the orientation can be strengthened using protease experiments, which should degrade the outer membrane region of the protein which could then be detected using mass spectroscopy to work out which sites are exposed. This is a lengthy process requiring in-depth analysis of the sequence and careful selection of the protease.

The predicted regulation of iron oxide precipitation functionality of the proteins is supported by the data shown, by the distinct difference between electroporated vesicles with and without the proteins incorporated.

Increased nucleation of electron dense material within the vesicles that incorporate proteins suggests an iron oxide nucleating function of the protein. Measurement of internal pH gradients is difficult, but would help confirm what appears to be happening. Energy dispersive X-ray could provide confirmation of the elements present, and selected area electron diffraction could probe the crystallinity of these electron dense cores to confirm whether they are iron oxide.

There is a distinct difference between the vesicles containing MmsF and Mms6. For example, MmsF incorporation has yielded a much higher quality vesicle population, (Figure 8.8) in comparison to vesicles after Mms6 incorporation (Figure 8.10), which appear to be interconnected with some forming what appears to be a network of organic material. This could arise from the self-assembling properties of the MmsF, which has been proven to form highly monodisperse proteinosomes.<sup>5</sup> If the proteinosomes are being incorporated as assembled, they are likely to have an effect on the dispersity of the resulting vesicles. The MmsF incorporated vesicles also appear to have increased and more homologous precipitation indicated by electron dense cores. This may indicate improved nucleation properties of MmsF. This is particularly evident when compared to Mms6 incorporated vesicles, in which the precipitate does not fill the vesicle core, and appears much more heterogeneous. As all other conditions were kept constant between the two samples, the difference in vesicle appearance and amount of the precipitate can be attributed to the presence of the two different proteins. With these preliminary data corresponding with the literature,<sup>209</sup> which suggests improved nucleation and regulation of iron oxide precipitation in the case of MmsF.

The apparent success of the coiled coil vesicular incorporation is again a novel process, and whilst these experiments need further characterisation to confirm their success, this is a positive advancement in the creation of an artificial magnetosome. The coiled-coil scaffold proteins are much easier to express and purify than the native MTB proteins, alleviating difficulties experienced with purification and solubility, particularly with respect to refolding proteins such as Mms6. Due to their easy purification, it is possible to achieve yields which are orders of magnitude higher than with the full protein. This makes their incorporation into a synthetic vesicle much more feasible, particularly with regards to scale-up for application and possible future commercialisation.

# **CHAPTER 9:**

---

## **BIOMEDICAL APPLICATION OF MAGNETO-VESICLES**

## 9.1 INTRODUCTION

One ultimate aim of this project is that the artificial magnetosome developed will be functional for future use in biomedicine. More specifically, it is hoped that superior magnetic properties as a consequence of the biomimetic synthesis route will yield superior MRI contrast agents and/or hyperthermic materials for ablation of tumour tissue. With this in mind *in vitro* testing of magneto-nano-vesicles produced throughout this thesis have been tested by both myself and collaborators with expertise in these areas. The data presented in this chapter is as a proof-of concept, but is designed to give an indication of the potential of artificial magnetosomes for future biomedical application.

The samples tested in this chapter for their biomedical potential were those that were the most successful in vesicle synthesis (as optimised throughout chapters 6, and 7) when examining the different transport methods for mineralisation within vesicles. Specifically, these include; electroporated (750 V) DSPC EHDA synthesised liposomes (shown in figure 7.5), PBD-PEO electroporated (2500 V) polymersomes (Figure 6.4), PMOXA-PDMA-PMOXA electroporated (750 V) polymersomes and PEG<sub>113</sub>-PHPMA<sub>400</sub> /PMPC<sub>28</sub>-PHPMA<sub>400</sub>, *via* all three transport routes tested (electroporation, ionophore and flocculated). These were chosen as they appeared to show a good amount of electron dense material, presumed to be iron oxide, in TEM imaging, within the vesicle structure. Of particular interest were the vesicles with NPs in differing position in the vesicle structure, particle size and amount of iron oxide present, and how these differences affect the magnetic properties, and therefore their potential for biomedical use.

The values obtained for the samples above are compared to literature values, physiological conditions and commercially available nanoparticles. For MHT ILP values measured from these magneto-vesicle samples, these have been compared to an average ILP of 2.5-3 nHm<sup>2</sup>kg<sup>-1</sup> in current literature, and an ILP of approximately 3 nHm<sup>2</sup>kg<sup>-1</sup> for current commercially available particles.<sup>145</sup> Similarly, MRI relaxation rates obtained from measurements on magneto-vesicles were compared to the R<sub>2</sub>\* relaxation rate of grey matter, which is 30 s<sup>-1</sup>.<sup>210</sup>

The particle's relaxation rate must be greater than this value to be effective *in vivo* as a contrast agent. A  $T_2$  relaxation rates of  $146 \text{ mmol}^{-1}\text{s}^{-1}$  for MTB magnetosomes and  $62 \text{ mmol}^{-1}\text{s}^{-1}$  for synthetic dextran iron oxide coated nanoparticles<sup>148</sup> has also been used for comparison.

## 9.2 *IN VITRO* MAGNETIC HYPERTHERMIA TESTS

All initial magnetic hyperthermia tests were conducted using a Magnetherm (Nanotherics) system. This comprises either a 9 or 17 turn coil in the centre of which the sample is placed. The magnetic field strength and its alternating frequency are determined by a power supply (from which a current is generated) and a frequency generator respectively. These parameters are dependent on the coil/capacitor combinations which are chosen to obtain specific field frequency and field strength. The system is tuned to resonance using a digital oscilloscope to avoid over heating of the coil which in turn heats the sample. Additional measures are taken to prevent coil heating by attachment of the system to a water supply. There must be a minimal water flow rate around the coil for the system to be operational. In this case the system was connected to a recirculating water bath set at either  $10^\circ\text{C}$  or  $20^\circ\text{C}$ .

### 9.2.1 CALIBRATION OF THE MAGNETHERM

The collection of reliable calibration data is difficult due to the many parameters that can affect heating.<sup>145</sup> These were previously outlined in the paper by Wildeboer *et al.*<sup>145</sup>, who discuss the common inaccuracies encountered during the measurement of the heating capabilities of materials and how this can widely affect the value obtained. Their work also highlights that there is not yet a universally accepted method of SAR/ILP measurement.<sup>145</sup> Typical inaccuracies arise firstly from heat transfer between the sample and its surroundings or vice versa.

This means that heat from the particles in the sample can be lost, resulting in the SAR/ILP value being underestimated. Conversely, these values can be inflated if there is heating from the solution, or as the result of convection currents in the sample, either of which contributes to the overall temperature difference. Ideally, measurements would be carried out under adiabatic conditions which would ensure the SAR or ILP measurement is unaffected by the heat transfer discussed above. However, in terms of practicality of the measurements, this is unfeasible, as it is impossible to obtain an entirely adiabatic system.

Therefore it was decided that measurement data presented in this chapter would be calibrated for the heating power of the solvent and for heat loss to the surroundings. This was achieved by measurement of the temperature change to the surroundings of the sample, as closely as possible. Of course, this cannot account for heat loss to the container, but any change in temperature was added to or subtracted from the final temperature change. Similar subtractions were made with regards to the heating capability of the solvent. This was done by taking repeat measurements of the temperature increase of the solvent when subjected to an alternating magnetic field. This was then subtracted from any heat increase observed in the presence of the particles, ensuring the same sample volume was used. It was found that changing the sample volume of the control PBS sample could change the temperature increase observed as much as 2-3 °C for a 1 ml sample, when compared to 7-8 °C when only 100-300 µl are used. Therefore, to ensure heating power of only the magneto-vesicles was measured, the volume transferred to the heating chamber was kept consistent between samples. Also critical to the outcome of the measurement is the shape of the sample container, with flat-bottomed containers offering more evenly distributed heating and therefore more accurate measurements. Similarly the position of the temperature probe can affect the result; it was found that tests in which the probe was placed at the bottom of the sample container (particularly with tests conducted in Eppendorf's) appeared to have increased heating. This is reinforced by Wildeboer *et al.*<sup>145</sup>, who recommend the use of a flat bottomed vial, with a centrally located probe. This should give an accurate reading of the mean temperature of the sample  $\pm 1^\circ\text{C}$ .<sup>145</sup>

After much experimentation, a method was designed for measurement of the heating capability of magneto-vesicles, as accurately as practicalities would allow. This consisted of measurement of a defined volume of the sample solvent alone, in a glass bottomed vial, followed by measurement of the same volume of solvent, now with the addition of the vesicles. In each case, the temperature of the solution was left to equilibrate for 10-20 minutes before the magnetic field was applied. This is because it was also found that this fluctuated less when the recirculating water bath temperature was higher (20 °C). The temperature change was then measured for 15 minutes. Before plotting, both the starting temperature and the temperature of the solvent alone were subtracted. This is especially important as a thermocouple was used to measure the temperature increase (as provided by Nanotherics and it is standard equipment), but due to metal components, is believed to also have induced heating in an AMF.

### 9.2.2 MAGNETO-VESICLE HEATING CAPABILITY

The most promising magneto-vesicle samples from each set of experiments presented throughout this thesis were tested for their potential use as hyperthermia agents. This was done by placement of the vesicle solutions (following clean-up to remove external iron oxide precipitate) in an alternating magnetic field. The temperature increase when samples were placed in an alternating magnetic field (AMF), of  $H = 7.68 \text{ kA m}^{-1}$ , is shown in figure 9.1. The heating ability was recorded every second for 15 minutes (following equilibration of the baseline temperature), over three runs, and an average temperature increase was calculated and plotted (Figure 9.1). In all samples, initial temperature increase was observed in the first 30-60 seconds; it is from this initial temperature gradient that the heating capability of the sample can be obtained. All ILP calculations are measured using the iron concentration in the sample based on ICP-MS measurements. Due to the variation in the concentration of the magneto-vesicles between samples, comparison of and the reproducibility of the heating effects has been difficult. Presented here is some preliminary work that needs to be further optimised to ensure reproducibility of the results seen.

Most samples showed a discernible temperature increase, with the exception of the electroporated tri-block magneto-polymerosomes (PMOXA-PDMA-PMOXA). In this case, the solution decreased in temperature over the 15 minute measurement period in the AMF. These polymerosomes appeared to be distorted post-electroporation (Chapter 6). While these morphological defects may dampen the heating capability of the polymerosomes, it is not expected that they would cause a decrease in temperature, so this reaction to an alternating field is somewhat surprising.

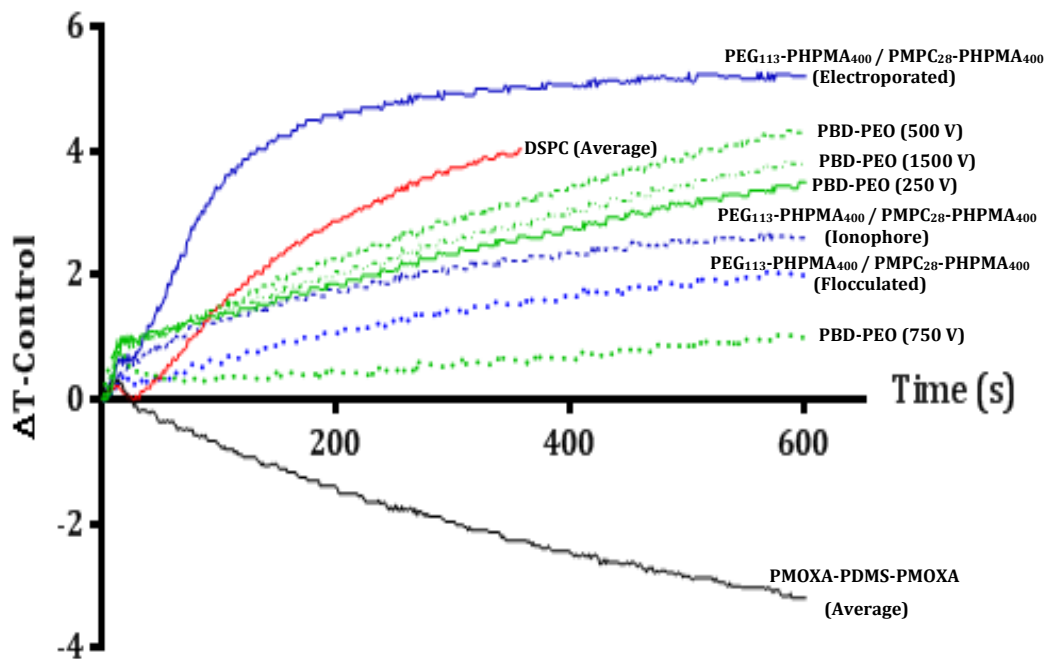


**Figure 9.1:** Temperature increase induced by various iron oxide filled vesicles after 10 minutes in alternating magnetic field at 739 kHz and field strength of  $7.68 \text{ kAm}^{-1}$ , control PBS heating and the initial temperature have both been subtracted from the plots.

One hypothesis for why this may have occurred is that the particles in the polymerosomes do not cause any heat dissipation in an AMF. This may be for one of two reasons, the first being that their position in the membrane hinders their switching. This would mean that the MNPs produce no heat at this applied field strength. Secondly, and more likely, is that the particles are not magnetic and therefore have no response to the alternating field.

In either case, the decrease in temperature yields an ILP value of  $-1.69 \text{ nHm}^2 \text{ k}^{-1}$  and is likely to be due to be the flow around the coil from recirculating water bath cooling the sample. For PEG<sub>113</sub>-PHPMA<sub>400</sub> / PMPC<sub>28</sub>-PHPMA<sub>400</sub> the samples which were electroporated to initiate iron ion transport gave the greatest temperature increase, and continued to increase at a faster rate than the other samples. The maximum final temperature increase was  $5.2^\circ\text{C}$ , which would be sufficient to damage/destroy cancerous cells.

Sample	MNP Formation method	ILP ( $\text{nHm}^2 \text{ kg}^{-1}$ )
PMOXA-PDMS-PMOXA	Electroporated (750 V)	-1.69
DSPC (EHDA synthesised)	Electroporated (750 V)	3.65
	Electroporated (750 V)	3.5
PEG <sub>113</sub> -PHPMA <sub>400</sub> / PMPC <sub>28</sub> -PHPMA <sub>400</sub>	Ionophore (A23187)	1.8
	Flocculated (RTCP)	0.4
PBD-PEO	Electroporated (250 V)	1.05
	Electroporated (500 V)	1.01
	Electroporated (750 V)	0.13
	Electroporated (1500 V)	1.37

**Table 9.1:** ILP values corresponding to the heating capabilities of samples plotted in figure 9.1.

The temperature increase produced by the same polymer in which the A23187 ionophore was incorporated was lower at 4.0°C, which would also be sufficient to have ablation effects on the surrounding tissue. The temperature increase achieved with the flocculated PEG<sub>113</sub>-PHPMA<sub>400</sub>/PMPC<sub>28</sub>-PHPMA<sub>400</sub> polymer was lower still at 2.8° C. A temperature increase of this kind can have a detrimental effect *in vivo*, as the gentle warming (2-3 °C) of cancer cells can actually accelerate division of the tumour cells, with the consequence of helping to spread the tumour tissue.

These results are not surprising with respect to electroporation and transport *via* the ionophore, as it known that electroporation reliably porates the vesicle membrane multiple times per pulse.<sup>160, 164</sup> This means that a much higher uptake of soluble iron is likely, which can be further increased by multiple pulses in some cases (Figure 6.14). This is in contrast to transport using the A23187 ionophore, in which it takes two ionophore molecules to transport a single ferrous ion across the membrane, therefore the mass of iron transported across the vesicle membrane is likely much lower. Furthermore, the A23187 is divalent cation specific; therefore the precipitation of magnetite within the core requires a significant proportion of the transported ferrous ions to be oxidised to ferric iron and successfully mineralise magnetite. On this basis, it is unlikely that the same amount of magnetic iron oxide is being precipitated within the ionophore porated vesicles as is achieved by electroporation. More surprising is the heating capability of the flocculated sample, which is significantly lower than with the other transport methods used for this polymer. Incubation in a room temperature coprecipitation before flocculation to isolate the polymersomes (section 2.3.4) should have the highest probability of successfully precipitating magnetite. This is because the polymersomes are incubated in a controlled magnetite precipitation reaction. However, the low heating capability raises concerns that reagents are not penetrating the polymersome membrane effectively. This means that the electron dense material observed in the TEM is unlikely to be magnetite, as magnetite would have a direct effect on the heating ability of the magneto-polymersomes.

Electroporated DSPC vesicles which had been synthesised using EHDA show similarly high heating capabilities to commercially available iron oxide nanoparticles. These produce an ILP of 3.65 nHm<sup>2</sup> k<sup>-1</sup> over a 15 minute heating period.

This heightened heating is likely to be the result of an iron oxide filled vesicle core, the composition of which was confirmed to be magnetic iron oxide; either magnetite or maghemite (see section 7.4.4). The filled vesicle core will also give a high iron ion concentration in ICP-MS measurements on which the ILP calculation is based. This increase compared to other samples with much lower ILPs (Table 9.1) suggests that other polymersomes perhaps contain another less magnetic iron oxide, causing the vast difference in calculated ILP.

The most interesting results are in the ILP measurements of PBD-PEO electroporated polymersomes. The ILP's of the samples measured on the Magnetherm show no correlation to increasing the applied voltage, with the sample at 750 V showing the lowest heating capability. This is a voltage which yields an ILP of  $3.65 \text{ nHm}^2 \text{ k}^{-1}$  in DSPC liposomes. All other PBD-PEO samples measured give values of approximately  $1 \text{ nHm}^2 \text{ k}^{-1}$ . Control readings are taken of the blank solution and thermocouple heating, this is then subtracted and the reading set to zero before measuring the magneto-polymersome sample. It's possible that despite subtracting control data, coupling is occurring between the magneto-polymersome solution and the thermocouple. This would lead to the magneto-polymersome solution heating, this heats the thermocouple, this in turn further heats the solution which then becomes cyclic. This requires further investigation using an alternative probe, such as a fibre optic probe (which has been recently purchased by the Staniland group). Therefore, all experiments will be repeated as part of further work with the fibre optic probe.

These polymersomes (electroporated at 2500 V) were tested on a different system to test the hypothesis that heating from the probe is introducing inaccuracies into hyperthermia reading from the Magnetherm (Nanotherics). These experiments were repeated under different parameters (1 MHz,  $1.32 \text{ kAm}^{-1}$ ) using alternative equipment (MACH (Magnetic Alternating Current Hyperthermia) system, Resonant Circuits Limited, UK) by experts in the field (UCL, Nanomagnetism Lab), an observed temperature change of  $6^\circ\text{C}$  was achieved, with an ILP of 9.3, (Figure 9.2) a value which is triple the ILP of commercially available nanoparticles. The ILP was calculated from a more accurate iron oxide concentration (as measured by SQUID).

Furthermore, the temperature increase was measured using a fibre optic probe as opposed to a thermocouple, which does not heat in an AMF and therefore should provide more accurate readings.

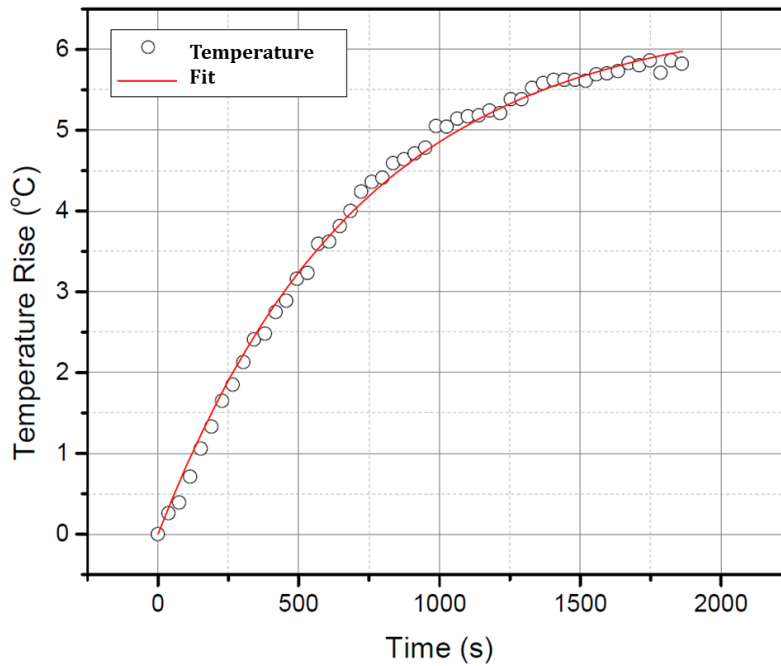


**Figure 9.2:** Temperature increase induced by PBD-PEO magneto-polymsomes after 30 minutes in an alternating magnetic field at 1 MHz and field strength of  $13.2 \text{ kAm}^{-1}$ , yielding an ILP of 9.3 for an estimated iron oxide concentration of  $22 \mu\text{g ml}^{-1}$ .

A hypothesis for the increased heating capability of this sample is the precipitation of the iron oxide nanoparticles in the polymer membrane. It is possible that *in situ* formation of MNPs, as opposed to encapsulation of pre-formed MNPs, may lead to tighter association with the vesicles membrane. Due to the particle size (2-3 nm) they are superparamagnetic, and therefore will undergo Brownian rotation. If particles are tightly associated with a membrane, this is likely to cause friction between the membrane and the MNP rather than free in fluid, as the particle flips. This friction will generate heat, therefore heightening the heating ability of the particles beyond what is expected for their size.

Figure 9.3 shows repeated measurements of a second PBD-PEO polymersome sample electroporated at two different voltages (750 V and 1500 V, a repeat of the data shown in figure 9.1). This repeat was again performed at UCL using the MACH (Magnetic Alternating Current Hyperthermia) system, (Resonant Circuits Limited, UK) and again, the results are highly inconsistent with the data collected using the Magnetherm.

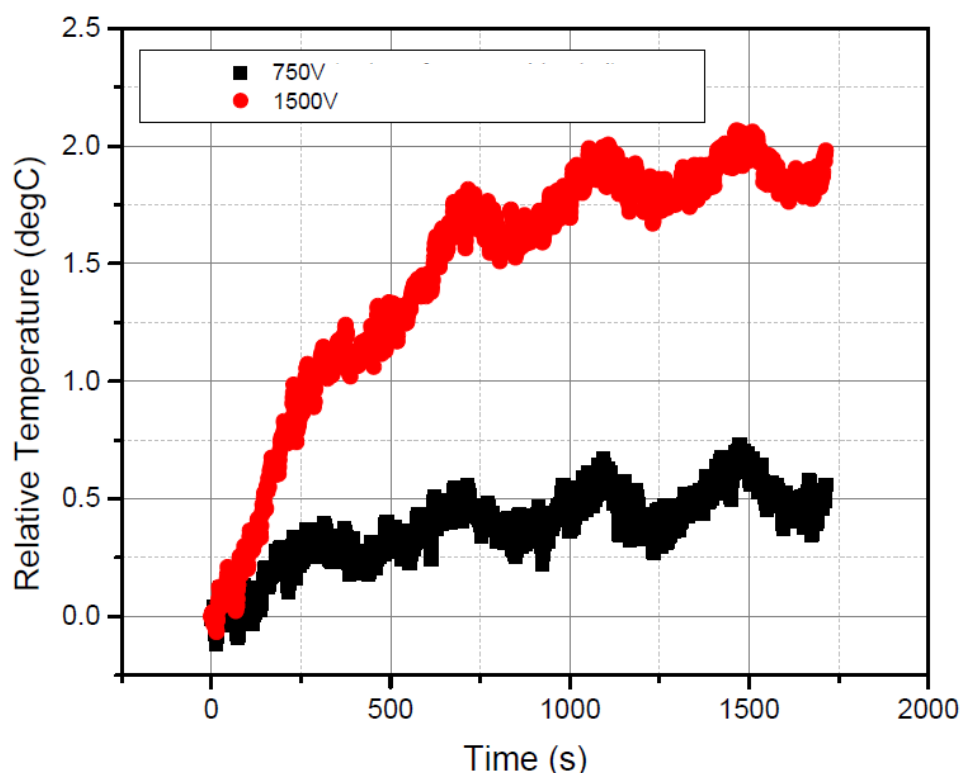


**Figure 9.3:** Temperature increase induced by PBD-PEO magneto-polymersomes electroporated at 750 V and 1500 V after 30 minutes in an alternating magnetic field at 944 kHz and field strength of  $9.9 \text{ kAm}^{-1}$ , heating of a blank water sample has been subtracted from these plots to normalise for contributions from the buffer and container.

The data shown in figure 9.3 of PBD-PEO polymersomes were electroporated at 750 V and 1500 V and were subsequently tested at the UCL Nanomagnetism Lab (as in the case of data shown in figure 9.2) to rule out inaccuracies from thermocouple heating. Although there is a large amount of noise in the traces (due to the small sample size), the heating capability of the samples still show a trend closer to that expected (i.e. increasing ILP as function of applied voltage). This time an increase of  $2^\circ\text{C}$  was observed in the sample electroporated at 1500 V when compared to only  $0.5^\circ\text{C}$  from the sample electroporated at 750 V.

Calculation of the ILPs from this sample are shown in figure 9.4. Figure 9.4 a) shows comparison of the three different PBD-PEO magneto-polymersome samples, synthesised at the three different electroporation voltages. Relative ILP values for these three samples are based on the total iron concentration in the sample (measured by ICP-MS) and are shown in figure 9.4 b). These have the predicted trend of increasing ILP as a function of increasing applied electroporation voltage (relative to Fe concentration).

However, a much greater ILP is obtained from figure 9.2, where the ILP is calculated from the concentration of magnetic iron oxide present in the sample (as measured by SQUID at UCL).

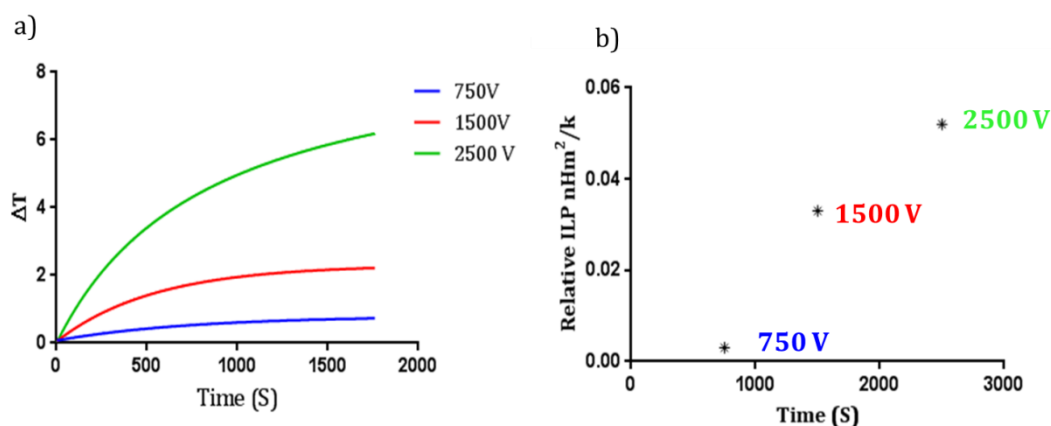


**Figure 9.4:** Temperature increase induced by PBD-PEO magneto-polymerosomes electroporated at 750 V , 1500 V, 2500 V after 30 minutes in an alternating magnetic field at 944 kHz and field strength of  $9.9 \text{ kAm}^{-1}$ . b) Relative ILP values (relative to total iron concentration in the sample) for the temperature increase induced by the magneto-polymerosomes electroporated at the three different voltages.

## 9.3 MAGNETO-VESICLES AS MRI CONTRAST AGENTS

All MRI measurements were performed by Dr Aneurin Kennerley (Magnetic Resonance Physicist for fMRI facility, Department of Psychology, University of Sheffield)

### 9.3.1 CALIBRATION OF MEASUREMENTS

Magneto-vesicles were tested for their potential as MRI contrast agents. All tests were carried out on a 7 Tesla Bruker MRI, with samples of equal volume in glass vials, or in capillary tubing suspended in Agar (to avoid distortion of the magnetic field due to the surrounding/vessel; known as shimming) in a capillary model system.

In each case, the vesicles were compared to a control saline solution to ensure that any contrast seen was due to the vesicles in the sample. Initial tests confirmed that PBD-PEO magneto-polymerosomes had increased contrast at both high (approximately 60 mg ml<sup>-1</sup>) and low concentration (approximately 1 mg ml<sup>-1</sup>) when compared to saline (Figure 9.5). Conversely the contrast was much lower than commercially available magnetic iron oxide nanoparticles (MION, 10 mg ml<sup>-1</sup>) (Figure 9.5).

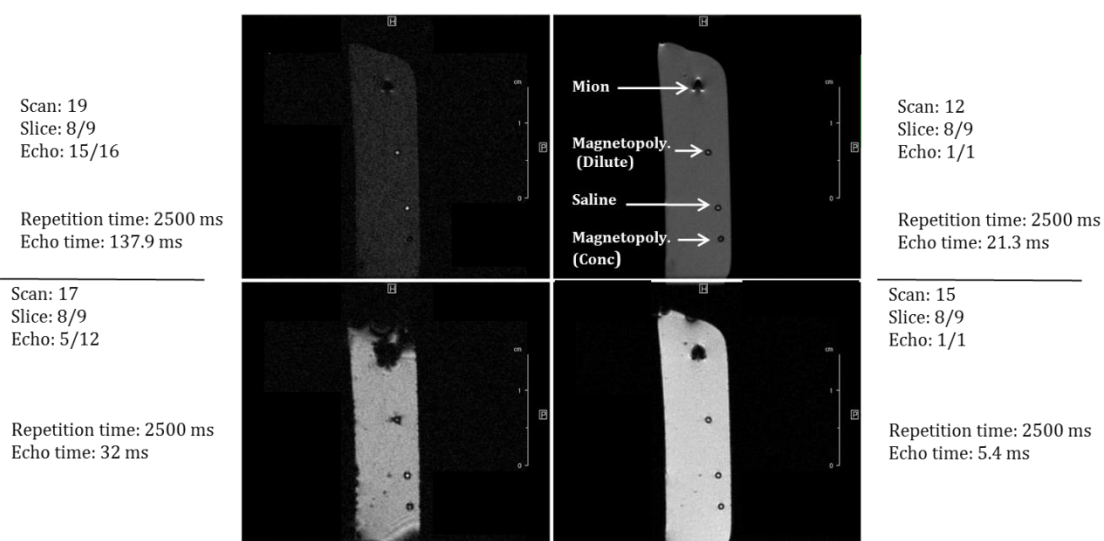


**Figure 9.5:** MRI images of contrast provided by two different magneto-polymerosome concentrations compared to a blank saline sample and a control sample of magnetic iron oxide nanoparticle (MION) solution.

The same concentration effect can be seen in the relaxation rates of the magneto-polymerosome samples, where serial dilutions of the samples have a proportional decrease in the  $R_2$  relaxation rate (Figure 9.6). This effect is also observed as the iron oxide concentration in the sample increases from 10 mg ml<sup>-1</sup> (Figure 9.6 a) to 60 mg ml<sup>-1</sup> (Figure 9.6 b) and c) gives rise to an increase in  $R_2$  relaxation from 1.65 to 7.52 and 7.47 (arbitrary units) respectively.

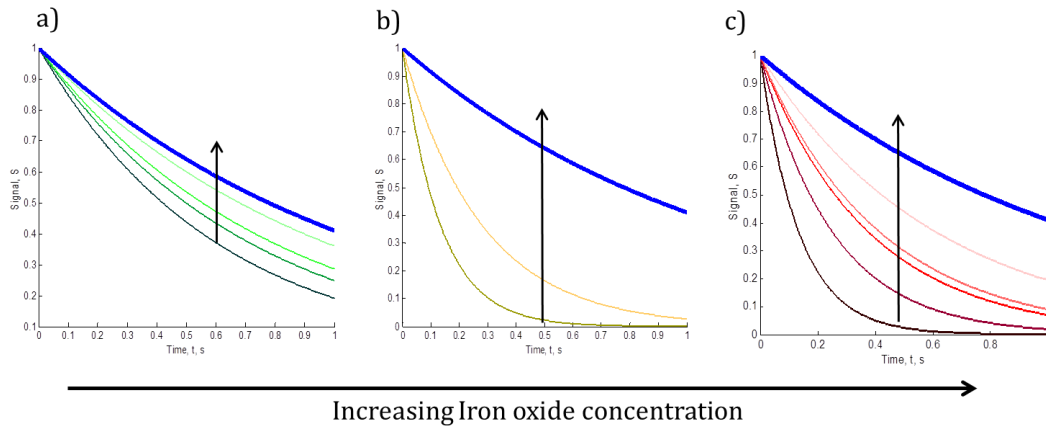


**Figure 9.6:** R2 relaxation rates of serially diluted PBD-PEO magneto-polymerosomes of increasing concentration a) 10 mg ml<sup>-1</sup> to b)/c) 60 mg ml<sup>-1</sup>. Arrows on the each graph indicates increasing dilution of each sample. Blue trace on each graph is a saline control.

The same effect was observed in measurement of  $R_2^*$  relaxation rates as a function of sample concentration. Again there was a general trend of increasing relaxation rate as a function of concentration, but without the same linearity due to the presence of a number of anomalies (Figure 9.7). It is believed that these anomalies are as a result of shimming from the glass vials used to house the sample, which can introduce inaccuracies.

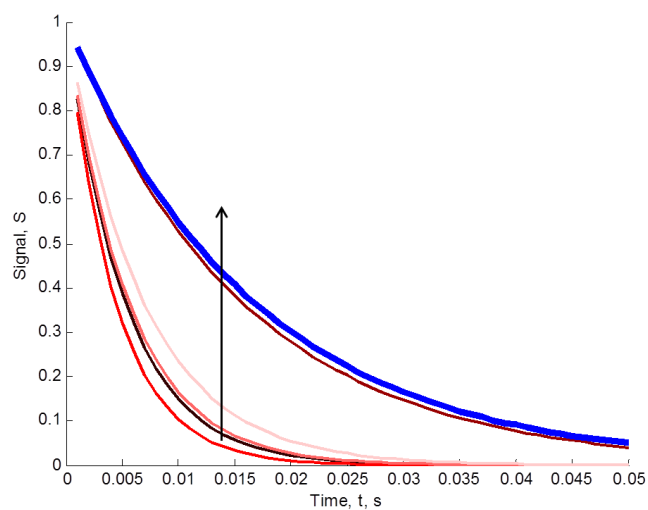


**Figure 9.7:**  $R_2^*$  relaxation rates of serially diluted PBD-PEO magneto-polymerosomes. Arrow indicates increasing dilution of the sample. Blue trace represents a saline control.

### 9.3.2 MAGNETO-VESICLE MRI MEASUREMENTS

Both DSPC magneto-vesicles synthesised by EHDA and electroporated PBD-PEO magneto-polymsomes were imaged in a saline phantom (control sample to reflect physiological conditions) to assess their contrast capabilities (Figure 9.8). Images taken at several echo times suggested that the DSPC samples were experiencing a degree of sedimentation, with contrast decreasing as the time increased. This trend shows higher concentrations at the bottom of the vial (probably due to sedimentation), with contrast being lost completely over time. Therefore, the measurements need to be repeated with more optimised sample preparation, such as suspension in more viscous solution to prevent sedimentation. The opposite was true in the case of PBD-PEO, in which there was a dramatic increase in the contrast of the image (when compared to the saline phantom) as the scan number and echo time increase (Figure 9.8).

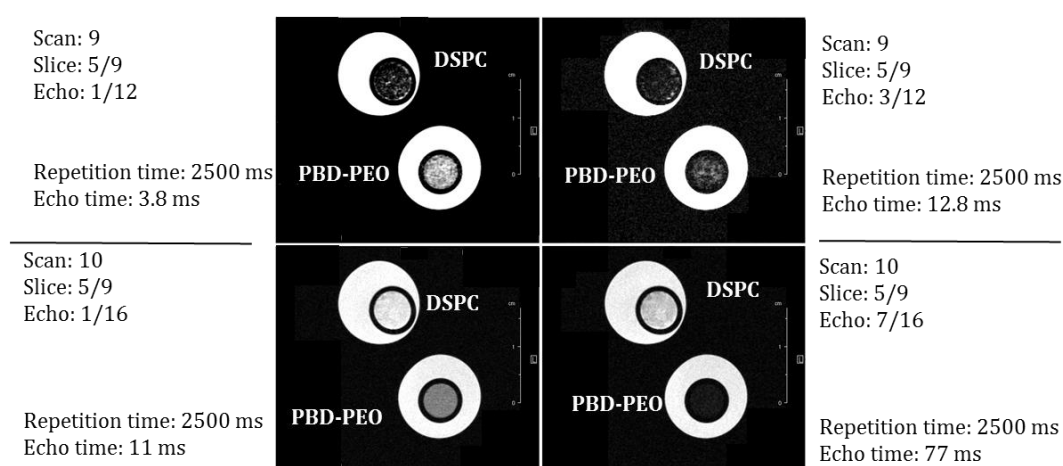


**Figure 9.8:** MRI contrast images of DSPC EHDA synthesised iron oxide liposomes (top) and PBD-PEO magneto-polymsomes (bottom), vesicle samples (inner circle), are sat in a saline phantom control sample (white circle), darker vesicle sample is equal to better contrast agent.

Therefore a more in-depth analysis of the MRI properties of the polymsome sample was performed (Figure 9.9). Relaxometry results (at 7 Tesla) for the  $R_2$  and  $R_2^*$  rates of the magneto-polymsome sample in PBS were  $22.7 \text{ s}^{-1}$  and  $148.8 \text{ s}^{-1}$  respectively (Figure 9.9). The  $R_2$  relaxivity was normalised for sample iron concentration (as measured by ICP-MS) was  $9.1 [\text{Fe mM}]^{-1} \text{ s}^{-1}$ .

Similarly,  $R_2^*$  data shows enhanced decay with the presence of MNPs, although it was not possible to extract a clear relationship between MNP concentration and decay due to the very rapid relaxation. It is clear from comparison to the saline relaxation rate (Figure 9.9), that the precipitation of small superparamagnetic particles within the magneto-polymersome membrane has positive effects on the contrast in MRI. Firstly, the  $2.5 \pm 0.5$  nm MNPs precipitated within the magneto-polymersome membrane have a much greater surface area than conventional MNPs used as MRI contrast agents (these are usually about 20 nm in diameter). Secondly, diffusion effects are often observed when measuring  $R_2$  decay data, if more diffusion occurs MNPs will come into closer contact with water, more often, which will affect the overall contrast agent ability of the vesicles.

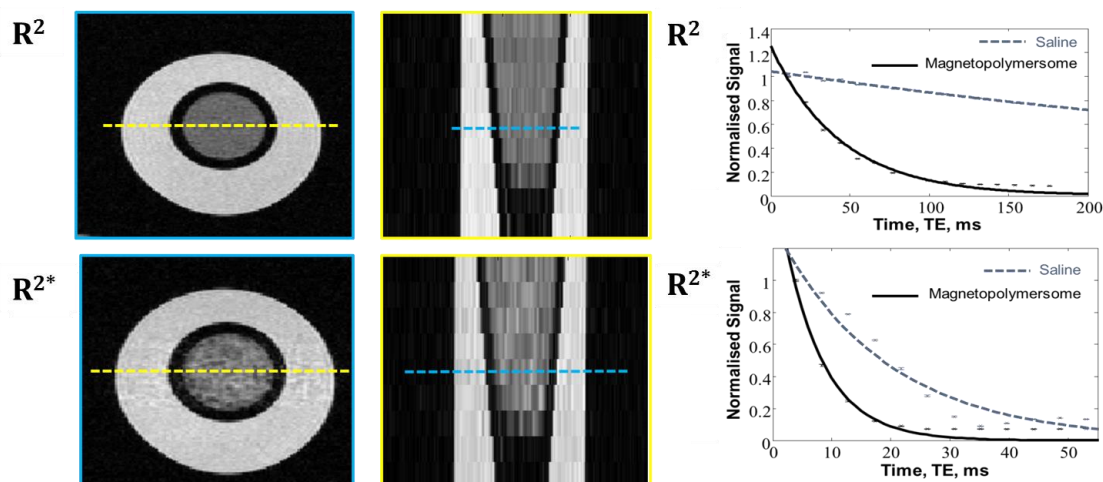


**Figure 9.9:** 7 T Magnetic resonance  $R_2$  relaxometry data (16 echoes, 9 slices, image shows the 5th slice) and 7 T Magnetic resonance  $R_2^*$  relaxometry data (12 echoes, 9 slices, image shows the 5th slice). Both  $R_2$  and  $R_2^*$  relaxometry rates show significant difference between saline (dashes) and electroporated PBD PEO magneto-polymersomes (solid).

This is particularly of note due to the position of MNPs within the membrane. MNPs are immobilised in close proximity to the permeable water molecules, essentially creating more random magnetisation dephasing interactions that cannot be refocused with conventional spin-echo (MR). This enhances the contrast to a higher degree than expected. Peters *et al*<sup>210</sup> measured the  $R_2^*$  relaxation rate of brain tissue to be  $30 \text{ s}^{-1}$ .

This is significantly different to the  $R_2^*$  relaxation rate measured for the magneto-polymerosomes ( $148.8 \text{ s}^{-1}$ ). This large difference suggests that, with optimisation, magneto-polymerosomes have potential as future *in vivo* biomedical MRI contrast agents. However, this requires further dose and toxicity related investigation, in particular with respect to measurements from an *in vivo* environment, such as within cultured tissues or a mouse model.

### 9.3.3 ALTERING THE IRON CONCENTRATION: EFFECTS IN MRI

Control tests (Figure 9.10) conducted on magneto-polymerosomes, unelectroporated polymerosomes and saline samples show a difference in  $R_2$  relaxometry upon addition of MNPs in the polymer membrane. Electroporated polymerosomes display a significantly faster decay than saline and unelectroporated controls. It is also evident that the rate of decay is dependent on magneto-polymerosome concentration, with the rate decreasing as the concentration of magnetopolymerosomes decreases (Figure 9.10). The decay of the control unelectroporated polymerosomes is comparable to that of the saline sample. This confirms that little or none of the contrast shown in figure 9.9 is the result of signal coming from the polymerosome membrane.  $R_2^*$  control data shows faster decay with the presence of magnetopolymerosome MNPs, although it was not possible to extract a clear relationship between magnetopolymerosome MNP concentration and decay. This is due to the decay being faster than the time window needed to collect sufficient data points to form a suitable exponential decay curve. Therefore, the control  $R_2^*$  can only offer us a qualitative comparison at this point.

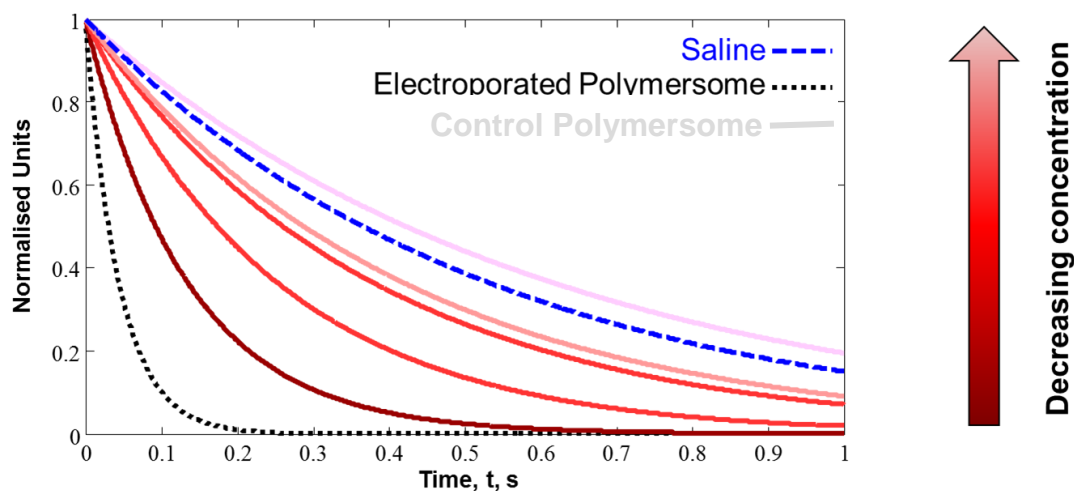


**Figure 9.10:**  $R_2$  relaxation rate of saline, control polymersomes (with no iron present) and electroporated magneto-polymersomes which were serially diluted. Starting iron concentration  $28 \text{ mg L}^{-1}$  (as measured by ICP-MS), each dilution was a 2 x dilution.

Precipitation of MNPs using electroporation has the potential to be tuned to give magneto-polymersomes with differing numbers and sizes of MNPs. This would be done by varying a number of parameters as shown in chapter 6. Figure 9.11 a) shows that, in general, relaxivity per mM Fe concentration increases as the applied voltage increases during electroporation. However, there seems to be two distinct mechanisms of electroporation, with lower and higher voltages displaying differing trends. At lower voltages, relaxivity per mM Fe concentration increases as a function of iron concentration in the vesicles, which was increased by applying an increasing voltage from 250 V to 750 V, yielding increased iron ion uptake (in ppm).

Similarly, an increase in relaxivity per mM Fe concentration as a function of measured iron content (ppm) in the vesicles is observed for the magneto-polymersomes electroporated at between 1500 and 2500 V. However, there is a crossover in behaviour when magneto-polymersomes are electroporated at 1000 V. At this point, the magneto-polymersomes contain smaller particles in increased numbers (as shown by grainsizing from TEM in figure 6.15) compared to polymersome electroporated at low voltage. This appears to be responsible for the increased relaxivity per mM Fe concentration. This suggests that increased contrast is achieved by increasing the MNP particle number rather than increased particle size within the magneto-polymersome membranes.

This supports the hypothesis discussed in section 9.3.2 that diffusion in and around the membrane plays a key role in the enhanced relaxation properties of the vesicle membrane, as more particles would result in increased diffusion effects.

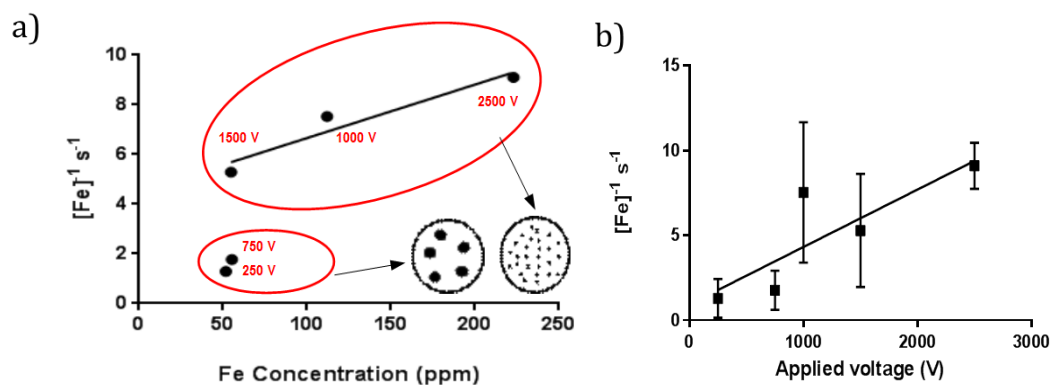


**Figure 9.11:** a) Average MNP particle size of MNPs in magneto-polymersomes that were electroperated at 200, 1000, and 2500 V. Red circles indicate high voltage and low voltage electroperation mechanisms the results of which are shown in the schematic associated to each mechanism (indicated by the arrows), as established in figure 6.15 b) Plot shows relaxation rate per mole of iron as a function of the voltage applied during electroperation.

This effect is also observed in figure 9.11 b), with increased  $R_2$  relaxivity per mM Fe concentration seen from 1.3  $[\text{Fe mM}]^{-1} \text{ s}^{-1}$  to 9.1  $[\text{Fe mM}]^{-1} \text{ s}^{-1}$ . This effect is not solely dependent on the iron concentration or the electroperation voltage applied during mineralisation, the size of the particles also has an effect. This is because, as water diffuses in and around the vesicle membrane, a greater number of protons will come into contact with MNPs. This contact increases if there are a larger number of smaller sized particles sat in the membrane as opposed to smaller numbers of large particles. This explains why the relaxivity per mM Fe concentration can vary significantly between samples with almost identical iron content.

## 9.4 DISCUSSION OF BIOMEDICAL APPLICATIONS OF MAGNETO-VESICLES

While the data presented in this chapter is far from conclusive, it is a good indicator of the future potential the magneto-vesicles (particularly the polymersomes) in biomedical theranostic applications. The proof-of-concept data presented shows promising magnetic hyperthermia heating ranging from a heat increase of between 1 and 6°C, depending on the sample analysed. ILP values varied greatly depending on the sample, measurement method and equipment used. This highlights the reproducibility issues that can occur with this new and experimental technique. Although it would be unwise to quote these values as accurate ILP values at this stage, it can be accepted that the magneto-vesicle samples have potential for development for use in magnetic hyperthermia.

It should be noted that the acquisition of these data can be improved, particularly with respect to optimising the type and position of the temperature probe. During calibration of the system, significant heating was observed from the thermocouple provided with the system. Data collection could be vastly improved with use of a fibre optic probe, which would avoid unwanted heating from the probe and improve the accuracy of obtaining a more realistic heat increase measurement. This is evident across the current literature in the field, with SAR and ILP values sometimes conflicting between measurements for similar samples.<sup>145</sup> With clinical trials beginning in humans, the call for standardisation of hyperthermia data acquisition is becoming evermore prominent. This should make published data values more comparable, and the ILP values presented in this chapter more meaningful to the field in the future.

MRI contrast properties of the magneto-vesicles were tested for DSPC and PBD-PEO. Although, in the case of the DSPC liposomes, they appear to show good contrast initially (figure 9.8 top row), there are obvious issues with the sample sedimenting as contrast is lost over time. Therefore, MRI contrast with DSPC magneto-liposomes requires optimisation of the sample preparation, as it is likely that re-suspension in more viscous (agar) solution will result in more reliable measurements.

This optimisation of the sample sedimentation will need to be characterised using a different technique (possibly fluorescence or DLS measurements) due to the expensive nature of MRI measurements.

The relaxation rates obtained for the electroporated PBD-PEO magneto-polymerosomes were extremely high, especially when the low concentration of iron oxide in the polymerosomes sample (1-1.4 %) is taken into account. The relaxation rate for the iron oxide was confirmed by comparison of the relaxation rate of the magneto-polymerosomes to the relaxation rate of unelectroporated polymerosomes. This was done to rule out the possibility that this effect was due to the polymer membrane or buffer alone. This relaxation rate also increases as a function of both polymerosome and iron concentration. It is believed that the relaxation rate can be altered by tuning of the electroporation parameters used to mineralise the magneto-polymerosomes. Initial data suggests that these two parameters are inherently linked, that as applied electroporation voltage increases, so does the MRI relaxation rate. However, there is a clear anomaly when the magneto-polymerosomes were electroporated at 1000 V, in which a change in the particle size and number are also observed within the magneto-polymerosomes. At this point, the MRI contrast increases, and these preliminary data suggests that this is due to the increase in particle size and number. It appears that even higher electroporation voltages (1500 V and 2500 V) yields a greater number of small MNPs, whereas lower voltages (250 V and 750 V) result in fewer particles which are bigger in size. Despite having equivalent iron oxide content, the MRI relaxivities are significantly different. This is essentially because, at the higher electroporation voltages, there are more particles for protons from water to come into contact with. Before this hypothesis can be proven and fully explained, so that magneto-polymerosomes can be exploited for biomedical applications, more needs to be understood regarding how electroporation controls the mechanism of mineralisation. This should yield a more consistent and reproducible response in MRI and magnetic hyperthermia response activity. Further work and optimisation of both sample preparation (with respect to electroporation) and data collection (particularly magnetic hyperthermia) is required before the biomedical potential of the magneto-vesicles can be realised, with *in vivo* tests of magneto-polymerosomes on the horizon.

# CHAPTER 10:

---

## FUTURE WORK AND CONCLUSIONS

## 10.1 CONCLUSIONS

This work overall has demonstrated that it is possible to design and create an artificial magnetosome. This has been done by the development of a vesicular nanoreactor for compartmentalisation of a magnetite precipitation reaction. These magneto-vesicles have then been tested to determine their magnetic and materials properties, using both classical characterisation techniques (e.g. SQUID and EDX) and testing for biomedically useful properties (MHT and MRI).

### 10.1.1 VESICLE OPTIMISATION FOR MINERALISATION

To develop magnetite mineralisation nanoreactors has required optimisation of both lipid and polymer vesicle properties. It has been determined that overall PBD-PEO and DPhPC, offered the best vesicle composition of appropriate size, permeability and stability. Although DSPC and PEG<sub>113</sub>-PHPMA<sub>400</sub> /PMPC<sub>28</sub>-PHPMA<sub>400</sub> were also largely successful, depending on the synthesis route and iron ion transport method employed. With each vesicle forming material, room temperature co-precipitation of magnetite using NaOH (10 mM), and iron chloride salts in the stoichiometric ratio for magnetite precipitation ( $\text{Fe}^{3+}$  2:1  $\text{Fe}^{2+}$ ) was carried out. Conditions were established that are the most appropriate for effective precipitation of electron dense, iron oxide material, using environmentally friendly conditions. Due to this benign mineralisation method, these magneto-vesicles are also likely to have relatively low toxicity, which bodes well for future use in biomedical application. Electroporation of the both lipid and polymer vesicle membranes was discovered to be the most effective method for iron oxide mineralisation of the vesicles across the board.

The use of electroporation allows for the remote triggering of MNP precipitation by application of an electric field. This is hugely advantageous, from a practical point of view, in that MNPs can be highly sensitive to oxidation which can incur long-term stability problems.

Electroporation at the point of use would deliver the freshest MNPs to ensure the timely delivery of high quality, stable MNPs for application, removing shelf-life issues. Additionally, remotely triggering polymersomes to form magneto-polymersomes *via* electroporation can present a host of opportunities in further applications. For example, in cases where a magnetic response would be valuable during application both *in vivo* and *in vitro*, such as in the case of iron sensing assays. Furthermore, the structure of the PBD-PEO and PMOXA-PDMA-PMOXA magneto-polymersomes, in which MNPs are localised to the membrane, leaves the vesicle core free for encapsulation of e.g. hydrophilic drugs. This shows their great potential as therapeutic agents, and opens up extensive engineering opportunities with respect to MNP /polymersome properties for various applications. This approach permits the creation of a simple biocompatible nanoreactor, activated by the application of an electric field for the engineering of precise magneto-polymersomes.

Attempts to spectroscopically quantify both iron ion transport and eventual iron oxide concentration were unsuccessful. Each assay developed was unable to quantify iron ion transport effectively once incorporated into the vesicles. For this reason, most samples were characterised only qualitatively (*via* TEM), with more in-depth analysis only able to be applied to samples that looked promising for future development. Successful development of a transport assay would allow quantitative analysis of all samples, and give a better picture of iron ion transport to inform further optimisation. This thesis presents the first cloning, expression and purification of MTB transporter MamMB and the use of MTB proteins and artificial MTB coiled coil proteins into synthetic vesicles. However, a similar problem was encountered with quantifying the incorporation of purified MTB proteins and biomimetic MTB protein. Again analysis was limited to qualitative characterisation *via* detection of the proteins using electrophoresis and observing morphological changes by TEM imaging. Although all of this points to successful incorporation, mutation of each of the proteins/scaffolds is required to allow for the detection and conclusively confirm their incorporation. Once this has been achieved it will be possible to further this work by determining their orientation and functionality.

A novel and high yield method of artificial magnetosome synthesis (i.e. a vesicle of appropriate size of which the core is entirely filled with a single magnetite crystal) has been developed. This was optimised using EHDA synthesised DSPC lipid vesicles, with electroporation used to induce mineralisation.

It was also discovered that particles could preferentially be formed in the core of the vesicle or within the membrane (leaving the core free for future drug encapsulation) depending on the material and electroporation voltage used. For example, it has been found that electroporation of EHDA synthesised DSPC lipid at 750 V yields a single particle in the core, whereas electroporating PBD-PEO polymer at 2500 V causes *in situ* precipitation of MNPs in the membrane. These data essentially demonstrate proof of concept data for the future development of a “toolbox” of MNP decorated vesicles, the design of which can be tailored to suit the application depending on the size and position of the particles required. This would require a large amount of further optimisation. However, this thesis has demonstrated that, by informed selection of materials and the tuning of applied electroporation voltage, it is possible to design control of the size and location of the nanoparticles mineralised.

However, as eluded to throughout this thesis, the benefits of this system are that it can be engineered to suit a desired application. Therefore, although not currently showing the type of coercivity usually observed in hard ferrimagnetic nanoparticles, incorporation of hardening elements such as cobalt is entirely feasible by adjustment of the electroporation solution composition. This will then harden the magnet by doping, thus giving the artificial magnetosomes increased coercivity. This should make it more difficult to switch the magnetisation by applying an alternating field and generate more heat for hyperthermia applications. A change of material, like in the case of DOPC, leads to bigger vesicles and hence bigger particles, which would be presumed to display more ferrimagnetic behaviour.<sup>211</sup>

The magneto-vesicles are designed to mimic the production of magnetosomes within MTB. This has a number of important advantages. Firstly, it provides a simplified abiotic model of the biomineralisation process, observed in MTB. This model system could be used to probe the biomineralisation process itself, by sequentially inserting biomineralisation proteins; as discussed throughout chapters 5 and 8, to better understand their function.

Secondly, and crucially, the system enables the development of a commercially viable route of creating monodispersed populations of lipid encapsulated, precise single-domain MNPs. These artificial magnetosomes offer enormous potential for modification that is simply not possible for natural magnetosomes, facilitating the high-yield production of a wealth of new nanomaterials for biomedical and nanotechnological applications.

This has been a broad, multi-disciplinary project, which has involved high-throughput trialling of a wide range of materials and synthesis routes for the creation of a synthetic magnetosome. Three modes of transmembrane transport have been explored starting entirely biological, then exploring biomimetic and bioinspired transmembrane transport, before finally entirely synthetic transport modes. An artificial magnetosome has been designed and developed, which shows potential for biomedical application. Further to this unexpected results with regards to the electroporation of polymersomes. These have yielded a versatility which wasn't expected, and has revealed potential for a highly adaptable nanoreactor system in which the particles can be preferentially precipitated in the membrane or vesicle core, of a material to suit a specific application. These results are summarised in table 10.1:

	<b>Synthetic</b>	<b>Biomimetic</b>	<b>Biological</b>
<b>Vesicle</b>	Polymers	N/A	Phospholipids
<b>Transport Method</b>	Electroporation	Ionophore (A23187)	Transporter proteins (MamMB)
<b>Morphological control</b>	Vesicle Core	COOH Terminated Polymers/ Coiled coils	MTB Proteins (MmsF, Mms6)

**Table 10.1:** Summary of various methods used throughout the project

With future applications of this “toolbox” (various material and transport method combinations to yield specific results) in mind it has also been shown that the bioinspired synthesis routes presented have huge potential for use as MRI contrast agents and therapeutic nanocarriers for use in magnetic hyperthermia treatment.

### **10.1.2 CHARACTERISATION OF MAGNETO-VESICLES FOR USE IN BIOMEDICAL APPLICATIONS**

Despite further optimisation being required, the initial studies presented in chapter 9 demonstrate the extremely fast relaxation rates and exceptional heating ability of magneto-polymerosomes. This is despite the relatively small concentrations of iron oxide present when compared to unsupported MNPs currently used for such applications. However, this does need further work and optimisation with respect to better quantification of both iron oxide content and sample concentrations. This is difficult at this stage due to the nature of the small sample size at these initial stages before scale up. For example, traditional characterisation methods are currently impractical, as techniques like X-ray powder diffraction or SQUID require too large a quantity for reliable, accurate analysis, access to single area electron diffraction would also help to confirm mineral composition. The small sample size may also contribute to some of the reproducibility issues, as was demonstrated by variability in measurements e.g. using DLS and gas chromatography.

## **10.2 FUTURE WORK**

There are a number of other potential routes to magneto-vesicle synthesis which could be explored to improve upon the work presented here. Co-functionalising them with fluorophores (e.g. on the lipids or polymers used to construct the magneto-vesicles) would allow easy tracking for both *in vitro* and *in vivo* applications. It would also be prudent to examine whether magneto-vesicles can be selectively functionalised on both the internal and external surfaces.

Controlled external functionalisation of the magneto-vesicles would allow the demonstration of the potential targeting capabilities of these assemblies. The external decoration of magneto-vesicles with targeting moieties may allow them to localise at a designed target (e.g. a cell line displaying a particular cancer marker).

This may also encourage differential uptake of magneto-vesicles at the target site, selectively concentrating them, and thus their cargo, within the diseased tissues. Internal functionalisation of magneto-vesicles could be used to add drugs or other desired molecules to their lumen in a controllable manner.

It would also be of interest to explore whether the magneto-polymerosomes presented in chapter 9 are magneto-responsive, i.e. can be ruptured and release cargo by continued application of an alternating magnetic field. A previous study in the literature have shown that vesicle decorated with MNPs can be engineered to be magneto-responsive in an alternating magnetic field, thus releasing a fluorescent cargo upon irradiation by the field.<sup>212</sup> If this possible with the magneto-polymerosomes, which appear to be responsive in the alternating magnetic field applied in chapter 9, then encapsulation of both hydrophilic and/or hydrophobic drugs (perhaps simultaneously) could be explored without further vesicle functionalisation. This would involve further tests to determine if a) magneto-vesicles can incorporate drugs and/or drug proxies, and b) magneto-vesicles can be triggered to rupture/leak upon the application of an alternating field.

For example, the Kros lab makes use of coiled-coil proteins to induce membrane fusion of two separate vesicles, with the aim of fusing vesicle carriers to cells. This is done by incorporation of complementary heterodimer coiled-coil peptides in to two separate liposomes.<sup>213</sup> Assembly of these two complementary halves of the heterodimer forces fusion of the two liposomes, and more importantly, mixing of the two encapsulates.<sup>213</sup> It would be interesting to investigate whether such coiled-coil heterodimers could be used in this manner for our own system. Not only would this ensure the vesicular integration of the scaffold, but also precipitation of magnetite upon membrane fusion if vesicles were designed so as to encapsulate NaOH and iron chloride solutions in separate vesicles. It could also be possible to design hetero-trimer systems that are able to assemble vesicles incorporating three different components in a controlled manner. This could include a co-precipitation system ( $\text{Fe}^{2+}$ ,  $\text{Fe}^{3+}$  and base) or a partial oxidation ( $\text{Fe}^{2+}$ , oxidiser and base) or reduction reactions ( $\text{Fe}^{3+}$ , reducing agent and base) for the production of magnetite within vesicles.

It would be interesting to see if the nanoreactor system developed in this project can be applied to the biomineralisation of other materials such as calcite, hydroxyapatite, silica to form similar capsules for drug delivery, or mineralisation of titania for use in photovoltaics<sup>214</sup> or quantum dot for fluorescence functionality<sup>215</sup> and gold nanoparticle for surface plasmon imaging.<sup>127a, 127b, 216</sup> The next natural step would be to combine these functionalities in to a single carrier vesicle, (e.g. magnets and quantum dots) together in one to create e.g. magneto-optical vesicles.<sup>94b, 128, 132a</sup>

There is still a large amount of work to be done before a fully functional artificial magnetosome and its application in biomedicine is realised. This work shows that it is not only possible, but also has the potential to be fully tuneable with respect to the properties of the final product. This would allow for fully tuneable electroporation and biological transport, yielding a functional biomimetic magnetosome, and the “toolbox” of properties required for successful and efficient biomedical application.

# BIBLIOGRAPHY

1. (a) Amemiya, Y.; Arakaki, A.; Staniland, S. S.; Tanaka, T.; Matsunaga, T., Controlled formation of magnetite crystal by partial oxidation of ferrous hydroxide in the presence of recombinant magnetotactic bacterial protein Mms6. *Biomaterials* **2007**, *28* (35), 5381-5389; (b) Kirschvink, J. L.; Hagadorn, J. W., 10 A grand unified theory of biomineralization. *The Biomineralisation of Nano-and Micro-Structures*. Wiley-VCH Verlag GmbH, Weinheim, Germany **2000**, 139-150; (c) Staniland, S. S.; Bain, J., Bioinspired nanoreactors for the biomineralisation of metallic-based nanoparticles for nanomedicine. *Physical Chemistry Chemical Physics* **2015**.
2. (a) Warren, N. J.; Mykhaylyk, O. O.; Ryan, A. J.; Williams, M.; Doussineau, T.; Dugourd, P.; Antoine, R.; Portale, G.; Armes, S. P., Testing the Vesicular Morphology to Destruction: Birth and Death of Diblock Copolymer Vesicles Prepared via Polymerization-Induced Self-Assembly. *Journal of the American Chemical Society* **2015**, *137* (5), 1929-1937; (b) LoPresti, C.; Massignani, M.; Fernyhough, C.; Blanz, A.; Ryan, A. J.; Madsen, J.; Warren, N. J.; Armes, S. P.; Lewis, A. L.; Chirasatitsin, S.; Engler, A. J.; Battaglia, G., Controlling Polymersome Surface Topology at the Nanoscale by Membrane Confined Polymer/Polymer Phase Separation. *Acs Nano* **2011**, *5* (3), 1775-1784.
3. Cornell, R. M.; Schwertmann, U., *The iron oxides: structure, properties, reactions, occurrences, and uses*. Vch Verlagsgesellschaft Mbh: 2003.
4. Mann, S.; Hannington, J. P.; Williams, R. J. P., PHOSPHOLIPID-VESICLES AS A MODEL SYSTEM FOR BIOMINERALIZATION. *Nature* **1986**, *324* (6097), 565-567.
5. Rawlings, A. E.; Bramble, J. P.; Walker, R.; Bain, J.; Galloway, J. M.; Staniland, S. S., Self-assembled MmsF proteinosomes control magnetite nanoparticle formation in vitro. *Proceedings of the National Academy of Sciences* **2014**, *111* (45), 16094-16099.
6. Young, J. R.; Davis, S. A.; Bown, P. R.; Mann, S., Coccolith Ultrastructure and Biomineralisation. *Journal of Structural Biology* **1999**, *126* (3), 195-215.
7. Bain, J.; Ruiz-Pérez, L.; Kennerley, A. J.; Muench, S. P.; Thompson, R.; Battaglia, G.; Staniland, S. S., In situ formation of magnetopolymersomes via electroporation for MRI. *Scientific Reports* **2015**, *5*, 14311.
8. Takeno, N., Atlas of Eh-pH diagrams. *Geological Survey of Japan Open File Report* **2005**, (419).
9. (a) Nardin, C.; Thoeni, S.; Widmer, J.; Winterhalter, M.; Meier, W., Nanoreactors based on (polymerized) ABA-triblock copolymer vesicles. *Chemical Communications* **2000**, (15), 1433-1434; (b) Nardin, C.; Hirt, T.; Leukel, J.; Meier, W., Polymerized ABA triblock copolymer vesicles. *Langmuir* **2000**, *16* (3), 1035-1041.
10. (a) Ruby, C.; Aïssa, R.; Géhin, A.; Cortot, J.; Abdelmoula, M.; Génin, J.-M., Green rusts synthesis by coprecipitation of Fe II-Fe III ions and mass-balance diagram. *Comptes Rendus Geoscience* **2006**, *338* (6), 420-432; (b) Ruby, C.; Géhin, A.; Abdelmoula, M.; Génin, J.-M. R.; Jolivet, J.-P., Coprecipitation of Fe (II) and Fe (III) cations in sulphated aqueous medium and formation of hydroxysulphate green rust. *Solid state sciences* **2003**, *5* (7), 1055-1062.
11. Blundell, S., *Magnetism in condensed matter*. Oxford University Press: 2001; Vol. 54.
12. Newey, C.; Weaver, G., *Materials Principles and Practice*. Butterworth Heinemann Oxford, 1990.
13. Pankhurst, Q. A.; Connolly, J.; Jones, S. K.; Dobson, J., Applications of magnetic nanoparticles in biomedicine. *Journal of Physics D-Applied Physics* **2003**, *36* (13), R167-R181.

14. Chang, L.; Rainford, B. D.; Stewart, J. R.; Ritter, C.; Roberts, A. P.; Tang, Y.; Chen, Q., Magnetic structure of greigite (Fe<sub>3</sub>S<sub>4</sub>) probed by neutron powder diffraction and polarized neutron diffraction. *Journal of Geophysical Research: Solid Earth (1978–2012)* **2009**, *114* (B7).
15. Sorescu, M., Phase transformations induced in magnetite by high energy ball milling. *Journal of materials science letters* **1998**, *17* (13), 1059-1061.
16. (a) Özdemir, Ö.; Dunlop, D. J.; Moskowitz, B. M., The effect of oxidation on the Verwey transition in magnetite. *Geophysical Research Letters* **1993**, *20* (16), 1671-1674; (b) Verwey, E., Electronic conduction of magnetite (Fe<sub>3</sub>O<sub>4</sub>) and its transition point at low temperatures. *Nature* **1939**, *144* (3642), 327-328; (c) Verwey, E.; Heilmann, E., Physical properties and cation arrangement of oxides with spinel structures I. Cation arrangement in spinels. *The Journal of Chemical Physics* **1947**, *15* (4), 174-180.
17. Samiullah, M., Verwey transition in magnetite: Finite-temperature mean-field solution of the Cullen-Callen model. *Physical Review B* **1995**, *51* (16), 10352.
18. Laurent, S.; Forge, D.; Port, M.; Roch, A.; Robic, C.; Vander Elst, L.; Muller, R. N., Magnetic Iron Oxide Nanoparticles: Synthesis, Stabilization, Vectorization, Physicochemical Characterizations, and Biological Applications. *Chemical Reviews* **2008**, *108* (6), 2064-2110.
19. Rahman, M. M.; Khan, S. B.; Aslam Jamal, M. F.; Aisiri, A. M., Iron Oxide Nanoparticles. *Nanomaterials, Edited by Rahman M* **2011**, 43-66.
20. (a) Lenders, J. J.; Altan, C. L.; Bomans, P. H.; Arakaki, A.; Bucak, S.; de With, G.; Sommerdijk, N. A., A Bioinspired Coprecipitation Method for the Controlled Synthesis of Magnetite Nanoparticles. *Crystal Growth & Design* **2014**, *14* (11), 5561-5568; (b) Asuha, S.; Suyala, B.; Siqintana, X.; Zhao, S., Direct synthesis of Fe<sub>3</sub>O<sub>4</sub> nanopowder by thermal decomposition of Fe-urea complex and its properties. *Journal of Alloys and Compounds* **2011**, *509* (6), 2870-2873; (c) Ahn, T.; Kim, J. H.; Yang, H.-M.; Lee, J. W.; Kim, J.-D., Formation Pathways of Magnetite Nanoparticles by Coprecipitation Method. *The Journal of Physical Chemistry C* **2012**, *116* (10), 6069-6076; (d) Zhu, L. P.; Xiao, H. M.; Zhang, W. D.; Yang, G.; Fu, S. Y., One-pot template-free synthesis of monodisperse and single-crystal magnetite hollow spheres by a simple solvothermal route. *Crystal Growth and Design* **2008**, *8* (3), 957-963; (e) Jeong, Y. K.; Shin, D. K.; Lee, H. J.; Oh, K. S.; Lee, J. H.; Riu, D. H., Nano magnetite particles prepared under the combined addition of urea and ammonia. In *Science of Engineering Ceramics Iii*, Ohji, T.; Sekino, T.; Niihara, K., Eds. 2006; Vol. 317-318, pp 203-206; (f) Regazzoni, A. E.; Urrutia, G. A.; Blesa, M. A.; Maroto, A. J. G., Some observations on the composition and morphology of synthetic magnetites obtained by different routes. *Journal of Inorganic & Nuclear Chemistry* **1981**, *43* (7), 1489-1493; (g) Kim, D.; Lee, N.; Park, M.; Kim, B. H.; An, K.; Hyeon, T., Synthesis of Uniform Ferrimagnetic Magnetite Nanocubes. *Journal of the American Chemical Society* **2009**, *131* (2), 454-455.
21. (a) Ho, C.-H.; Tsai, C.-P.; Chung, C.-C.; Tsai, C.-Y.; Chen, F.-R.; Lin, H.-J.; Lai, C.-H., Shape-Controlled Growth and Shape-Dependent Cation Site Occupancy of Monodisperse Fe<sub>3</sub>O<sub>4</sub> Nanoparticles. *Chemistry of Materials* **2011**, *23* (7), 1753-1760; (b) Asuha, S.; Suyala, B.; Siqintana, X.; Zhao, S., Direct synthesis of Fe<sub>3</sub>O<sub>4</sub> nanopowder by thermal decomposition of Fe-urea complex and its properties. *Journal of Alloys and Compounds* **2011**, *509* (6), 2870-2873.
22. Sugimoto, T.; Matijevic, E., Formation of uniform spherical magnetite particles by crystallization from ferrous hydroxide gels. *Journal of Colloid and Interface Science* **1980**, *74* (1), 227-243.
23. Matijević, E., Preparation and characterization of monodispersed metal hydrous oxide sols. In *Colloids and Surfaces*, Springer: 1976; pp 24-35.
24. Lang, C.; Schüler, D.; Faivre, D., Synthesis of Magnetite Nanoparticles for Bio- and Nanotechnology: Genetic Engineering and Biomimetics of Bacterial Magnetosomes. *Macromolecular Bioscience* **2007**, *7* (2), 144-151.

25. Asuha, S.; Zhao, S.; Wu, H. Y.; Song, L.; Tegus, O., One step synthesis of maghemite nanoparticles by direct thermal decomposition of Fe-urea complex and their properties. *Journal of Alloys and Compounds* **2009**, *472* (1–2), L23-L25.
26. Baumgartner, J.; Bertinetti, L.; Widdrat, M.; Hirt, A. M.; Faivre, D., Formation of magnetite nanoparticles at low temperature: from superparamagnetic to stable single domain particles. **2013**.
27. Skinner, H.; Jahren, A., Biomineralization. *Treatise on geochemistry* **2003**, *8*, 117-184.
28. Mann, S., *Biomineralization: principles and concepts in bioinorganic materials chemistry*. Oxford University Press, USA: 2001; Vol. 5.
29. (a) Tanaka, M.; Mazuyama, E.; Arakaki, A.; Matsunaga, T., Mms6 protein regulates crystal morphology during nano-sized magnetite biomineralization in vivo. *Journal of Biological Chemistry* **2011**, *286* (8), 6386-6392; (b) Murat, D.; Falahati, V.; Bertinetti, L.; Csencsits, R.; Körnig, A.; Downing, K.; Faivre, D.; Komeili, A., The magnetosome membrane protein, MmsF, is a major regulator of magnetite biomineralization in *Magnetospirillum magneticum* AMB-1. *Molecular Microbiology* **2012**, *85* (4), 684-699.
30. Westbroek, P.; Young, J.; Linschooten, K., Coccolith production (biomineralization) in the marine alga *Emiliania huxleyi*. *The Journal of protozoology* **1989**, *36* (4), 368-373.
31. Kröger, N.; Deutzmann, R.; Sumper, M., Polycationic peptides from diatom biosilica that direct silica nanosphere formation. *Science* **1999**, *286* (5442), 1129-1132.
32. Belcher, A. M.; Wu, X.; Christensen, R.; Hansma, P.; Stucky, G.; Morse, D., Control of crystal phase switching and orientation by soluble mollusc-shell proteins. **1996**.
33. (a) Niemeyer, C. M.; Mirkin, C. A., *Nanobiotechnology: concepts, applications and perspectives*. John Wiley & Sons: 2006; (b) Abe, S.; Niemeyer, J.; Abe, M.; Takezawa, Y.; Ueno, T.; Hikage, T.; Erker, G.; Watanabe, Y., Control of the Coordination Structure of Organometallic Palladium Complexes in an apo-Ferritin Cage. *Journal of the American Chemical Society* **2008**, *130* (32), 10512-10514; (c) Ueno, T.; Suzuki, M.; Goto, T.; Matsumoto, T.; Nagayama, K.; Watanabe, Y., Size-Selective Olefin Hydrogenation by a Pd Nanocluster Provided in an Apo-Ferritin Cage. *Angewandte Chemie* **2004**, *116* (19), 2581-2584.
34. Kirschvink, J. L.; Kobayashi-Kirschvink, A.; Woodford, B. J., Magnetite biomineralization in the human brain. *Proceedings of the National Academy of Sciences* **1992**, *89* (16), 7683-7687.
35. Blakemore, R., Magnetotactic bacteria. *Science* **1975**, *190* (4212), 377.
36. Morillo, V.; Abreu, F.; Araujo, A. C.; de Almeida, L. G.; Enrich-Prast, A.; Farina, M.; de Vasconcelos, A. T.; Bazylinski, D. A.; Lins, U., Isolation, cultivation and genomic analysis of magnetosome biomineralization genes of a new genus of South-seeking magnetotactic cocci within the Alphaproteobacteria. *Frontiers in microbiology* **2014**, *5*.
37. Blakemore, R. P., Magnetotactic bacteria. *Annual Reviews in Microbiology* **1982**, *36* (1), 217-238.
38. Frankel, R., The discovery of magnetotactic/magnetosensitive bacteria. *Chin. J. Ocean. Limnol.* **2009**, *27* (1), 1-2.
39. (a) Faivre, D.; Schüler, D., Magnetotactic bacteria and magnetosomes. *Chemical Reviews* **2008**, *108* (11), 4875-4898; (b) Gorby, Y. A.; Beveridge, T. J.; Blakemore, R. P., Characterization of the bacterial magnetosome membrane. *Journal of Bacteriology* **1988**, *170* (2), 834; (c) Jogler, C.; Schüler, D., Genomics, genetics, and cell biology of magnetosome formation. *Annual Review of Microbiology* **2009**, *63*, 501-521; (d) Nies, D. H., How iron is transported into magnetosomes. *Molecular Microbiology* **2011**, *82* (4), 792-796; (e) Arakaki, A.; Nakazawa, H.; Nemoto, M.; Mori, T.; Matsunaga, T., Formation of magnetite by bacteria and its application. *Journal of the Royal Society*

- Interface* **2008**, 5 (26), 977-999; (f) Frankel, R. B.; Blakemore, R. P.; Wolfe, R. S., Magnetite in freshwater magnetotactic bacteria. *Science* **1979**, 203 (4387), 1355.
40. Frankel, R. B.; Blakemore, R. P., Magnetite and magnetotaxis in microorganisms. *Bioelectromagnetics* **1989**, 10 (3), 223-237.
  41. Frankel, R. B.; Bazylinski, D. A., How magnetotactic bacteria make magnetosomes queue up. *Trends in Microbiology* **2006**, 14 (8), 329-331.
  42. Bazylinski, D. A.; Frankel, R. B., Magnetosome formation in prokaryotes. *Nature Reviews Microbiology* **2004**, 2 (3), 217-230.
  43. Smith, M.; Sheehan, P.; Perry, L.; O'Connor, K.; Csonka, L.; Applegate, B.; Whitman, L., Quantifying the magnetic advantage in magnetotaxis. *Biophysical Journal* **2006**, 91 (3), 1098-1107.
  44. Guerin, W. F.; Blakemore, R. P., Redox cycling of iron supports growth and magnetite synthesis by *Aquaspirillum magnetotacticum*. *Applied and environmental microbiology* **1992**, 58 (4), 1102-1109.
  45. Blakemore, R. P., Magnetotactic Bacteria. *Annual Review of Microbiology* **1982**, 36 (1), 217-238.
  46. Stephens, C., Bacterial cell biology: Managing magnetosomes. *Current Biology* **2006**, 16 (10), R363-R365.
  47. Nudelman, H.; Zarivach, R., Structure prediction of magnetosome-associated proteins. *Frontiers in microbiology* **2014**, 5.
  48. Tanaka, M.; Arakaki, A.; Matsunaga, T., Identification and functional characterization of liposome tubulation protein from magnetotactic bacteria. *Molecular microbiology* **2010**, 76 (2), 480-488.
  49. Komeili, A.; Li, Z.; Newman, D. K.; Jensen, G. J., Magnetosomes are cell membrane invaginations organized by the actin-like protein MamK. *Science* **2006**, 311 (5758), 242-245.
  50. Komeili, A.; Vali, H.; Beveridge, T. J.; Newman, D. K., Magnetosome vesicles are present before magnetite formation, and MamA is required for their activation. *Proceedings of the National Academy of Sciences of the United States of America* **2004**, 101 (11), 3839.
  51. Schüler, D.; Frankel, R. B., Bacterial magnetosomes: microbiology, biomineralization and biotechnological applications. *Applied Microbiology and Biotechnology* **1999**, 52 (4), 464-473.
  52. Uebe, R.; Junge, K.; Henn, V.; Poxleitner, G.; Katzmann, E.; Plitzko, J. M.; Zarivach, R.; Kasama, T.; Wanner, G.; Pósfai, M., The cation diffusion facilitator proteins MamB and MamM of *Magnetospirillum gryphiswaldense* have distinct and complex functions, and are involved in magnetite biomineralization and magnetosome membrane assembly. *Molecular Microbiology* **2011**.
  53. (a) Nakamura, C.; Kikuchi, T.; Burgess, J. G.; Matsunaga, T., Iron-Regulated Expression and Membrane Localization of the MagA Protein in *Magnetospirillum* sp. Strain AMB-1. *Journal of Biochemistry* **1995**, 118 (1), 23-27; (b) Nakamura, C.; Burgess, J. G.; Sode, K.; Matsunaga, T., An iron-regulated gene, magA, encoding an iron transport protein of *Magnetospirillum* sp. strain AMB-1. *Journal of Biological Chemistry* **1995**, 270 (47), 28392-28396.
  54. Matsunaga, T.; Nemoto, M.; Arakaki, A.; Tanaka, M., Proteomic analysis of irregular, bullet-shaped magnetosomes in the sulphate-reducing magnetotactic bacterium *Desulfovibrio magneticus* RS-1. *Proteomics* **2009**, 9 (12), 3341-3352.
  55. Stolz, J. F.; Chang, S.-B. R.; Kirschvink, J. L., Magnetotactic bacteria and single-domain magnetite in hemipelagic sediments. **1986**.
  56. Siponen, M. I.; Legrand, P.; Widdrat, M.; Jones, S. R.; Zhang, W.-J.; Chang, M. C.; Faivre, D.; Arnoux, P.; Pignol, D., Structural insight into magnetochrome-mediated magnetite biomineralization. *Nature* **2013**, 502 (7473), 681-684.
  57. Murat, D.; Falahati, V.; Bertinetti, L.; Csencsits, R.; Körnig, A.; Downing, K.; Faivre, D.; Komeili, A., The magnetosome membrane protein, MmsF, is a major

- regulator of magnetite biomineralization in *Magnetospirillum magneticum* AMB-1. *Molecular Microbiology* **2012**.
58. (a) Grünberg, K.; Müller, E.-C.; Otto, A.; Reszka, R.; Linder, D.; Kube, M.; Reinhardt, R.; Schüler, D., Biochemical and proteomic analysis of the magnetosome membrane in *Magnetospirillum gryphiswaldense*. *Applied and environmental microbiology* **2004**, *70* (2), 1040-1050; (b) Tanaka, M.; Okamura, Y.; Arakaki, A.; Tanaka, T.; Takeyama, H.; Matsunaga, T., Origin of magnetosome membrane: proteomic analysis of magnetosome membrane and comparison with cytoplasmic membrane. *Proteomics* **2006**, *6* (19), 5234-5247.
59. (a) Greene, S. E.; Komeili, A., Biogenesis and subcellular organization of the magnetosome organelles of magnetotactic bacteria. *Current opinion in cell biology* **2012**, *24* (4), 490-495; (b) Prozorov, T.; Bazylinski, D. A.; Mallapragada, S. K.; Prozorov, R., Novel magnetic nanomaterials inspired by magnetotactic bacteria: topical review. *Materials Science and Engineering: R: Reports* **2013**, *74* (5), 133-172.
60. Mann, S.; Sparks, N.; Blakemore, R., Structure, morphology and crystal growth of anisotropic magnetite crystals in magnetotactic bacteria. *Proceedings of the Royal Society of London B: Biological Sciences* **1987**, *231* (1265), 477-487.
61. Arakaki, A.; Webb, J.; Matsunaga, T., A novel protein tightly bound to bacterial magnetic particles in *Magnetospirillum magneticum* strain AMB-1. *Journal of Biological Chemistry* **2003**, *278* (10), 8745-8750.
62. Galloway, J. M.; Arakaki, A.; Masuda, F.; Tanaka, T.; Matsunaga, T.; Staniland, S. S., Magnetic bacterial protein Mms6 controls morphology, crystallinity and magnetism of cobalt-doped magnetite nanoparticles in vitro. *Journal of Materials Chemistry* **2011**, *21* (39), 15244-15254.
63. Cullis, P. R.; Bally, M. B.; Madden, T. D.; Mayer, L. D.; Hope, M. J., PH GRADIENTS AND MEMBRANE-TRANSPORT IN LIPOSOMAL SYSTEMS. *Trends in Biotechnology* **1991**, *9* (8), 268-272.
64. Andersson, M.; Jackman, J.; Wilson, D.; Jarvoll, P.; Alfredsson, V.; Okeyo, G.; Duran, R., Vesicle and bilayer formation of diphytanoylphosphatidylcholine (DPhPC) and diphytanoylphosphatidylethanolamine (DPhPE) mixtures and their bilayers' electrical stability. *Colloids and Surfaces B: Biointerfaces* **2011**, *82* (2), 550-561.
65. Vriezema, D. M.; Comellas Aragonès, M.; Elemans, J. A.; Cornelissen, J. J.; Rowan, A. E.; Nolte, R. J., Self-assembled nanoreactors. *Chemical reviews* **2005**, *105* (4), 1445-1490.
66. (a) Israelachvili, J. N., *Intermolecular and surface forces: revised third edition*. Academic press: 2011; (b) Israelachvili, J. N.; Mitchell, D. J.; Ninham, B. W., Theory of self-assembly of lipid bilayers and vesicles. *Biochimica et Biophysica Acta (BBA)-Biomembranes* **1977**, *470* (2), 185-201.
67. Hummer, G.; Garde, S.; Garcia, A.; Pratt, L., New perspectives on hydrophobic effects. *Chemical Physics* **2000**, *258* (2), 349-370.
68. Clarke, S., The hydrophobic effect: Formation of micelles and biological membranes, 2nd edition (Tanford, Charles). *Journal of Chemical Education* **1981**, *58* (8), A246.
69. Zhang, S. G., Fabrication of novel biomaterials through molecular self-assembly. *Nature Biotechnology* **2003**, *21* (10), 1171-1178.
70. Israelachvili, J. N., *Intermolecular and surface forces*. Academic press: 2011.
71. (a) Maherani, B.; Arab-Tehrany, E.; Mozafari, M. R.; Gaiani, C.; Linder, M., Liposomes: A Review of Manufacturing Techniques and Targeting Strategies. *Current Nanoscience* **2011**, *7* (3), 436-452; (b) Al-Jamal, W. T.; Kostarelos, K., Liposomes: From a Clinically Established Drug Delivery System to a Nanoparticle Platform for Theranostic Nanomedicine. *Accounts of Chemical Research* **2011**, *44* (10), 1094-1104; (c) Immordino, M. L.; Dosio, F.; Cattel, L., Stealth liposomes: review of the basic science, rationale, and clinical applications, existing and potential. *International journal of nanomedicine* **2006**, *1* (3), 297-315; (d) Jesorka, A.; Orwar, O., Liposomes: Technologies

- and Analytical Applications. In *Annual Review of Analytical Chemistry*, 2008; Vol. 1, pp 801-832.
72. Tan, Y.-C.; Hettiarachchi, K.; Siu, M.; Pan, Y.-R.; Lee, A. P., Controlled microfluidic encapsulation of cells, proteins, and microbeads in lipid vesicles. *Journal of the American Chemical Society* **2006**, *128* (17), 5656-5658.
73. Monnard, P. A., Liposome-entrapped Polymerases as Models for Microscale/Nanoscale Bioreactors. *J. Membrane Biol.* **2003**, *191* (2), 87-97.
74. Tester, C. C.; Wu, C.-H.; Weigand, S.; Joester, D., Precipitation of ACC in liposomes—a model for biomineralization in confined volumes. *Faraday Discussions* **2012**, *159*, 345-356.
75. Walde, P.; Namani, T.; Morigaki, K.; Hauser, H., Formation and properties of fatty acid vesicles (liposomes). *Liposome technology. 3rd ed. New York: Informa Healthcare* **2007**, 1-20.
76. Shebanova, O. N.; Lazor, P., Raman spectroscopic study of magnetite (FeFe<sub>2</sub>O<sub>4</sub>): a new assignment for the vibrational spectrum. *Journal of Solid State Chemistry* **2003**, *174* (2), 424-430.
77. Santhosh, P. B.; Kiryakova, S. I.; Genova, J. L.; Ulrih, N. P., Influence of iron oxide nanoparticles on bending elasticity and bilayer fluidity of phosphatidylcholine liposomal membranes. *Colloids and Surfaces A: Physicochemical and Engineering Aspects* **2014**, *460*, 248-253.
78. Walde, P.; Cosentino, K.; Engel, H.; Stano, P., Giant vesicles: Preparations and applications. *Chembiochem* **2010**, *11* (7), 848-865.
79. Torchilin, V., Liposomes as targetable drug carriers. *Critical reviews in therapeutic drug carrier systems* **1985**, *2* (1), 65.
80. duPlessis, J.; Ramachandran, C.; Weiner, N.; Muller, D. G., The influence of lipid composition and lamellarity of liposomes on the physical stability of liposomes upon storage. *International Journal of Pharmaceutics* **1996**, *127* (2), 273-278.
81. Karanth, H.; Murthy, R. S. R., pH-Sensitive liposomes-principle and application in cancer therapy. *Journal of Pharmacy and Pharmacology* **2007**, *59* (4), 469-483.
82. Yu, B.; Lee, R. J.; Lee, L. J., MICROFLUIDIC METHODS FOR PRODUCTION OF LIPOSOMES. In *Methods in Enzymology Liposomes, Pt G*, Duzgunes, N., Ed. 2009; Vol. 465, pp 129-141.
83. Brinkhuis, R. P.; Rutjes, F. P. J. T.; van Hest, J. C. M., Polymeric vesicles in biomedical applications. *Polymer Chemistry* **2011**, *2* (7), 1449-1462.
84. Discher, D. E.; Eisenberg, A., Polymer vesicles. *Science* **2002**, *297* (5583), 967-973.
85. Malinova, V.; Belegriou, S.; de Bruyn Ouboter, D.; Meier, W. P., Biomimetic block copolymer membranes. In *Organic Electronics*, Springer: 2010; pp 213-258.
86. Discher, B. M.; Won, Y.-Y.; Ege, D. S.; Lee, J. C.-M.; Bates, F. S.; Discher, D. E.; Hammer, D. A., Polymersomes: Tough Vesicles Made from Diblock Copolymers. *Science* **1999**, *284* (5417), 1143-1146.
87. Blanazs, A.; Madsen, J.; Battaglia, G.; Ryan, A. J.; Armes, S. P., Mechanistic Insights for Block Copolymer Morphologies: How Do Worms Form Vesicles? *Journal of the American Chemical Society* **2011**.
88. Mai, Y.; Eisenberg, A., Selective Localization of Preformed Nanoparticles in Morphologically Controllable Block Copolymer Aggregates in Solution. *Accounts of Chemical Research* **2012**.
89. (a) Nardin, C.; Widmer, J.; Winterhalter, M.; Meier, W., Amphiphilic block copolymer nanocontainers as bioreactors. *The European Physical Journal E* **2001**, *4* (4), 403-410; (b) Pawar, P. V.; Gohil, S. V.; Jain, J. P.; Kumar, N., Functionalized polymersomes for biomedical applications. *Polymer Chemistry* **2013**, *4* (11), 3160-3176; (c) Schmaljohann, D., Thermo- and pH-responsive polymers in drug delivery. *Advanced drug delivery reviews* **2006**, *58* (15), 1655-1670; (d) Lee, J. S.; Feijen, J., Polymersomes for drug delivery: Design, formation and characterization. *Journal of*

*Controlled Release* **2012**, 161 (2), 473-483; (e) Massignani, M.; Lomas, H.; Battaglia, G., Polymersomes: A Synthetic Biological Approach to Encapsulation and Delivery.

[Without Title] **2010**, 1-40.

90. (a) Li, M. H.; Keller, P., Stimuli-responsive polymer vesicles. *Soft Matter* **2009**, 5 (5), 927-937; (b) Ganta, S.; Devalapally, H.; Shahiwala, A.; Amiji, M., A review of stimuli-responsive nanocarriers for drug and gene delivery. *Journal of controlled release* **2008**, 126 (3), 187-204.

91. Discher, D. E.; Ortiz, V.; Srinivas, G.; Klein, M. L.; Kim, Y.; Christian, D.; Cai, S.; Photos, P.; Ahmed, F., Emerging applications of polymersomes in delivery: From molecular dynamics to shrinkage of tumors. *Progress in Polymer Science* **2007**, 32 (8-9), 838-857.

92. Bain, J.; Ruiz-Pérez, L.; Kennerley, A. J.; Muench, S. P.; Thompson, R.; Battaglia, G.; Staniland, S. S., In situ formation of magnetopolymersomes via electroporation for MRI. *Scientific reports* **2015**, 5.

93. Bain, J.; Berry, M. E.; Dirks, C. E.; Staniland, S. S., Synthesis of ABA Tri-Block Co-Polymer Magnetopolymersomes via Electroporation for Potential Medical Application. *Polymers* **2015**, 7 (12), 2558-2571.

94. (a) Kumar, M.; Grzelakowski, M.; Zilles, J.; Clark, M.; Meier, W., Highly permeable polymeric membranes based on the incorporation of the functional water channel protein Aquaporin Z. *Proceedings of the National Academy of Sciences* **2007**, 104 (52), 20719-20724; (b) Thevenot, J.; Oliveira, H.; Lecommandoux, S., Polymersomes for theranostics. *Journal of Drug Delivery Science and Technology* **2013**, 23 (1), 38-46; (c) Prakash Jain, J.; Yenet Ayen, W.; Kumar, N., Self assembling polymers as polymersomes for drug delivery. *Current pharmaceutical design* **2011**, 17 (1), 65-79.

95. Krishnamoorthy, B.; Karanam, V.; Chellan, V. R.; Siram, K.; Natarajan, T. S.; Gregory, M., Polymersomes as an effective drug delivery system for glioma—a review. *Journal of drug targeting* **2014**, 22 (6), 469-477.

96. Evans, C. W.; Fitzgerald, M.; Clemons, T. D.; House, M. J.; Padman, B. S.; Shaw, J. A.; Saunders, M.; Harvey, A. R.; Zdyrko, B.; Luzinov, I.; Silva, G. A.; Dunlop, S. A.; Iyer, K. S., Multimodal Analysis of PEI-Mediated Endocytosis of Nanoparticles in Neural Cells. *Acs Nano* **2011**, 5 (11), 8640-8648.

97. Whitesides, G. M., The origins and the future of microfluidics. *Nature* **2006**, 442 (7101), 368-373.

98. Brinkhuis, R. P.; Rutjes, F. P.; van Hest, J. C., Polymeric vesicles in biomedical applications. *Polymer Chemistry* **2011**, 2 (7), 1449-1462.

99. (a) Discher, D. E.; Ahmed, F., POLYMERSOMES. *Annual Review of Biomedical Engineering* **2006**, 8 (1), 323-341; (b) Lee, J. C. M.; Bermudez, H.; Discher, B. M.; Sheehan, M. A.; Won, Y. Y.; Bates, F. S.; Discher, D. E., Preparation, stability, and in vitro performance of vesicles made with diblock copolymers. *Biotechnology and bioengineering* **2001**, 73 (2), 135-145; (c) Harris, J. K.; Rose, G. D.; Bruening, M. L., Spontaneous generation of multilamellar vesicles from ethylene oxide/butylene oxide diblock copolymers. *Langmuir* **2002**, 18 (14), 5337-5342; (d) Lu, Y.; Dong, L.; Zhang, L.-C.; Su, Y.-D.; Yu, S.-H., Biogenic and biomimetic magnetic nanosized assemblies. *Nano Today* **2012**, 7 (4), 297-315.

100. (a) Meier, W.; Nardin, C.; Winterhalter, M., Reconstitution of channel proteins in (polymerized) ABA triblock copolymer membranes. *Angewandte Chemie International Edition* **2000**, 39 (24), 4599-4602; (b) Nardin, C.; Winterhalter, M.; Meier, W., Giant free-standing ABA triblock copolymer membranes. *Langmuir* **2000**, 16 (20), 7708-7712.

101. Onaca, O.; Nallani, M.; Ihle, S.; Schenk, A.; Schwaneberg, U., Functionalized nanocompartments (Synthosomes): Limitations and prospective applications in industrial biotechnology. *Biotechnology journal* **2006**, 1 (7-8), 795-805.

102. Ishii, F.; Takamura, A.; Ishigami, Y., Procedure for preparation of lipid vesicles (liposomes) using the coacervation (phase separation) technique. *Langmuir* **1995**, *11* (2), 483-486.
103. Mui, B.; Hope, M. J.; Gregoriadis, G., Formation of large unilamellar vesicles by extrusion. *Liposome technology* **2006**, *1*, 55.
104. Roy, M. T.; Gallardo, M.; Estelrich, J., Bilayer Distribution of Phosphatidylserine and Phosphatidylethanolamine in Lipid Vesicles. *Bioconjugate Chemistry* **1997**, *8* (6), 941-945.
105. (a) Pautot, S.; Frisken, B. J.; Weitz, D., Engineering asymmetric vesicles. *Proceedings of the National Academy of Sciences of the United States of America* **2003**, *100* (19), 10718; (b) Pautot, S.; Frisken, B. J.; Weitz, D. A., Production of unilamellar vesicles using an inverted emulsion. *Langmuir* **2003**, *19* (7), 2870-2879.
106. (a) Shum, H. C.; Lee, D.; Yoon, I.; Kodger, T.; Weitz, D. A., Double emulsion templated monodisperse phospholipid vesicles. *Langmuir* **2008**, *24* (15), 7651-7653; (b) Park, J. W., Effect of Phospholipid Bilayer Phase Asymmetry on Phospholipase D Reaction-Induced Vesicle Rupture. *J. Membr. Biol.* **2011**, *244* (2), 55-59.
107. (a) Hwang, W. L.; Chen, M.; Cronin, B. d.; Holden, M. A.; Bayley, H., Asymmetric Droplet Interface Bilayers. *Journal of the American Chemical Society* **2008**, *130* (18), 5878-5879; (b) Richmond, D. L.; Schmid, E. M.; Martens, S.; Stachowiak, J. C.; Liska, N.; Fletcher, D. A., Forming giant vesicles with controlled membrane composition, asymmetry, and contents. *Proceedings of the National Academy of Sciences* **2011**, *108* (23), 9431-9436.
108. Blanazs, A.; Armes, S. P.; Ryan, A. J., Self-Assembled Block Copolymer Aggregates: From Micelles to Vesicles and their Biological Applications. *Macromolecular Rapid Communications* **2009**, *30* (4-5), 267-277.
109. Ai, H.; Jones, S. A.; Lvov, Y. M., Biomedical applications of electrostatic layer-by-layer nano-assembly of polymers, enzymes, and nanoparticles. *Cell biochemistry and biophysics* **2003**, *39* (1), 23-43.
110. Letchford, K.; Burt, H., A review of the formation and classification of amphiphilic block copolymer nanoparticulate structures: micelles, nanospheres, nanocapsules and polymersomes. *European journal of pharmaceuticals and biopharmaceutics* **2007**, *65* (3), 259-269.
111. Bermudez, H.; Brannan, A. K.; Hammer, D. A.; Bates, F. S.; Discher, D. E., Molecular weight dependence of polymersome membrane structure, elasticity, and stability. *Macromolecules* **2002**, *35* (21), 8203-8208.
112. Smart, T. P.; Ryan, A. J.; Howse, J. R.; Battaglia, G., Homopolymer Induced Aggregation of Poly (ethylene oxide) n-b-poly (butylene oxide) m Polymersomes. *Langmuir* **2009**, *26* (10), 7425-7430.
113. (a) Eltayeb, M.; Stride, E.; Edirisinghe, M., Electrospayed core-shell polymer-lipid nanoparticles for active component delivery. *Nanotechnology* **2013**, *24* (46), 465604; (b) Pareta, R.; Edirisinghe, M., A novel method for the preparation of biodegradable microspheres for protein drug delivery. *Journal of the Royal Society Interface* **2006**, *3* (9), 573-582.
114. (a) Stride, E.; Edirisinghe, M., Novel microbubble preparation technologies. *Soft Matter* **2008**, *4* (12), 2350-2359; (b) Farook, U.; Stride, E.; Edirisinghe, M., Preparation of suspensions of phospholipid-coated microbubbles by coaxial electrohydrodynamic atomization. *Journal of the Royal Society Interface* **2009**, *6* (32), 271-277.
115. Jaworek, A.; Krupa, A. In *Main modes of electrohydrodynamic spraying of liquids*, Third International Conference on Multiphase Flow, Lyon, France. Retrieved from: [http://www.imp.gda.pl/fileadmin/old\\_imp/ehd/lyon-98s.pdf](http://www.imp.gda.pl/fileadmin/old_imp/ehd/lyon-98s.pdf), 1998.
116. Xu, L.; Wang, X.; Lei, T.; Sun, D.; Lin, L., Electrohydrodynamic deposition of polymeric droplets under low-frequency pulsation. *Langmuir* **2011**, *27* (10), 6541-6548.

117. Abkarian, M.; Loiseau, E.; Massiera, G., Continuous droplet interface crossing encapsulation (cDICE) for high throughput monodisperse vesicle design. *Soft Matter* **2011**.
118. Loiseau, E.; Abkarian, M.; Massiera, G., Continuous droplet interface crossing encapsulation for high through-put monodisperse vesicle design. *European Biophysics Journal with Biophysics Letters* **2011**, *40*, 238-238.
119. Sun, J.-B.; Zhao, F.; Tang, T.; Jiang, W.; Tian, J.-s.; Li, Y.; Li, J.-L., High-yield growth and magnetosome formation by *Magnetospirillum gryphiswaldense* MSR-1 in an oxygen-controlled fermentor supplied solely with air. *Applied microbiology and biotechnology* **2008**, *79* (3), 389-397.
120. Mayer, L. D.; Hope, M. J.; Cullis, P. R., Vesicles of variable sizes produced by a rapid extrusion procedure. *Biochimica et Biophysica Acta (BBA) - Biomembranes* **1986**, *858* (1), 161-168.
121. (a) Mann, S.; Hannington, J. P., FORMATION OF IRON-OXIDES IN UNILAMELLAR VESICLES. *Journal of Colloid and Interface Science* **1988**, *122* (2), 326-335; (b) Mann, S.; Hannington, J. P.; Williams, R. J. P., Phospholipid vesicles as a model system for biomineralization. *Nature* **1986**, *324* (6097), 565-567.
122. Faure, C.; Meyre, M.-E.; Trépout, S.; Lambert, O.; Lebraud, E., Magnetic Multilamellar Liposomes Produced by In Situ Synthesis of Iron Oxide Nanoparticles: "Magnetonions". *The Journal of Physical Chemistry B* **2009**, *113* (25), 8552-8559.
123. Sangregorio, C.; Wiemann, J. K.; O'Connor, C. J.; Rosenzweig, Z., A new method for the synthesis of magnetoliposomes. *Journal of Applied Physics* **1999**, *85* (8), 5699-5701.
124. Megens, M.; Korman, C. E.; Ajo-Franklin, C. M.; Horsley, D. A., Faster-than-anticipated Na<sup>+</sup>/Cl<sup>-</sup> diffusion across lipid bilayers in vesicles. *Biochimica et Biophysica Acta (BBA)-Biomembranes* **2014**.
125. Mann, S.; Williams, R. J. P., Precipitation within unilamellar vesicles. Part 1. Studies of silver (I) oxide formation. *J. Chem. Soc., Dalton Trans.* **1983**, (2), 311-316.
126. Kim, K. T.; Meeuwissen, S. A.; Nolte, R. J.; van Hest, J. C., Smart nanocontainers and nanoreactors. *Nanoscale* **2010**, *2* (6), 844-858.
127. (a) Saha, K.; Agasti, S. S.; Kim, C.; Li, X.; Rotello, V. M., Gold nanoparticles in chemical and biological sensing. *Chemical Reviews* **2012**, *112* (5), 2739-2779; (b) Zeng, S.; Yong, K.-T.; Roy, I.; Dinh, X.-Q.; Yu, X.; Luan, F., A review on functionalized gold nanoparticles for biosensing applications. *Plasmonics* **2011**, *6* (3), 491-506; (c) Pankhurst, Q.; Thanh, N.; Jones, S.; Dobson, J., Progress in applications of magnetic nanoparticles in biomedicine. *Journal of Physics D: Applied Physics* **2009**, *42* (22), 224001; (d) Pankhurst, Q. A.; Connolly, J.; Jones, S.; Dobson, J., Applications of magnetic nanoparticles in biomedicine. *Journal of physics D: Applied physics* **2003**, *36* (13), R167-R181.
128. (a) Santhosh, P. B.; Ulrih, N. P., Multifunctional Superparamagnetic Iron Oxide Nanoparticles: Promising Tools in Cancer Theranostics. *Cancer letters* **2013**; (b) Svenson, S., Theranostics: Are We There Yet? *Molecular pharmaceuticals* **2013**.
129. Rizzo, L. Y.; Theek, B.; Storm, G.; Kiessling, F.; Lammers, T., Recent progress in nanomedicine: therapeutic, diagnostic and theranostic applications. *Current opinion in biotechnology* **2013**, *24* (6), 1159-1166.
130. Jia, L.; Cui, D.; Bignon, J.; Di Cicco, A.; Wdzieczak-Bakala, J.; Liu, J.; Li, M.-H., Reduction-responsive cholesterol-based block copolymer vesicles for drug delivery. *Biomacromolecules* **2014**, *15* (6), 2206-2217.
131. Laurent, S.; Bridot, J. L.; Vander Elst, L.; Muller, R. N., Magnetic iron oxide nanoparticles for biomedical applications. *Future* **2010**, *2* (3), 427-449.
132. (a) Fang, C.; Kievit, F. M.; Veiseh, O.; Stephen, Z. R.; Wang, T.; Lee, D.; Ellenbogen, R. G.; Zhang, M., Fabrication of magnetic nanoparticles with controllable drug loading and release through a simple assembly approach. *Journal of controlled*

- release **2012**, 162 (1), 233-241; (b) Janib, S. M.; Moses, A. S.; MacKay, J. A., Imaging and drug delivery using theranostic nanoparticles. *Advanced drug delivery reviews* **2010**, 62 (11), 1052-1063; (c) Qiu, D.; An, X.; Chen, Z.; Ma, X., Microstructure study of liposomes decorated by hydrophobic magnetic nanoparticles. *Chemistry and physics of lipids* **2012**, 165 (5), 563-570; (d) Ren, T.; Liu, Q.; Lu, H.; Liu, H.; Zhang, X.; Du, J., Multifunctional polymer vesicles for ultrasensitive magnetic resonance imaging and drug delivery. *Journal of Materials Chemistry* **2012**, 22 (24), 12329-12338; (e) Sanson, C.; Diou, O.; Thevenot, J.; Ibarboure, E.; Soum, A.; Brulet, A.; Miraux, S.; Thiaudiere, E.; Tan, S.; Brisson, A.; Dupuis, V.; Sandre, O.; Lecommandoux, S., Doxorubicin loaded magnetic polymersomes: theranostic nanocarriers for MR imaging and magneto-chemotherapy. *ACS Nano* **2011**, 5 (2), 1122-40.
133. Ding, X.; Cai, K.; Luo, Z.; Li, J.; Hu, Y.; Shen, X., Biocompatible magnetic liposomes for temperature triggered drug delivery. *Nanoscale* **2012**, 4 (20), 6289-6292.
134. Oliveira, H.; Pérez-Andrés, E.; Thevenot, J.; Sandre, O.; Berra, E.; Lecommandoux, S., Magnetic field triggered drug release from polymersomes for cancer therapeutics. *Journal of Controlled Release* **2013**, 169 (3), 165-170.
135. (a) Lauterbur, P. C., Image formation by induced local interactions: examples employing nuclear magnetic resonance. *Nature* **1973**, 242 (5394), 190-191; (b) Mansfield, P.; Pykett, I. L., Biological and medical imaging by NMR. *Journal of Magnetic Resonance (1969)* **1978**, 29 (2), 355-373.
136. Goldhawk, D. E.; Rohani, R.; Sengupta, A.; Gelman, N.; Prato, F. S., Using the magnetosome to model effective gene-based contrast for magnetic resonance imaging. *Wiley Interdisciplinary Reviews: Nanomedicine and Nanobiotechnology* **2012**, 4 (4), 378-388.
137. Vlaardingerbroek, M. T.; Boer, J. A., *Magnetic resonance imaging: theory and practice*. Springer Science & Business Media: 2013.
138. Steen, H.; Schwenger, V., Good MRI images: to Gad or not to Gad? *Pediatr Nephrol* **2007**, 22 (9), 1239-1242.
139. Jun, Y.-w.; Huh, Y.-M.; Choi, J.-s.; Lee, J.-H.; Song, H.-T.; Kim, Y.; Yoon, S.; Kim, K.-S.; Shin, J.-S.; Suh, J.-S.; Cheon, J., Nanoscale Size Effect of Magnetic Nanocrystals and Their Utilization for Cancer Diagnosis via Magnetic Resonance Imaging. *Journal of the American Chemical Society* **2005**, 127 (16), 5732-5733.
140. (a) Drummond, D. C.; Zignani, M.; Leroux, J., Current status of pH-sensitive liposomes in drug delivery. *Progress in lipid research* **2000**, 39 (5), 409-60; (b) Simões, S.; Moreira, J. N.; Fonseca, C.; Düzgüneş, N.; Pedroso de Lima, M. C., On the formulation of pH-sensitive liposomes with long circulation times. *Advanced drug delivery reviews* **2004**, 56 (7), 947-965.
141. (a) Kumar, C. S. S. R.; Mohammad, F., Magnetic nanomaterials for hyperthermia-based therapy and controlled drug delivery. *Advanced drug delivery reviews* **2011**; (b) Hergt, R.; Dutz, S.; Müller, R.; Zeisberger, M., Magnetic particle hyperthermia: nanoparticle magnetism and materials development for cancer therapy. *Journal of Physics: Condensed Matter* **2006**, 18 (38), S2919.
142. (a) Dobson, J., Magnetic nanoparticles for drug delivery. *Drug development research* **2006**, 67 (1), 55-60; (b) Dobson, J., Magnetic micro- and nano-particle-based targeting for drug and gene delivery. *Nanomedicine* **2006**, 1 (1), 31-37.
143. Deatsch, A. E.; Evans, B. A., Heating efficiency in magnetic nanoparticle hyperthermia. *Journal of Magnetism and Magnetic Materials* **2014**, 354, 163-172.
144. Alphandéry, E.; Guyot, F.; Chebbi, I., Preparation of chains of magnetosomes, isolated from *Magnetospirillum magneticum* strain AMB-1 magnetotactic bacteria, yielding efficient treatment of tumors using magnetic hyperthermia. *International journal of pharmaceutics* **2012**, 434 (1-2), 444-452.

145. Wildeboer, R.; Southern, P.; Pankhurst, Q., On the reliable measurement of specific absorption rates and intrinsic loss parameters in magnetic hyperthermia materials. *Journal of Physics D: Applied Physics* **2014**, *47* (49), 495003.
146. Li, Z.; Kawashita, M.; Araki, N.; Mistumori, M.; Hiraoka, M., Effect of Particle Size of Magnetite Nanoparticles on Heat Generating Ability under Alternating Magnetic Field. *Bioceramics Development and Applications* **1**.
147. (a) Tanaka, T.; Maruyama, K.; Yoda, K.; Nemoto, E.; Udagawa, Y.; Nakayama, H.; Takeyama, H.; Matsunaga, T., Development and evaluation of an automated workstation for single nucleotide polymorphism discrimination using bacterial magnetic particles. *Biosensors and Bioelectronics* **2003**, *19* (4), 325-330; (b) Yoshino, T.; Kato, F.; Takeyama, H.; Nakai, M.; Yakabe, Y.; Matsunaga, T., Development of a novel method for screening of estrogenic compounds using nano-sized bacterial magnetic particles displaying estrogen receptor. *Analytica Chimica Acta* **2005**, *532* (2), 105-111; (c) Tanaka, T.; Matsunaga, T., Fully Automated Chemiluminescence Immunoassay of Insulin Using Antibody-Protein A-Bacterial Magnetic Particle Complexes. *Analytical Chemistry* **2000**, *72* (15), 3518-3522; (d) Sode, K.; Kudo, S.; Sakaguchi, T.; Nakamura, N.; Matsunaga, T., Application of bacterial magnetic particles for highly selective mRNA recovery system. *Biotechnol Tech* **1993**, *7* (9), 688-694; (e) Yoza, B.; Arakaki, A.; Matsunaga, T., DNA extraction using bacterial magnetic particles modified with hyperbranched polyamidoamine dendrimer. *Journal of Biotechnology* **2003**, *101* (3), 219-228.
148. (a) Xie, J.; Chen, K.; Chen, X., Production, modification and bio-applications of magnetic nanoparticles gestated by magnetotactic bacteria. *Nano research* **2009**, *2* (4), 261-278; (b) Herborn, C. U.; Papanikolaou, N.; Reszka, R.; Grünberg, K.; Schüler, D.; Debatin, J. F., [Magnetosomes as biological model for iron binding: relaxivity determination with MRI]. *Rofo* **2003**, *175* (6), 830-834.
149. Hergt, R.; Hiergeist, R.; Zeisberger, M.; Schüler, D.; Heyen, U.; Hilger, I.; Kaiser, W. A., Magnetic properties of bacterial magnetosomes as potential diagnostic and therapeutic tools. *Journal of Magnetism and Magnetic Materials* **2005**, *293* (1), 80-86.
150. Alphandery, E.; Faure, S.; Seksek, O.; Guyot, F. o.; Chebbi, I., Chains of magnetosomes extracted from AMB-1 magnetotactic bacteria for application in alternative magnetic field cancer therapy. *ACS nano* **2011**, *5* (8), 6279-6296.
151. Lee, Y.; Lee, J.; Bae, C. J.; Park, J.-G.; Noh, H.-J.; Park, J.-H.; Hyeon, T., Large-scale synthesis of uniform and crystalline magnetite nanoparticles using reverse micelles as nanoreactors under reflux conditions. *Advanced Functional Materials* **2005**, *15* (3), 503-509.
152. Fenske, D. B.; Cullis, P. R., Encapsulation of drugs within liposomes by pH-gradient techniques. *Liposome Technology: Entrapment of drugs and other materials into liposomes* **2007**, *2*, 27-50.
153. Denning, E. J.; Beckstein, O., Influence of lipids on protein-mediated transmembrane transport. *Chemistry and physics of lipids* (0).
154. Mann, S.; Kime, M. J.; Ratcliffe, R. G.; Williams, R. J. P., Precipitation within unilamellar vesicles. Part 2. Membrane control of ion transport. *J. Chem. Soc., Dalton Trans.* **1983**, (4), 771-774.
155. Mamasheva, E.; O'Donnell, C.; Bandekar, A.; Sofou, S., Heterogeneous liposome membranes with pH-triggered permeability enhance the in vitro antitumor activity of folate-receptor targeted liposomal doxorubicin. *Molecular pharmaceuticals* **2011**, *8* (6), 2224-2232.
156. Gurtovenko, A. A.; Vattulainen, I., Ion leakage through transient water pores in protein-free lipid membranes driven by transmembrane ionic charge imbalance. *Biophysical journal* **2007**, *92* (6), 1878-1890.
157. Paula, S.; Volkov, A.; Van Hoek, A.; Haines, T.; Deamer, D. W., Permeation of protons, potassium ions, and small polar molecules through phospholipid bilayers as a function of membrane thickness. *Biophysical journal* **1996**, *70* (1), 339.

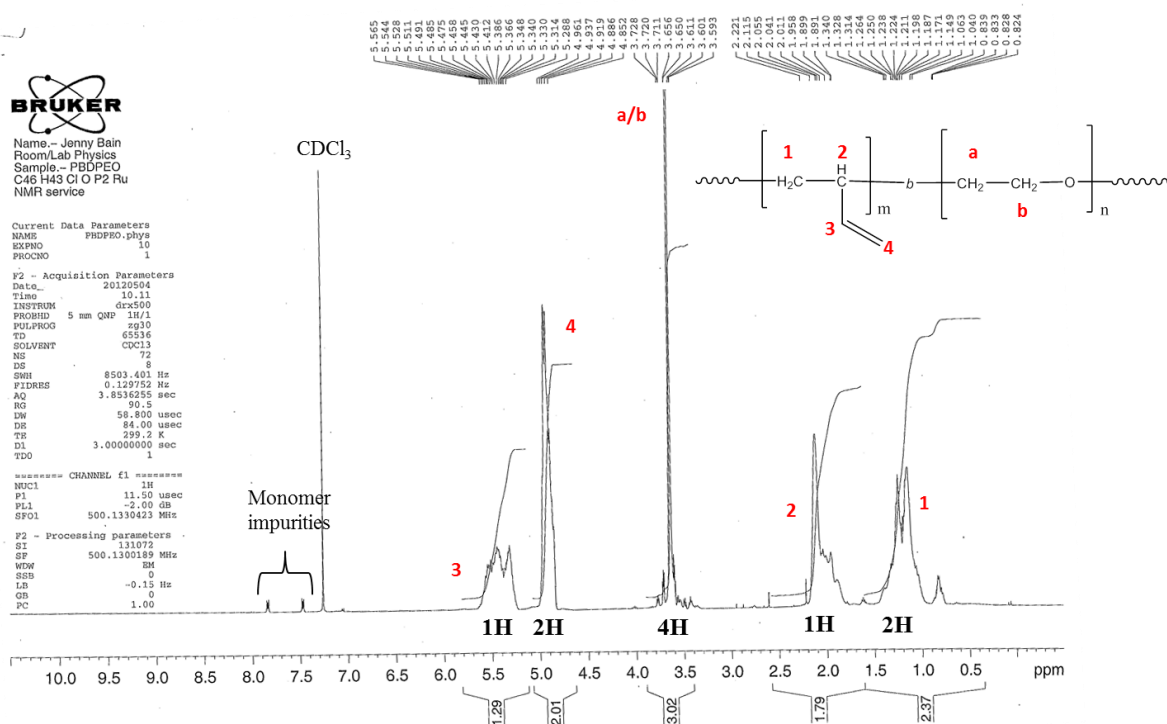
158. Chakrabarti, A. C.; Veiro, J. A.; Wong, N. S.; Wheeler, J. J.; Cullis, P. R., Generation and characterization of iron-and barium-loaded liposomes. *Biochimica et Biophysica Acta (BBA)-Biomembranes* **1992**, *1108* (2), 233-239.
159. (a) Weaver, J. C., Electroporation: a general phenomenon for manipulating cells and tissues. *Journal of cellular biochemistry* **1993**, *51* (4), 426-435; (b) Gehl, J., Electroporation: theory and methods, perspectives for drug delivery, gene therapy and research. *Acta Physiologica Scandinavica* **2003**, *177* (4), 437-447.
160. (a) Tieleman, D. P., The molecular basis of electroporation. *BMC biochemistry* **2004**, *5* (1), 10; (b) Weaver, J. C.; Chizmadzhev, Y. A., Theory of electroporation: a review. *Bioelectrochemistry and bioenergetics* **1996**, *41* (2), 135-160.
161. Wang, L.; Chierico, L.; Little, D.; Patikarnmonthon, N.; Yang, Z.; Azzouz, M.; Madsen, J.; Armes, S. P.; Battaglia, G., Encapsulation of Biomacromolecules within Polymersomes by Electroporation. *Angewandte Chemie International Edition* **2012**, *51* (44), 11122-11125.
162. Lopez, A.; Rols, M.; Teissie, J., Phosphorus-31 NMR analysis of membrane phospholipid organization in viable, reversibly electropermeabilized Chinese hamster ovary cells. *Biochemistry* **1988**, *27* (4), 1222-1228.
163. (a) Tieleman, D. P.; Leontiadou, H.; Mark, A. E.; Marrink, S.-J., Simulation of pore formation in lipid bilayers by mechanical stress and electric fields. *Journal of the American Chemical Society* **2003**, *125* (21), 6382-6383; (b) Bennett, W. D.; Sapay, N.; Tieleman, D. P., Atomistic simulations of pore formation and closure in lipid bilayers. *Biophysical journal* **2014**, *106* (1), 210-219.
164. Escoffre, J. M.; Portet, T.; Wasungu, L.; Teissié, J.; Dean, D.; Rols, M. P., What is (still not) known of the mechanism by which electroporation mediates gene transfer and expression in cells and tissues. *Molecular biotechnology* **2009**, *41* (3), 286-295.
165. Mürbe, J.; Rechtenbach, A.; Töpfer, J., Synthesis and physical characterization of magnetite nanoparticles for biomedical applications. *Materials Chemistry and Physics* **2008**, *110* (2-3), 426-433.
166. Mori, S.; Barth, H. G., *Size exclusion chromatography*. Springer Science & Business Media: 2013.
167. (a) Reed, P. W.; Lardy, H. A., A23187: a divalent cation ionophore. *Journal of Biological Chemistry* **1972**, *247* (21), 6970-6977; (b) Drobnies, A. E.; Deber, C. M., Cation transport properties of a synthetic Ca<sup>2+</sup>-selective peptide ionophore in phospholipid and sarcoplasmic reticulum vesicles. *Biochimica et Biophysica Acta (BBA) - Biomembranes* **1982**, *691* (1), 30-36.
168. Thet, N. T.; Jenkins, A. T. A., An electrochemical sensor concept for the detection of bacterial virulence factors from *Staphylococcus aureus* and *Pseudomonas aeruginosa*. *Electrochemistry Communications* **2015**.
169. Hennessy, D. J.; Reid, G. R.; Smith, F. E.; Thompson, S. L., Ferene-a new spectrophotometric reagent for iron. *Canadian journal of chemistry* **1984**, *62* (4), 721-724.
170. Karyakin, A. A., Prussian blue and its analogues: electrochemistry and analytical applications. *Electroanalysis* **2001**, *13* (10), 813-819.
171. Twigg, R., Oxidation-reduction aspects of resazurin. *Nature* **1945**, *155* (3935), 401-402.
172. Mullis, K. B.; Erlich, H. A.; Arnheim, N.; Horn, G. T.; Saiki, R. K.; Scharf, S. J., One of the first Polymerase Chain Reaction (PCR) patents. Google Patents: 1987.
173. Joseph, S.; David, W. R., Molecular cloning: a laboratory manual. *Cold Spring Harbor Laboratory Press, Cold Spring Harbor, New York* **2001**, *2*.
174. Sanger, F.; Nicklen, S.; Coulson, A. R., DNA sequencing with chain-terminating inhibitors. *Proceedings of the National Academy of Sciences* **1977**, *74* (12), 5463-5467.
175. Studier, F. W., Protein production by auto-induction in high-density shaking cultures. *Protein expression and purification* **2005**, *41* (1), 207-234.

176. Hengen, P. N., Purification of His-Tag fusion proteins from *Escherichia coli*. *Trends in biochemical sciences* **1995**, *20* (7), 285-286.
177. Williams, D. B.; Carter, C. B., *The transmission electron microscope*. Springer: 1996.
178. Berne, B. J.; Pecora, R., *Dynamic light scattering: with applications to chemistry, biology, and physics*. Courier Corporation: 2000.
179. Housecroft, C., E., Constable, Edwin, C., *Chemistry: An Introduction to Organic, Inorganic and Physical Chemistry: 3rd Edition*. **2006**, 1285.
180. Egerton, R., *Electron energy-loss spectroscopy in the electron microscope*. Springer Science & Business Media: 2011.
181. Sawicki, M.; Stefanowicz, W.; Ney, A., Sensitive SQUID magnetometry for studying nanomagnetism. *Semiconductor Science and Technology* **2011**, *26* (6), 064006.
182. Laemmli, U. K., Cleavage of structural proteins during the assembly of the head of bacteriophage T4. *nature* **1970**, *227* (5259), 680-685.
183. Martineau, C.; Whyte, L. G.; Greer, C. W., Development of a SYBR safe™ technique for the sensitive detection of DNA in cesium chloride density gradients for stable isotope probing assays. *Journal of microbiological methods* **2008**, *73* (2), 199-202.
184. Hull, M. C.; Sauer, D. B.; Hovis, J. S., Influence of lipid chemistry on the osmotic response of cell membranes: Effect of non-bilayer forming lipids. *Journal of Physical Chemistry B* **2004**, *108* (40), 15890-15895.
185. Akutsu, H., Direct determination by Raman scattering of the conformation of the choline group in phospholipid bilayers. *Biochemistry* **1981**, *20* (26), 7359-7366.
186. Kirby, C.; Clarke, J.; Gregoriadis, G., EFFECT OF THE CHOLESTEROL CONTENT OF SMALL UNILAMELLAR LIPOSOMES ON THEIR STABILITY INVIVO AND INVITRO. *Biochemical Journal* **1980**, *186* (2), 591-598.
187. Whittenton, J.; Harendra, S.; Pitchumani, R.; Mohanty, K.; Vipulanandan, C.; Thevananther, S., Evaluation of asymmetric liposomal nanoparticles for encapsulation of polynucleotides. *Langmuir* **2008**, *24* (16), 8533-8540.
188. Hillmyer, M. A.; Bates, F. S., Synthesis and Characterization of Model Polyalkane-Poly(ethylene oxide) Block Copolymers. *Macromolecules* **1996**, *29* (22), 6994-7002.
189. Dinu, M. V.; Spulber, M.; Renggli, K.; Wu, D.; Monnier, C. A.; Petri-Fink, A.; Bruns, N., Filling Polymersomes with Polymers by Peroxidase-Catalyzed Atom Transfer Radical Polymerization. *Macromolecular Rapid Communications* **2015**, *36* (6), 507-514.
190. Jogler, C.; Schüler, D., Genomics, Genetics, and Cell Biology of Magnetosome Formation. *Annual Review of Microbiology* **2009**, *63* (1), 501-521.
191. Kim, H.; Lee, H.; Shin, D., The FeoA protein is necessary for the FeoB transporter to import ferrous iron. *Biochemical and Biophysical Research Communications* **2012**, *423* (4), 733-738.
192. Schoenbach, K. H.; Beebe, S. J.; Buescher, E. S., Intracellular effect of ultrashort electrical pulses. *Bioelectromagnetics* **2001**, *22* (6), 440-448.
193. Danino, D., Cryo-TEM of Molecular Assemblies. *Current Opinion in Colloid & Interface Science* **2012**, 316-329.
194. Powell, K. T.; Weaver, J. C., Transient aqueous pores in bilayer membranes: a statistical theory. *Bioelectrochemistry and bioenergetics* **1986**, *15* (2), 211-227.
195. Melikov, K. C.; Frolov, V. A.; Shcherbakov, A.; Samsonov, A. V.; Chizmadzhev, Y. A.; Chernomordik, L. V., Voltage-induced nonconductive pre-pores and metastable single pores in unmodified planar lipid bilayer. *Biophysical journal* **2001**, *80* (4), 1829-1836.
196. Lomora, M.; Itef, F.; Dinu, I. A.; Palivan, C. G., Selective ion-permeable membranes by insertion of biopores into polymersomes. *Physical Chemistry Chemical Physics* **2015**.

197. Itel, F.; Chami, M.; Najer, A.; Lörcher, S.; Wu, D.; Dinu, I. A.; Meier, W., Molecular Organization and Dynamics in Polymersome Membranes: A Lateral Diffusion Study. *Macromolecules* **2014**, *47* (21), 7588-7596.
198. P. Bakhshi, J. B., M. Gul, E. Stride, M. Edirisinghe, S. S. Staniland Manufacturing Man-made Magnetosomes: High-Throughput in situ synthesis of biomimetic magnetite loaded nanovesicles. *Nature Nanotechnology Under Review*.
199. Bazylinski, D. A.; Williams, T. J., Ecophysiology of magnetotactic bacteria. In *Magnetoreception and magnetosomes in bacteria*, Springer: 2007; pp 37-75.
200. (a) Lee, C.; Bain, C. D., Raman spectra of planar supported lipid bilayers. *Biochimica et Biophysica Acta (BBA) - Biomembranes* **2005**, *1711* (1), 59-71; (b) Lhert, F.; Capelle, F.; Blaudez, D.; Heywang, C.; Turllet, J. M., Raman Spectroscopy of Phospholipid Black Films. *The Journal of Physical Chemistry B* **2000**, *104* (49), 11704-11707.
201. Loudet, A.; Burgess, K., BODIPY dyes and their derivatives: syntheses and spectroscopic properties. *Chemical reviews* **2007**, *107* (11), 4891-4932.
202. Alphandéry, E.; Faure, S. p.; Seksek, O.; Guyot, F. o.; Chebbi, I. n., Chains of Magnetosomes Extracted from AMB-1 Magnetotactic Bacteria for Application in Alternative Magnetic Field Cancer Therapy. *Acs Nano* **2011**, *5* (8), 6279-6296.
203. Galloway, J. M.; Bramble, J. P.; Rawlings, A. E.; Burnell, G.; Evans, S. D.; Staniland, S. S., Nanomagnetic Arrays Formed with the Biomineralization Protein Mms6. *Journal of Nano Research* **2012**, *17*, 127-146.
204. (a) Lang, C.; Schüller, D., Expression of green fluorescent protein fused to magnetosome proteins in microaerophilic magnetotactic bacteria. *Applied and environmental microbiology* **2008**, *74* (15), 4944-4953; (b) Yoshino, T.; Hirabe, H.; Takahashi, M.; Kuhara, M.; Takeyama, H.; Matsunaga, T., Magnetic cell separation using nano-sized bacterial magnetic particles with reconstructed magnetosome membrane. *Biotechnology and bioengineering* **2008**, *101* (3), 470-477.
205. Wang, W.; Bu, W.; Wang, L.; Palo, P. E.; Mallapragada, S.; Nilsen-Hamilton, M.; Vaknin, D., Interfacial properties and iron binding to bacterial proteins that promote the growth of magnetite nanocrystals: X-ray reflectivity and surface spectroscopy studies. *Langmuir* **2012**, *28* (9), 4274-4282.
206. Gurnon, D. G.; Whitaker, J. A.; Oakley, M. G., Design and Characterization of a Homodimeric Antiparallel Coiled Coil. *Journal of the American Chemical Society* **2003**, *125* (25), 7518-7519.
207. Burkhard, P.; Stetefeld, J.; Strelkov, S. V., Coiled coils: a highly versatile protein folding motif. *Trends in cell biology* **2001**, *11* (2), 82-88.
208. Brown, D.; London, E., Functions of lipid rafts in biological membranes. *Annual review of cell and developmental biology* **1998**, *14* (1), 111-136.
209. Murat, D.; Quinlan, A.; Vali, H.; Komeili, A., Comprehensive genetic dissection of the magnetosome gene island reveals the step-wise assembly of a prokaryotic organelle. *Proceedings of the National Academy of Sciences* **2010**, *107* (12), 5593-5598.
210. Peters, A. M.; Brookes, M. J.; Hoogenraad, F. G.; Gowland, P. A.; Francis, S. T.; Morris, P. G.; Bowtell, R., T2\* measurements in human brain at 1.5, 3 and 7 T. *Magnetic Resonance Imaging* **2007**, *25* (6), 748-753.
211. (a) Staniland, S.; Williams, W.; Telling, N.; Van Der Laan, G.; Harrison, A.; Ward, B., Controlled cobalt doping of magnetosomes in vivo. *Nature nanotechnology* **2008**, *3* (3), 158-162; (b) Chinnasamy, C.; Senoue, M.; Jeyadevan, B.; Perales-Perez, O.; Shinoda, K.; Tohji, K., Synthesis of size-controlled cobalt ferrite particles with high coercivity and squareness ratio. *Journal of colloid and interface science* **2003**, *263* (1), 80-83; (c) Byrne, J. M.; Coker, V.; Moise, S.; Wincott, P.; Vaughan, D.; Tuna, F.; Arenholz, E.; van der Laan, G.; Patrick, R.; Lloyd, J., Controlled cobalt doping in biogenic magnetite nanoparticles. *Journal of The Royal Society Interface* **2013**, *10* (83), 20130134.

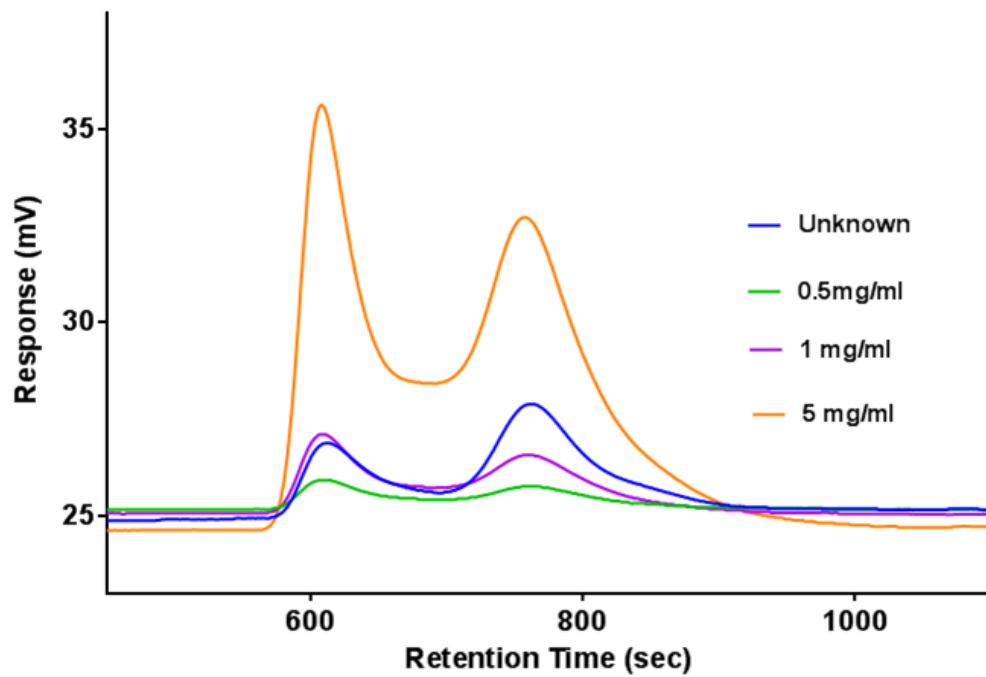
212. Katagiri, K.; Nakamura, M.; Koumoto, K., Magneto-responsive smart capsules formed with polyelectrolytes, lipid bilayers and magnetic nanoparticles. *ACS applied materials & interfaces* **2010**, *2* (3), 768-773.
213. Versluis, F.; Voskuhl, J.; van Kolck, B.; Zope, H.; Bremmer, M.; Albregtse, T.; Kros, A., In Situ Modification of Plain Liposomes with Lipidated Coiled Coil Forming Peptides Induces Membrane Fusion. *Journal of the American Chemical Society* **2013**, *135* (21), 8057-8062.
214. (a) Coakley, K. M.; Liu, Y.; McGehee, M. D.; Frindell, K. L.; Stucky, G. D., Infiltrating Semiconducting Polymers into Self-assembled Mesoporous Titania Films for Photovoltaic Applications. *Advanced Functional Materials* **2003**, *13* (4), 301-306; (b) Coakley, K. M.; McGehee, M. D., Photovoltaic cells made from conjugated polymers infiltrated into mesoporous titania. *Applied Physics Letters* **2003**, *83* (16), 3380-3382.
215. (a) Ghaderi, S.; Ramesh, B.; Seifalian, A. M., Fluorescence nanoparticles "quantum dots" as drug delivery system and their toxicity: a review. *Journal of drug targeting* **2011**, *19* (7), 475-486; (b) Ron, H., A Toxicologic Review of Quantum Dots: Toxicity Depends on Physicochemical and Environmental Factors. *Environmental Health Perspectives* **2006**, *114* (2), 165-172.
216. (a) Ataka, K.; Heberle, J., Bioenergetics at the gold surface: SEIRAS probes photosynthetic and respiratory reactions at the monolayer level. *Biochemical Society transactions* **2008**, *36* (Pt 5), 986; (b) Shin, Y.; Dohnalkova, A.; Lin, Y., Preparation of homogeneous gold-silver alloy nanoparticles using the apoferritin cavity as a nanoreactor. *The Journal of Physical Chemistry C* **2010**, *114* (13), 5985-5989; (c) Genc, R.; Clergeaud, G.; Ortiz, M.; O'Sullivan, C., Shape directed biomineralization of gold nanoparticles using self-assembled lipid structures. *Biomaterials Science* **2014**.

## APPENDIX



**NMR analysis of block co-polymer.** A nuclear magnetic resonance spectrum of block copolymer PBD-PEO used for polymersome formation was taken before the polymer was utilised in film rehydration synthesis. NMR spectrum confirms expected structure for PBD-PEO (1-4 addition).

To determine the dilution effect of the polymersome clean-up, gas chromatography was used to estimate the final concentration of the samples this was by relation of the polymer peak area in the chromatograph the polymer concentration by integration of the areas under the peak an comparison to a sample of a known concentration



Gas chromatography calibration for determination of polymersome concentration. Carried out after dialysis and column clean-up for removal of the basic supernatant prior to iron electroporation.

**Estimation of magnetic material:**

Magnetopolymer film mass = 0.7 mg

Gas chromatography polymer concentration = 0.2 mg/ml

Polymersome area =  $4\pi \times 2.5 \times 10^{-7} = 1.57 \times 10^{-65} \text{ cm}^3$

Volume of Polymer (x) =  $\frac{2x \times 10^{-4}}{1.11}$

N x Area =  $x \times 1.8 \times 10^{-4}$

N<sup>o</sup> of vesicles =  $\frac{x}{Area} = \frac{1.8 \times 10^{-4}}{1.57 \times 10^{-65}} = 1.146 \times 10^{61}$

Therefore volume occupied =  $n \times 100 \text{ nm}^3$

Magnetic film total mass = 0.7 mg/ml

Polymer mass = 0.2 mg/ml

Therefore theoretical internal volume = 0.7 – 0.2 = 0.5 mg/ml

$$4\pi r^2 \times 5 : \frac{3}{4}\pi r^3$$

$$4 \times \pi \times 50^2 \times 5 : \frac{3}{4} \times \pi \times 55^2$$

$$157080 : 392012$$

$$1 : 2.5$$

$$0.2 : 0.5$$

Elemental analysis

2000 : 22.3 ppm

2000 : 28.46 ppm (correction for magnetite Mw)

2000 : 28.99 ppm (correction for maghemite Mw)

$$\% \text{ Magnetite} = \frac{\text{Magnetite ppm}}{\text{Polymer+Magnetite ppm}} \times 100 = \frac{28.46}{2028.46} \times 100 = 1.40 \%$$

$$\% \text{ Maghemite} = \frac{\text{Maghemite ppm}}{\text{Polymer+Maghemite ppm}} \times 100 = \frac{28.99}{2028.99} \times 100 = 1.42 \%$$

$$\text{Magnetic saturation (from SQUID measurement)} = 3.76 \times 10^{-5} \text{ emu } g^{-1}$$

$$\text{If magnetite} = \frac{\text{emu}}{g} = 91 \text{ therefore } g = \frac{3.76 \times 10^{-5}}{91} = 4.13 \times 10^{-7}$$

$$\% \text{ Magnetite material} = \frac{4.13 \times 10^{-4}}{0.200413} \times 100 = 0.20 \%$$

$$\text{If magnetite} = \frac{\text{emu}}{g} = 80 \text{ therefore } g = \frac{3.76 \times 10^{-5}}{80} = 4.7 \times 10^{-7}$$

$$\% \text{ Magnetite material} = \frac{4.7 \times 10^{-4}}{0.20047} \times 100 = 0.23 \%$$

### MTB iron Transporter sequences

**MamN**

MVGFITLAVFIATFAVIYRWAEGSHLAVLAGAAVLVVIGTISGTYTPRMAVQSIYFETLA  
LIFGMAAISALLARSGVYAYLAAGTAELSQQGRWILVMMALVTYGISLASNSLITVAVV  
VPVTLTVCFRTGIDPVPVIAEIIAANLGGSSTMIGDFPNMILASAGKLFNDFIGGMMP  
ACLILLAVTFLFFEYRQGDWKKAEIPVDLAWVRGEQLRYSIDIDHRLRLRYGLIIFITVIG  
LVLAGPLKVRPGWIAFVAGLTALALGRFKDEEFFSACGGSDILFFGGLFVMVGALTSVGI  
LDWAVAWLEGVTAGHDRVRAILLMWMAAGVTIFVGGGTSAAVFAPVAATLRLDGDGQAA  
WWALALGIMAGSCAALSGATAGALAMNQYSGFVKRHPELASAAAAGLQFTHREYVRWGLP  
LMGIFLVLSTVYIAVLAG

**MamB**

MKFENCRDCREEVWWAFTADICMTLFGILGLMSGVALVADSLHSGADVVASGVTQLSL  
KISNKPADERYPFGYGNIQYISSAIVGSLLLIGASFLMYGSVVKLISGTYEAPSIFAALGASVTVIV  
NELMYRYQICVGNENNSPAIIANAWDNRSDAISSAAMVGVIASVIGFPIADTIAAIGVSALVG  
HIGLELIGKAVHGLMDSSVDTELLQTAWQIATDTPLVHSIYFLRGRHVGEDVQFDIRLRVDPN  
LRIKDSSMVAEAVRQRIQDEIPHARDIRLFVSPAPAAVTVRV

**MamM**

MRKSGCAVCSRSIGWVGLAVSTVLMVMKAFVGLIGGSQAMLADAMYSLKDMLNALMVIIGT  
TISSKPLDAEHPYGHGKVEFILSMVSVVVFIVLTGYLLVHAVQILLDESLHRTPHLIVLWAALSI  
GVNVGMYFYSRCVAIETNSPLIKTMAKHHHGDATA SGAVALGIIGAHYLNMPWIDPAVALW  
ETIDLLLLGKVVFMDAYRGLMDHTAGEAVQNRIVEAAERVPGVRGVIHLRARYVGQDIWAD  
MIIGVDPENTVEQAHEICEAVQAAVCGKIRRIESLHVSAAEAREIGDTTKPSFSDQPLSFDEVML  
SKVDN

**FeOA**

MPALDSQKIIQGRDAIFQRSRPVAQQMNSDTLSLADLRPEQQGEIVKIETEDGVFK  
RMQSLGVVAGTPVTLDRSAPLGDPRISYSLMGYSGLRNAAEQQIRIRVK

**FeOB**

MHEIKRIAIAGVPNSGKTTLFNALTGATQKVGNWPGVTVEKIEGKFSKLGSTVELVD  
LPGTYNLSPTEDQKVAERVIRDGEYDLIINVVDATNLSRNFLTMDLKERTDQIIVL  
LNMLDVAENEGLEISIDKLSKEIGLPVIPVIAVDKGSVAAVKSIEITADNLPPHNSHA  
TKQEVMDTVKKYAFIDSIYGKVVKEKKDRSQNFTNRVDNLVMNRFAAIIPIFLASMF  
TFWFAIGLGSVFIDFFDIMAGLIFVDIPSELLASINAPELITVILAGGIGAGIQTVAATFVP  
VVFFMFLALAILEDFGYMARVAVVADRFRMRKIGLPGSAFIPMVVGFCTVPAVMAAR  
TLTSKRDRFMTIFMAPFMSCGARLPVYALFCVALFGAYSGLAVFLIYLSGLVMAIFTG  
FLLKNTLFKGTSPSHFVMDLPLYHIPRISAVFKSAWLRLKGFIKRAGIIVVSAVFLSML  
NTIGLENGEISFGNEDSQASILAHAGKTISPIFKPMGISEENWPASVALFTGLFAKEAI  
VGTVNSLYSTMDMQETPADPAAGEEAEGLDIGGTVNEAFTTVYEGLIGVVTSVDLLG  
IGLVTEDSATVSEEIGADATVYKHLAANFTVFSAFAYLLFVLMYFPCLAVIGATRQEM  
GGFYSGVMAVYCTGLGWSVATLFYQITEGRNLFYIALSLAILAGIYATLKYIGNKEVEQ  
TPQLQPL

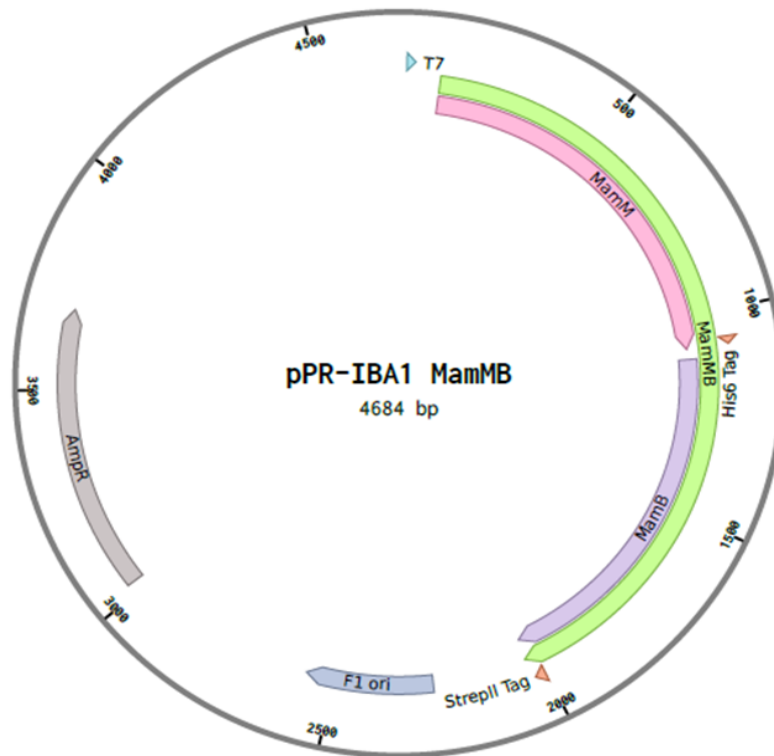
**MamO**

MIEVGETMGELPTNKIVFCERSWKTPVSILAFILFVTFWAWGIYLLDHYDEDDNFHGADDLSVG  
QFLVRNIAMPHVQRLYHTVPPAVVGVGGGGVNAGPVASGAIVGANGYVITTLHSVSNLPEISV  
QVATTGGIRRFPAQVVKTIPTGHDLALLKMQTTEKFLHFRMADVQTVVPGQQVFAFGRNMAG  
APLVRQGLVQSADAPLAVGATQITHLLRSDAVYSWEQTGGPLVNAQGDVLGIN  
IAATGPTGKVEGFTVPAQVIVSHLQDVVRFKKGSAATAPGQPQTQTVAAGSTNWWSKARAV  
VGGPTAIPGMGMNVVQGNVVKGNVAPSIPSGMPFIDTDHVGGAKIGGYSVADIVGLVMLA  
LAAGVTGGMMTMGGGVQLVAGMMVFFGYGMYLIRPVVFLTNVVVYGAASLRNDKAQLVQW  
DKVKLIPWGIAGVILGYFIGNAIGDSVVGILLGLFALIMAGKAVMEILQPNAGEETAES  
ISAAEAEDMDELMALADGTSRPKASGLALPEGHARS AVLGLPMGLFSGILGISGGVIEV  
PLQRYVGRISLQNAIANSSVLVFWASVAGSVVAFHGSSTGLIHWEAPVTLALVMIPGAY  
VGGIIGARLMRVLPRVRLKGVYAATMAAIALKMLTSV

**MagA**

MELHHPELTYAAIVALAAVLCGGMMTRLKQPAVVG YILAGVVLGSPGFGLVSNRDAVATL  
AEFGVLMLLFVIGMKLDIIRFLEVWKTAFITTVLQIAGSVGTALLLRHGLGWSLGLAVVL  
GCAVAVSSTAVVIKVLSSDELDTVPVGRITTLGILIAQDMAVVPMMMLVLESFETKALLPAD  
MARVVLSVLFLVLLFWWLSKRRIDLPIARLSRSDLATLSTLAWCFGTAAISGVLDLSP  
AYGAFLGGVVLGNSAQRDMLLKRAQPIGSVLLMVFFLSIGLLDFKFIWKNLGTVLTLLA  
MVTLFKTALNVTALRLARQDWPSAFLAGVALAQIGEFSSLLAETGKAVKLISAQETKLVV  
AVTVLSLVLSPFWLFMRRMHRVAAVHVHSFRDLVTRLYGDEARAFARTARRARVLVRRG  
SWRDDPNAGPGSGI

## Plasmid Maps



### DNA sequence mamMB

```

ATGCGTAAAAGCGGCTGTACTGTATGCTCTCGTTCATTGGCTGGGTGGGCTGGCGGTTAACACCGTCCTGATGG
TTATGAAAGCATTTGTGGGTCTGATTGGCGGTAGCCAGGCGATGCTGGCGGATGCTATGTAATCCCTGAAAGATAT
GCTGAACGCTCTGATGGTCTTATCGGCACCACTATTAGCTCCAACCCTGGACGCGGAACACCCGTACGGCCAT
GGTAAAGTGGAGTTCATCCTGTCTATGGTCGTCTCTGTGGTTTTCATCGGTCGACCGGTACCTGCTGGTGCATG
CTGTCCAGATTTCTGCTGGACGAAAGCATGCACCGCACCCCTCACCTGATCGTTCTGTGGGCCGCTCTGGTTAGCGT
GGGTGTAACCGTTGCAATGTAATCTTATCCCGTTGCGTCGCAATCGAAACCACTCCCGATCATTAAAACCATG
GCTAAACACCACCGGTGACGCGACCGCAAGCGGTGCGGTAGCGCTGGGTATCATCGGTGCCACTACTCTGAACA
TGCCGTGGATCGATCCGGCTGTGGCTCTGTGGGAAACGATCGACCTGCTGTGCTGGGTAAAGTGGTATTTCATGGA
TGCGTATCGTGGTCTGATGGATCATACTGCTGGCGAAGCTGTGCGAACCAGCATCGTGGATACCGCGAAGCTGTT
CCTGGTGTACGTGGCGTTATTCATCTGCGTGCTCGTTACGTAGGCCAGGACATCTGGGCCGACATGATATCGGCG
TTGACCCGGAACACACCGGTAGAGCAGGCACACGATATCTGCGAAGCTGTTGAGGCCGCGGTTTGGCGTAAATGCG
CCGCATCGAATCTCTGCACGTTTCTGCTGAAGCGCGTGAAGCAGGTGATACCTCCAACCAGCTTTTCCGAAGAA
CCACTGACTTAGACGAAGTAATGCTGTCTAAAGTAGACAACGGTCTCACCATCATCACCACATTAAAGTTAAC
TTAAGAAGGAGATATACAATGAAATTCGAAAACCTGCCGTGATGCGCGTGAAGAAAGTGGTGTGGTGGGCATTAC
CGCTGACATCTGTATGACCTGTTCAAAGGTGTTCTGGGTCTGATGTTCTGGCTCTGTGGCTCTGGTTGCGGACAGC
CTGCACCTCTGGCGCAGATGTGGTTGCGAGCGGTGTAACCCAGCTGTCTCTGAAGATCAGCAATAAACCGCCGACG
AACGTTACCCGTTCCGTTATGGCAACATCCAGTACATCTCCTTCCATCGTAGGTTCCCTGCTGCTGATTGGCGC
ATCCTTCTGATGTACGGCTCTGTAATGAACTGATCTCCGGTACGTATGAAGCGCCATCTATTTTCCGCGCGGCT
GGCGCTAGCGGTGACGGTGATCGTAAACGAACTGATGTACCGTTATCAGATCTGTGTTGGCAACGAAAACAATTCTC
CAGCTATTATCGCAAACGCTTGGGATAACCGCTCTGACGCGATTAGCTCTGCCGCGGTGATGGTTGGCGTTATTGC
TTCCGTTATCGGCTTTCCGATCGCGGACACTATCGCTGCAATTGGTGTCTTCTGCCCTGGTTGGCCGTATCGCCCTG
GAACTGATCGGTACGAGCATCCATGGTCTGATGGATAGCTCTGTTGACACCGAGCTGCTGCAGACTGCATGGCAGG
TGCCATGGATACCCCAATGGTGCACCTCATCTACTTCTGCGTGGCCGTACGTTGGTGGAGACGTGCAGTTTGA
TATCCGCTGCGTGTGACCCGAATCTGCGTATCAAGGACTCTTCTATGGTTGCAGAGGCGGTTCCGCCCGGCATC
CAGGAAGAAATCCCGCACGCCCGTATCCGCTGTTCGTATCTCCGGTCCGCGGCTGCAGCCCGTGTCTAGCG
CTTGGAGCCACCCGAGTTCGAAAATAATAA

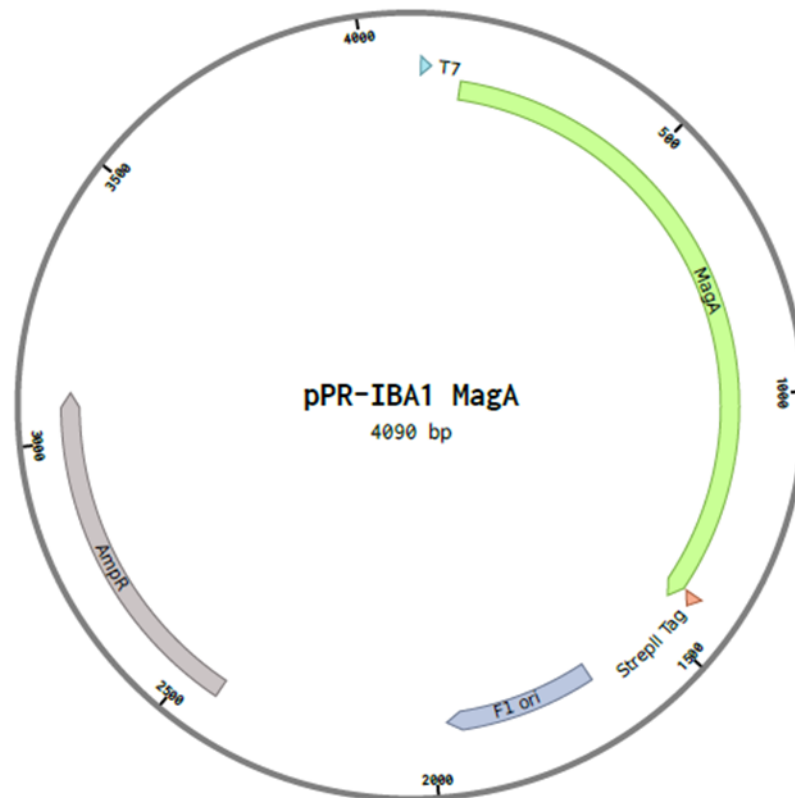
```

### Translation

```

MRKSGCTVCSRSIGWVGLAVNTVLMVMKAFVGLIGGSQAMLADAMYSLKMDLNLMMVVI GTTIS SKPLDAEHPYGH
GKVEFII SMVVS VVFI GLTGYLLVHAVQ ILLDESMHRTPHLIVLWAAALVSVGVNVAMYFYSRCVAIETNSPIIKTM
AKHHHG DATASGAVALGI IGAHYLNMPWIDPAVALWETIDLLLLGKVVFM DAYRGLMDHTAGEAVQNRIVDTAERV
PGVRGVIHLRARIYVGDQIWDAMIIGVDPEHTVEQAHDICEAVQAACVCGKMRRIESLHVSAAEAREAGDTSKPTFSEE
PLTYDEVMLSKVDNGSHHHHHH*V*L*EGDIQMKFENCRDCREEVVMWAFTADI CMTLFKGV LGLMSGSVALVADS
LHSGADVVASGVTQLSLKISNKPADERYPFGYGNIQYISSIVGSLLLIGASF LMYGSMVKLISGTYEAPSIFAAV
GASVTVI VNELMYRQICVGNENNSPAI IANAWDNRSDAISSAAMVGVIASVIGFPIADTIAAIGVSALVGRIGL
ELIGTSHGLMDSVDTELLQTAWQVAMDTPMVHSIYFLRGRHVGEDVQFDIRL RVDPNLRIRKDSMVAEAVRRRI
QE EIPHARDIRL FVSPAPAAAARASAWSHPFQFEK**

```



### DNA sequence magA

```

ATGGAAGTGCATCATCCCGAACTGACCTATGCCGCCATCGTCGCCCTGGCCGCCGTGCTGTGCCGGGGATGATGA
CGGCCTGAAGCAGCCGGCCGTGCTCGGCTACATCCTGGCGGGGTGGTGGTGGGACCCAGCGCTTCGGGCTGGT
GAGCAACCGCAGCCCGTGGCCACCCTGGCCGAGTTCGGCGTGTGATGCTGCTGTTTCGTCATCGGCATGAAGCTG
GACATCATCCGCTTCTCGAAGTGTGGAAGACGGCCATCTTACCACGGTTCTGCAGATCGCCGGCAGCGTGGGCA
CGGCCCTGCTGCTGCGTCACGGCCTGGGCTGGAGCCTGGGCTGGCGGTGGTGTGGGCTGTGCCGTGGCGGTGTC
GTCCACCGCCGTAGTGATCAAGGTGCTGGAATCCTCGGACGAGCTGGACACGCCGGTTCGGCCGACCACCCTTGGC
ATCCTGATCGCCAGGACATGGCGGTGGTGCCCATGATGCTGGTGTGGTGGTGGTGGTGGTGGTGGTGGTGGTGGT
CCGCCGACATGGCCCGGGTGGTGTGCTGGTGTGTTCTGGTGTGCTGTTCTGGTGGTGTGTTCTGGTGGTGTGTTCT
CGACCTGCCGATCACCGCCCGGCTTCCCGCATCTGACCTTGCCACCCTGTCGACCTGGCCTGGTGTTCGGC
ACCGCCGCATCTCCGGCGTGGACTTGTGCGCCGCCTATGGCGCCTTCTGGCGCGGTGGTGTGGCAATT
CCGCCAGCGGACATGCTGTTGAAGCGTGCCAGCCCATCGGCAGCGTGTGCTGATGGTGTTCCTGCTCCAT
CGGGCTGTGCTCGACTCAAGTTCATCTGGAAGAATCTGGGCACCCTTCTCACCTGCTGGCCATGGTACCCTG
TTCAAGACGGCGTGAACGTCACGGCGCTGCGCCTGGCGCGGCAAGGACTGGCCAGCGCCTTCTGGCCGGCGTGG
CCCTGGCCAGATCGGCGAGTTCGTTCTGCTGGCCGAGACCGGCAAGGCGTCAAGCTGATCAGCGCCAGGA
GACCAAGCTGGTGGTGGCGGTACCGTGTGCTCCCTGGTGTGTCGCCGTTCTGGCTGTTACCATGCGGCGCATG
CACCGGTGGCGGCGGTGCATGTCCATTTCGTTCCGCGATCTGGTACGCGGCTGTATGGCGACAGGCCCGCGCTT
TCGCCCGCACCGCGCGGCGGCCGTGTGCTGGTGGCGGTGGTCTCTGGAGGATGACCCCAATGCCGACCTGG
CTCTGGAATTAGCGCTTGGAGCCACCCGAGTTCGAAAAATAATAA

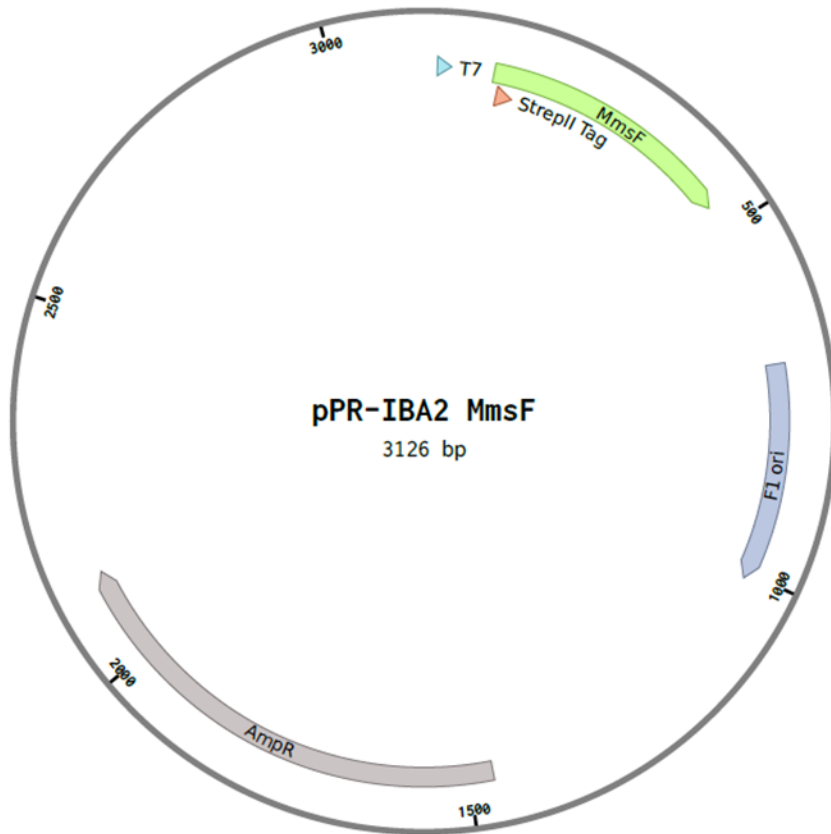
```

### Translation

```

MELHHPELTYAAIVALAAVLGGMMTRLKQPAVVGYYILAGVVLGPGSGFLVSNRDAVATLAEFGVLMLLFVIGMKL
DIIRFLEVWKTAIFTTVLQIAGSVGTALLLRHGLGWSLGLAVVLGCAVAVSSTAVVIKLESSDELDTPVGRITLGL
ILIAQDMAVVPMLLVLESFETKALLPADMARVVLVFLVLLFWWLSKRRIDLPIITARLSRSDLATLSTLAWCFG
TAAISGVLDLSPAYGAFLLGGVVLGNSAQRDMLLKRAQPIGSVLLMVFFLSIGLLDFKFIWKNLGTVLTLLAMVTL
FKTALNVTALRLARQDWPSAFLAGVALAQIGFSLAETGKAVKLI SAQETKLVAVTVLSLVLSPFWLFTMRRM
HRVAHVHVSFRDLVTRLYGDEARAFARTARRARVLVRRGSRDDPNAGPGSGISAWSHPQFEK**

```



### DNA sequence mmsF

```

ATGGCTAGCTGGAGCCACCCGAGTTCGAAAAAGGCGCCATGACTGAAGCTATCCTTCGCAGCAGCCTCGGTGCGC
GCACGACGGTCATGGCGGCGCTGTCCTATCTCAGCGTCTTGTGCTTCGTTCCGCTTCTGGTGGATCGGGACGACGA
ATTCGTCTACTTCCACGCCAAGCAGGGGCTGGTGATCTGGATGTGGGGCGTTTTGGCGCTGTTCCGCGCTGCATGTT
CCCGTTCGGGGAAGTGGATTTTCGGTTTCTCGTCCATGGGGGTCTGGTGTCTCCCTGCTCGGCCTGGTTTCCG
TAGTGTTCACGGGCGTGGAAGCTGCCCTGATCAGCTGGGTCGCCACCGGATCTGA

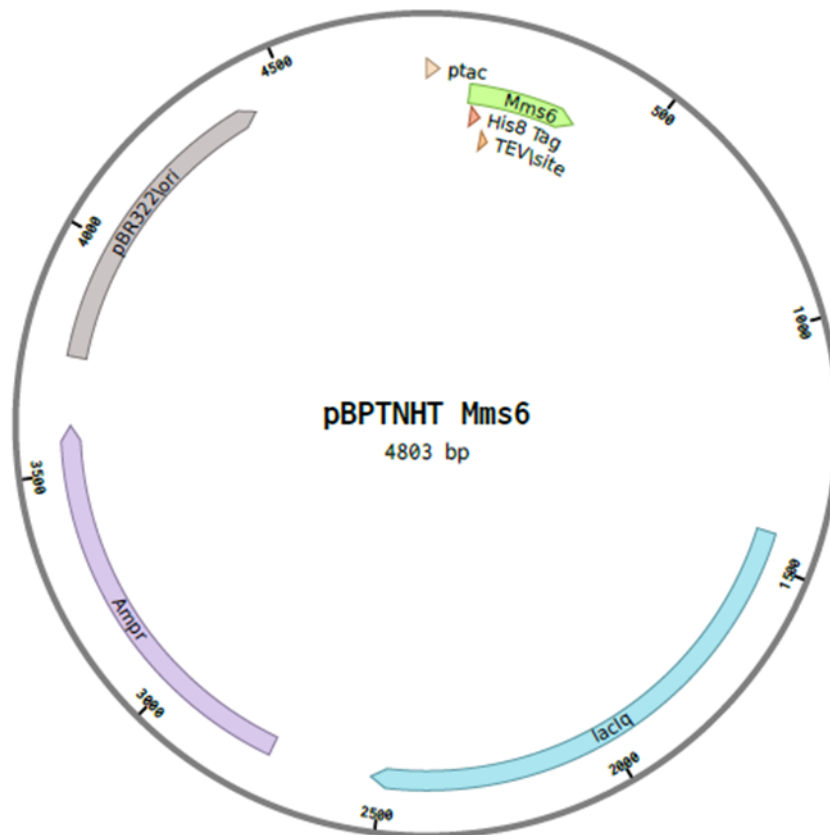
```

### Translation

```

MASWSHPQFEKGAMTEAAILRSTLGARTTVMAAALSYLSVLCFVPLLVDREDFVYFHAKQGLVIWMWGVLALFALHV
PVLGKWI FGFSSMGLVLFSLGLVSVVFQRAWKLPLISWVAHRI *

```



### DNA sequence mms6

```
ATGGGCTCTCATCATCACCATCACCATCACCATGGTTCCACGGAAAACCTGTATTTTCAGGGTCCTAGGATGGGTG
GAACCATCTGGACCGGTAAGGGGCTGGGCCTCGGTCTGGGTCTCGGTCTGGGCCTGGGGCCGATCATTTCTCGG
CGTTGTTGGCGCCGGGGCGGTTTACGCGTATATGAAGAGCCGTGATATCGAATCGGCGCAGAGCGACGAGGAAGTC
GAACTGCGCGACGCGCTGGCC
```

### Translation

```
MGSHHHHHHHGSTENLYFQGPRMGGTIWTGKGLGLGLGLGAWGP IILGVVGAGAVYAYMKSRDIESAQSDEEV
ELRDALA*
```